THE UNIVERSITY *of* EDINBURGH

This thesis has been submitted in fulfilment of the requirements for a postgraduate degree (e.g. PhD, MPhil, DClinPsychol) at the University of Edinburgh. Please note the following terms and conditions of use:

- This work is protected by copyright and other intellectual property rights, which are retained by the thesis author, unless otherwise stated.
- A copy can be downloaded for personal non-commercial research or study, without prior permission or charge.
- This thesis cannot be reproduced or quoted extensively from without first obtaining permission in writing from the author.
- The content must not be changed in any way or sold commercially in any format or medium without the formal permission of the author.
- When referring to this work, full bibliographic details including the author, title, awarding institution and date of the thesis must be given.

Coordinated control and network integration of wave power farms

Anup Jayaprakash Nambiar

A thesis submitted for the degree of Doctor of Philosophy.
The University of Edinburgh.
September 2012

Abstract

Significant progress has been made in the development of wave energy converters (WECs) during recent years, with prototypes and farms of WECs being installed in different parts of the world. With increasing sizes of individual WECs and farms, it becomes necessary to consider the impacts of connecting these to the electricity network and to investigate means by which these impacts may be mitigated. The time-varying and the unpredictable nature of the power generated from wave power farms supplemented by the weak networks to which most of these farms will be connected to, makes the question of integrating a large quantity of wave power to the network more challenging.

The work reported here focuses on the fluctuations in the rms-voltage introduced by the connection of wave power farms. Two means to reduce these rms-voltage fluctuations are proposed. In the first method, the physical placement of the WECs within a farm is selected prior to the development of the farm to reduce the fluctuations in the net real power generated. It is shown that spacing the WECs or the line of WECs within a farm at a distance greater than half the peak wavelength and orienting the farm at 90° to the dominant wave direction produces a much smoother power output. The appropriateness of the following conclusions has been tested and proven for a wave power farm developed off the Outer Hebrides, using real wave field and network data.

The second method uses intelligent reactive power control algorithms, which have already been tested with wind and hydro power systems, to reduce voltage fluctuations. The application of these intelligent control methods to a 6 MW wave power farm connected to a realistic UK distribution network verified that these approaches improve the voltage profile of the distribution network and help the connection of larger farms to the network, without any need for network management or upgrades. Using these control methods ensured the connection of the wave power farm to the network for longer than when the conventional control methods are used, which is economically beneficial for the wave power farm developer.

The use of such intelligent voltage - reactive power (volt/VAr) control methods with the wave power farm significantly affects the operation of other onshore voltage control devices found prior to the connection of the farm. Thus, it is essential that the control of the farm and the onshore control devices are coordinated. A voltage estimation method, which uses a one-step-ahead demand predictor, is used to sense the voltage downstream of the substation at the bus where the farm is connected. The estimator uses only measurements made at the substation and historical demand data. The estimation method is applied to identify the operating mode of a wave power farm connected to a generic 11 kV distribution network in the UK from the upstream substation. The developed method introduced an additional level of control and can be used at rural substations to optimise the operation of the network, without any new addition of measuring devices or communication means.

Declaration of originality

I hereby declare that the research recorded in this thesis and the thesis itself was composed and originated entirely by myself in the Institute for Energy Systems at The University of Edinburgh.

Anup Jayaprakash Nambiar

Acknowledgements

This work was a part of the Work Stream 7 of the SuperGen Marine Energy Research Consortium, which was supported by the UK Engineering and Physical Sciences Research Council (EPSRC). The Institute for Energy Systems, where the work was done, is supported by the Scottish Funding Council and is part of the Joint Research Institute with the Heriot-Watt University, which is a part of the Edinburgh Research Partnership in Engineering and Mathematics (ERPem). I am thankful to both the SuperGen Marine project and the School of Engineering for their financial support to carry out this research program.

I would like to acknowledge and convey my sincere gratitude to Professor Robin Wallace, my supervisor, for all his support and encouragement during my work and stay here. The work presented here has taken this form mainly because of his guidance, which ensured that what I did was much more than a purely academic endeavour.

I also owe many thanks to Dr. David Forehand and Dr. Aristides Kiprakis for being the ideal collaborators in this work and also my very good friends. Their mentoring at different stages of my PhD helped me immensely. David made my transition to PhD life easy and helped me understand various aspects of wave and WEC modelling. Aristides provided me the platform on which to build, through his work as a PhD student and a research fellow in the SuperGen Marine Phase I. He has been a friendly reviewer and critic of a large part of my work.

I would also like to thank the whole IES community for providing me with a pleasant, friendly and encouraging environment conducive to research and learning. I would like to thank Dr. Sasa Djokic, in particular, for the discussions we had during the initial phase of my work.

I have made many good friends during my time here and this friendship is something I will cherish all my life. A particular mention of my friends in room F4.120, the Edinburgh University Vedic Society, Swaryatra and the SitarProject has to be made here. They were a part of my family away from home.

This page would be incomplete if I did not mention the support I have always received from my grandparents, parents and my wife. A lot of what I am today is because of them and this is something I will always remember.

Contents

List of figures

List of tables

Acronyms and abbreviations

AC	Alternating Current
ACSR	Aluminium Conductor Steel-Reinforced
ANN	Artificial Neural Network
AVPFC	Automatic Voltage and Power Factor Control
CHP	Combined Heat and Power
CPF	Cumulative Probability Function
CWT	Continuous Wavelet Transform
DC	Direct Current
DDPM	Digital Displacement Pump/Motor
DFIG	Doubly-Fed Induction Generator
DFT	Discrete Fourier Transform
DG	Distributed Generation/Generator
DNO	Distribution Network Operator
DWT	Discrete Wavelet Transform
EIR	Energy Index Ratio
FLPFC	Fuzzy Logic Power Factor Control
FT	Fourier Transform/Theory
HV	High Voltage
IDFT	Inverse Discrete Fourier Transform
IEEE	Institute of Electrical and Electronic Engineers
JONSWAP	JOint North Sea WAve Project
LDC	Load Drop Compensator
MEC	Marine Energy Converter
MV	Medium Voltage
(N)ARMAX	(Nonlinear) AutoRegressive Moving Average eXogenous
(N)ARX	(Nonlinear) AutoRegressive eXogenous
(N)BJ	(Nonlinear) Box-Jenkins
(N)FIR	(Nonlinear) Finite Impulse Response

(N)OE	(Nonlinear) Output-Error
OLTC	On-Load Tap Changing
OWC	Oscillating Water Column
PF	Power Factor
PI	Proportional-Integral
PID	Proportional-Integral-Derivative
PM	Pierson-Moskowitz
PSD	Power Spectral Density
PTO	Power Take-Off
PWM	Pulse Width Modulation
RMS	Root Mean Squared
ROC	Renewables Obligation Certificate
SCIG	Squirrel Cage Induction Generator
SG	Synchronous Generator
SI	System Identification/Identified
STATCOM	Static Synchronous Compensator
SVC	Static VAr Compensator
UPF	Unity Power Factor
VFI	Voltage Fluctuation Index
WEC	Wave Energy Converter
WFT	Windowed Fourier Transform
WS	Work Stream
X/R	Inductive Reactance to Resistance ratio

Nomenclature

a	Acceleration
$A(q)...F(q)$	Polynomials in linear time invariant system model structure
$A_{j,k}$	Wave amplitude of the wave component (j,k)
$au + b$	Linear term in wavenet
b	Damping
$B(\omega)$	Radiation damping
b_{es}	Damping coefficient of end-stops
b_{PTO}	Damping introduced by the power take-off
b_k	Neuron bias
c_k	Discrete wavelet transform
d	Distance between two neighbouring wave energy converters
d'	Effective distance between two neighbouring wave energy converters
$D(f, \theta)$	Angular spreading function
$d_{j,k}$	Discrete wavelet transform
$E(f, \theta, t)$	Sea spectrum for short-crested seas
$E(f, t)$	Sea spectrum for long-crested seas
$e(t-k)$	Prediction error
e_m	Efficiency of the hydraulic motor
$e_u(t-k)$	Simulation error
F	Force
f	Frequency in Hz
$f*$	Non-dimensional frequency
f_{es}	Force due to the operation of the end-stops
f_{ex}	Wave excitation force
f_{loss}	Net force due to energy losses
f_{peak}	Peak frequency of the sea spectrum
f_{pto}	Force provided by the power take-off

f_e	Wave excitation force
f_r	Wave radiation force
$F_r(\omega)$	Radiation force in the frequency domain
F_s	Sampling frequency
f_s	Spring force
g	Acceleration due to gravity
$g(\varphi(t), \theta)$	Nonlinear function parameterised by θ
$g(k)$	Impulse response function of linear time invariant system
$G(q)$	Impulse pulse transfer function
H	Mean water depth
h	Wave height of individual wave
$H(q)$	Noise pulse transfer function
H_s	Significant wave height
$\mathbf{I}$	Complex current
j	Scaling parameter/index
J	Training cost function
k	Spring stiffness
$K(\tau)$	Impulse response function for the radiation force
k_{dr}	Direct-axis component of rotor voltage (V), current (i) and flux (λ)
k_{ds}	Direct-axis component of stator voltage (V), current (i) and flux (λ)
k_{es}	Stiffness coefficient of end-stops
$k_{i/j}$	Wave number
k_{qr}	Quadrature-axis component of rotor voltage (V), current (i) and flux (λ)
k_{qs}	Quadrature-axis component of stator voltage (V), current (i) and flux (λ)
k_g	Specific heat ratio
K_i	Cumulative Probability Function weighing coefficients
l	Cumulative Probability Function class
L	Wavelength of individual wave
L_m	Mutual inductance
L_r	Rotor leakage inductance
L_s	Stator leakage inductance
m	Mass
$M(\omega)$	Added mass

m_k	k^{th} moment of the sea spectrum
p	Differentiation operator
P	Number of poles
$p(l)$	Cumulative probability
$P(t)$	Percentage error
p_{acc}	System/accumulator pressure
P_{max}	Maximum allowed accumulator pressure
p_{pre}	Pre-charged pressure of the accumulator
P_B	$P_G - P_L$
P_G	Real power generated
P_k	Cumulative Probability Function curve level with assigned probability of being exceeded
P_L	Real power load
P_r	Real power carried by the rotor
P_s	Real power carried by the stator
PF_{ref}	Reference power factor
PF_B	Maximum lagging power factor
PF_d	Power factor deadband
PF_T	Maximum leading power factor
q^{-1}	Backward shift operator
Q_{ref}	Reference reactive power
$Q_{STATCOM}$	Reactive power exchanged by the STATCOM
Q_B	$Q_G - Q_L$
Q_G	Reactive power generated
Q_L	Reactive power load
Q_m	Flow from the accumulator to the hydraulic motor
Q_p	Flow from the piston to the accumulator
Q_r	Reactive power carried by the rotor
Q_s	Reactive power carried by the stator
$q - factor$	Interaction factor in array
r	Radius of the cylindrical buoy
R	Resistance
$R(t)$	Residual
R_{set}	LDC resistive compensation

$\mathbf{S}$	Complex power
$S(k)$	Power spectral density at frequency $k\Delta\omega$
s_{max}	Maximum allowed slip of the generator
ti	Translation index of wavelet unit
t	Time
T_1	Average zero-crossing time period
t_d	Time delay
T_e	Electrical torque
T_L	Load torque
T_z	Average zero-up-crossing wave period
Tap_{max}	Extreme upper tap position
Tap_{min}	Extreme lower tap position
Te_{ref}	Reference electrical torque
$U(\omega)$	Velocity in the frequency domain
$u(t-k)$	Input at time $t = k$
$v(t)$	Lumped disturbance function
$\mathbf{V}$	Complex voltage
$V(t)$	Terminal voltage
V_{bus}	Bus voltage
V_{ref}	Reference voltage
V_a	Accumulator volume
V_d	Voltage deadband
V_f	Fluid volume within the accumulator
V_h	Upper limit of the voltage
V_i	Voltage at i^{th} time instant
V_k	Controlled voltage of the STATCOM
v_k	Output of summer in input layer of neuron
V_l	Lower limit of the voltage
V_s	Output voltage of the STATCOM
$w(t)$	Impulse response function for the excitation force
w_{ki}	Weight of i^{th} input
$Wf(u,s)$	Wavelet transform of signal

(x, y)	Location in the wave field
X	Reactive inductance
$X(k\Delta\omega)$	Magnitude of the DFT at frequency $k\Delta\omega$
X_{set}	LDC inductive reactance compensation
$x_1 ... x_i$	Inputs to neuron
X_s	Inductive reactance of the STATCOM
$y(t-k)$	Output at time $t = k$
y_k	Output of a neuron
$\hat{y}_u(t-k\|\theta)$	Simulated output from past values alone
$z(t)$	Displacement of the heaving wave energy converter
$\dot{z}(t)$	Velocity of the heaving wave energy converter
Z_{eff}	Effective impedance
Pfarm	Real power generated
Pmech	Power at the motor-generator coupling
Pwec	Raw mechanical power extracted by wave energy converter
Qfarm	Reactive power generated
VAr	Reactive power
α	Orientation of farm with dominant wave direction
$\alpha_{j,k}$	Wavelet coefficient
β	Coefficient of hyperbolic-secant squared spreading function
β_j	Scaling function
$\Delta\omega$	Width of the angular frequency bin
$\Delta\theta$	Width of the angular direction bin
Δf	Width of the frequency bin
ΔJ	Gradient of the cost function
ΔT_e	Error in the electrical torque
ΔV	Voltage difference with respect to limit
γ_k	Translation function
κ	Mother wavelet function
λi	Scaling index of wavelet unit
λ_{peak}	Peak wavelength
μ_∞	Added mass at infinite frequency

μ_1, μ_2	Membership level of activation
μ_i	Neural network learning rate
ω	Frequency in rad/sec
ω_{min}	Cut-in speed of generator
ω_{rated}	Rated speed of generator
ω_r	Rotational speed of the induction generator
ω_s	Synchronous speed of the induction generator
Φ	Kitaigordskii's factor
$\phi(t)$	Scaling function
$\phi_{j,k}$	Phase of the wave component (j,k)
$\psi(t)$	Wavelet function
ρ	Density of water
τ	Time-shift operator (convolution)
θ	Parameter vector
θ_m	Mean wave direction
$\varphi(.)$	Activation function of neuron
$\varphi(t, \theta)$	Regression vector
ξ	Wave elevation

Chapter 1
Introduction

1.1 Research background

The ambitious carbon dioxide emission reduction targets set in the UK and the world have given impetus to developments in renewable energy sources [1, 2]. Of the different renewable energy options being considered, wind energy conversion has come of age and is presently considered a mainstream power technology [3]. The world today has an installed wind capacity of approximately 196 GW out of which nearly 50% is in Europe [4]. Large offshore wind farms have been constructed, and considering the opposition to land based wind power in many developed countries, might take an increasingly important role in the future [5]. Based on current interest, solar generation comes second after wind even with the relatively higher costs associated with the manufacture of solar cells. The US, Germany, Japan and Spain are the leading countries in solar energy and have expanded their solar power generation capacity over the last few years [6]. Hydro-power is the oldest and the largest renewable source used for power generation. However, there is considerable opposition to the construction of new large hydro-power plants with increasing environmental awareness. There are other less widely used renewable energy options used today, details of which are available in [7].

Generating energy from waves and tides are two options that have been considered and steady progress has been made in the last few years [8, 9]. In the case of wave energy, the western coast of Europe, the Pacific coastlines of North and South America, Southern Africa, Australia and New Zealand have significant wave resource. A large number of wave and tidal energy devices have been developed and tested. At present there are full scale prototype wave and tidal energy devices deployed in Europe, both singly and as farms [10, 11].

In the UK, the best wave resource is found off the northern and the western coasts of Scotland [12]. These are remote, rural areas where the electrical loads are low and the electricity distribution network is weak. The low capacity, low and medium voltage electricity networks in these areas were originally designed to distribute electricity generated from central power stations to

rural areas. When the direction of the power flow reverses, with the addition of distributed generators (DG) in these networks, issues arise. Even with only a relatively small increase in the output from the connected generators, large voltage fluctuations are seen which are attributed to the low reactance to resistance ratio at the edges of the distribution network. The varying and unpredictable nature of the ocean waves further adds to the challenge of integrating large wave power farms to the network. Some of the network issues and constraints associated with an increase in renewable energy penetration into the network act as impediments to the growth of this sector. Work has been completed to overcome some of these issues mainly with respect to the more prevalent wind generators. Though some parallels may be drawn, the effects of connecting large wave power farms to the network need to be studied further. The power generated from ocean waves has several useful characteristics, different from that generated by wind power farms, which can be used advantageously.

1.2 SuperGen Marine project

The work reported in this thesis was a part of the research performed by the SuperGen Marine Energy Research Consortium (Phase II). The Marine Energy Consortium is supported by the UK Engineering and Physical Sciences Research Council and was brought together to explore the potential and the future of marine energy. Phase I of the project (October 2003 - September 2007) aimed at improving the understanding of the extraction of energy from the sea and reducing the uncertainty in the development and deployment of marine technology so as to enable the progression of marine energy as a viable alternative for power production [13].

Phase II of the program (October 2007 - September 2011) built on the research completed in Phase I and included work on arrays of devices, nonlinear modelling, design of devices, numerical and physical model consistency, moorings, etc. The objectives were divided among 12 Work Streams of which this project is a part of Work Stream 7 titled “Advanced control/Network integration”. This Work Stream follows from the work completed in the work package 4 of Phase I in which a wave-to-wire model of an array of non-interacting wave energy converters (WECs) was built. The objectives of the Work Stream 7 of Phase II, as stated in the project proposal, were the following:

1. Development of a non-linear wave model
2. Study of the effects of different degrees of wave non-linearity on response of a generic WEC model

3. Creation of a scheme for analysis and synthesis of non-stationary waves in wave energy conversion
4. Study on short-term prediction of waves for optimised MEC control and energy capture
5. Study on the interaction between different modes of response of WECs
6. Development of predictive/adaptive/evolving control of MECs to mitigate resource non-stationarity
7. Development of structured MEC array control schemes including supervised, autonomous and master-slave control
8. Simulation and exploration of the electricity network impacts and their mitigation through advanced MEC and network control

The collaborators in the Work Stream, spread across the University of Edinburgh, the Heriot-Watt University and the Lancaster University, shared these tasks. This thesis deals mainly with tasks 7 and 8 in the list. The group at Heriot-Watt University has been working on the prediction of waves, the modelling of non-linear waves and the influence of moorings on the power from WECs. The group at Lancaster University has been developing methods to control the WECs hydrodynamics for improved performance. A colleague, Dr. David Forehand, at the University of Edinburgh has built a time domain model of arrays of WECs taking into account all the interactions between the individual WECs.

1.3 Thesis

The thesis of the work was that: appropriately placing the wave energy converters within a wave power farm and the use of intelligent voltage and reactive power control algorithms applied to the farm should significantly reduce the voltage fluctuations introduced in the electricity network by the farm and help keep the network voltage within statutory limits. Further, means to coordinate the control of the wave power farm and the other voltage control elements in the distribution network can be devised to ensure that they complement each other and improve network operation.

1.4 Project objectives and scope

The key project objectives were as follows:

- Develop the wave-to-wire model built in Phase I
- Investigate the effects of farm size and physical placement of WECs on the quality of the power generated
- Analyse effects of connecting wave power farms to weak, rural distribution network
- Develop means to mitigate these negative effects
- Compare the performance of the control options suggested
- Study the effects of using these control algorithms on other control elements in the network
- Look at means to overcome some of the negative effects of the interaction between the control elements
- Develop a new modelling framework to model wave power farms using system identification

1.5 Contribution to knowledge and deliverables

Generally, the rationale behind the application of any control algorithm on a WEC is to maximise power extraction. The inherent quality of the power generated, which has a direct influence on voltage quality in the electricity network, is not considered very significant. The main objective of this work was to explore the impacts on voltage quality of connecting farms of WECs to weak, rural electricity networks. The term 'voltage quality' usually covers many different voltage characteristics. In this work, though, voltage quality refers purely to fluctuations in the rms-voltage magnitude. Much of the work performed was about quantifying and minimising these effects. Means to improve the quality of the power generated from small and large wave power farms were studied through mainly two pieces of work. The first examined how the size of the farm, location and wave field characteristics at the site of the farm and the spacing and the orientation of the WECs within a farm can be advantageously used for smoothing power. The second investigated how further smoothing in the network voltage can be obtained through the dispatch of reactive power from the Doubly-Fed Induction Generators (DFIGs) used in the farm. Intelligent controllers for primary voltage control were tested for this purpose. Indices to compare the performance of these methods were also suggested. The effects of the primary control method used in the farm on other voltage control elements in the

network were evaluated and a technique using voltage estimation was proposed to overcome these. A new modelling framework to model wave power farms using system identification was also built, which allows accurate and fast simulations without losing the time-resolution of the detailed dynamic model.

These are the main deliverables from this research:

- System identified wave-to-wire model of wave power farms - System identified models significantly improve the simulation speed when compared to the detailed physical models, without losing the accuracy of the detailed models. Such models become important when the number of devices in the wave power farm increases and longer simulation runs are required.
- Establishment of ways to optimise the layout of wave power farms for power smoothing - Some power smoothing and voltage quality improvement will be obtained by optimising the layout of the WECs within a farm, making use of the spatially sinusoidal and the directional nature of the wave field.
- Intelligent electrical control options for wave power farm - These intelligent voltage/power factor controllers further improve the voltage quality and ensure that the voltage remains within the allowed limits. This in turn ensures the connectivity of the farm to the network for longer, thus, increasing production.
- Voltage estimation technique for coordinating control of two control elements in distribution networks - The intelligent controllers of the wave power farm may interact negatively with already present voltage controllers in the network. The operation of the distribution network can be optimised by coordinating both the controllers, using voltage estimation techniques.
- Indices to quantify fluctuations in the rms-voltage magnitude - These indices can be used to quantify and compare the different voltage/power factor controllers and coordination means.

1.6 Thesis outline

This chapter was the introduction to the scope of this project and the results that will be discussed further in the thesis. The literature review has been distributed through out the thesis and

all relevant literature have been cited in appropriate sections. Therefore, there is no separate chapter discussing all the relevant literature.

Chapter 2 describes the wave-to-wire model of the wave power farm used for generating the results in this work.

The system identified (SI) model of the wave power farm is presented in Chapter 3. Results of the comparative study performed between the SI model and the detailed model are also discussed in this chapter.

Chapter 4 examines the smoothing in the real power generated by different array layouts. Effects of increasing the array size on the quality of the power generated are discussed. Whether appropriately spacing the WECs within the array and orienting the array has any affect on power smoothing is presented in this chapter.

Further smoothing control through the use of power electronic converters and intelligent control options is dealt with in Chapter 5.

Chapter 6 investigates the effects of using the intelligent controllers with the wave power farm on the substation on-load tap changing transformer. A method using neural networks to estimate the voltage at the bus where the farm is connected from the upstream substation is described. An application of the developed estimation method in identifying the operating mode of the farm is also described in this chapter.

Indices to quantify voltage fluctuations have been reviewed and the results and inferences are presented in Chapter 7.

Chapter 8 summarises the work reported in this thesis and discusses the scope for further research.

Chapter 2
Modelling wave power farms - Part I

2.1 Introduction

In order to study the electricity network impacts of connecting large wave power farms, a time domain model of the farm is required. In this chapter, the model of the wave power farm developed is described. The model has been developed in MATLAB/Simulink because of their acceptance and widespread use in both academic and industrial communities.

For developing a discrete-time model, two aspects define the model's performance - the order of the model and the simulation time-step. Selecting a high order may not produce a marked improvement in the model performance, but the simulation time increases. On the other hand, inaccurate results are produced when a low order model is used. Sub-transient simulations require time-steps less than 1 ms (even less than 1 μs at times), while dynamic/transient simulations require time-steps of approximately 10 ms. For fundamental frequency simulations of the power system, dynamic/transient model are sufficient. Since this work aims at analysing the effects of connecting wave power farms on the network voltage magnitude, a dynamic model has been used. A power flow solver written in MATLAB [14] has been used with the dynamic model to study the network impacts of connecting wave power farms. The model accurately reproduces the responses of both the electrical and the mechanical control of the wave energy converters (WECs) and also correctly captures the effects of the variable input power.

A WEC constrained to move in heave has been modelled for this work. Since a modular approach has been used in the wave-to-wire model, the WEC block alone may be replaced for modelling some other WEC type moving in surge or a combination. For example, this block may be replaced by the array model developed by Dr. David Forehand, a researcher in the SuperGen Marine II consortium, which also incorporates the hydrodynamic interactions of the WECs within the array [15]. A doubly-fed induction generator driven by a hydraulic power take-off system has been selected for use in this work. The generator in the wave-to-wire model may also be replaced by other generator types because the model is modular.

The control methods investigated for controlling the generator (see Chapter 5) may be applied with any generator type connected to the network through back-to-back pulse width modulated (PWM) converters.

A significant part of the wave-to-wire model was developed by Dr. Aristides Kiprakis during his tenure as a researcher in the SuperGen Marine I consortium. Significant changes have been made to make the model closer to reality.

This chapter describes in detail the wave-to-wire model that has been used for this work. For the analysis of the electrical network impacts over longer durations without a loss in time-resolution, a Nonlinear AutoRegressive eXogenous (NARX) model of the wave power farm has been developed and is the subject of the second part of this chapter (Chapter 3). The performance of both the detailed model and the NARX model has been compared and the results are discussed there. The developed NARX model allows the use of personal computers to run simulations of large wave power farms over extended durations extremely quickly.

2.2 Modelling the wave resource

The primary input to the wave-to-wire model of the wave power farm is the time-series of wave surface elevations at each location where a WEC is placed in the wave field. The time-series can come directly from buoy measurements or can be generated using spectral representations obtained from an analysis of the historical sea state at the location. Using spectral representations of the sea assumes that the sea may be represented linearly and that the sea is stationary. The former is valid for small amplitude waves and when the WECs are placed in deep water and when they are working under normal operating conditions. However, the latter is not a valid assumption because the sea state varies continually with time and thus is inherently non-stationary. Therefore, a model of the wave resource which represents the irregularity, the non-stationarity and the directionality of ocean waves is required.

2.2.1 Sea spectra for synthesising irregular waves

In this work, the sea surface motions have been generated using spectral representations of the sea. The wave energy density spectrum gives the distribution of the energy content of the waves with frequency. These are suitable for long-crested seas for which the directional aspect can be ignored. Spectral representations of the sea can be used to predict the frequency response of different structures in the sea. The power generated by a WEC can also be calculated using

the spectrum of the sea and the frequency response of the WEC. These procedures constitute a frequency domain approach of modelling structures in the sea.

The appropriate application of spectral moments of the spectrum yields different parameters which are used to characterise sea states. Of particular interest to wave energy developers are the significant wave height H_s and the mean time period T_1. Most commonly used spectra are functions of these parameters. The significant wave height H_s is defined as the average height of the highest $1/3^{rd}$ of the waves over the time period under consideration [16]. The significant wave height may also be calculated from the 0^{th} spectral moment of the sea spectrum, where the k^{th} spectral moment is given by $m_k = \int_0^\infty \omega^k E(\omega) d\omega$. In this expression, ω is the frequency and $E(\omega)$ is the energy density function. The significant wave height in terms of the 0^{th} moment is $H_s = 4\sqrt{m_0}$. The mean wave period T_1 given by $2\pi m_0/m_1$, where m_1 is the first moment. It is the inverse of the average frequency of the spectrum and cannot be obtained from a wave elevation time-series. Another commonly used time period measurement is the average zero-up-crossing wave period T_z given by $2\pi(m_0/m_2)^{0.5}$, where m_2 is the second moment. T_z can be calculated from a time-series of wave elevations by dividing the record length by the number of waves in the record.

The Pierson-Moskowitz (PM) spectrum - for fully developed seas [17], the JONSWAP spectrum - for seas with a limited fetch [18] and the Bretschneider spectrum - for open seas, are some of the commonly used spectral representations of seas. The large fetch across the Atlantic Ocean makes the Bretschneider spectrum suitable for use for modelling seas off the north and north west coasts of Scotland. The two parameter Bretschneider spectrum has been used in this work. The spectrum in terms of the significant wave height H_s and the mean wave period T_1 is given by [19]:

$$E(f,t) = 0.11\, H_s^2\, T_1\, (T_1 f)^{-5}\, exp[-0.443/(T_1\, f)^4], \tag{2.1}$$

where f is the frequency in Hertz, H_s is in metres and T_1 in seconds. The spectra for four different H_s, T_1 pairs are plotted in Figure 2.1. Typical values of H_s and T_1 found in the seas off the Outer Hebrides have been obtained from the Wavenet database [20] and have been used for simulating the wave power farm in this work. A statistical analysis of the distribution of the energy content in the sea and the directional spreading of the sea found at this site is discussed in Chapter 4.

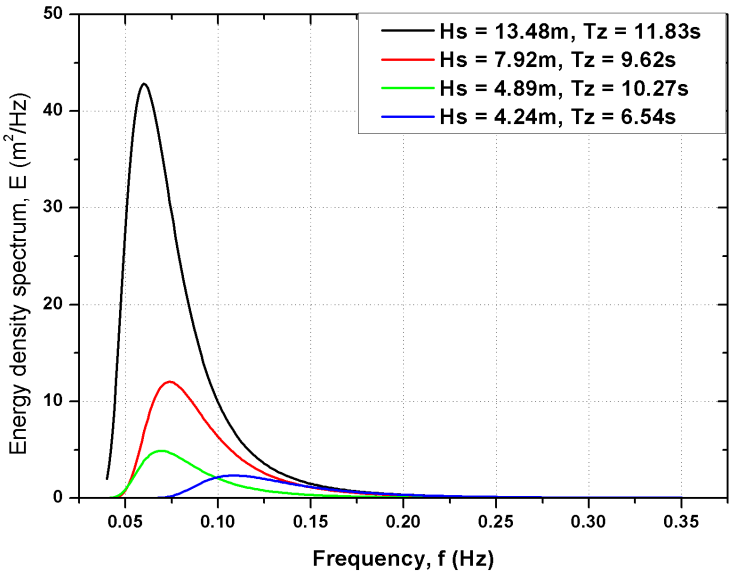

Figure 2.1: *Bretschneider spectra for four H_s, T_z pairs.*

2.2.2 Modelling multi-directional waves

Short-crested seas are multi-directional and cannot be wholly represented by the spectrum shown in Equation (2.1). Real seas generally have a dominant direction and an angular spread about the dominant direction. The larger the spread, the more short-crested the wave becomes. The directional aspect of the short-crested seas has been modelled using the following two-dimensional spectrum [21]:

$$E(f,\theta,t) = E(f,t)\,D(f,\theta) \tag{2.2}$$

where $E(f,t)$ is the one-dimensional spectral density function (from Equation (2.1)) and $D(f,\theta)$ is the angular spreading function. In this work, the hyperbolic-secant-squared spreading function has been used since it better represents wind-waves [22]. The function is defined by:

$$D(f,\theta) = 0.5\,\beta sech^2\beta[\theta - \theta_m(f)], \tag{2.3}$$

where

$$\beta = \begin{cases} 2.61(f/f_{peak})^{13} & \text{if } 0.56 < (f/f_{peak}) < 0.95 \\ 2.28(f/f_{peak})^{-13} & \text{if } 0.95 < (f/f_{peak}) < 1.6 \\ 1.24 & \text{if } (f/f_{peak}) > 1.6 \end{cases} \tag{2.4}$$

and θ_m is the mean wave direction of the wave with frequency f. This spreading function is narrower than the commonly used cosine squared spreading function, which means that the

wave field generated will have longer crest lengths. Owing to the large fetch across the North Atlantic ocean, the north west coast of Scotland will see wind generated waves of this nature [23]. Figure 2.2 shows the directional spreading functions for three frequencies f, with the peak frequency f_{peak} = 0.1180 Hz (corresponding to a sea state with $T_z = 6$ s).

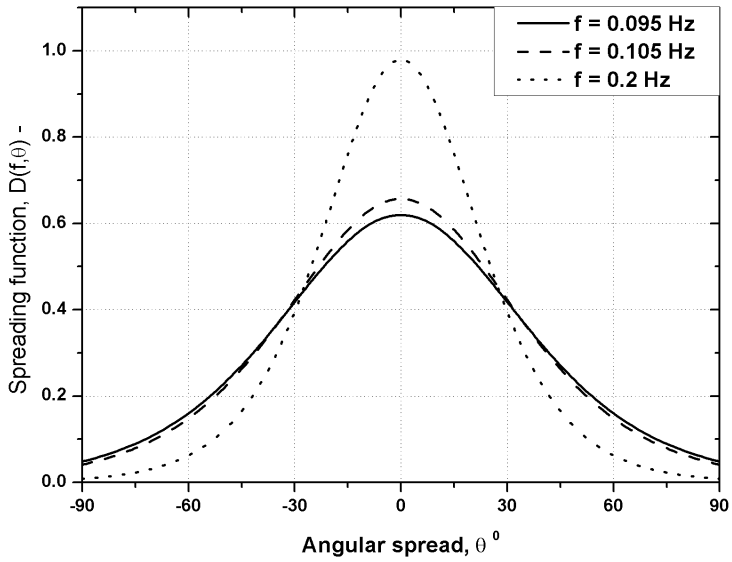

Figure 2.2: *Hyperbolic-secant-squared spreading function for three frequencies.*

2.2.3 Computing the wave elevation time-series from the spectrum

Once the two-dimensional spectrum is computed, the time-series of the wave elevation has to be constructed from it. Assuming wave linearity, the Inverse Discrete Fourier Transform (IDFT) has been used for this purpose. The wave elevation at an instant of time has been obtained from [24]:

$$\xi = \sum_{j=1}^{J} \sum_{k=1}^{K} A_{j,k}\, sin(2\pi f_j t \; - \; k_j\, x\, cos\theta_k \; - \; k_j\, y\, sin\theta_k \; + \; \phi_{j,k}), \tag{2.5}$$

where $A_{j,k} = (E(f_j, \theta_k, t) 2\pi \Delta f_j \Delta\theta_k)^{0.5}$ is the wave amplitude, (x, y) denotes the position coordinates in the wave field and k_j, f_j, ϕ_{jk}, and θ_k respectively denote the wave number, frequency, the random phase component and the angular spread of wave component jk. The random phase component ϕ_{jk} is uniformly distributed between 0 and 2π. The wave number k_j has been obtained from the deep water dispersion relation: $\omega_j^2 = gk_j$, where $g = 9.81 \mathrm{m/s^2}$ is the acceleration due to gravity.

2.2.4 Modelling non-stationary wave elevation time-series

The statistical characteristics of the sea state such as H_s and T_1 are generally averaged over time intervals between 20 minutes and 1 hour. Wave buoys used to collect wave data usually record only these average values. The sea state is considered to be stationary between two records. In this work, the parameters of the sea state in between two wave records have been obtained through interpolation and thus the stationary spectrum (in Equation (2.1)) has been used for non-stationary wave generation. Figure 2.3 shows the energy density spectrum varying over a day at a site off the north west coast of Scotland.

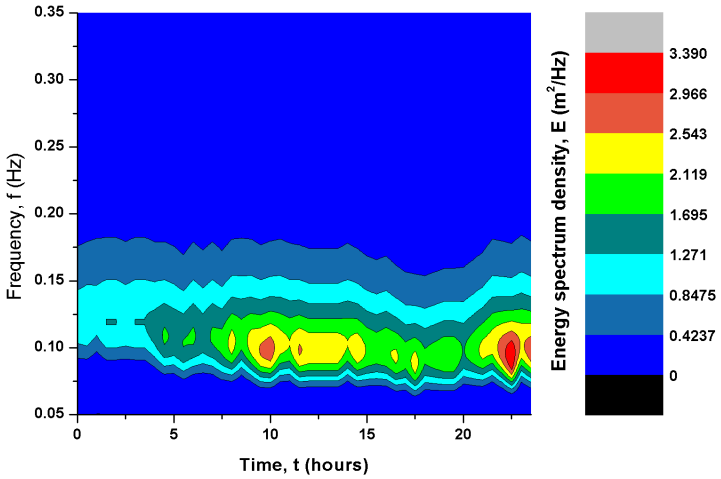

Figure 2.3: *Energy density spectrum over a day.*

Some of the simulations in the thesis which have been run for less than 10 minutes, have used irregular waves generated using constant H_s and T_1 values. When such simulations are run, due to the discrete nature of the time-series generated, a cyclic repetition in the wave elevation will be observed with a period of $2\pi/(\Delta\omega) = 1/(\Delta f)$. This cyclic repetition has been avoided by altering the phase angle ϕ_{jk} by a small value for every frequency at each time step.

2.2.5 Modelling the wave resource for shallow waters

The modelling procedure described until now assumes that the wave elevation time-series are being generated for the deep-water case, where the depth is greater than $\lambda_{peak}/4$, where λ_{peak} is the peak wavelength [19]. Mooring and maintenance requirements currently force the deployment of WECs closer to the shore where the mean water depth is between 30 and 50 metres. This is the case especially for WECs using heave motion to generate power [25], which have

been considered in this thesis. For use in shallow waters, the spectrum described in Equation (2.1) needs to be modified.

The similarity of the wind-wave spectrum for deep and shallow waters was established in [26]. The multiplication of the spectrum in Equation (2.1) by the depth dependent Kitaigordskii's factor makes it suitable for use in shallow water [27]. The modified spectrum thus becomes,

$$E(f, H, t) = E(f, t).\Phi(f*, H), \tag{2.6}$$

where $E(f, t)$ is the energy spectrum density defined in Equation (2.1), $\Phi(f^*, H)$ is the non-dimensional Kitaigordskii's factor, f^* is the non-dimensional frequency given by $f^* = f(H/g)^{0.5}$ and H is the mean water depth. The relationship between the Kitaigordskii's factor and the non-dimensional frequency is shown in Figure 2.4.

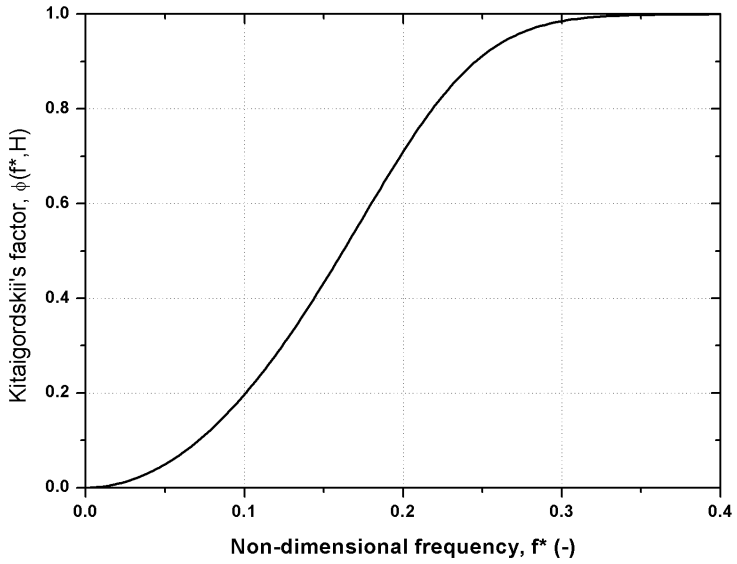

Figure 2.4: *The Kitaigordskii's factor versus non-dimensional frequency.*

The similarity in the deep water and the shallow water spectrum was identified for the limited-fetch JONSWAP spectrum in [28]. The same procedure has been followed in this work to obtain the shallow water spectrum from the deep water Bretschneider spectrum. This is possible because the Bretschneider spectrum is the more generalized form of the JONSWAP spectrum without the peak enhancement function [19, 29]. The shallow water spectra for $H_s = 7.16$ m and $T_z = 9.82$ s for different depths are shown in Figure 2.5. The energy content in the sea, which is measured by the area under the spectrum, reduces with a decrease in depth. This occurs due to an increase in the energy losses due to enhanced dissipation in shallow

water. To calculate the wave number for the shallow water case the more generalised form of the dispersion relation $\omega_i^2 = gk_i\, tanh(k_i H)$ is used. To solve for k_i from this relation, the Newton-Raphson method has been used in this work [30].

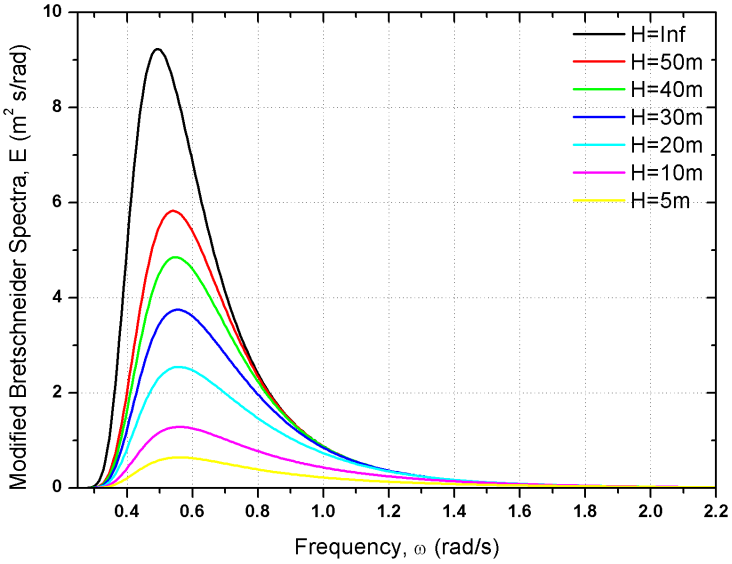

Figure 2.5: *Self similar Bretschneider spectra with the same parameters for different water depths H.*

Once the deep water spectrum is modified for use in shallow water, the wave elevation time-series can be obtained by replacing $E(f,t)$ with $E(f,H,t)$ in Equation (2.5). Figure 2.6 shows a sample of the wave elevation time-series generated for a sea with $H_s = 4$ m and $T_z = 6$ s.

2.2.6 Comment on wave linearity

The linearity assumption places constraints on the H_s and T_1 values that can be used for generating the wave elevation time-series. Waves with large amplitudes and steepnesses cannot be treated as linear waves [31]. When the waves are steep they tend to break. Breaking is said to occur in irregular waves when the steepness ratio of the wave (h/L) is greater than 1/9, where h is the wave height and L is the wavelength of the wave [29]. Statistical moments like skewness and kurtosis have also been used to measure wave linearity [31]. A large number of steepness coefficients that can be used to measure wave linearity like the down-crossing steepness, front steepness, crest-back steepness, etc., were described in [32]. In this work, extreme and freak waves have not been considered and only those waves which can be treated as linear have been used. It must also be noted that in this work end-stops have been used, which ensures that the

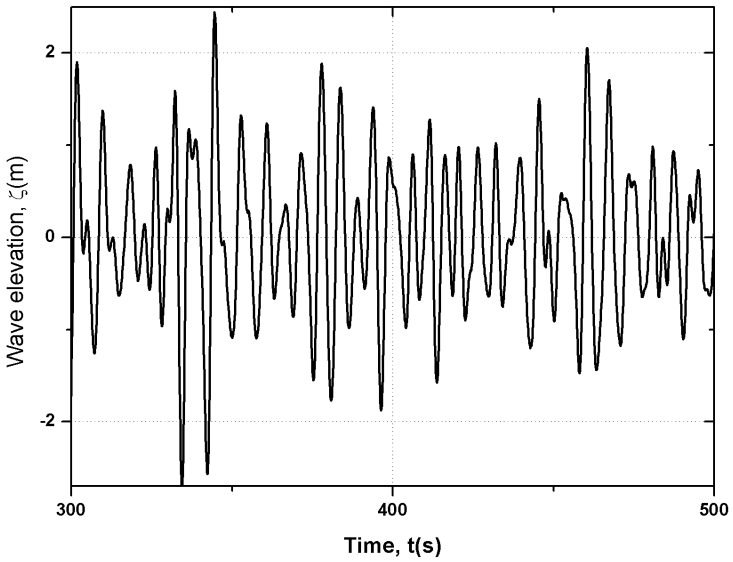

Figure 2.6: *Wave elevation time-series.*

motion of the WECs irrespective of the sea state used is still a linear problem.

2.3 Time domain wave energy converter model

Different types of WECs have been developed which use different methods to capture the energy of the waves. WECs can either be point absorbers or buoys [25, 33, 34], attenuator devices [10, 35], terminator devices, Oscillating Water Column devices [36], or overtopping devices [37–39]. A review of the different technologies was discussed in [8]. A list of all the WEC manufacturers (numbering around 150) and the devices that they have developed is given in [40].

For this work, the focus has been on point absorber type WECs. The modelled WEC is a semi-submerged, vertical, cylindrical buoy like the one described in [41]. It has a radius of 3.3 m and a draft of 3.1 m. All the simulation work in this thesis has been performed for WECs constrained to move in heave. The power rating of the modelled WEC has been set at 125 kW which is representative of prototypes under test in various parts of the world today [25, 42, 43]. As a part of the Work Stream 7 of the SuperGen Marine phase II, Dr. David Forehand has developed a model of an array of WECs which is completely generalised [15].

2.3.1 Equation of motion

By Newton's second law, the sum of all the forces acting on a body accelerates the body in the same direction as the net force and this acceleration is proportional to the force applied and inversely proportional to the mass of the body. Thus, $F = ma$, where F and a are vectors. Figure 2.7 shows the free body diagram of a heaving WEC. The equation of motion of the WEC can be represented by

$$f_e - f_{loss} - f_r - f_s - f_{pto} - f_{es} = ma, \tag{2.7}$$

where f_e is the wave excitation force, f_{loss} is the net force due to energy losses, f_r is the wave radiation force, f_s is the spring force, f_{pto} is the force provided by the power take-off and f_{es} is the force due to the operation of the end-stops.

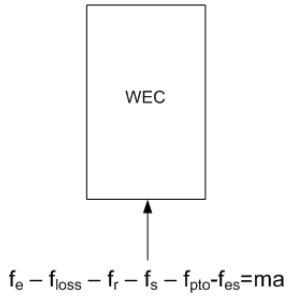

Figure 2.7: *Free body diagram of a WEC in heave.*

The excitation force f_e has two components - one due to the undisturbed incident wave when the body is kept fixed such that there are no radiated waves and the second due to the diffracted waves [44, 45]. The diffraction force causes the change in direction (or diffraction) of the incoming waves. The non-causal relationship between the wave elevation and the excitation force [46] is defined by: $f_e(t) = w(t) * \xi(t)$, where $*$ denotes convolution. $w(t)$ is the convolution kernel, also called the impulse response function for the excitation force. The excitation impulse response function for a cylindrical buoy is shown in Figure 2.8 [44]. The scales are non-dimensionalised, which means that the units associated with the variables have been removed completely by appropriate variable substitutions. The non-dimensionalised functions need to be dimensionalised using the radius of the cylindrical buoy to obtain the impulse response function for buoys of different dimensions. The non-dimensionalised function varies with change in the radius to draft ratio and the water depth to radius ratio. Since the impulse response function is defined for all non-dimensional time from -10 to 10, it means that for computing the convolution both past and future values of the wave elevation are required (non-causal).

The spring force f_s has contributions from the buoyancy of the buoy and from other means of

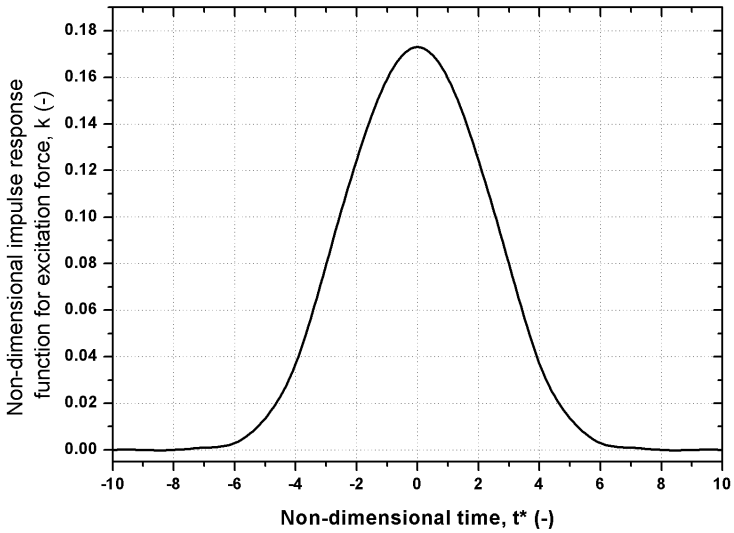

Figure 2.8: *Impulse response function for excitation force of a cylindrical buoy.*

reaction (provided by moorings and other mechanical springs). In this work, the spring force provided by the buoyancy of the buoy alone has been considered. The buoyancy spring stiffness $k = \rho g \pi r^2$, where ρ is the density of sea water, g is the acceleration due to gravity and r is the radius of the cylindrical buoy.

It has been assumed here that each WEC reacts against the sea floor through a taut mooring cable. The horizontal component of the force acting on the WEC is therefore small and has been ignored. [47] shows the effects on the heave motion of similarly modelled WECs with and without moorings. It was shown that the effects of the mooring is not significant for the mooring option chosen in this work. A study of different mooring configurations and attachment points showed that for some configurations, no significant changes to the energy extraction spectrum of point absorbers moving in heave, surge and pitch will be seen, when compared to the case where the buoys were placed in the sea without moorings [48].

When the body is made to oscillate without any incident wave, the body radiates waves. The force acting on the oscillating body due to the waves it radiates is the radiation force. In the frequency domain, the radiation force is defined by $F_r(\omega) = [B(\omega) + i\omega M(\omega)]U(\omega)$, where $B(\omega)$ is the radiation damping and $M(\omega)$ is the added mass [49]. Taking the inverse Fourier transform of the radiation force in the frequency domain, gives the expression for the radiation force in the time domain, which is:

$$f_r(t) = \mu_\infty a(t) + \int_0^t K(\tau)\, u(t-\tau)\, d\tau \tag{2.8}$$

The first term in the equation represents the added mass at infinite frequency. The second term depends on past values of velocity. The kernel of the convolution integral $K(\tau)$ is called the impulse response function for the radiation force. Figure 2.9 shows the radiation impulse response function for a cylindrical buoy. Like the impulse response function for the excitation force, the impulse response function for the radiation force also depends on the radius to depth ratio and the radius to draft ratio.

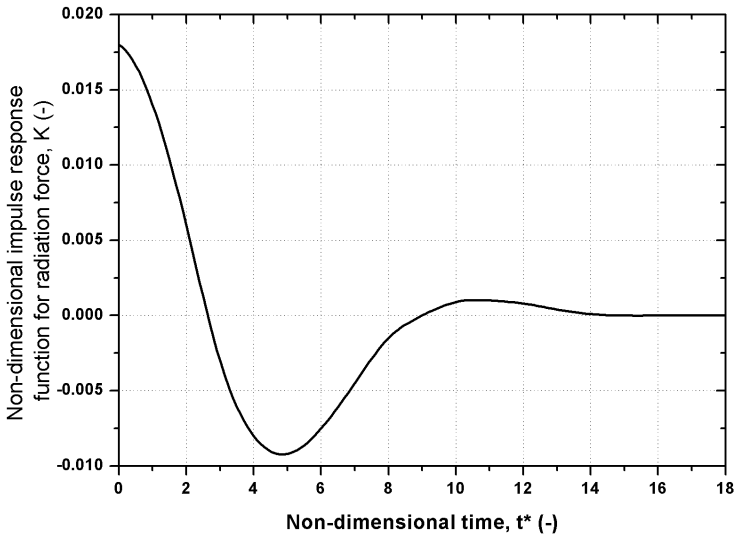

Figure 2.9: *Impulse response function for radiation force of a cylindrical buoy.*

The power take-off (PTO) force f_{PTO} is the force on the WEC due to the PTO system. The PTO system for the modelled WEC is explained in detail in the next section. In this work, only real control of the WEC has been performed, wherein the PTO damping coefficient b_{pto} alone is available for control [45]. The net force due to energy losses has been incorporated as an additional damping (represented by f_{loss} in Figure 2.7).

End-stops are required to limit the stroke length of the piston [50] (see Figure 2.14). In this work, the end-stops have been modelled as an additional spring-damper at both the top and bottom of the piston [41]. The end-stop device helps decelerate the piston's motion and reduces the possibility of mechanical damage to the cylinder. The modelled WEC has a draft of 3.1 m and therefore a limiting displacement of 2 m has been chosen. The end-stop force has been modelled as:

$$f_{es} = \begin{cases} 0 & \text{if } z(t) < \text{the limiting displacement} \\ b_{es}\dot{z}(t) + k_{es}z(t) & \text{if } z(t) >= \text{the limiting displacement} \end{cases} \tag{2.9}$$

where b_{es} and k_{es} are the damping and the stiffness coefficients of the end-stop. Figure 2.10 shows the effects of having end-stops on the displacement and velocity of a heaving WEC modelled in a stationary but irregular sea state with $H_s = 6$ m and $T_z = 10$ s. The use of end-stops almost acts like a limit placed on the displacement and hence the velocity of the WEC. The end-stop force is also shown in the figure, which exists only when the displacement of the WEC exceeds the 2 m limit. The damping and stiffness of the end-stops have been set to be ten times the damping coefficient of the PTO and the buoyancy stiffness respectively.

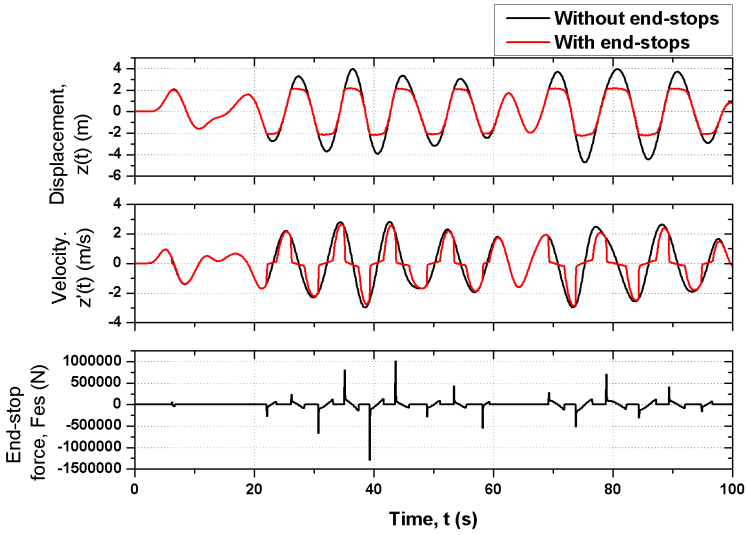

Figure 2.10: *The effects of using end-stops.*

Substituting the different forces into the equation of motion of the WEC (Equation(2.7)), the linear hydrodynamic model of the WEC can be represented by the following integro-differential equation [51]:

$$f_{ex}(t) = (M + \mu_\infty)\,\ddot{z}(t) + \int_0^t \dot{z}(\tau) K(t-\tau) d\tau + b\,\dot{z}(t) + k\,z(t), \tag{2.10}$$

where M is the mass of the buoy, μ_∞ is the added mass at infinite frequency, $z(t)$ is the vertical displacement of the buoy, $K(t)$ is the impulse response function for radiation force also called the radiation kernel, b is the damping coefficient, k is the stiffness of the system and $f_{ex}(t)$ is the excitation force. In the equation, the damping coefficient b includes the damping introduced by the PTO, the damping representing the energy losses and that introduced by the end-stops. Similarly, the stiffness coefficient k in the equation includes both the buoyancy of the WEC and the spring component of the end-stops. Figure 2.11 shows the displacement and the velocity of a WEC generated using Equation (2.10).

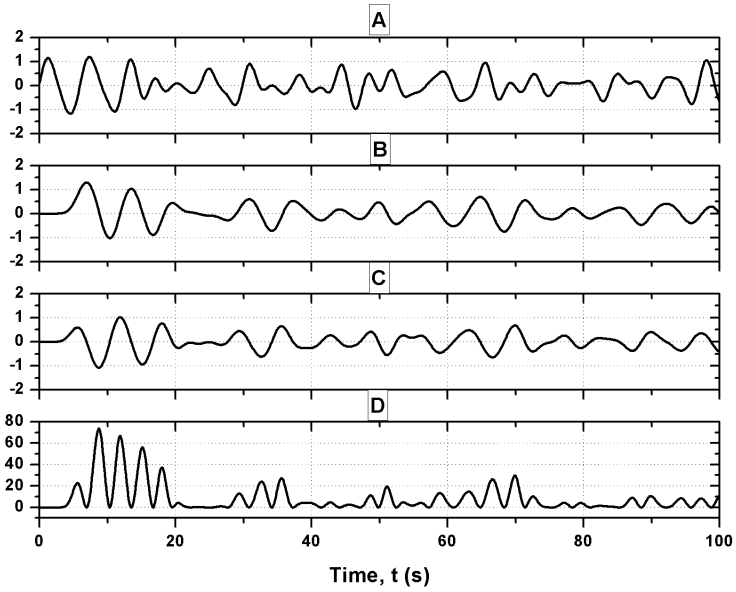

Figure 2.11: *The (a) wave elevation (m), (b) WEC displacement (m), (c) WEC velocity (m/s) and (d) the raw mechanical power extracted by the WEC (kW) for a sea state with $H_s = 2$ m and $T_z = 6$ s.*

2.3.2 Other approaches for modelling WECs

WECs may also be modelled in the frequency domain. In the frequency domain approach, two important quantities in the equation of motion are the added mass and the radiation damping, which respectively replace μ_∞ and the radiation kernel $K(t)$ in the time domain (Equation (2.10)). These coefficients and their variation with frequency can be obtained from commercially available software like WAMIT [52]. Literature also points to analytical functions for calculating the added mass and the damping coefficients for buoys moving in heave and in the other degrees of freedom [53, 54]. For the long-wave approximation, simple analytical means have been established to determine the frequency domain coefficients [55].

Since the time domain equation of motion of the buoy has been used in this work, no further analysis of the frequency domain added mass and radiation damping has been performed. Some of the contemporary literature [56–58] treats the modelling of heaving buoys similar to what has been followed in this work. The methods used in these papers to formulate the kernel function vary. In all these publications the WEC was essentially analysed as a mass-spring-damper system.

2.4 Power take-off model

2.4.1 Damping coefficient for optimal control

As mentioned in the preceding section, the PTO imposes a reaction force on the WEC, which has been modelled by $f_{pto}(t) = b_{pto}\dot{z}(t)$. The instantaneous power given by the WEC has been modelled by $P_{pto}(t) = b_{pto}(\dot{z}(t))^2$ as given in [57]. Since only real control of the PTO has been performed here, the PTO force is always in phase with the velocity.

The value for the PTO damping is selected for maximising the power extraction by the WEC. A detailed description of the various PTO control methods and the associated impedances (in the frequency domain) was presented in [45]. An analytical expression for the optimal b_{pto} required to maximise power extraction was also derived. In this work a similar procedure has been followed, wherein for a particular peak time period a range of values for b_{pto} have been iteratively tested and the one that produces the maximum power extraction was chosen.

Figure 2.12 shows the average raw mechanical power extracted over 600 seconds for different values of the PTO damping coefficient when a WEC is excited by sea states with different peak time periods. For the two sea states with a peak frequency of 0.7414 rad/s, it is seen that the optimal value of the damping coefficient is approximately 40 kNs/m. For the sea states with peak frequencies of 1.1184 rad/s and 0.5592 rad/s, the optimal b_{pto} values are 14 kNs/m and 80 kNs/m respectively. From these results it becomes clear that when the sea is non-stationary the value of the damping coefficient has to be tuned continuously for maximising the power extraction. In this work, the damping coefficient has been pre-calculated before simulation runs are performed. In the case of stationary seas this is permissible. For non-stationary seas, the peak frequency is seen to lie within a small band of frequencies (see Figure 2.3). In such simulations, the damping coefficient has been calculated based on the average peak frequency seen during the entire period.

The raw mechanical power extracted when using sub-optimal damping coefficients is shown in Figure 2.13. This is for the sea state with $H_s = 4$ m and $T_z = 6$ s for which the optimal damping coefficient calculated is 40 kNs/m. It is seen that for the optimal damping case the power extracted is higher than when sub-optimal values are used for the damping coefficient. There are certain periods (e.g. between 235 and 236 seconds) when the sub-optimal damping coefficient gives a higher instantaneous raw mechanical power (Pwec). This is attributed to the

fact that the sea state is a mixture of waves with different time periods. Power extraction will be the highest only when the wave period is close to the period to which the WEC is tuned.

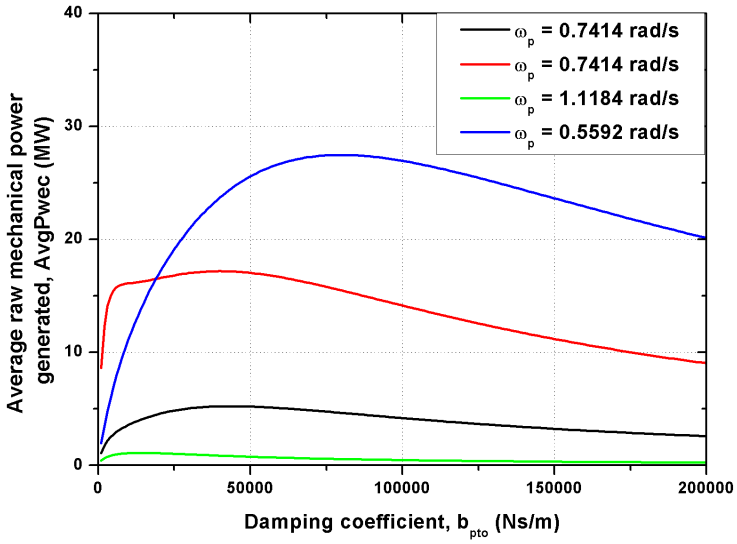

Figure 2.12: *Selection of the PTO damping coefficient for different sea states.*

2.4.2 Other approaches for controlling WECs

To maximise the power extracted by the WEC, the excitation force and the velocity of the WEC have to be in phase [59]. For this, the frequency of the WEC has to be equal to the peak frequency of the sea spectrum. The effects of tuning the WEC frequency to the energy frequency, peak frequency and weighted average of several peak frequencies were tested and compared in [57]. In that publication it was shown that tuning the WEC to the peak frequency of the sea spectrum results in the maximum mean captured power. Latching is another method in which the oscillating body is alternatively locked and released so that the body heaves in phase with the excitation force [60]. This method requires additional mechanical elements which will have to deal with extreme stresses when operating.

When using reactive power control of the WEC, an additional variable stiffness k_{pto} is introduced in the PTO. The aim is to tune the two PTO coefficients b_{pto} and k_{pto} such that the excitation force and the velocity are always in phase. The stochastic nature of the sea may require an adaptive control system which continuously seeks b_{pto} and k_{pto}. For doing so, prediction of the wave climate may be required. The SuperGen Marine Energy Consortium has a research group in Work Stream 7 at the Heriot Watt University investigating how the wave

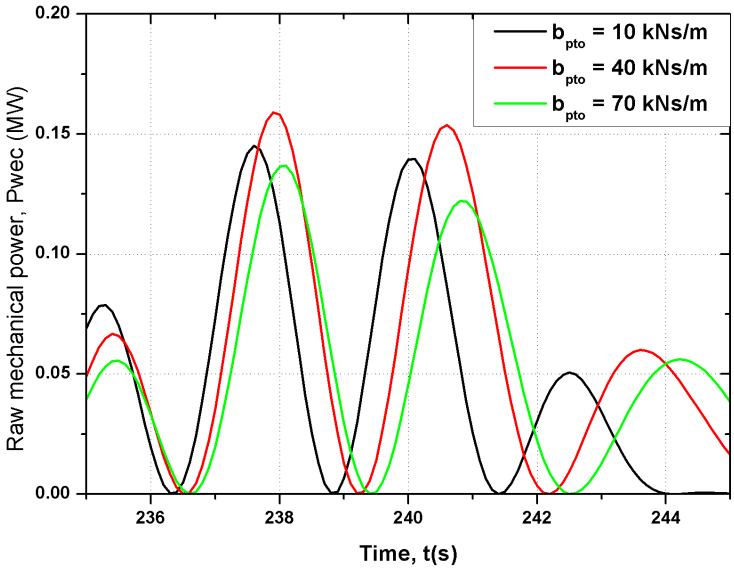

Figure 2.13: *Raw mechanical power extracted from the sea for different PTO damping coefficients b_{pto}.*

climate may be predicted, which is an invaluable input for controlling WECs. The SuperGen Marine research group at Lancaster University, which is also a part of WS7, explored how the different control system set points and target values can be decided and how they can be maintained to maximise yield.

2.4.3 Physical modelling of the PTO

The PTO system converts the power available in the heaving WEC to a suitable form for driving the generator. There are mainly two options being used by WEC developers today. The first one is the linear generator based direct drive system [61, 62]. Different linear generators have been built and tested. Some of them are: vernier hybrid machines [63, 64], air-cored tubular linear generators [65], and variable reluctance permanent magnet machines [66].

The second option for the power take-off is a hydraulic system. In such systems, the translatory motion due to the heaving of the WEC acts on rams which force the flow of high-pressure oil through the hydraulic circuit. The fluid flow transfers the power extracted from the waves to a hydraulic motor/pump system which in turn drives the generator. The hydraulic system acts in the motoring mode when real power control is applied to the WEC as has been the case in this work. When reactive power control of the WEC is used, small fractions of power may need to be returned to the sea to maximise the energy absorption. During such periods, the

hydraulic system acts as a pump drive. Such a hydraulic PTO system has been modelled and used in this work. The hydraulic PTO system was chosen because of its robustness, relatively lower costs and the speed control facility it gives [67]. Power conditioning through the use of on-board storage accumulators is an option tendered by these systems alone. Figure 2.14 shows the schematic of the hydraulic PTO system.

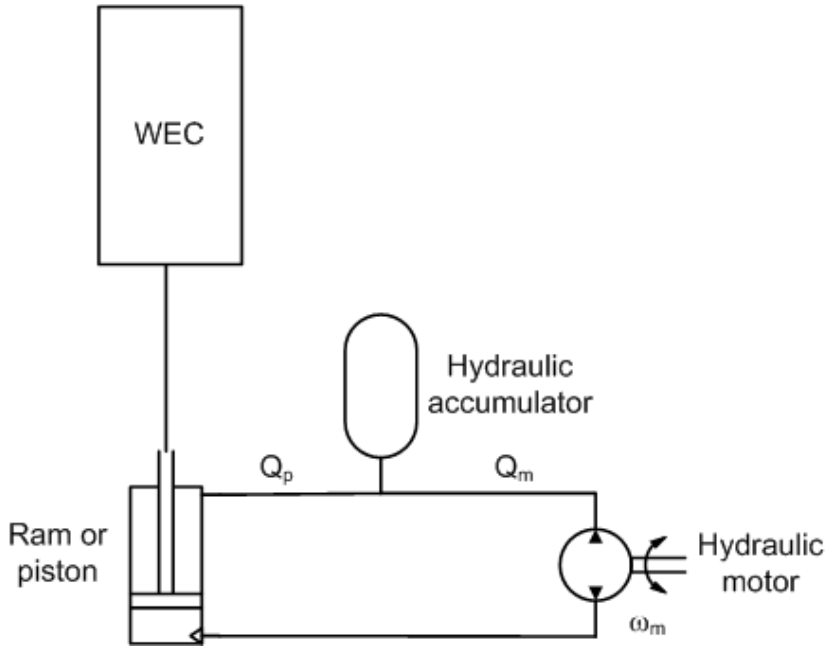

Figure 2.14: *Schematic of the hydraulic PTO system.*

2.4.3.1 Hydraulic accumulator model

Using a hydraulic PTO system allows the use of some on-board storage in the form of accumulators. An accumulator consists of a pre-charged gas chamber and a fluid chamber separated by a bladder (in the case of bladder accumulators [68]). The gas used is pressurised Nitrogen. The pressure of the gas in the accumulator is called the pre-charge or the pre-load pressure. When the fluid pressure at the inlet of the accumulator increases beyond the pre-charge pressure, the fluid enters the fluid chamber of the accumulator thus compressing the gas in the gas chamber. The pressure in the gas chamber is normally equal to the fluid pressure unless the fluid pressure is less than the pre-charge pressure of the accumulator. Under such a scenario, the accumulator pressure is constant and equal to the pre-charge pressure. Figure 2.15 shows the operation of the accumulator. Sub-figure (a) shows the case when the pressure in the fluid system is less than the pre-charge pressure and when the pressure within the gas chamber is maintained at the pre-charged pressure. When the pressure in the fluid system increases beyond the pre-charge pressure, the bladder is compressed thus raising the pressure of the gas (sub-figure (b)). When

the pressure in the gas chamber increases beyond the maximum allowed pressure, the gas release valve ensures that the excess pressure within the gas chamber is expelled by the release of some of the gas from within the chamber (sub-figure (c)). When the fluid pressure in the system goes below the pressure within the gas chamber, the gas chamber pushes the fluid from the fluid chamber to the system.

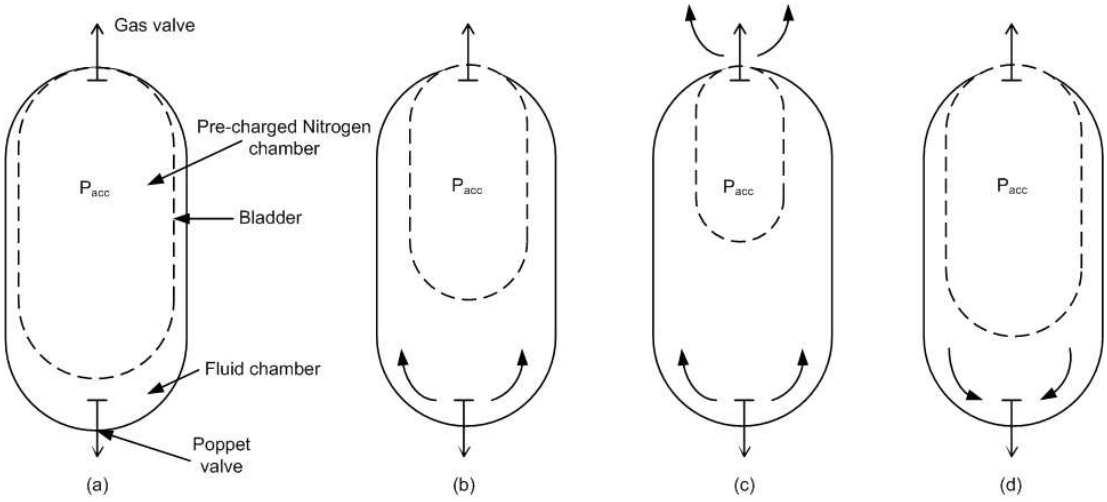

Figure 2.15: *Operation of a bladder accumulator.*

The equations on the basis of which the hydraulic accumulator has been modelled are:

$$\Delta Q(t) = Q_p(t) - Q_m(t) = \frac{dV_f(t)}{dt}, \tag{2.11}$$

$$V_f(t) = \begin{cases} V_a(1 - (p_{pre}/p_{acc}(t)))^{1/k_g} & \text{if } p_{acc}(t) > p_{pre} \\ 0 & \text{if } p_{acc}(t) < p_{pre} \end{cases} \tag{2.12}$$

where Q_p is the flow from the piston to the accumulator, Q_m is the flow from the accumulator to the hydraulic motor, V_f is the fluid volume within the accumulator, V_a is the accumulator volume, p_{acc} is the system pressure, p_{pre} is the pre-charged pressure and k_g is the specific heat ratio [69, 70]. The relation between the flow through the accumulator and the accumulator pressure, which has been used in the model, is shown in Figure 2.16. P_{max}/P_{set} in the figure is the maximum allowed accumulator pressure, beyond which the excess pressure is released through the gas valve.

Figure 2.17 shows the performance of a 0.5 m^3 accumulator when the WEC is placed in a stationary but irregular sea state with $H_s = 6$ m and $T_z = 10$ s. The fluid flow from the piston Q_p follows the variation in the heave velocity of the WEC and has a peak at every peak of the velocity time-series. The fluid flow from the accumulator to the hydraulic motor Q_m

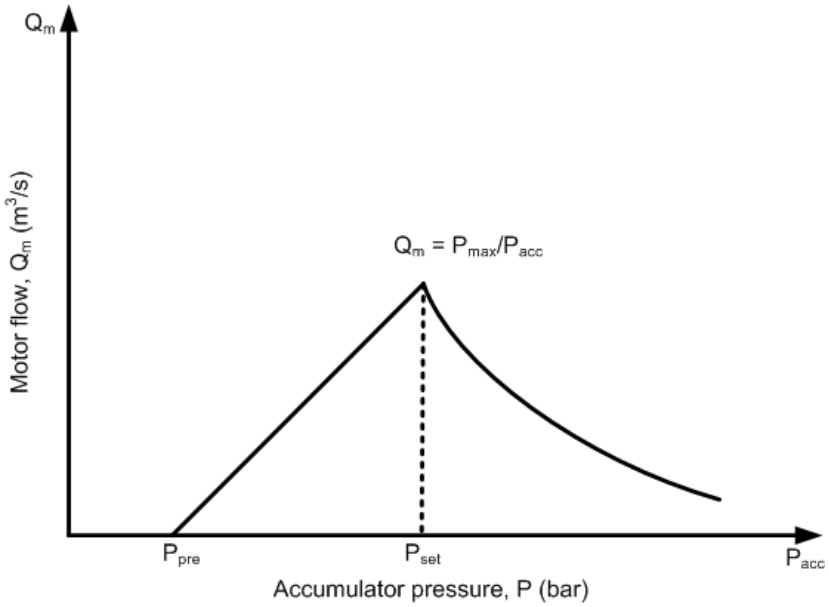

Figure 2.16: *Motor flow versus accumulator pressure characteristic.*

shows a significant reduction in fluctuations when compared to Q_p. The volume of fluid in the accumulator during the 600-second period is also shown in the figure. Figure 2.18 shows the energy stored in the accumulator, calculated by multiplying the fluid volume in the accumulator with the gas pressure in the accumulator. The stored energy has been expressed in kWh to get a more realistic sense of the amount of storage involved.

2.4.3.2 Hydraulic motor model

A simplified model of a digital displacement pump/motor (DDPM), like the one developed by Artemis Intelligent Power Ltd. [71], has been used in this work. Each motor has six cylinders (hydraulic pistons) which are placed radially around an eccentric. Valves are placed around the periphery of the motor. The operation of the valves, during both pumping and motoring, has been described in [72, 73]. The DDPM is a variant of a radial piston pump [74]. The pistons push against the eccentric to produce rotatory motion. At any instant of time, half the cylinders push the working fluid against the eccentric while the other half feeds the fluid to the outlet. The fluid flow can be varied by selecting/deselecting the cylinders in the motor. In the developed model, this functionality has been mathematically modelled based on Figure 2.16, where the system pressure determines the fluid flow rate through the motor (Q_m). The maximum flow rate through the motor has been determined by the volume capacity of the cylinders and the rotational speed of the eccentric.

The power output of the motor has been modelled using $Pmech(t) = e_m p_{acc}(t) Q_m(t)$, where

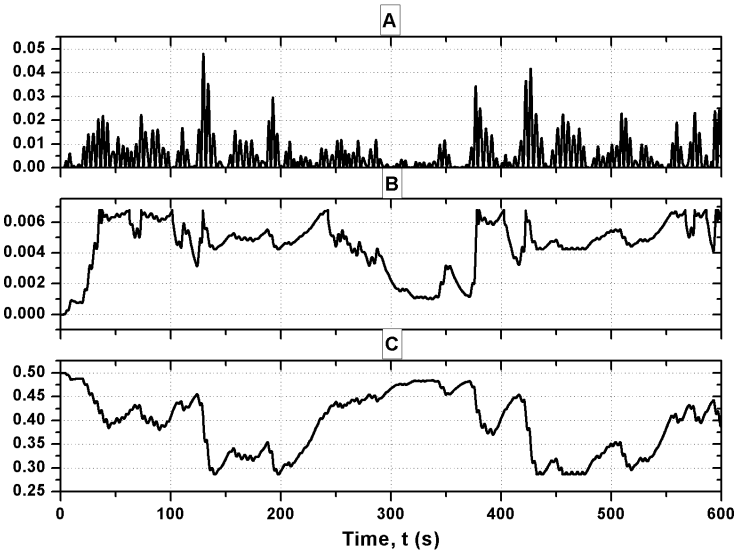

Figure 2.17: *Plots of the different accumulator quantities: (a) fluid flow rate from the piston, Q_p $(\mathrm{m}^3/\mathrm{s})$ (b) fluid flow rate from the accumulator to the motor, Q_m $(\mathrm{m}^3/\mathrm{s})$ (c) volume of fluid in the accumulator, V_f (m^3).*

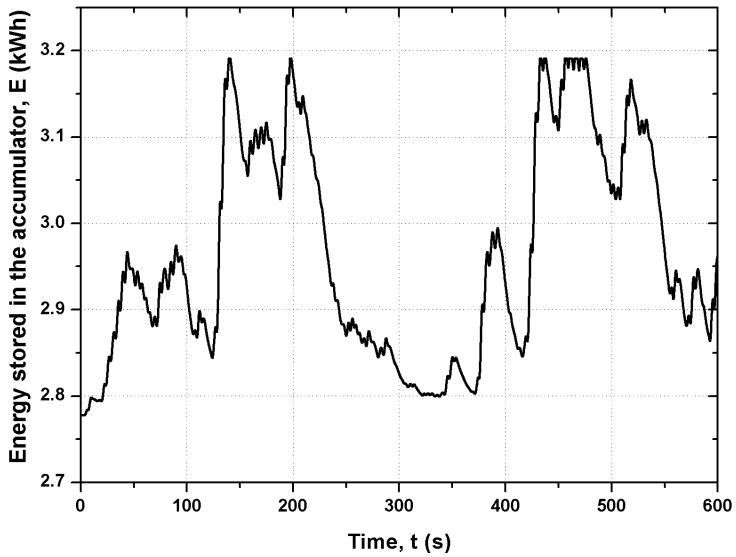

Figure 2.18: *Energy stored in the accumulator.*

e_m is the hydraulic efficiency of motor. The expression is in terms of the pressure in the gas chamber of the accumulator because this is equal to the pressure in the hydraulic system. A constant efficiency of 92% has been used in this work, which is representative of DDPM efficiencies for the flow rates expected in a PTO system [71]. The much improved part-load efficiency is one of the biggest advantages of using the DDPMs in the PTO system [75].

2.5 Generator model

Some of the generators and power converter technologies that have been used in wind turbines are suitable for wave energy devices too. Figure 2.19 shows some of the most common generator topologies that may be considered for use with hydraulic PTO systems. The topology (a) involves the operation of a squirrel cage induction generator. For this the speed of rotation of the machine should be greater than the synchronous speed. This topology is the cheapest and the most robust of the available options, but lacks options for active control of the generator. The same squirrel cage induction machine may be connected to the network through an AC/DC/AC power converter (b). The converter allows the decoupling of the frequency in the network and the rotational speed of the generator. Thus, variable speed operation of the generator is possible. Two disadvantages of this topology are: an increased cost due to the presence of the power converter and the harmonics introduced in the network due to the fully rated power converter.

Synchronous generators may also be used with a hydraulic PTO system and there are two options for their use. In (c) the generator is directly connected to the network. In this case, the generator speed has to be maintained constant. If driven by a low speed prime mover, gearboxes must be used to step up the speed or low-speed synchronous generators with a large number pole pairs may be used. The use of a full power converter in (d) allows variable speed operation with the synchronous generators.

A doubly-fed induction generator (DFIG) with back-to-back PWM converters is shown in (e). In this topology, a voltage is injected to the rotor using the converter. This configuration allows a $\pm$ 30% variation around the synchronous speed (a slip range of $+s_{max} = 0.30$ to $-s_{max} = -0.30$). For this operation, the converters need to be only rated at $s_{max}\, P_s$, where P_s is the power carried by the stator [76]. Unlike topologies (b) and (d) where the converters are fully rated, in this case the converter can be rated at 30% of the machine rating, which leads to significant reduction in the investment on converters. The lower rating of the converters reduces

the harmonics introduced to the network by their connection.

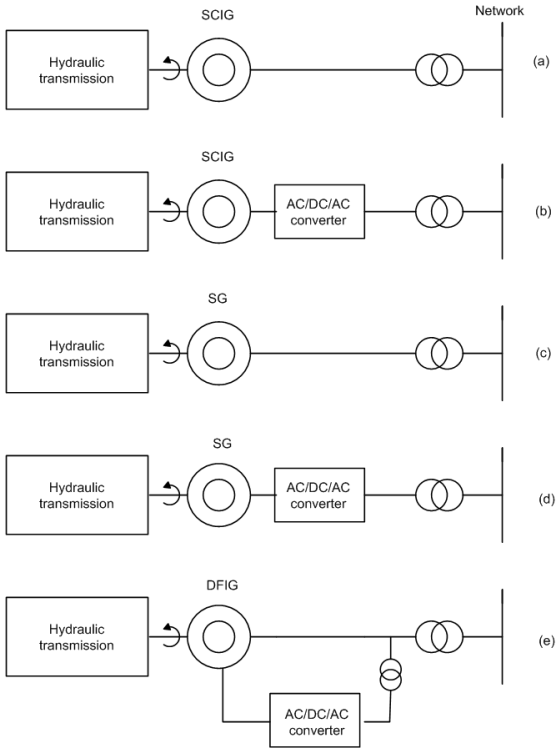

Figure 2.19: *Common generator topologies.*

A detailed comparison of the available options was made in [77–79]. From these articles it becomes clear that using DFIGs with back-to-back PWM converters offers advantages over the other generator topologies. DFIGs provide both the ruggedness of induction machines and some of the control flexibility provided by synchronous machines. This is the system that has been considered in this work. It is important to note that the control and coordination methods discussed in Chapters 5 and 6 are not machine specific and can be used with other generator topologies which use back-to-back PWM converters.

2.5.1 Modelling the DFIG

The dynamics of the DFIG have been modelled using its per-unit state equations [80]:

$$V_{ds} = -R_s i_{ds} - \omega \lambda_{qs} + p\lambda_{ds} \tag{2.13}$$

$$V_{qs} = -R_s i_{qs} + \omega \lambda_{ds} + p\lambda_{qs} \tag{2.14}$$

$$V_{dr} = -R_r i_{dr} - (\omega - \omega_r)\lambda_{qr} + p\lambda_{dr} \tag{2.15}$$

$$V_{qr} = -R_r i_{dr} - (\omega - \omega_r)\lambda_{dr} + p\lambda_{qr} \tag{2.16}$$

where $[k_{qd0s}]^T = [k_{qs}\, k_{ds}\, k_{0s}]$ (k represents current, voltage or flux), subscripts d and q refer respectively to the direct and quadrature axis components of voltage (V), current (i) and flux (λ), subscripts s and r are used respectively for the stator and rotor quantities, R is the resistance, ω is the angular speed of the reference frame, ω_r is the angular speed of the rotor and p is the differentiation operator. The stator flux oriented reference scheme for modelling the DFIG has been adopted where the d-axis is in phase with the maximum of the stator flux. Therefore, $\lambda_{qs} = 0$ and $\lambda_{ds} = \lambda_s$ [81, 82]. Since the flux linked with the d and q axes induce an emf in the q and d axes respectively, $V_{ds} = 0$ and V_{qs} equals the terminal voltage of the machine. The stator flux rotates at synchronous speed and therefore $\omega = \omega_s$.

The flux linkage expressions, in terms of the current, which have been used in Equations (2.13)to (2.16), are:

$$\lambda_{ds} = -(L_s + L_m)i_{ds} - L_m i_{dr} \tag{2.17}$$

$$\lambda_{qs} = -(L_s + L_m)i_{qs} - L_m i_{qr} \tag{2.18}$$

$$\lambda_{dr} = -(L_r + L_m)i_{dr} - L_m i_{ds} \tag{2.19}$$

$$\lambda_{qr} = -(L_r + L_m)i_{qr} - L_m i_{qs} \tag{2.20}$$

where L_m is the mutual inductance, L_s is the stator leakage inductance and L_r is the rotor leakage inductance. The speed ω_r in Equations (2.13) to (2.14) is related to the developed electrical and mechanical torques as:

$$T_e = T_L + (2/P)J\frac{d\omega_r}{dt}, \tag{2.21}$$

where T_e is the electrical torque generated, T_L is the load torque, J is the rotor inertia and P is the number of poles.

The stator active and reactive powers are respectively

$$P_s = V_{ds} i_{ds} + V_{qs} i_{qs} \tag{2.22}$$

and

$$Q_s = V_{qs} i_{ds} - V_{ds} i_{qs}, \tag{2.23}$$

while the rotor active and reactive power are respectively

$$P_r = V_{dr} i_{dr} + V_{qr} i_{qr} \tag{2.24}$$

and

$$Q_r = V_{qr} i_{dr} - V_{dr} i_{qr}. \tag{2.25}$$

The real and reactive power generated by the DFIG thus becomes $P_s + P_r$ and $Q_s + Q_r$. $P_s + P_r$ thus is the total real power the DFIG exchanges with the network. $Q_s + Q_r$ is the reactive power of the machine. The network-side power electronic converter connected in the rotor circuit allows the control of the absorbed/generated reactive power independently, while the rotor-side converter supplies the reactive power required by the DFIG. Q_r therefore is removed from the equation. Generally, the reactive power that the converter exchanges with the network is kept at zero to reduce the rating of the converter and the losses. Since the converter cannot store real power, the power it exchanges with the network is P_r, neglecting converter losses.

2.5.2 Control of the DFIG

Figure 2.20 shows the block diagram of a wave energy converter equipped with a DFIG operating with a hydraulic power take-off system.

2.5.2.1 Speed/Torque control of the DFIG

From the stator Equations (2.13) and (2.14), since the stator flux does not vary, $p\lambda_{qs} = 0$. Neglecting the stator resistance gives $V_{ds} = 0$ and $V_{qs} = \omega_s \lambda_{ds}$. Substituting Equation (2.18) in Equation (2.22) gives

$$P_s = \omega_s \lambda_{ds} (L_m / (L_m + L_s)) i_{qr}. \tag{2.26}$$

From this equation it is understood that the real power output from the generator may be varied by changing i_{qr} (or V_{qr}).

Figure 2.21 shows the speed/torque control scheme of the DFIG which has been used in this work [76, 81]. A linear speed controller has been used which provides a torque reference for

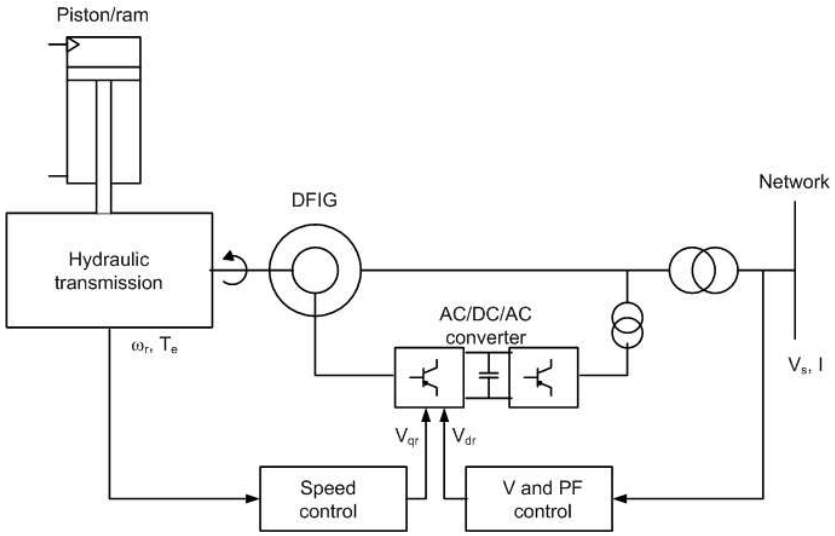

Figure 2.20: *Schematic of the WEC with the machine control and the electrical network.*

a measured speed input. A proportional-integral controller has been used to obtain V_{qr} for the error in the electric torque ΔT_e.

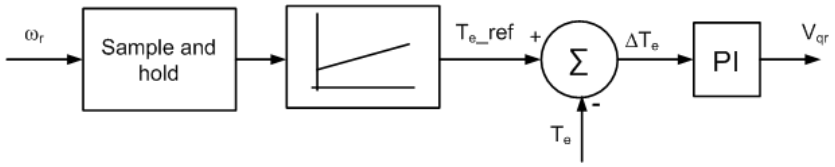

Figure 2.21: *Speed control scheme of the DFIG.*

2.5.2.2 Voltage and power factor control of the DFIG

Substituting Equation (2.17) in Equation (2.23) gives

$$Q_s = -\omega_s \lambda_{ds}(\lambda_{ds} + L_m i_{dr})/(L_s + L_m). \tag{2.27}$$

From this equation it is understood that the reactive power output from the generator may be varied changing i_{dr} (or V_{dr}). The first part of the RHS in the equation is the reactive power required to magnetise the DFIG. If this is set as the reactive power reference, the rotor inverter will provide only the reactive power required to magnetise the DFIG. The operating power factor of the DFIG thus becomes unity.

Figure 2.22 shows the voltage and the power factor control scheme of the DFIG [76]. Proportional-integral controllers have been used for generating the reference V_{dr} component of the voltage which is sent to the rotor side inverter. When operating in the power factor control mode Q_{ref} is the input to the controller and when operating in the voltage control mode V_{ref} is the input. Both these control operations of the DFIG are dealt with in detail in Chapter 5.

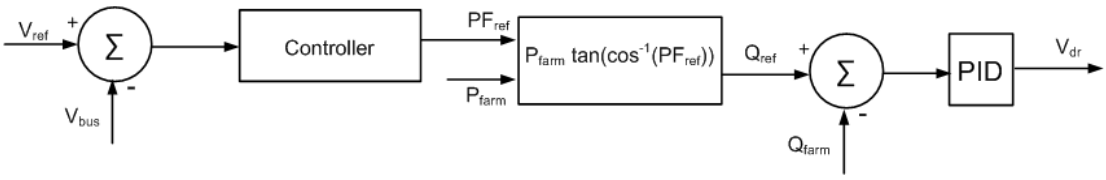

Figure 2.22: *Voltage and power factor control scheme of the DFIG.*

2.5.2.3 Modelling the power electronic converters

For dynamic simulations at the fundamental frequency, a simulation step time between 10 and 50 ms is normally chosen. Under this condition, it is sufficient to model the power electronic converters as controlled voltage sources [83]. The voltage set points are assumed to be instantaneously reached. The advances in power electronic converters that operate at high frequencies justify this decision. Moreover, the higher order effects of the rotor-side converter do not affect the operation of the system with respect to the time constants associated with wave energy conversion. A comparative study, discussed in [84], of the two modelling approaches showed that modelling the converters as controlled voltage sources suffices for power system dynamic studies.

The network-side converter normally exchanges only real power with the network. However, the network-side converter may also contribute towards reactive power control. This would require the rating of the network-side converter to be more than the 30% rating mentioned earlier, to provide the reactive power. This would increase the cost and the harmonics injected to the network, but can play an important role in voltage regulation, in cases when the reactive power control of the rotor-side converter alone is not adequate.

2.6 Electrical layout and network integration of the wave power farm

So far in this chapter, only the developed model of a single WEC was described. Figure 2.23 shows the schematic of the developed WEC model. WEC installations will normally have multiple units as farms of WECs. Models of such wave power farms have been developed by cloning the model of the individual WEC. The wave elevation time-series at the locations in the wave field where the individual WECs are placed are the inputs to the individual WECs.

Figure 2.24 shows a simple array of three WECs. WECs 1 and 2 lie along the dominant wave direction, while WECs 1 and 3 lie perpendicular to the dominant wave direction. The spacing

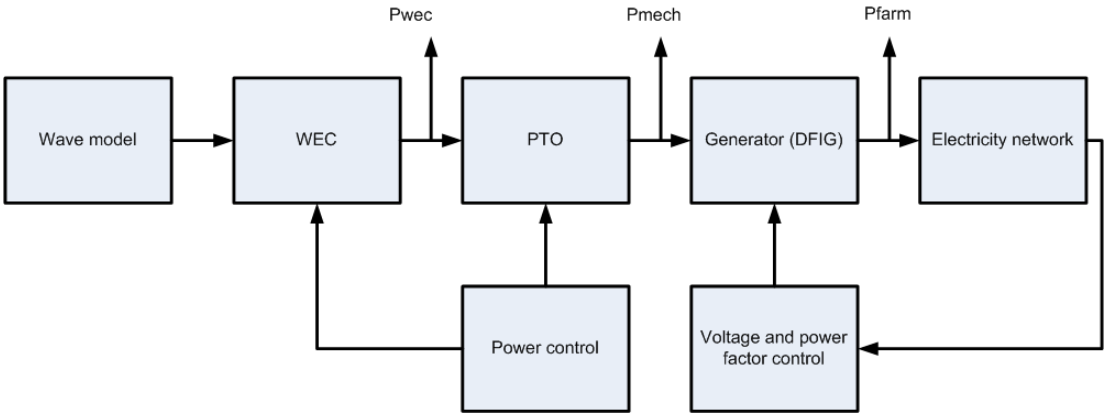

Figure 2.23: *Schematic of a wave energy converter.*

between the WECs d has been taken as 50 m here. Figure 2.25 shows the wave elevation time-series at each location and the raw mechanical power extracted by the WECs. The power shown is the power extracted before being subject to smoothing and storage. The wave elevation time-series seen by WEC 2 is almost the time-shifted wave elevation seen by WEC 1, since WEC 2 lies behind WEC 1 along the dominant wave direction. Increasing the distance d between these two WECs would make the wave elevation seen by WEC 2 very different from the one seen by WEC 1 because of the random nature of multi-directional sea states.

The difference in the wave elevation perpendicular to the dominant wave direction, seen by WECs 1 and 3, is determined by the crest length of the oncoming waves. Peaks and troughs in the wave elevation seen by both the WECs occur at the same instants of time, but the wave amplitude and hence the power extracted by the WECs are different. Increasing the distance d between WECs 1 and 3, beyond the average crest length, would make the wave elevation seen by the two WECs out of phase and different.

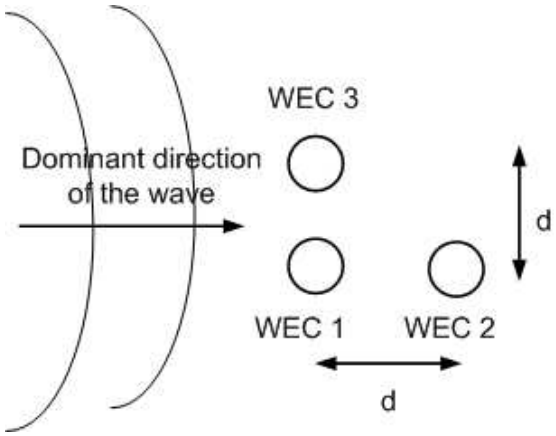

Figure 2.24: *Wave power farm layout.*

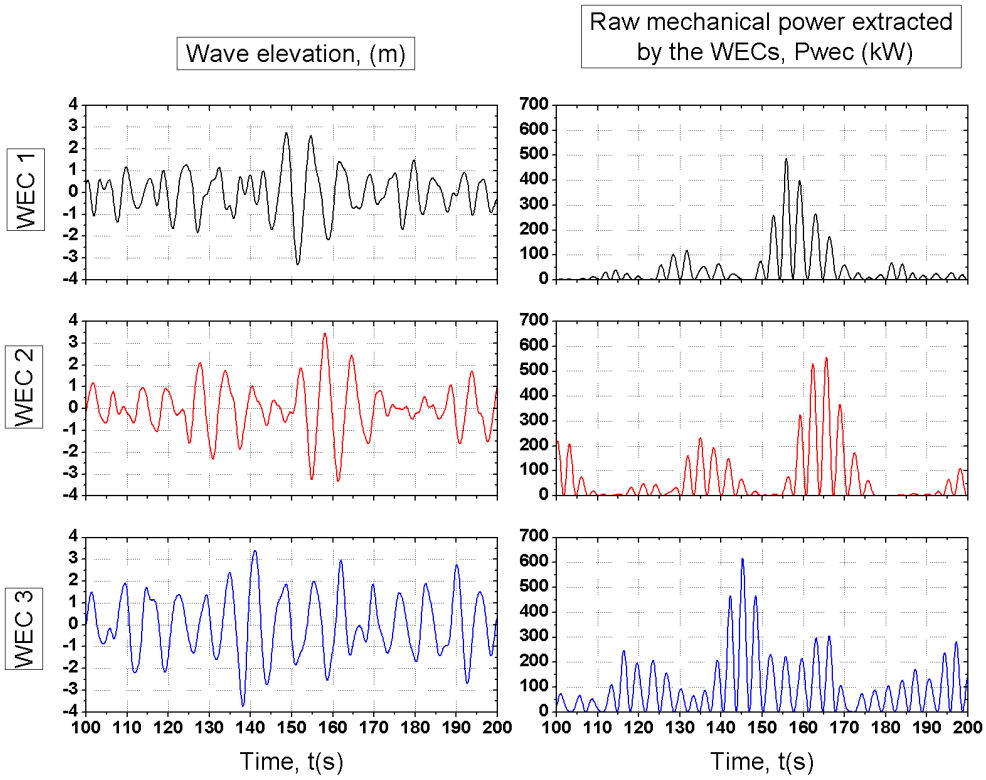

Figure 2.25: *Wave elevation time-series and raw mechanical power extracted by the three WECs.*

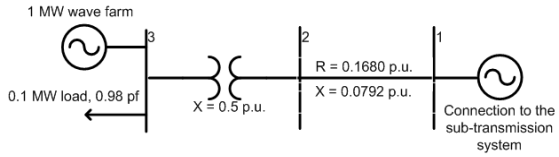

Figure 2.26: *Radial network model (with three buses) of a hypothetical rural distribution feeder with the wave power farm and the distributed loads.*

A number of factors like the depth of the sea, the type of the WEC, the mooring system, the type of the sea bed, etc., determine the layout of a wave power farm. The electrical connection to the shore depends on the size of the generators in the farm, the size of the farm and the distance of the farm from the shore. For early deployment of WECs, AC links are likely to be used because of the small size of the farms and the proximity to the shore. For example, heaving buoys would be placed in waters with a mean depth of 30-50 m, which would be between 1-5 km from the shore in the UK.

In this work, the wave power farm has been modelled with the mean water depth taken as 40 m. The site considered has been assumed to be 1 km offshore and the wave power farm has been connected to the on-shore network through 11 kV AC sub-sea cables. For larger farms further offshore, the power transmission may be at higher voltages. As the farm size and/or the distance from the shore increases further, high voltage DC links may also be used. Different wave power farm sizes and layouts have been used in different chapters in this thesis to investigate network impacts. The farm layout, the electrical connection to the shore, and the on-shore network to which the farm is connected are described in each chapter. A simple three-bus network, which has been used in some of the preliminary analysis, is shown in Figure 2.26.

In this thesis, the interference between the WECs in a farm has been taken to be negligible. Wave power farms are normally sparse due to physical considerations, justifying this choice [85, 86]. In all the chapters dealing with the electrical control of the generator, the developed algorithms will work irrespective of whether the interactions between the WECs are considered or not.

2.7 Summary

In this chapter, the developed dynamic wave-to-wire model of a wave power farm was described. A non-stationary sea was modelled from spectral representations. The model was made suitable even in shallow-waters. Both the directional aspect and the irregularity of a realistic sea were modelled.

A heaving WEC was considered and its equation of motion was obtained from the forces acting on it. In this thesis, the effects of mooring on the WEC have not been considered and it was assumed that the WECs, constrained to move in heave, are held in place by a monopile (or other taut moorings). Moorings would be seen as additional spring forces on the WEC, which may be incorporated in the model. A SuperGen Marine research group at the University of Exeter has been researching the effects of moorings on the motion of WECs.

Different options available for the control of the WEC for maximising energy extraction were then explained. In this work, a simple control option has been used where the damping coefficient of the PTO system is changed depending on the sea state. As has been explained in the chapter, changing the damping coefficient only causes a phase shift and an increase/reduction in the peak raw mechanical power extracted. The generated power profile remains similar, irrespective of the damping coefficient. The voltage fluctuations in the network, that these variations in the generated power profile introduce, is the main focus in this thesis. In the subsequent chapters, wave power farms that have been modelled in different sea states, from extremely low energy sea states to extremely high energy sea states are discussed.

The model of the hydraulic PTO system, which drives a DFIG, was described in detail. The reasons why the hydraulic PTO system was chosen over the direct drive PTO and why the DFIG was chosen over other generator types were discussed. The active power and reactive power control capabilities of the DFIG and how these quantities may be controlled were also examined.

In the next chapter, the developed detailed model of the wave power farm is used to train wavelet neural networks to build an equivalent Nonlinear AutoRegressive eXogenous (NARX) model of the wave power farm. The performance of the NARX model is then compared to the detailed model.

Chapter 3
Modelling wave power farms - Part II

3.1 Introduction

The development of a time domain model of a wave power farm was described in the previous chapter. This detailed model can be used to study the impacts of connecting wave power farms to electricity networks. Examples of such studies have been presented in different parts of this thesis. One drawback of using the detailed model is that, being a dynamic model, it is computationally intense and the simulation runs take an extremely long time. The simulation time and the computing resource used increase further as the size (number of devices) of the farm increases. It was necessary to have a large number of simulation runs of wave power farms of different sizes over long periods of time. This being the case, an alternative modelling technique became necessary.

This chapter describes the use of system identification techniques for modelling wave power farms. A Nonlinear AutoRegressive eXogenous (NARX) model of a WEC has been system identified and the procedure for doing so is explained in this chapter. System identification has been performed using data collected from simulating the detailed model. The data obtained was then used to train wavelet neural networks. The performance of the NARX model has been compared with that of the detailed model for a range of sea states found off western Scotland and the results are discussed in this chapter.

Before examining the development of NARX models, a brief description of some of the mathematical and theoretical concepts required to understand NARX modelling is presented. Definitions of the different model types with a special focus on linear time-invariant systems are furnished. The different black-box model structures are listed and their generic form is derived. This gives a clear picture of how the model can be used to predict future output values. Later in the chapter, wavelets, neural networks and wavelet neural networks are dealt with, since these have been used to identify the NARX model of the WEC. The section on NARX modelling follows smoothly from this discussion on its mathematical basis.

The NARX model was found to significantly improve the simulation speed when compared to the detailed model. A high precision was also maintained. The developed NARX model of an individual WEC has been cloned to model wave power farms. The real power generated by the wave power farm may be obtained from the NARX model, which can then be used to study the network impacts of connecting wave power farms to the electricity network over extended periods of time. Since the main focus of this thesis is on the fluctuations in the rms-voltage seen in the network with wave power farms, a high resolution study is required which is made possible using the NARX model. Personal computers can be used to run simulations of the NARX model with a high time resolution as required by the control loop times of the WECs.

3.2 Models of dynamic systems

Many physical systems can be considered as linear time-invariant systems, with nonlinear systems considered as generalisations of the linear ones [87]. In this section, the construction of linear black-box models of time-invariant systems is addressed first. The theory for the linear case developed is then extended for the nonlinear case. Different properties of such systems are also defined in this section.

3.2.1 Types of models

A **model** of a system is a tool to answer questions about the system, without having to experimentally work on the system. Models can be of four kinds - mental models, verbal models, physical models and mathematical models [88]. Chapter 2 described in detail the development of a mathematical model of a WEC. The WEC was broken down into modules whose properties were known. Mathematical relations were used to describe the relationship between quantities within each module. The different modules were then linked up and connected to a model of the electrical network to form the wave-to-wire model of the WEC. Through physical modelling, thus, a mathematical model of the WEC was developed. The detailed model of Chapter 2 can also be called a **white-box model**, which was constructed entirely from prior knowledge and physical insights.

Another approach to mathematical modelling requires observations of the system to be made. These observations are used to fit the model's properties to that of the system. This way of developing mathematical models is called **identification**, which is the main topic of this chapter. The models developed using this approach can be of two types - grey-box models and black-box models. **Grey-box models** are those built when some physical insight of the sys-

tem is available and when the observations are required to find values of certain parameters in the model. **Black-box models** are those that are entirely built using observations of the system, where little or no physical insight is available. The model of the WEC developed in this chapter can be classified as a black-box model. Data obtained from simulations of the detailed white-box model have been used to construct the black-box model.

Models can also be classified based on how the signals in the model are defined as functions of time. **Continuous time models** are those that represent the mathematical relationships between time continuous signals. Practically, the signals normally dealt with are sampled ones. Models which represent the relationship between signals at the instants of sampling are called **discrete time models**. Both the detailed model of the WEC and the model of the WEC dealt with in this chapter are discrete time models.

3.2.2 Definitions

Time-invariant systems (or models) are those in which a time delay or a time advance of the input signal causes the same time delay or time advance in the output signal, i.e. the output signal does not depend on absolute time [89, 90].

A model is said to be **linear** if it satisfies the principle of superposition, i.e. if its output to a linear combination of inputs is equal to the linear combination of the outputs of the same individual inputs [89, 90].

Causal systems (or models) are those in which the current value of the output only depends on the current and past values of the input [89, 90].

3.2.3 Linear black-box models

The output of a linear, time-invariant, causal, single input single output (SISO) and discrete time model can be represented by its impulse response ($g(k)$) as follows [88]:

$$y(t) = \sum_{k=1}^{\infty} g(k)u(t-k);\ t = 0, 1, 2, ... \tag{3.1}$$

where $y(t)$ is the current output and $u(t)$ is the current input. This equation suggests that the current output of a model can be predicted by knowing the current and the past values of the input. This is not always the case because there are some signals, which are not one of the inputs, that affect the output of the model. These signals, also called disturbance, need to be

added:

$$y(t) = \sum_{k=1}^{\infty} g(k)u(t-k) + v(t); \tag{3.2}$$

where $v(t)$ is the lumped disturbance and is given by:

$$v(t) = \sum_{k=0}^{\infty} h(k)e(t-k). \tag{3.3}$$

Defining the backward shift operator q^{-1} as follows: $q^{-1}u(t) = u(t-1)$, Equation (3.2) can be rewritten as:

$$y(t) = \sum_{k=1}^{\infty} g(k)u(t-k) + \sum_{k=0}^{\infty} h(k)e(t-k) \tag{3.4}$$

$$y(t) = \sum_{k=1}^{\infty} g(k)(q^{-k}u(t)) + \sum_{k=0}^{\infty} h(k)(q^{-k}e(t)) \tag{3.5}$$

$$y(t) = [\sum_{k=1}^{\infty} g(k)q^{-k}]u(t) + [\sum_{k=0}^{\infty} h(k)q^{-k}]e(t) \tag{3.6}$$

$$y(t) = G(q)u(t) + H(q)e(t). \tag{3.7}$$

In Equation (3.7), $G(q)$ is called the input pulse transfer function while $H(q)$ is the noise pulse transfer function. This equation shows the structure of linear black-box models. Equation (3.7) can be modified as follows [87, 91]:

$$A(q)y(t) = \frac{B(q)}{F(q)}u(t) + \frac{C(q)}{D(q)}e(t). \tag{3.8}$$

where

$$A(q) = 1 + a_1q^{-1} + ... + a_{na}q^{-na} \tag{3.9}$$

$$B(q) = b_1q^{-1} + ... + b_{nb}q^{-nb} \tag{3.10}$$

$$C(q) = 1 + c_1q^{-1} + ... + c_{nc}q^{-nc} \tag{3.11}$$

$$D(q) = 1 + d_1q^{-1} + ... + d_{nd}q^{-nd} \tag{3.12}$$

$$F(q) = 1 + f_1q^{-1} + ... + f_{nf}q^{-nf}. \tag{3.13}$$

Equation (3.8) is a general representation of the input-output relationship. Depending on which polynomials $A(q)$ to $F(q)$ are used, 32 different model structures can be derived from the equation. Some of the most commonly used structures are listed in Table 3.1.

Model name	Condition
Finite Impulse Response (FIR)	$A = C = D = F = 1$
Box-Jenkins (BJ)	$A = 1$
AutoRegressive Moving Average with eXogenous inputs (ARMAX)	$F = D = 1$
Output-Error (OE)	$A = C = D = 1$
AutoRegressive with eXogenous inputs (ARX)	$F = C = D = 1$

Table 3.1: *Model structures*

3.2.4 Prediction from linear black-box models

An expression for predicting $y(t)$ can be obtained by rearranging Equation (3.8) [92]:

$$\frac{A(q)D(q)}{C(q)}y(t) = \frac{B(q)D(q)}{F(q)C(q)}u(t) + e(t) \tag{3.14}$$

$$y(t) = [1 - \frac{A(q)D(q)}{C(q)}]y(t) + \frac{B(q)D(q)}{F(q)C(q)}u(t) + e(t). \tag{3.15}$$

Since A, D and C all start with a 1 (see Equations (3.9, 3.11 and 3.12)) the first expression on the right-hand side (RHS) contains the output $y(t)$ only until time $t-1$. Similarly, since the second term on the RHS contains B which starts with $b_1 q^{-1}$ and since D, F and C start with 1, the second term only consists of inputs on and before time $t-1$. $e(t)$ is the disturbance signal, which is taken to be white noise and cannot be predicted using previous values of $e(t)$, $u(t)$ or $y(t)$; and hence the best one-step-ahead predictor is given by:

$$\hat{y}(t|\theta) = [1 - \frac{A(q)D(q)}{C(q)}]y(t) + \frac{B(q)D(q)}{F(q)C(q)}u(t). \tag{3.16}$$

This equation means that the current value of the output $y(t)$ can be predicted from the past values of the inputs and the outputs. In Equation (3.16) the parameter vector θ represents the unknown parameters $a_1, ..., a_{na}, b_1, ..., b_{nb}, c_1, ..., c_{nc}, d_1, ..., d_{nd}, f_1, ..., f_{nf}$. Equation (3.16) can be rewritten as:

$$\hat{y}(t|\theta) = \theta^T \varphi(t, \theta), \tag{3.17}$$

where $\varphi(t)$ is called the regression vector, whose components are called regressors. In the general case depicted in Equation (3.16), the regressors are given by [91]:

- $u(t-k)$ (associated with $B(q)$)
- $y(t-k)$ (associated with $A(q)$)
- $\hat{y}_u(t-k|\theta)$, the simulated output from past values alone (associated with $F(q)$)

- $e(t-k) = y(t-k) - \hat{y}(t-k|\theta)$, the prediction error (associated with $C(q)$)
- $e_u(t-k) = y(t-k) - \hat{y}_u(t-k|\theta)$, the simulation error (associated with $D(q)$).

A special case of Equation (3.16), when $C(q)$, $D(q)$ and $F(q)$ are 1 leads to:

$$\hat{y}(t|\theta) = [1 - A(q)]y(t) + B(q)u(t). \tag{3.18}$$

This structure is called the AutoRegressive eXogenous (ARX) model. The first term on the right-hand side of Equation (3.18) forms the autoregressive part of the model, while the second term represents the exogenous input part. Expanding Equation (3.18) we get the linear difference equation:

$$\hat{y}(t|\theta) = a_1\, y(t-1) + a_2\, y(t-2) + ... + a_{na}\, y(t-na) + b_1\, u(t-1) + b_2\, u(t-2) + ... + b_{nb}\, u(t-nb). \tag{3.19}$$

The equation does not show the requirement of the current input u(t). This is because the equation represents a model used to predict the next output. When used for simulation, i.e. when the current output for the current input is required, the current value of the input would also be a part of the regressor set.

For the ARX model structure, thus, θ and $\varphi(t)$ in Equation (3.17) becomes:

$$\theta = [a_1, a_2, ..., a_{na}, b_1, b_2, ..., b_{nb}] \tag{3.20}$$

$$\varphi(t) = [y(t-1), y(t-2), ..., y(t-na), u(t-1), u(t-2), ..., u(t-nb)]. \tag{3.21}$$

3.2.5 Nonlinear black-box models

Nonlinear input-output models can be obtained from Equations (3.2) and (3.17) by replacing the linear function with a nonlinear function as follows:

$$y(t) = g(\varphi(t), \theta) + e(t), \tag{3.22}$$

$$\hat{y}(t|\theta) = g(\varphi(t), \theta). \tag{3.23}$$

where $g(.)$ is a nonlinear function parameterised by θ.

Similar to the linear model, different nonlinear model structures can be constructed using the generic structure given in Equation (3.23) [91]. They are:

- NFIR models - $u(t-k)$ in the regression vector
- NARX models - $u(t-k)$ and $y(t-k)$ in the regression vector
- NOE models - $u(t-k)$ and $\hat{y}(t-k|\theta))$ in the regression vector
- NARMAX models - $u(t-k)$, $y(t-k)$ and $\hat{e}(t-k|\theta)$ in the regression vector
- NBJ models - $u(t-k)$, $\hat{y}(t-k|\theta)$, $\hat{e}(t-k|\theta)$ and $\hat{e}_u(t-k|\theta)$ in the regression vector.

In this chapter, the development of a NARX model of a wave energy converter is described, and hence in the remaining sections the focus is on NARX models. The reasons why a nonlinear model representation of the WEC has been chosen over linear models are discussed in the next section.

3.3 System identification

So far in this chapter only systems with known parameters θ were dealt with. When the only known quantities are the measured input and output values and when the parameter vector and the nonlinear mapping function are unknown, the model of the system can be built by system identification. System identification can be defined as a systematic approach of building dynamic models of systems using statistical methods. Observed input-output data are used to develop models of unknown systems [93].

System identification has found application in other areas of engineering and science [94, 95]. In these publications, the models were derived from experimental set-ups. In the field of electrical power systems, system identification techniques have mainly been used to model power electronic converters [96–98]. Applications of system identification have also been used in failure/abnormal condition detection [99] and forecasting [100, 101].

In this section, how a NARX model of a WEC has been developed using system identification is described. Data obtained from simulating the detailed model of the WEC have been used for this. The different steps involved in the construction of NARX models are discussed and explained using the example of the PTO-DFIG unit of a WEC. Before describing the process used to construct the NARX model of the wave power farm, the theory behind wavelets, neural networks and wavelet networks are briefly dealt with. These are required to understand the NARX modelling framework adopted in this work.

3.3.1 Why nonlinear models

The WEC system, with the buoy, the PTO system and the DFIG, is inherently nonlinear. The nonlinearity has components introduced by the end-stops (see Section 2.3.1), by the on-board energy storage in the form of accumulators (see Section 2.4.3) and by the power curve of the DFIG. Figure 3.1 shows the power curve of the DFIG which has been used in this work. It is seen that power generation starts only above a cut-off speed (ω_{min} rad/s). The power generation increases linearly till the rated speed of the DFIG (ω_{rated} rad/s). The DFIG generates rated power at rated speed. Beyond the rated speed, the power generated by the DFIG is kept fixed at its rated power. The nonlinearity introduced by the accumulator and the end-stops were discussed in Chapter 2. The presence of these nonlinearities makes nonlinear black-box models the obvious choice for modelling WECs.

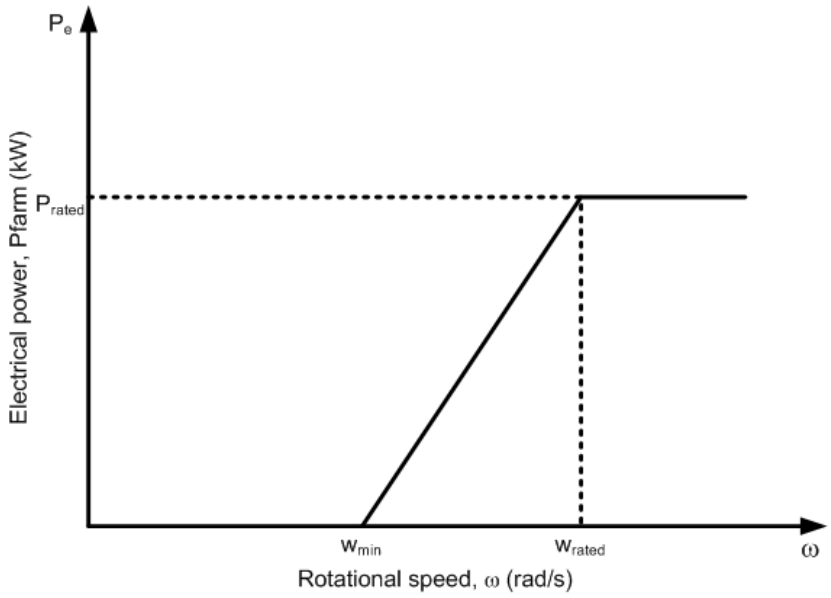

Figure 3.1: *Power curve of the modelled DFIG.*

3.3.2 Wavelet transform

It is known from Fourier theory that a signal $f(t)$ can be wholly represented as a sum of sinusoids of, probably, infinite frequencies. One of the drawbacks of using Fourier theory (FT) is that though the frequency content of a signal may be obtained, the time-localisation of the frequency content is lost. That is, one would not be able to know when certain frequencies were present in the signal. One alternative available is to cut the given signal into sections in time, and to perform Fourier analysis of each of these sections separately. This approach, called the Windowed Fourier Transform (WFT) [102], is more useful in the time-frequency wedding.

One question that comes up in this approach is regarding the size of the window to be used. Wrongly sized windows could lead to a loss of information.

Wavelet analysis is the most recent method developed to overcome the shortcomings of the Fourier and the Windowed Fourier approaches. It is similar to the WFT because both time and frequency domain information are obtained. The main difference is that while the WFT has a fixed time and frequency resolution, wavelet analysis looks at the signal at different frequencies with different resolutions [103]. A detailed description of the differences between these two can be found in chapter 1 of [104]. The advantages of using wavelet analysis over WFT and FT along with the properties of wavelet analysis and general areas of application were discussed in detail in [105]. The applicability of these approaches for an application in geophysics was compared in [106], which again proves the advantages of using wavelet transforms for obtaining a time-frequency picture of the dynamics of internal waves. Wavelets, thus, can be defined as a class of functions which can be used to find the frequency content of a signal $f(t)$ locally in time.

3.3.2.1 Continuous wavelet transform

In wavelet analysis, a scalable function is used as a window. This function is shifted along the signal till the end of the signal and the spectrum is calculated using all the scaled windows for every position. In the end, a collection of time-frequency representation of the signal is obtained [107]. A wavelet $\psi(t)$ is a small wave function which is used as the scalable function [108, 109]. It is a function with zero-average and is dilated with a scale parameter j and translated by k and is represented by [102, 110]:

$$\psi_{j,k}(t) = \frac{1}{s}\psi(\frac{t-k}{j}). \tag{3.24}$$

Haar, Daubechies, Gaussian, Meyer, Mexican hat and Morlet are the commonly used wavelets [111]. Figure 3.2 shows the translation and the scaling functions applied to a Haar wavelet. The wavelet transform of a signal $f(t)$ as a function of scale and translation is given by [102, 110]:

$$Wf(j,k) = \int_{-\infty}^{\infty} f(t)\psi^*_{j,k}(t)\,dt. \tag{3.25}$$

3.3.2.2 Discrete wavelet transform

So far, only signals present continually in time were dealt with and therefore the Equation (3.25) represents the Continuous Wavelet Transform (CWT). Since we are dealing with discrete-time

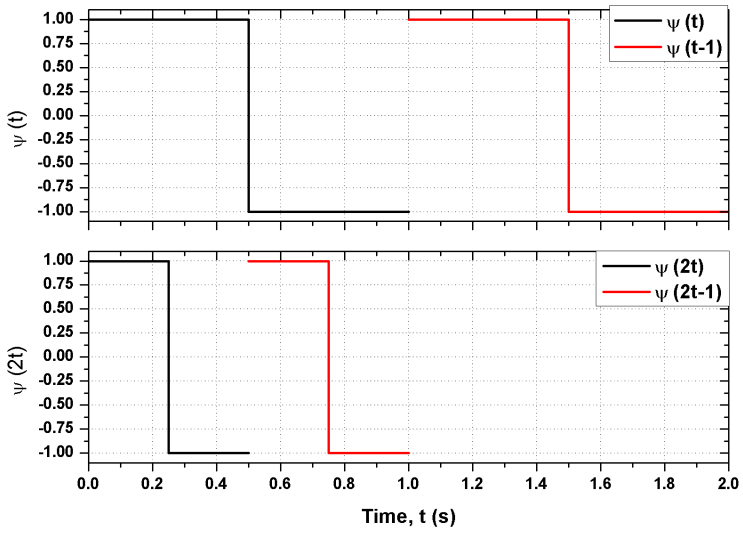

Figure 3.2: *Scaling and translation of the Haar wavelet function.*

signals, only discrete wavelets are useful. Only Discrete Wavelet Transforms (DWT) are discussed in the rest of this section.

The wavelet in Equation (3.25) when discretised becomes [102, 110]:

$$\psi_{j,k}(t) = 2^{j/2}\psi(2^j t - k), \tag{3.26}$$

where $2^{j/2}$ is a normalising constant, and j and k represent the scaling index and the translation index respectively. Any signal $f(t)$ with a finite energy can be represented using the wavelet represented in Equation (3.26) as [102, 110]:

$$f(t) = \sum_{j=-\infty}^{+\infty} \sum_{k=-\infty}^{+\infty} d_{j,k}\, \psi_{j,k}(t), \tag{3.27}$$

where $d_{j,k}$ constitute the discrete wavelet transform (DWT) of the function $f(t)$. To express $f(t)$ using Equation (3.27) a whole range of scaling and translation indices from $-\infty$ to $+\infty$ are required. Due to the availability of a finite amount of data this is not practical and hence a scaling function $\phi(t)$ is defined. Using the scaling function is akin to using a low pass filter [103] to capture all the information at the lowest frequencies. Thus, by collapsing all the low resolution terms, Equation (3.27) can be represented as:

$$f(t) = \sum_{k=-\infty}^{+\infty} c_k\, \phi(t) + \sum_{j=0}^{L} \sum_{k=-\infty}^{+\infty} d_{j,k}\, \psi_{j,k}(t), \tag{3.28}$$

where c_k and $d_{j,k}$ together represent the DWT of the function $f(t)$.

In this section, the basics of discrete wavelet transforms were explained for an easier understanding of the section on NARX modelling which follows. A deeper and a more mathematical explanation of wavelets and wavelet transforms can be found in chapter 10 of [112] and [104].

3.3.3 Neural networks

An artificial neural network (ANN) is a massively parallel distributed processor made up of a network of simple processing units called neurons. ANNs have the ability to store experiential knowledge and to use it in the future [113]. The application of ANNs was motivated by the human brain and resembles these two functionalities of the brain.

3.3.3.1 Mathematical model of a neuron

The smallest processing unit within an ANN is a neuron and its mathematical model is shown in Figure 3.3 [113]. The variables of the neuron are its inputs, represented by x_1 to x_m in the figure, and its output is represented by v_k. The output of the neuron is mathematically described by:

$$v_k = \sum w_{ki}\, x_i + b_k, \tag{3.29}$$

where w_{ki} are the weights associated with each input and b_k is a bias. These weights are used to store knowledge and their values are changed according to an appropriate learning algorithm.

The function $\varphi(.)$ in the figure is called the activation function and is a function of v_k. The output y_k is defined by $y_k = \varphi(v_k)$. The activation function defines the output of the neuron. The threshold function (Heaviside function), piecewise linear functions and sigmoid functions are commonly used activation functions. Other functions like the radial basis function and wavelets may also be used. These are used when local nonlinearities are to be represented, since the commonly used activation functions have an infinite range [114].

3.3.3.2 Neural network architecture

Neural networks are constructed using one or more neurons and thus represent a nonlinear function of one or more neurons. They are classified into two - feedforward networks and recurrent networks (networks with feedback). Feedforward neural networks can further be classified into the following types:

(a) Single layer feedforward networks: Such a network is shown in Figure 3.4(a) [113], where there is only one layer of neurons. There is an input layer which acts as inputs to the network.

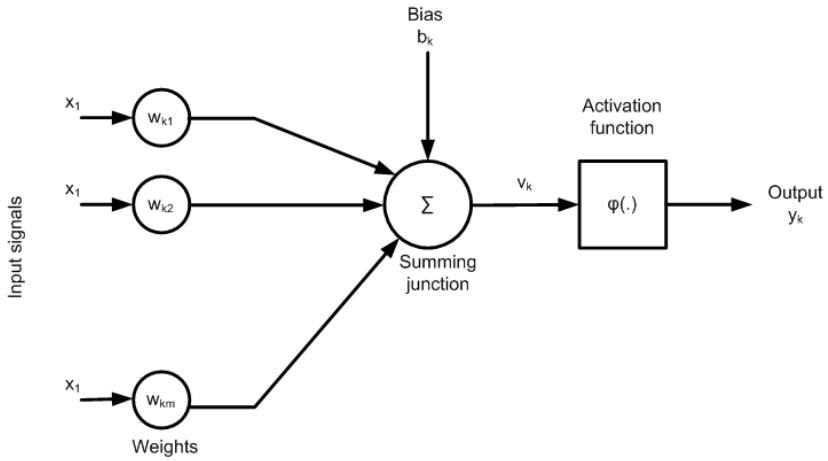

Figure 3.3: *Nonlinear model of a neuron.*

The output from the network is not fed back into the input layer and hence the name feedforward (also called acyclic networks). In the network shown in Figure 3.4(a) there are four input units and four output neuron units.

(b) Multilayer feedforward networks: In these networks there is a presence of one or more layers of hidden neurons. Such a network is shown in Figure 3.4(b). Generally, networks with hidden layers work better when higher-order statistics are involved and when the input layer is large. Figure 3.4(b) shows a network with four inputs in the input layer and four neurons in the hidden layer, which accept these inputs. The outputs of these four hidden neurons are the inputs to the output layer of neurons.

Recurrent networks are those in which the past values of outputs of the network are fed back as inputs to the hidden layer/single layer of neurons. The feedback can be from the hidden neurons and/or the output neurons. The time-delayed output from one neuron can be the input to the same neuron (self-feedback) or to other neurons. Feedforward networks being static in nature cannot be used to model dynamic systems. For dynamic modelling, recurrent networks need to be used.

There are different kinds of recurrent networks [chapter 15 in [113]], but in this work the focus is on input-output mapping networks. A generic form of such multilayer networks is shown in Figure 3.5 [113]. In the network shown, the current and past values of the inputs and the past values of the outputs (which are feedback from the output layer of the network) are inputs to the ANN. These are used to calculate the present value of the output. In the figure, a single-input-single-output network is shown, but the same principle can be extended to multiple-input-multiple-output networks too. The network architecture shown in the figure

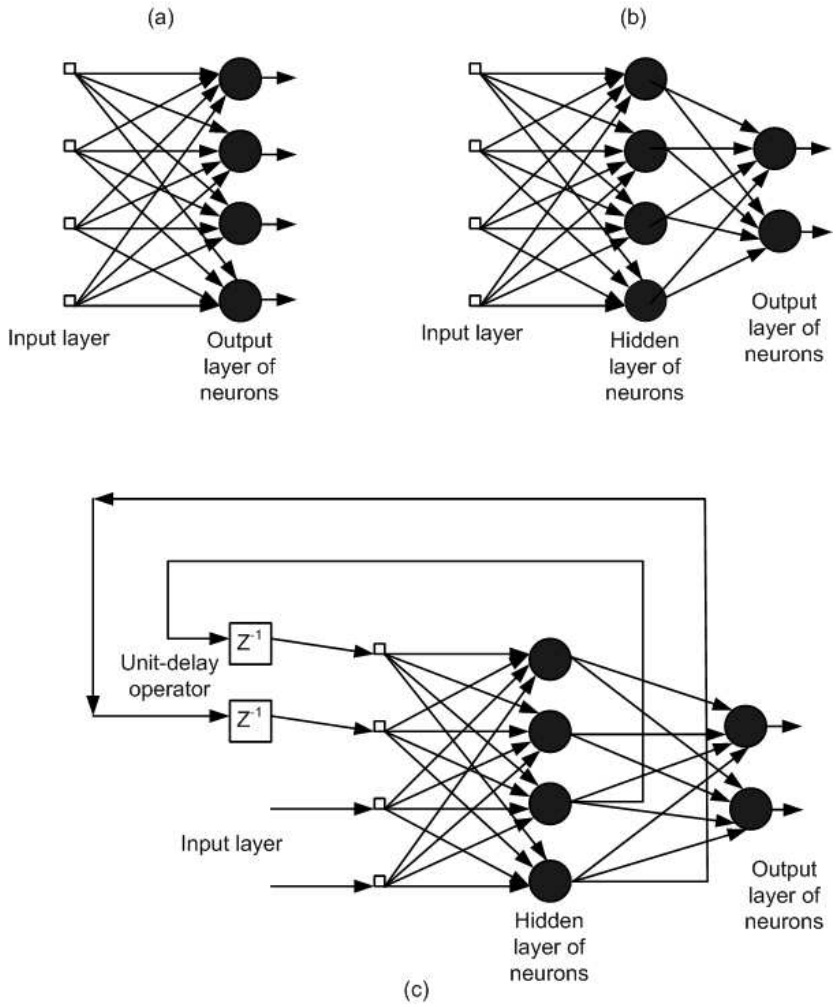

Figure 3.4: *Neural network architectures.*

can be used to model a system mathematically represented by Equation (3.23) (in this case a NARX model, which uses past input and output values alone). The dynamic NARX model is discussed in more detail in Section 3.3.6.

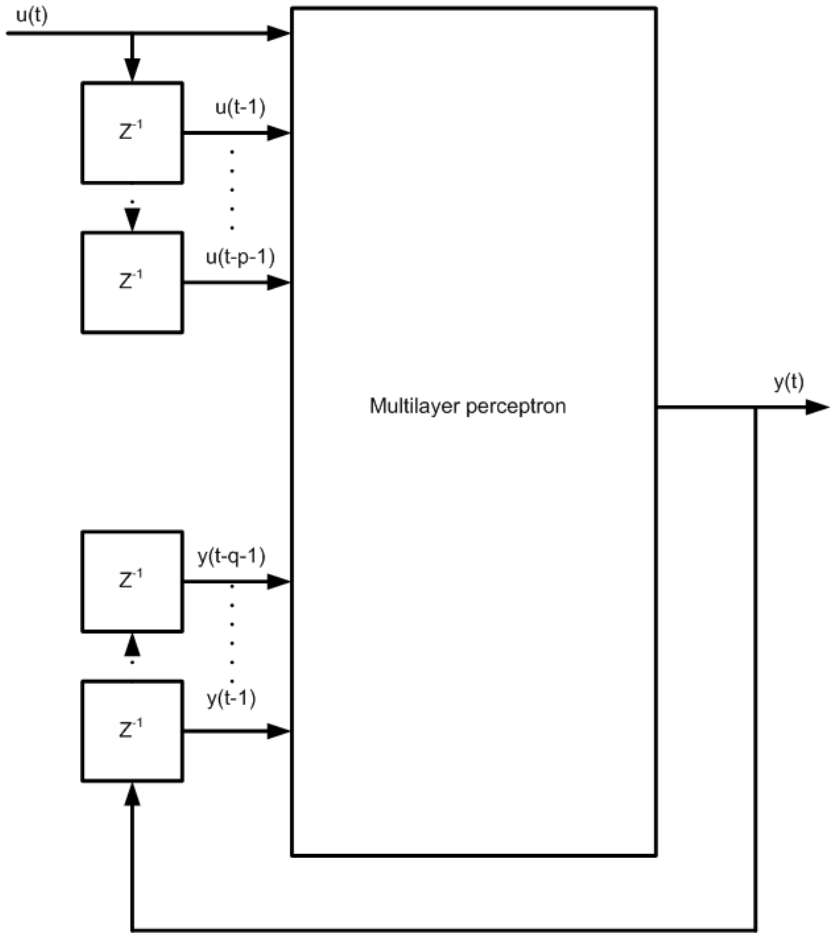

Figure 3.5: *Input-output mapping networks.*

3.3.4 Learning in neural networks

The simplest form of a neural network is one in which there is only one neuron. Such ANNs are called perceptrons. Figure 3.3, if taken as the entire ANN, represents a perceptron whose output may be represented as a function of the inputs x_k and weights w_k. Given an initial set of weights, the perceptron may be trained to calculate a specific target function ts. For training the perceptron a training set needs to be provided, which constitutes the experience of the perceptron. The training set normally would have values of the input x_k and their associated target function values. According to a learning algorithm the initial weights are varied such that the network's output most closely matches the training set. Once a matching set of weights is found, the ANN can be used to model the system from which the training set was derived.

Training neural networks means estimating the parameters of the neurons in a network. In the simpler case of a perceptron discussed earlier the weights w_k and the bias b_k of the network are established through training. Two categories of training are available: supervised and unsupervised training. In supervised training, the function that has to be estimated by the ANN is known at some points. With this information available, the ANN has to predict the function at other points. For input-output mapping networks, discussed in the preceding section, supervised training of the ANN is performed using input-output data obtained earlier. In unsupervised training only some data is available at hand and the ANN is tasked to cluster or find similarities/dissimilarities within the data set. No prior knowledge of the task is available.

In the case of input-output mapping networks (e.g. NARX models), a set of inputs x_k and outputs $y_k(x_k)$ of the system is available. This constitutes the training set. The neural network has to be trained to estimate the relationship between the input and the output. This is made difficult because of the finite size of the training data set available. Once constructed, the neural network will be a black-box model of the system under investigation. The cost function of the training process is given by:

$$J(w_k) = 0.5 \sum_{k=1}^{N} [y_k(x_k) - g(x_k, w_k)]^2, \tag{3.30}$$

where $g(x_k, w_k)$ is the nonlinear mapping between the input and the output modelled by the neural network. The optimal set of weights, thus, would be the one for which the least-squares cost function J is minimised. For finding the optimal set of weights, both the gradient of J with respect to w_k and w_k itself are to be considered, and this is performed by an iterative process. In the simplest case, the set of weights at a particular iteration is given by:

$$w_k(i) = w_k(i-1) - \mu_i \, \Delta J \, (w_k(i-1)), \tag{3.31}$$

where $w_k(i)$ represents the set of weights at the i^{th} iteration, μ_i is the learning rate (>1) and ΔJ is the gradient of the cost function with respect to the set of weights. Practically, the simple gradient descent method represented by Equation (3.31) is not used and more efficient algorithms like the Gauss-Newton and the Levenberg-Marquardt algorithms are used. An extensive description of the training process for NARX models and the algorithms used to solve for the least square error is available in chapters 2 and 4 in [114], chapter 15 in [113] and in [92].

3.3.5 Wavelet neural networks

A wavelet neural network is one in which the activation functions of the ANN are drawn from an orthonormal wavelet family. That is, each neuron has either the scaling function or the wavelet function as its activation function [115, 116].

The simplest form of a wavelet network is one with a single input and a single output, which is shown in Figure 3.6 [115]. The hidden layer in the network is made up of units of wavelet functions and scaling functions. The dilation and translation coefficients of the wavelet and the scaling functions are input parameters to the wavelet units. These are initialised before the training process. These parameters get modified during the training process as per the learning algorithm. These wavelet units produce a non-zero output only when the input is localised within the input domain. The different wavelet units respond to inputs in different localised areas in the input domain.

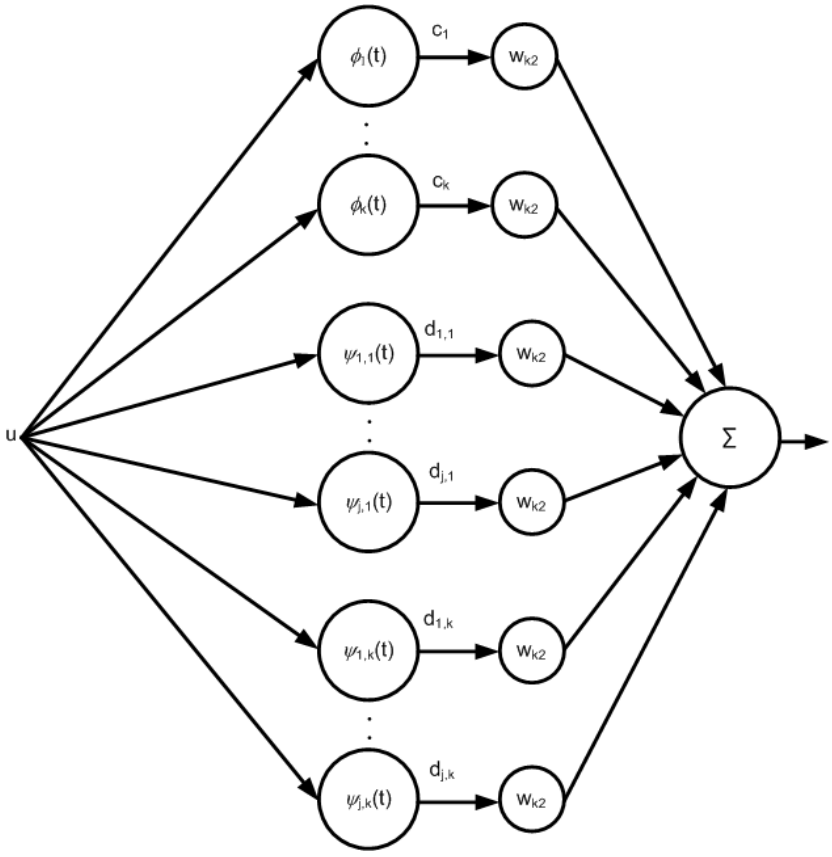

Figure 3.6: *Structure of a wavelet neural network.*

Figure 3.7 shows a wavelet unit with an input and its two parameters. The output is defined as:

$$\psi_{\lambda,t}(u) = \psi(\frac{u-t}{\lambda}), \tag{3.32}$$

where λ and t are respectively the scaling and the translation coefficients.

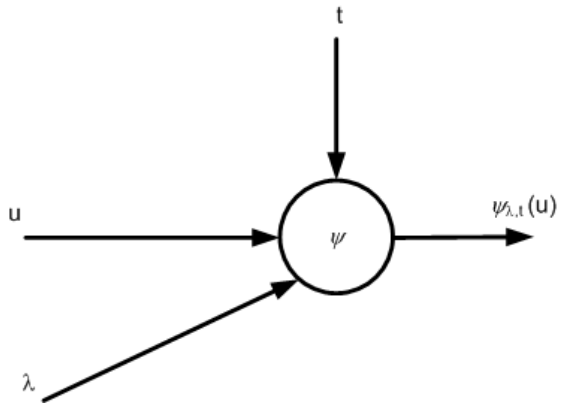

Figure 3.7: *A wavelet unit.*

When the hidden layer consists of N units, the output is the weighted sum of the output of each wavelet unit and is given by [117]:

$$y_\theta(u) = \sum_{i=1}^{N} w_i \, \psi_{\lambda i,ti}(u) + \bar{y}, \tag{3.33}$$

where $\bar{y}$ is introduced to deal with functions having nonzero mean.

There are two types of wavelet neural networks. In the first kind called wavenets, the input signal is first decomposed using wavelet analysis by the neurons in the hidden layer. The wavelet coefficients, which are output, are then weighted and summed. That is, in such networks the dilation and translation coefficients of the wavenet units are fixed at initialisation. Only the weights of the output summer are modified according to the learning algorithm. In the second kind of wavelet neural networks, called wavelet networks, the scaling and translation coefficients and the weights are modified during training. In this thesis, only wavenets have been used and considered from here on.

The training algorithms for wavenets can be obtained by replacing the set of weights w_k used in Equation (3.30) and (3.30) with θ. θ is a vector which has the parameters $\bar{y}$, w_i, λ_i and t_i. λ_i and t_i are parameters which are fixed at initialisation. The cost function thus becomes:

$$J(\theta) = 0.5 \sum_{k=1}^{N} [y_\theta(u) - f(u)]^2, \tag{3.34}$$

and, as explained earlier in Section 3.3.4, the minimum of $J(\theta)$ is found by calculating the partial derivative of J with respect to θ. The algorithms that are used to solve the cost function for sigmoidal or piecewise function neural networks can also be used to obtain the optimal

parameter vector when wavenets are considered. A thorough description of wavelet networks and radial basis functions are available in [117, 118].

3.3.6 Nonlinear AutoRegressive eXogenous (NARX) models

NARX models have the form (from Equation (3.23)):

$$\bar{y}(t|\theta) = g(y(t-1), y(t-2), ..., y(t-na), u(t-1), u(t-2), ..., u(t-nb)), \tag{3.35}$$

where g is an unknown nonlinear mapping function between the input and the output. In the parametric approach, the function g is represented as the function expansion:

$$g(\varphi(t), \theta) = \sum_{k=1}^{m} \alpha_k \, g_k(\varphi(t)), \tag{3.36}$$

with some basis function g_k. $g_k(\varphi(t))$ is normally generated by parameterising a mother function, denoted by $\kappa(\varphi(t))$ in Equation (3.37) [93]. Different forms of function expansions may be used, some of which are: polynomials, Volterra kernels, Fourier series, radial basis functions, wavelets, etc. Wavenets, described in the previous section, have been used for the nonlinearity estimation in this work. Wavenets are defined as one-hidden-layer neural networks whose activation functions are drawn from a family of orthogonal wavelets [116]. Mathematically, wavenets may be represented as:

$$g(\varphi(t), \theta) = \sum \sum \alpha_{j,k} \, \kappa(\beta_j(\varphi(t) - \gamma_k)), \tag{3.37}$$

where κ is the mother wavelet function, β_j is the scaling function, γ_k is the translation function and $\alpha_{j,k}$ is the wavelet coefficient.

As done in Equation (3.28) the nonlinear mapping function can be re-expressed as a sum of the scaled and translated scaling and wavelet functions as [91, 108]:

$$f(u) = g(\varphi(t), \theta) = \sum_{k=1}^{N} w_k \, \phi(u) + \sum_{j=1}^{M} w_j \, \psi(u) + \bar{y}, \tag{3.38}$$

where u represents the input to the neural network and $M+N$ represents the number of wavenet units in the hidden layer.

The training of the wavenet happens based on the cost function shown in Equation (3.34). The System Identification toolbox in MATLAB/Simulink, which has been used to develop the NARX model of a WEC, uses the Levenberg-Marquardt algorithm for the finding the optimal set of weights w_k and w_j in Equation (3.38) [119, 120]. In the toolbox, the scaling function and

the wavelet function used are $y(x) = e^{-0.5x'x}$ and $f(x) = (dim(x) - x'x)e^{-0.5x'x}$ respectively. They are shown in Figure 3.8.

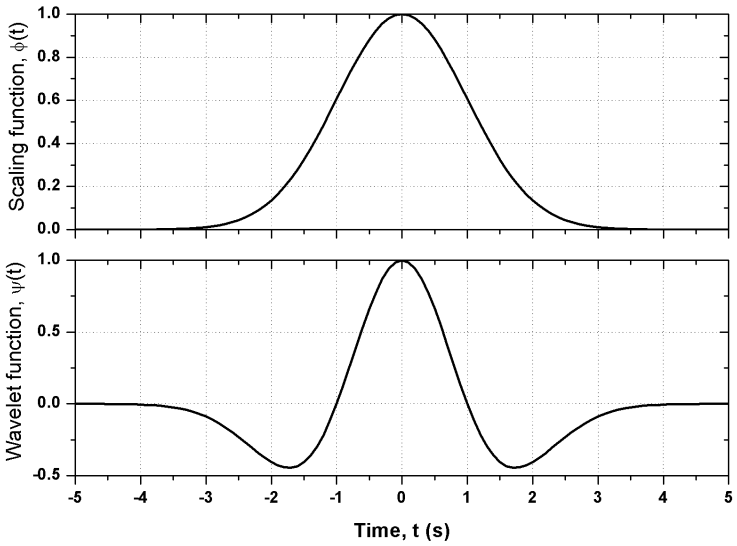

Figure 3.8: *The wavelet and scaling functions used.*

Figure 3.9 shows the schematic of the NARX model supported by the system identification toolbox of MATLAB/Simulink. The schematic is very similar to the NARX model shown in Figure 3.5. The only difference is the additional linear function in the model. The presence of the linear function modifies the output function shown in Equation (3.38) as follows:

$$f(u) = g(\varphi(t), \theta) + au + b, \tag{3.39}$$

where $au + b$ is the additional linear term. Both these constants a and b are also estimated during the training of the NARX model.

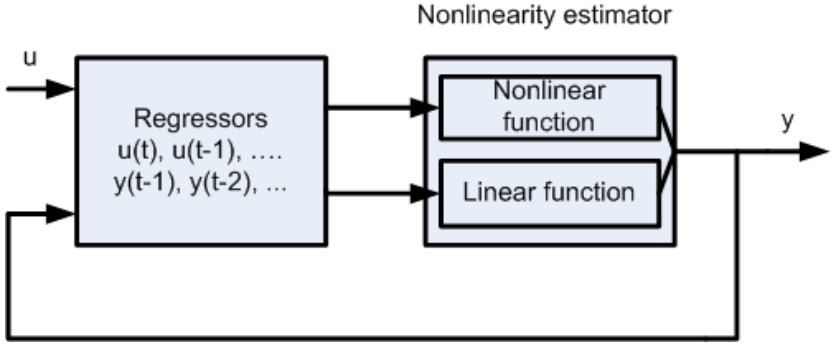

Figure 3.9: *Schematic of the NARX model.*

3.4 Developing the NARX model for a WEC

With all the mathematical and theoretical background covered in the preceding sections, this section deals with discussing the steps involved in the development of the NARX equivalent model of a WEC. A modular approach like that used for the development of the detailed model has been used in this case too. NARX models of the wave energy converter (in the sea), the PTO system and the DFIG have been developed separately. This approach has been followed because these entities can be independently controlled. The schematic of the developed NARX model of the whole system is shown in Figure 3.10. Referring to Figure 2.23 gives a clear picture of the modular nature of the developed NARX model.

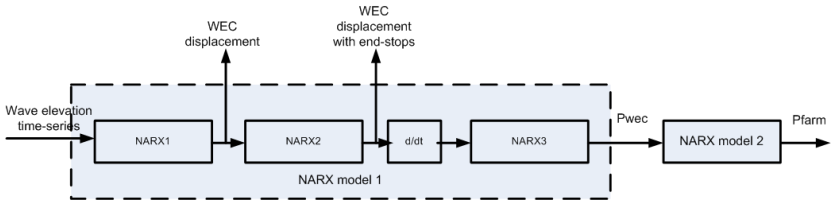

Figure 3.10: *Schematic of the developed NARX model of the WEC.*

The NARX model has two distinct parts. NARX model 1, which essentially models the WEC module in Figure 3.10, takes the wave elevation time-series as its input and returns the raw mechanical power extracted by the WEC (Pwec). A three step process is used to generate the Pwec time-series. In the first step, the NARX1 module takes the wave elevation as input and returns the WEC displacement without considering the presence of end-stops. In the second step, this WEC displacement is fed to the NARX2 module, which returns the WEC displacement including the effects of end-stops. Differentiating this displacement gives the velocity of the WEC. The derivation of Pwec from the velocity constitutes the third step in the WEC module. For this, the NARX3 module takes the velocity as its input and returns Pwec. The second distinct part of the complete model is NARX model 2, which takes the predicted Pwec time-series and returns the real power generated by the WEC (Pfarm).

Generating the Pwec time-series from the wave elevation time-series using the detailed model is a very fast process, since the WEC has been modelled as a mass-spring-damper system. Therefore, only the development of NARX model 2 is described in detail here. The development of NARX model 1 is dealt with briefly in Section 3.4.4.

Model development using system identification consists of the following stages [94, 121]:

- Acquisition of input-output data
- Selection of model structure
- Estimation of model parameters
- Model validation

3.4.1 Acquisition of input-output data

The detailed model of the WEC has been used to generate the time-series of Pfarm and Pwec, which have been used to train the NARX model 2. The Pwec time-series generated is the input while the Pfarm time-series is the output. Data obtained from simulating the detailed model of the WEC for 600 seconds were used as the estimation data for high energy sea states. The data were obtained by simulating the WEC in a stationary but irregular sea state with $H_s = 6$ m and $T_z = 10$ s. From the 600-second run with a time-step of 0.1 seconds, half the data were used for the estimation and the other half were used to validate the developed NARX model. The model developed was for WECs with an accumulator size of 0.5 m^3. The same simulation run with other accumulator sizes can be used to generate data, which could then be used to develop NARX models for WECs with different accumulator sizes.

3.4.2 Selection of the model structure

The wavenet network, which was described in detail earlier, has been chosen as the nonlinear function estimator. A modified form of the algorithm used in [100] has been used to select the optimal regression vector for the identification process. As the first step of the algorithm, an initial NARX model is developed, which only uses the current input in the regression vector. The fit between the simulated output and the validation data is then calculated. The 'fit' is a measure of how close the simulated NARX model output is to the detailed model output. It is defined by:

$$Fit = (1 - \frac{\sqrt{\sum (y - \hat{y})^2}}{\sqrt{\sum (y - \bar{y})^2}}) * 100 \tag{3.40}$$

where y is the output from the detailed model, $\hat{y}$ is the simulated model (NARX model) output, and $\bar{y}$ is the mean of y. A fit of 100% means a perfect fit and a fit of 0% is when there is no fit between the two data sets.

Next, another regressor, e.g. $u(t-1)$, is added to the regression vector and the fit is calculated again. If the fit is better with the new regression vector it is chosen over the previous regression

vector. If the fit obtained with the new regression vector has not improved, the newly added regressor is rejected and the previous regression vector is used. In the same fashion, a set of regressors is tested. The selection procedure is complete when the required fit is reached. Using this algorithm, a combination of regressors was selected. To model the Pwec-Pfarm relationship, the regression vector was constructed using the following regressors: $y(t-1)$, $y(t-2)$,..., $y(t-10)$, $u(t)$, $u(t-1)$,..., $u(t-9)$. A best fit of 98.45% was obtained between the simulated and the validation data.

3.4.3 Estimating the model parameters

After the model structure is decided, the next task is to parameterise the nonlinear function expansion shown in Equation (3.38). As mentioned earlier, the scaling and the translation coefficients of the wavelet and the scaling functions and the number of wavenet units are decided iteratively before the training procedure. Once this is performed, the Levenberg-Marquardt algorithm is used to parameterise the nonlinear function expansion. For NARX model 2, a wavenet with four units was chosen.

The NARX model developed using the input-output data was seen to be sufficient for moderately and highly energetic seas with $H_s^2 T_z \geq 64$. The model overestimated Pfarm when used to simulate the WEC in low energy sea states. To improve the accuracy of the NARX model, two other NARX sub-models were developed. The first sub-model was generated for sea states with $H_s^2 T_z <= 10$. The estimation/validation data for this sub-model were obtained by simulating the detailed model of the WEC with a stationary but irregular sea with $H_s = 1$ m and $T_z = 4$ s. The optimal regression vector was found and had the following regressors: $y(t-1)$, $y(t-2)$, $u(t)$ and $u(t-1)$. A wavenet with 52 units was seen to make the most accurate estimation. A best fit of 99.46% was obtained between the validation data and the simulated output of the NARX model. The second NARX sub-model was generated for sea states with $H_s^2 T_z$ between 10 and 64. The data obtained by simulating the detailed model for 600 seconds with a sea state with $H_s = 2$ m and $T_z = 6$ s were used for the estimation. The same set of regressors as the first sub-model and a wavenet with 9 units gave a best fit of 97.22%.

3.4.4 NARX model of the WEC module

In this section, the construction of the intermediary models in NARX model 1, shown in Figure 3.10, is described.

For NARX1, the current input, 39 past input values and 25 past output values were selected as the regressors to map the relationship between the wave elevation time-series and the displacement of the WEC. A wavenet with just one unit was seen to estimate the relationship most accurately. A best fit of 99.93% between the validation data and the simulated output was obtained.

The NARX2 model, which models the effects of having end-stops on the displacement of the WEC, takes in the unrestrained WEC displacement (output of NARX1) and returns the displacement of the WEC with end-stops. The current input and one past value of the input formed the optimal regression vector. A treepartition network with 1023 units was seen to estimate the relationship most accurately. A best fit of 98.65% was obtained.

The WEC's velocity (derivative of the output of NARX2) is the input to NARX3. The Pwec time-series is returned by NARX3. For developing this model, the optimal regression vector was constructed with the current value of the input and the squared of the current input. A wavenet with 9 units was chosen to best represent the mathematical relationship and a best fit of 100% was obtained using this model structure.

For constructing the three intermediary models in the NARX model 1, the data used for training were obtained by running a simulation of the detailed model for 600 seconds, in a sea state with $H_s = 6$ m and $T_z = 10$ s. This simulation run was performed with a constant PTO damping coefficient, selected by using the method described in Section 2.4. In reality, when adaptive controllers are used to continually find the optimal PTO coefficients, the NARX model 1 has to account for changes in the damping coefficient. To include the effects of changing PTO coefficients, a NARX model may be developed that takes in both the PTO coefficients and the wave elevation time-series as inputs and returns Pwec as the output. When this model is used in simulations, the adaptive controller would feed the PTO coefficients to the NARX model.

3.4.5 Model validation

In this section, the NARX model was validated for the same sea states used to obtain the data used for training. The 'fit' was used to quantify the closeness of the data obtained from the NARX model and the detailed models. A further process of thorough validation has been performed, both for single WECs and for wave power farms, and the results obtained from these validation runs are discussed in the next section.

3.5 Further model validation

The thorough validation process adopted in this section tests the appropriateness of the NARX model developed, when the WECs are placed in seas other than those used to train the wavenet. Two quantities - the residual and the percentage error - have been used to compare the operation of the NARX model with the detailed model. The residual is defined by:

$$R(t) = |y(t) - \hat{y}(t)|, \tag{3.41}$$

and the percentage error is defined by:

$$P(t) = (R(t)/y(t)) * 100, \tag{3.42}$$

where the quantities in these equations are as described earlier.

In this section, the results of the estimation of Pfarm from the wave elevation time-series when accumulators and end-stops are used are discussed. The results obtained for the accumulator size of $0.5\mathrm{m}^3$ are shown for the different sea states modelled. The validation performed for single WECs and for wave power farms are treated separately.

3.5.1 Validation of the NARX model of a single WEC

3.5.1.1 Stationary sea case

The applicability of the NARX model to simulate a single WEC in different stationary but irreregular seas has been tested and the results are discussed in this section. A range of significant wave height H_s and average zero-crossing wave period T_z values found off the west and north coasts of Scotland have been used. The different combination of H_s and T_z that have been used, and sorted based on the energy content of the sea state (measured by $H_s^2 T_z$), are listed in Table 3.2. The time-series of Pfarm obtained from 600-second simulation runs of the detailed model of the WEC have been compared with the results provided by the NARX model.

Figure 3.11 shows the maximum absolute and the average values of the residual in the estimated Pfarm time-series and the instantaneous percentage errors at the instants when the maximum residuals were obtained. Except for the sea states 11, 20 and 21 low values of the percentage errors are seen. For sea states 11, 20 and 21 though, the value of the residual is less than 5 kW, which means that the percentage error at these instants were high because of low power generation from the WEC. The average residual lies below 2 kW for all the sea states tested.

S. No.	$H_s(\mathrm{m})$	$T_z(\mathrm{s})$	$H_s^2 T_z(\mathrm{m^2 s})$
1	0.5	4	1
2	0.5	6	1.5
3	0.5	8	2
4	0.5	10	2.5
5	0.5	12	3
6	1	4	4
7	1	6	6
8	1	8	8
9	1	10	10
10	1	12	12
11	2	4	16
12	2	6	24
13	2	8	32
14	2	10	40
15	2	12	48
16	4	4	64
17	4	6	96
18	4	8	128
19	6	4	144
20	4	10	160
21	4	12	192
22	6	6	216
23	6	8	288
24	6	10	360
25	6	12	432

Table 3.2: *H_s and T_z combinations used for this study*

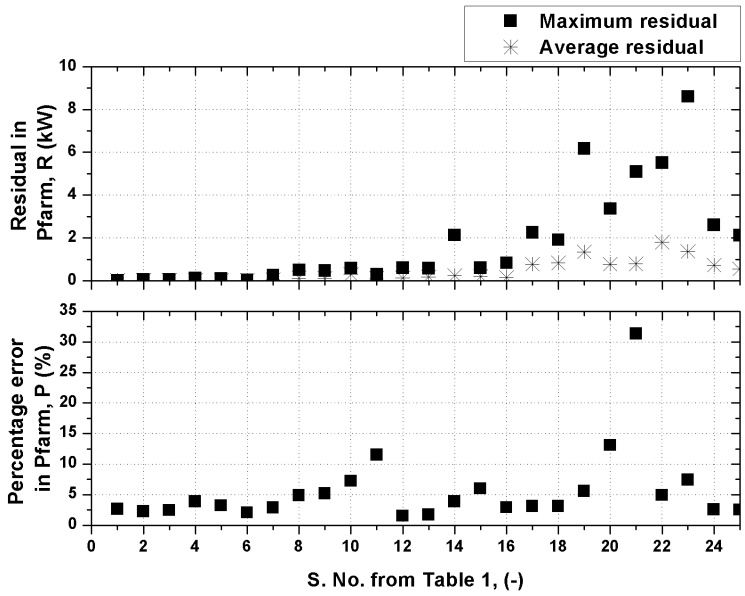

Figure 3.11: *Maximum absolute and average residuals in Pfarm when the model is validated with the 25 different stationary sea states.*

3.5.1.2 Non-stationary sea case

H_s and T_z do not vary much during 10, 20 or 30 minute intervals. Also, most wave buoys collect the H_s, T_z data averaged over such periods. Following this approach of keeping H_s and T_z constant for a certain duration (10 minutes in this work), a concatenated sea state has been constructed. The NARX model has been tested with a 1800-seconds sea state formed by the concatenation of a weakly, a moderately, and a highly energetic sea. The sea is highly energetic for the first 600-seconds period ($H_s = 6.03$ m, $T_z = 8.52$ s). During the period between 600 seconds and 1200 seconds the sea is weakly energetic ($H_s = 1.27$ m, $T_z = 4.82$ s) and during the last 600-second period the sea is moderately energetic ($H_s = 4.4$ m, $T_z = 6.78$ s).

Figures 3.12 and 3.13 show the Pfarm time-series generated by both the detailed model and the NARX model, along with the residual and the instantaneous percentage errors over a 200-second period and a 40-second period respectively. The values of the residual are less than 2.5 kW during the entire 1800-seconds run.

3.5.1.3 Non-stationary realistic sea case

The NARX model of the WEC has been validated with a 24-hour simulation run under a realistic, non-stationary sea state. Again, the Pfarm time-series generated by the NARX model was

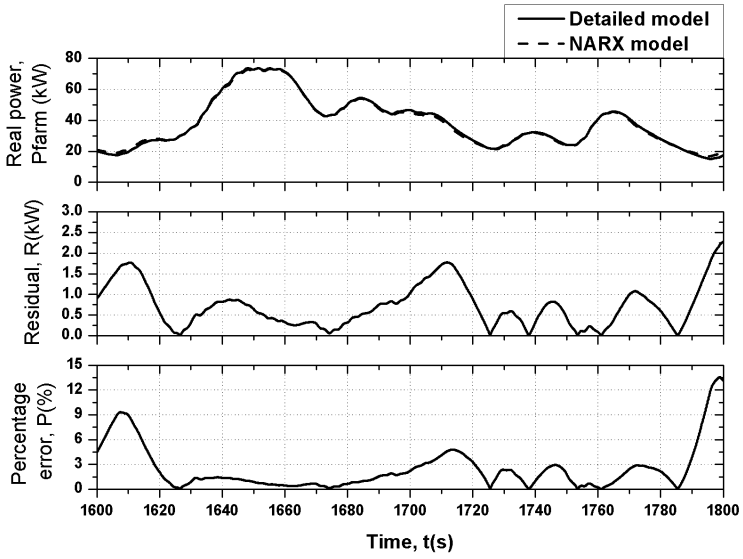

Figure 3.12: *NARX model and detailed model generated Pfarm time-series, residual and percentage error over 200 seconds, with the WEC excited by the 1800-seconds non-stationary sea state.*

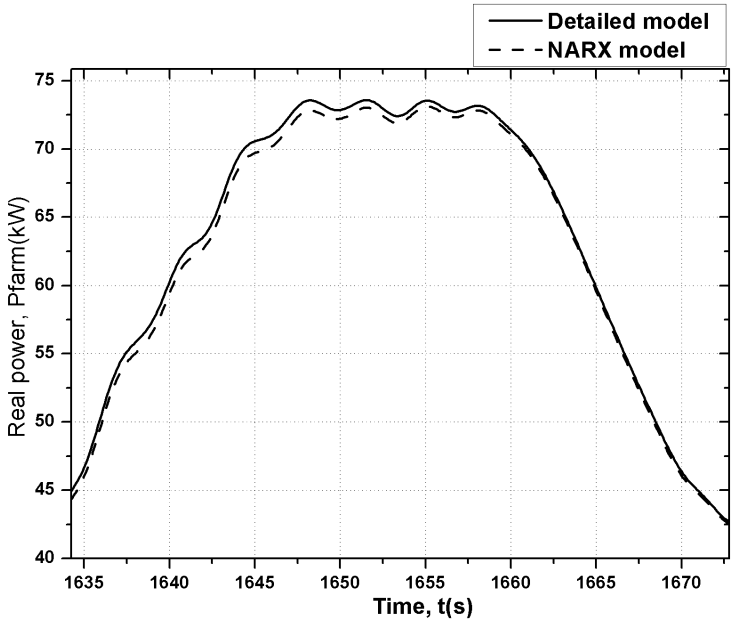

Figure 3.13: *Snapshot of the Pfarm time-series with the WEC excited by the 1800-seconds non-stationary sea state.*

compared with that generated by the detailed model.

Figures 3.14 and 3.15 show the Pfarm time-series generated by both the detailed model and the NARX model, along with the residual and the instantaneous percentage errors over a selected 300-second period and a 60-second period respectively. Acceptable levels of percentage error and the residual are seen during the entire run. A hard limit of 125 kW has been placed on the real power output of the NARX model, which is seen in Figure 3.15. Figure 3.16 shows the percentage distribution of the instantaneous percentage error in the estimated Pfarm values over the 24-hour period. It is seen that for most parts of the simulation run the percentage error lies below 4%. Such errors are acceptable for power flow studies, since these will not produce significant changes to the voltage profile envelope of the network.

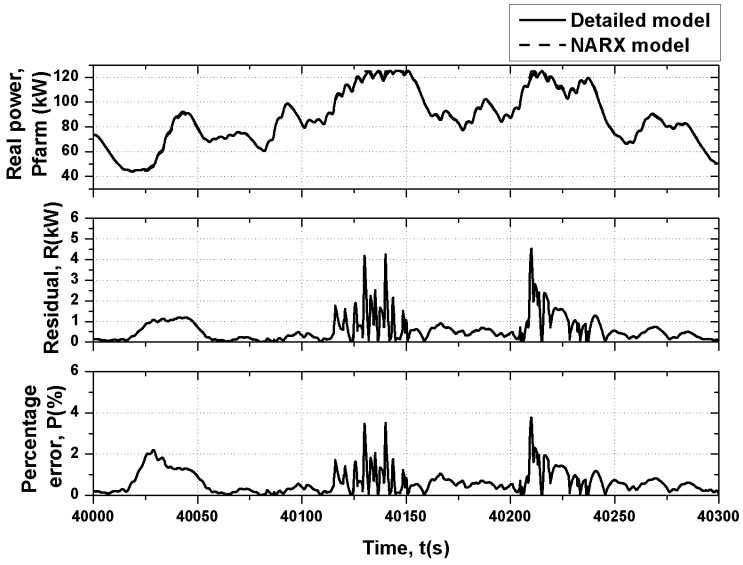

Figure 3.14: *NARX model and detailed model generated Pfarm time-series, residual and percentage error over 300 seconds, with the WEC excited by the 24-hour non-stationary sea state.*

3.5.2 Validation of the NARX model of wave power farms

Like in the case of the detailed model, since a modular approach has been used in modelling the WECs, wave power farms can be modelled by replicating the developed model of an individual WEC and by exciting it with different wave elevation time-series. The NARX model of a wave power farm with 8 WECs has been validated and the results are discussed in this section. The operation of the NARX model has been tested in both stationary and non-stationary sea states. The validation has been performed by comparing the time-series of the net real power

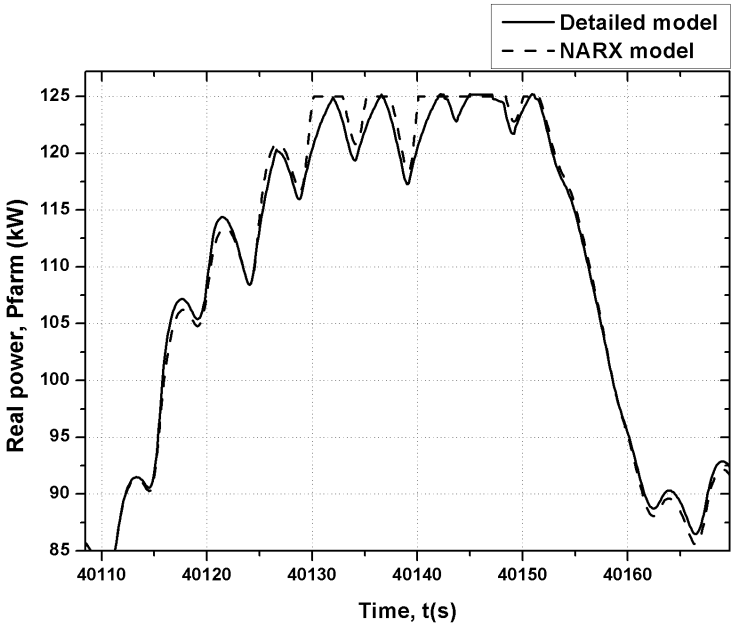

Figure 3.15: *Snapshot of the Pfarm time-series with the WEC excited by the 24-hour non-stationary sea state.*

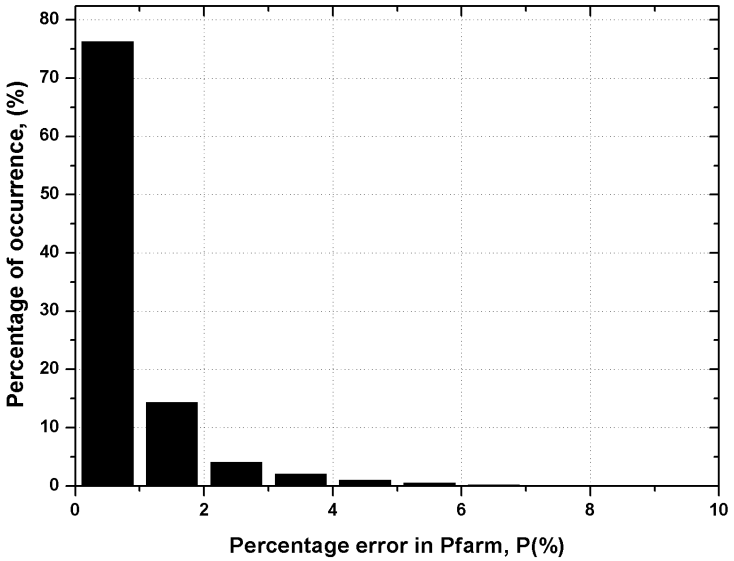

Figure 3.16: *Histogram of the percentage error in the estimated Pfarm time-series obtained from the 24-hour simulation.*

generated by the farm provided by the detailed model and the NARX model. A simple farm topology has been chosen where the WECs are placed in a line with a 100 m spacing between two neighbouring WECs.

Recent work suggests that interference between devices in a WEC farm can affect (positively or negatively) the individual and aggregated power output, especially when the distance between the WECs is less than 10 diameters [85, 86]. In this work, the wave power farm has been assumed to be sparse and hence the interference has not been taken into account.

As a part of the SuperGen Marine Energy consortium's WS7, a detailed hydrodynamic model of wave power farms has been developed by Dr. David Forehand [15]. A state-space model of the farm has been constructed, which takes into account all the radiation and diffractions from the WECs in the farm. The NARX model 2 developed in this study fits in well with the model Dr. Forehand has developed and both these models together form a more realistic wave-to-wire model of a wave power farm.

3.5.2.1 Stationary sea case

Figure 3.17 shows the average percentage error and the average value of the residual over the 600-second period for the 25 different stationary sea states used in Section 3.5.1.1. The results for wave power farms of four different sizes - with 2, 4, 6 and 8 WECs - are shown in the figure. For all the sea states tested, the average value of the residual and percentage error are less than 5 kW and 3% respectively. The average percentage error is seen to decrease with an increase in the size of the farm, which means that the NARX model of the WEC can be used to correctly model even larger farms.

3.5.2.2 Non-stationary sea case

The NARX model of a wave power farm with 8 WECs has been tested under highly energetic and weakly energetic non-stationary, realistic sea states. Figures 3.18 and 3.20 show the NARX model and the detailed model generated Pfarm time-series with the residual and the instantaneous percentage error when excited by both the sea states. Figures 3.19 and 3.21 show the same time-series over a shorter time period. It is seen from these figures that the NARX model gives a very good estimate of the net Pfarm generated by the wave power farm with 8 WECs.

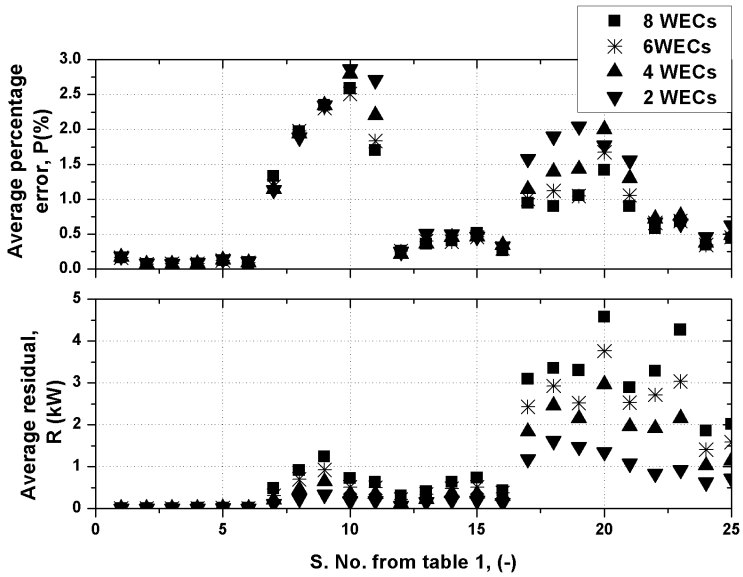

Figure 3.17: *Average percentage error and average value of the residual in the net Pfarm generated by a wave power farm with 2, 4, 6, and 8 WECs for the 25 stationary sea states (of Table 3.2).*

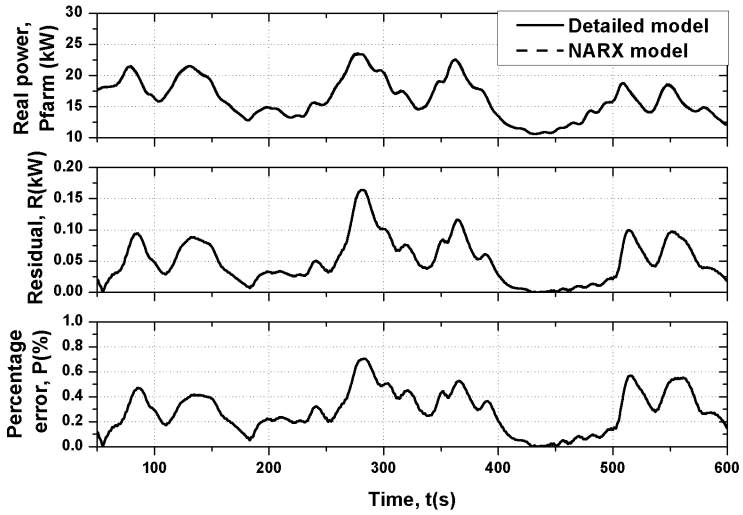

Figure 3.18: *NARX model and detailed model generated Pfarm time-series, residual and percentage error over 600 seconds, with the wave power farm with 8 WECs excited by the low energy non-stationary sea state.*

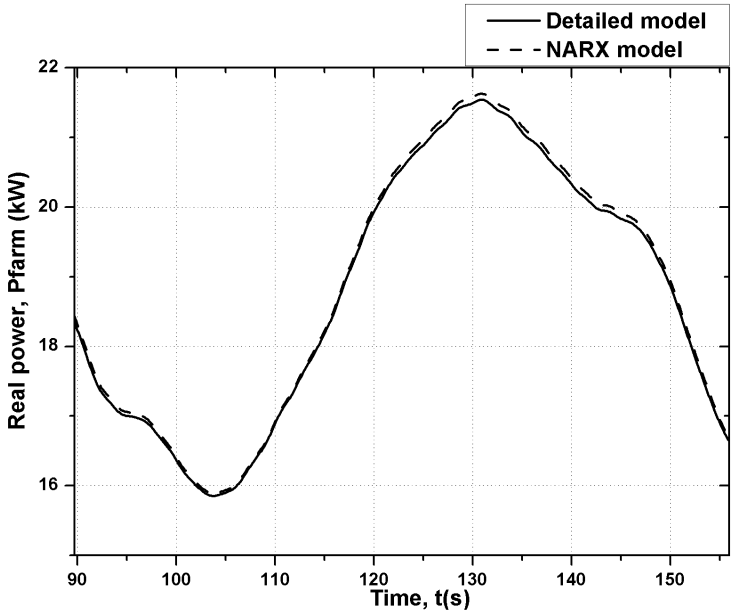

Figure 3.19: *Snapshot of the Pfarm time-series with the wave power farm with 8 WECs excited by the low energy non-stationary sea state*

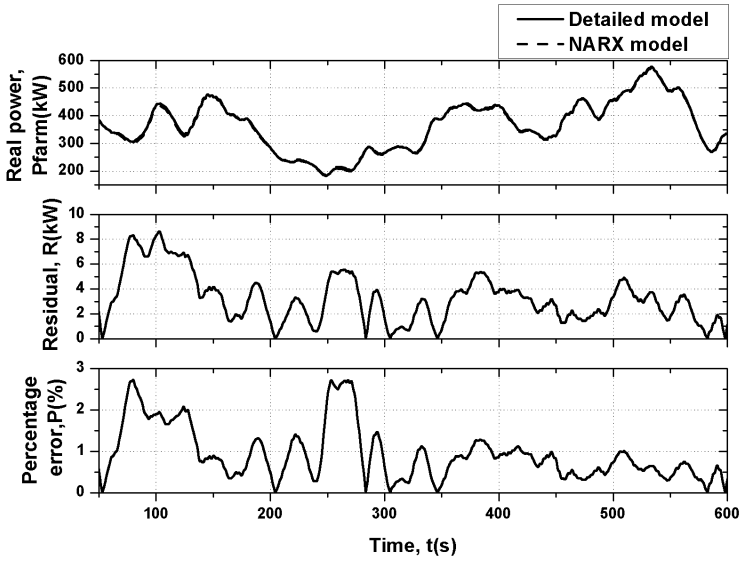

Figure 3.20: *NARX model and detailed model generated Pfarm time-series, residual and percentage error over 600 seconds, with the wave power farm with 8 WECs excited by the high energy non-stationary sea state.*

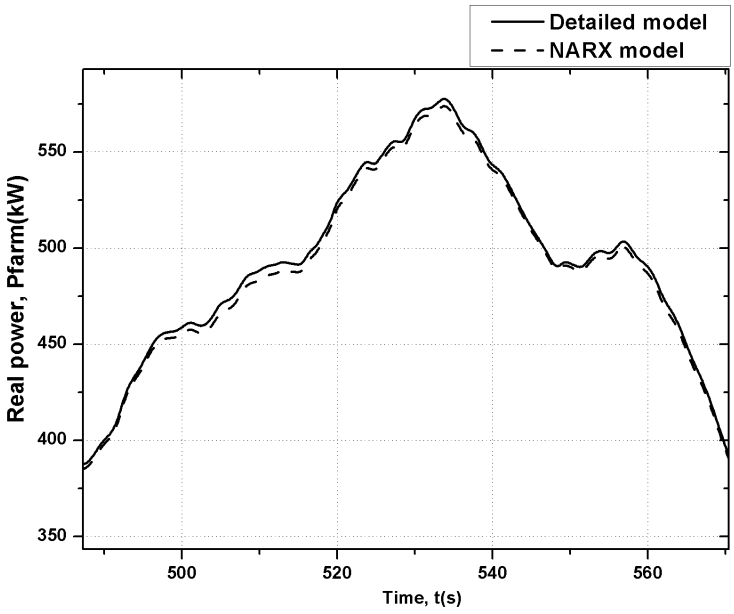

Figure 3.21: *Snapshot of the Pfarm time-series with the wave power farm with 8 WECs excited by the high energy non-stationary sea state.*

3.6 Summary

This chapter described an alternative modelling framework in which input-output data collected from a system are used to construct its black-box model. This framework, called system identification, was applied to model individual WECs and wave power farms. The detailed model of the WEC was used to generate the estimation data which were then used to train wavenet networks. After training, the wavenet network accurately maps the input-output relationship of the system being modelled.

The most significant advantage of using the NARX model of the WEC over the detailed model is the savings made in the simulation time and the computing resource. For example, when the detailed model of a wave power farm with 8 WECs takes an average of 194 seconds for a 100-second run, the NARX model takes on average 4.50 seconds. The savings in time and computing resource does not vary linearly with the change in the wave power farm size and simulation time period and, thus, will be more important when simulating larger farms over extended durations. The simulation runs of wave power farms having 48 WECs discussed later in this thesis would not have been possible without the equivalent NARX model.

Another advantage of using the NARX equivalent model comes from the fact that the improvement in the simulation run times does not come with a reduction in the time-resolution of the model. In all the simulations performed for this chapter, a time-step of 100 ms was used. Thus, the NARX model ensures the availability of a time-series of Pfarm, sampled every 0.1 seconds or less. Such time-steps are required to study the effects of connecting wave power farms to the electricity network on the supply voltage quality.

The NARX model was thoroughly validated with the simulated results obtained from the detailed model for different sea states. The results show the applicability of the NARX model for realistically modelling WECs and wave power farms. The performance of the NARX model was seen to improve with an increase in the farm size, which proved that the modelling approach can be used to model larger farms too. It is envisaged that the system identification modelling approach can also be used to model tidal and wind energy systems.

Chapter 4
Topologies of arrays of wave energy converters - effects on power smoothing

4.1 Introduction

The introduction to the thesis defined some of the problems that will need to be addressed before significant amounts of distributed generation (DG) can be connected to weak, rural electricity networks. It also mentioned that voltage fluctuations introduced in the electricity network by the connection of DG in general and wave power farms in particular is the focus of this thesis. When wave power farms are connected to the network, strict voltage quality requirements set by the distribution network operators [122] need to be met. This is challenging due to the time varying and the unpredictable nature of the power generation from these farms. In these weak networks, even small changes in the power generated by the wave power farm is likely to produce significant voltage fluctuations.

Power generation from ocean waves is different from the generation from tides and wind. In the case of tidal power, the change between high and low tides and between the arrival and the recession of tides is predictable. This makes designing the control system, to maintain voltage and power quality, relatively straightforward. Wind energy converters, on the other hand, deal with spatially random wind speeds which make output prediction difficult. Apart from the advantages of spacing the wind converters far enough to avoid the wake effect, no significant improvement in the voltage quality can be obtained by spacing the individual wind energy converters in wind power farms differently.

Ocean wave fields can be represented as a superposition of a large number of sinusoidal wave components across both time and space. The wave energy converters (WECs) are said to be in coherence, if in a wave power farm the WECs are spaced such that at the same instant of time each WEC produces maximum power. When the WECs are coherent, the net power generated

by the farm would tend to be more variable. The spatially sinusoidal nature of ocean wave fields leads to this feature, which can be exploited for voltage quality improvement and is investigated further in this chapter. The theory behind this approach is first discussed through simulation runs in which two WECs are placed in a purely sinusoidal sea. Whether this theory will hold good for mixed and stationary seas and for mixed and non-stationary seas is then examined with a simple line of WECs. The smoothness in the cumulative raw mechanical power extracted by the farm is inspected first. Whether the directional orientation of the line of WECs with respect to the dominant wave direction has any influence on the smoothness in the power produced is also examined.

Next in the chapter, the influence of spacing between the WECs in the linear array and the orientation of the linear array on the quality of the net real power generated by the farm is analysed. This is performed because the quantity of interest for network operators is the quality of voltage in the network, which is directly dependent on the quality of the real power fed to the network (assuming that no reactive power is exchanged with the network). The same test cases, as performed for the cumulative raw mechanical power, are repeated for studying the relation between different spacing and orientation, and the smoothness in the net real power generated by the farm. The advantages of using accumulators in smoothing the real power generated by the individual WECs and by the farm as a whole are also discussed.

From the simple line of eight WECs, the analysis then moves to a more realistic array of 48 WECs, which constitute a 6 MW wave power farm. The effects of increasing the size of the wave power farm on the smoothness in the generated power are first examined. Then the spacing effects seen in the simple array are tested with the 6 MW farm to see if the effects can be reproduced in the case of the larger array. The effects of changing the dominant wave direction on the smoothing obtained are also studied. A statistical study of the wave climate off the north western coast of Scotland using data collected over two years has been performed and is presented later in this chapter, which puts the results obtained into context. The work with the 6 MW farm is set in context of real array deployment in multi-directional seas.

Recent work suggests that interference between devices in a wave power farm can affect (positively or negatively) the individual and aggregated power output from the WECs. Most of the work performed on arrays of WECs has focussed on this aspect. There are publications that looked at how the interaction factor (q-factor) of an array of WECs and its net power production can be influenced by appropriately spacing the WECs [123–125]. Other publications

investigated the effects of different WEC control mechanisms on the net power produced by the array of WECs [126–128]. These publications though, have not considered the influence of these choices on the smoothness in the net real power generated by the array which directly influences voltage quality in the network. Also, in these publications the WECs were taken to be closely spaced such that they influence each other significantly.

Arrays of WECs are normally sparse due to deployment and operational reasons. For this work, the spacing between WECs of diameter 3.1 m has been taken to be greater than ten times the diameter. When the spacing between the WECs is large, the hydrodynamic interference between the WECs can be neglected [85, 86]. Other publications have also studied the effects of placing WECs on the wave climate downstream of the WECs [129, 130]. In these publications it was shown that beyond a certain distance the effects of the hydrodynamic interference are negligible. Therefore, the work performed for this chapter has neglected the hydrodynamic interference between the WECs within the array.

All the simulation runs completed for this chapter were performed using the NARX equivalent model of wave power farms developed in Chapter 3. It would not have been possible to run the simulations of the 6 MW farm (with 48 WECs), discussed in this chapter, if the detailed and computationally intense model of the WECs (described in Chapter 2) had been used. The nature and the number of simulation runs discussed in this chapter shows an application of system identified models.

4.2 Definition of terms

Pwec (raw mechanical power) is the power extracted from the sea by an individual WEC.

Cumulative Pwec (cumulative raw mechanical power) is the sum of Pwec across the wave power farm. This is not a quantity that we have access to and is not important from the net real power generation point of view. This quantity is used to assess and quantify the smoothing introduced by the spatially sinusoidal nature of the wave fields.

Pfarm (real power) is the real electrical power generated by an individual WEC.

Net Pfarm (net real power) is the sum of Pfarm across the wave power farm. It is the net real power output from the wave power farm.

Variance is defined by $Var = (\sum_{i=1}^{N}(P_{iavg} - P_i)^2)/N$, where P_i is the power output at instant

i, N is the total number of points in the power time-series and P_{iavg} is the average of P_i over N. In this chapter, the variance in both cumulative Pwec and net Pfarm have been calculated. For the former, P_{iavg} has been taken as the moving average, while for the latter the normal average over the N data points has been taken as P_{iavg}. This has been done to take into account both the high and the low frequency variations seen in the cumulative Pwec. In the case of the net Pfarm, the variance has been calculated with respect to the average net Pfarm, since most of the high frequency variations in the cumulative Pwec are filtered out by the power take-off system and the generator.

Coefficient of Variance is defined as the variance in the net Pfarm divided by the average net Pfarm over the observed time period. This coefficient is useful in comparing the variance in the net Pfarm when arrays of different sizes are placed in the same sea.

(See Figure 2.23 to understand the variables Pfarm and Pwec with respect to the schematic)

4.3 The theory

In this chapter, the effects of different WEC spacings, which vary from $0.25\lambda_{peak}$ to $0.5\lambda_{peak}$, on power smoothing are investigated. λ_{peak} here is the peak wavelength of the sea corresponding to the peak frequency of the ocean wave spectrum. The reason for choosing this range of WEC spacings can be appreciated using Figure 4.1. The figure shows two WECs placed in a purely sinusoidal sea at two different spacings - 0.25λ and 0.5λ. The power extracted by the individual WECs and the combined power extracted from the sea are shown for the two spacings. When the WECs are spaced 0.25λ apart, the powers extracted by the two WECs are out of phase. Their combined power output thus is relatively smooth. When, on the other hand, the WECs are spaced 0.5λ apart, their individual power outputs are in phase and thus the combined power output is not smooth.

For the sinusoidal sea used in this section, the smoothing that can be obtained by spacing WECs 0.25λ apart is fairly easy to understand. However, even for irregular seas governed by the Bretschneider spectrum, it is still possible that such smoothing will be seen when the WECs are spaced $0.25\lambda_{peak}$ apart. This will be tested in this chapter for both stationary and non-stationary seas. Also, thus far only the smoothness seen in the cumulative raw mechanical power extracted by an array of WECs was dealt with. How this smoothness is reflected in the smoothness of the net real power the wave power farm feeds to the electricity network is of consequence too, since it is the quality of the power fed to the network that determines to a

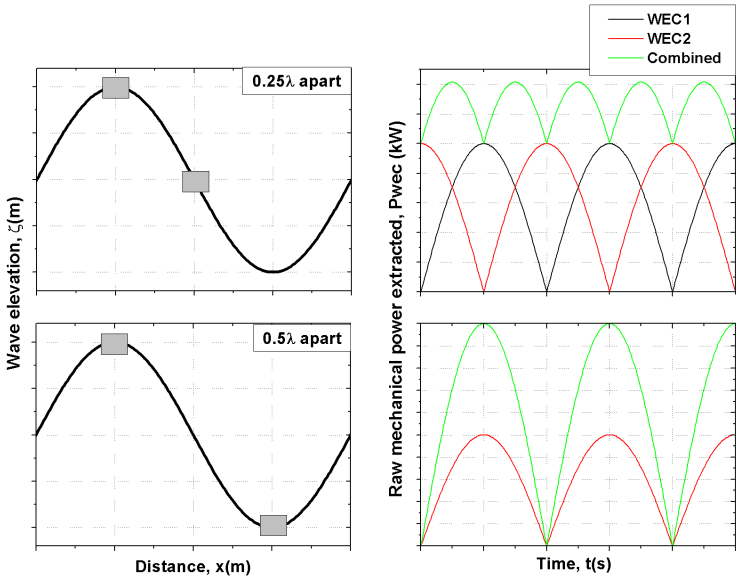

Figure 4.1: *The combined power from two WECs in a sinusoidal sea when they are placed 0.25λ and 0.5λ apart.*

large extent the voltage quality of the network. Whether the smoothing in the generated power from a simple linear array of WECs can be scaled to suit the case of larger arrays with more complex structures is also examined.

4.4 Effects of spacing and orientation on the cumulative raw mechanical power (Pwec) in a simple line of six WECs

In this section, the smoothing in the cumulative Pwec observed when the WECs $0.25\lambda_{peak}$ apart and placed in irregular seas is explored. The theory explained in the preceding section is tested in more realistic seas. A simple array topology in which the array is a line of six WECs has been considered. The array is shown in Figure 4.2. Though this is the most basic array configuration, it is believed that its analysis will reveal many characteristics, which will be important for more sophisticated array configurations. The applicability of these characteristics on more complex array topologies are dealt with later in this chapter.

The effects of spacing WECs differently on the power smoothing in this array when it is placed in both stationary and non-stationary seas have been analysed. The effects of changing the orientation of the array with respect to the dominant wave direction on the power smoothing obtained by spacing WECs appropriately has also be touched upon. Therefore, the two vari-

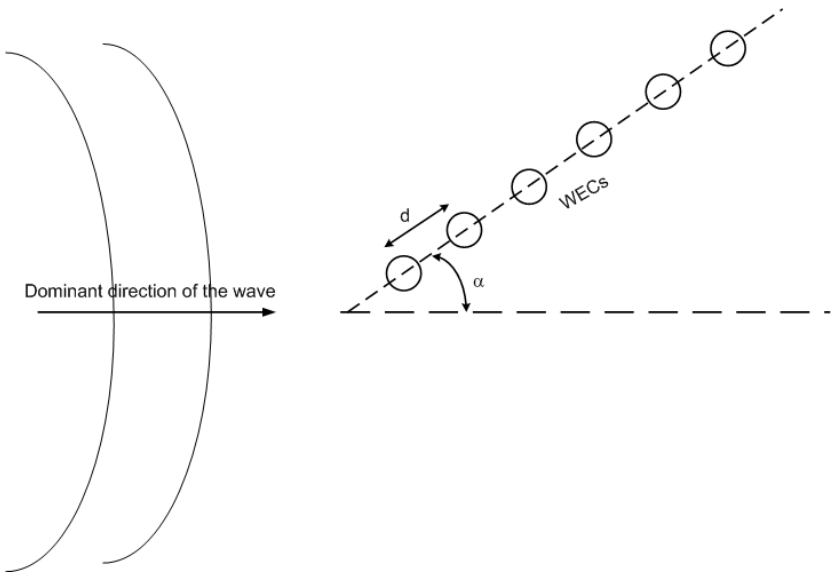

Figure 4.2: *Configuration of the line of six WECs with respect to the dominant direction of wave propagation.*

ables of interest here are the spacing between the WECs d and the orientation of the array α.

4.4.1 Stationary, irregular sea - effects of spacing

This section summarizes the results discussed in [131]. Figure 4.3 shows the frequency spectrum of the stationary but irregular sea state used in this section ($H_s = 4.4$ m and $T_z = 6.78$ s) and shows the peak frequency (f_{peak}) of the spectrum. The peak wavelength λ_{peak} can be calculated from f_{peak} using the dispersion relation. For the simulation runs described in this section, no accumulators were used.

Figure 4.4 shows the cumulative raw mechanical power extracted by the array when placed in the sea modelled, with α= 0°, for three spacings (0.25λ_{peak}, 0.375λ_{peak} and 0.50λ_{peak}). As was stated in [131], the cumulative raw mechanical power extracted is much smoother when the WECs are spaced a quarter peak-wavelength apart. When they are spaced a half peak-wavelength apart high frequency fluctuations are seen. Table 4.1 shows the variance in the cumulative Pwec with respect to the moving average for the three different spacings. A larger variance points to larger fluctuations. It is seen that the variance increases as the spacing increases from 0.25λ_{peak} to 0.5λ_{peak}.

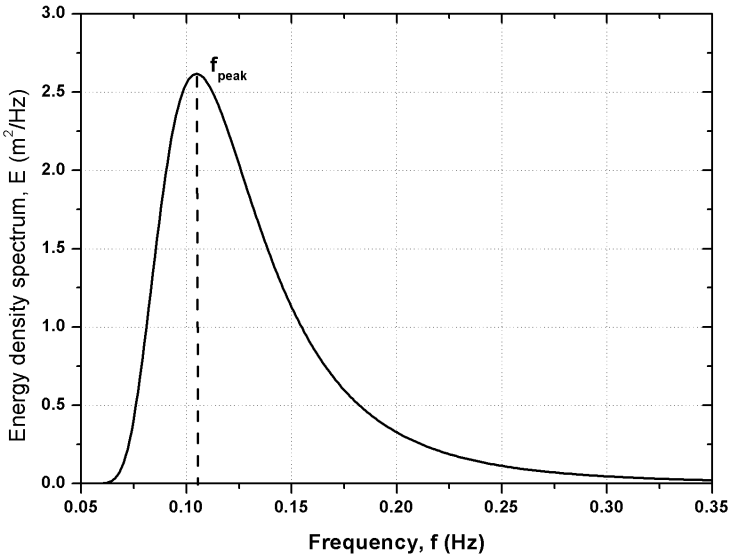

Figure 4.3: *Energy spectrum density of the used stationary but irregular sea state.*

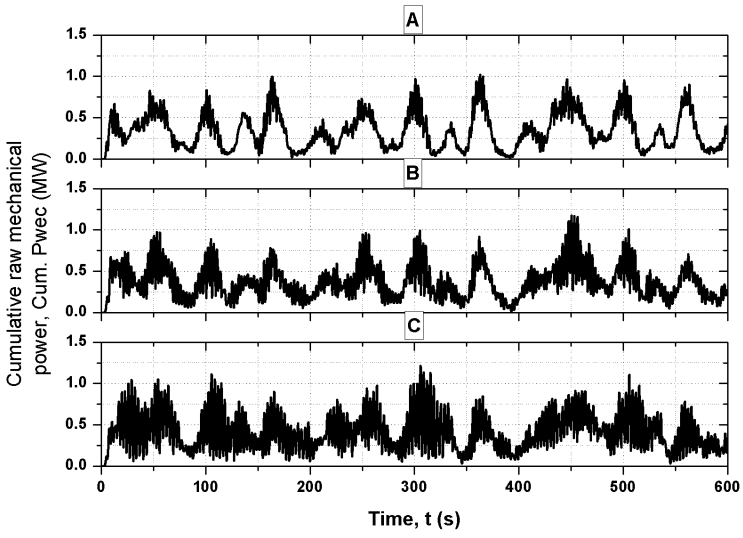

Figure 4.4: *The cumulative raw mechanical power extracted by the array for d = (a) 1/4λ_{peak} (b) 3/8λ_{peak} and (c) 1/2λ_{peak}, when placed in a stationary sea with $H_s = 4.4$ m and $T_z = 6.78$ s.*

Spacing d	**Variance in the cumulative Pwec (MW)**^{2}
$0.25\lambda_{peak}$	0.0042
$0.375\lambda_{peak}$	0.0119
$0.5\lambda_{peak}$	0.0299

Table 4.1: *Variance in the cumulative Pwec, for different array spacings, of the array modelled in a stationary sea with $H_s = 4.4$ m and $T_z = 6.78$ s*

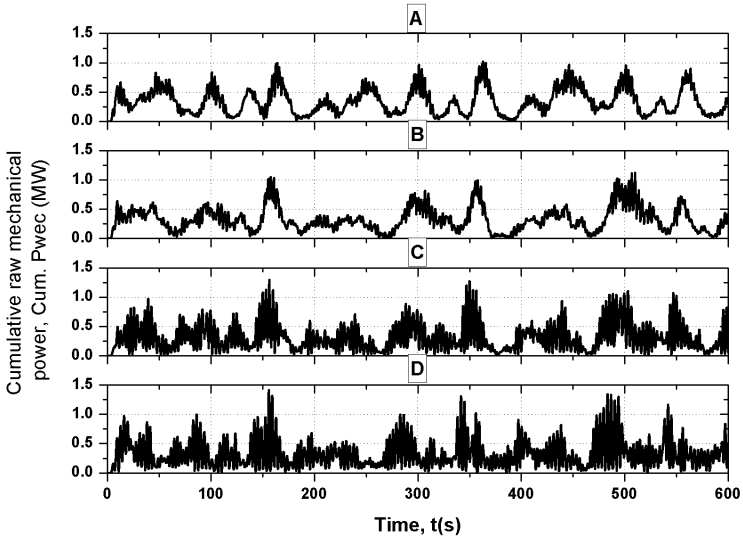

Figure 4.5: *The cumulative raw mechanical power extracted by the line of six WECs for α= (a) 0° (b) 30° (c) 60° and (d) 90°, when placed in a stationary sea with $H_s = 4.4$ m and $T_z = 6.78$ s.*

4.4.2 Stationary, irregular sea - effects of array orientation

Keeping the spacing d constant at $0.25\lambda_{peak}$, the orientation of the array with respect to the dominant wave direction is now changed. Figure 4.5 shows the cumulative raw mechanical power extracted for four different orientations α. The cumulative Pwec time-series is the smoothest when the array is oriented along the dominant wave direction. Even at α= 30°, the cumulative Pwec is as smooth as the α= 0° case. This is attributed to the directional spreading function used, which is significant up to 30° on both sides of the dominant wave direction. The fluctuations in the cumulative raw mechanical power extracted increases with an increase in α. The variance in the cumulative Pwec with respect to its moving average, listed in Table 4.2, confirms this. Under the worst case condition, when the line of WECs lies perpendicular to the dominant wave direction (α= 90°), the wave excitations at the locations of the WECs are in phase. This produces the most fluctuating cumulative Pwec, which is confirmed by the largest variance for the α= 90° case.

Orientation α	**Variance in the cumulative Pwec (MW)^2**
0°	0.0042
30°	0.0047
60°	0.0348
90°	0.0465

Table 4.2: *Variance in the cumulative Pwec, for different array orientations, of the line of six WECs modelled in a stationary sea with $H_s = 4.4$ m and $T_z = 6.78$ s*

4.4.3 Non-stationary, irregular sea - effects of spacing

The simulation runs used for the preliminary analysis used a stationary but irregular sea state. Those simulations were run for a period of 10 minutes. In this section, the inferences made earlier will be tested on the line of six WECs placed in a non-stationary wave field. The simulations in this section have been run for 5.5 hours, with the significant wave height and the average zero-crossing time period varying every 0.1 seconds. The effects of changing the spacing d and the orientation α have been studied and the results are discussed here.

Figure 2.3 showed the varying nature of the spectrum over a day, which is a characteristic of non-stationary seas. Therefore, selecting the peak wavelength λ_{peak} will not be as straight forward as when the sea was stationary. Figure 4.6 shows the variation of the peak frequency over a day and the data that has been used for the 5.5-hour simulation runs discussed in this section. The data selected shows the widest f_{peak} variation during the day. The f_{peak} used for appropriate WEC spacing has been calculated as the average of $f_{peak}(t)$ during the day. With the mean f_{peak} and the corresponding λ_{peak} calculated, the power smoothing in the cumulative Pwec has been analysed for different spacings d and orientations α.

The three spacings tested with the stationary sea case have been used here too. Figure 4.7 shows the cumulative Pwec extracted by the array of 6 WECs for the three different spacings. Only a 500-second snapshot of the generated cumulative Pwec time-series is plotted. The variance in the cumulative Pwec with respect to its moving average (over the plotted 500-second period) for the three cases is shown in Table 4.3. As observed in the figure, the cumulative Pwec time-series is smoothest when the WECs are placed $0.25\lambda_{peak}$ apart with the smoothness progressively decreasing as d increases to $0.5\lambda_{peak}$. The same smoothing in the cumulative Pwec can also be seen over the entire 5.5-hour simulation run. The results are in good agreement with the argument above pertaining to Figure 4.1 and sinusoidal seas. That is, even in irregular, non-stationary seas, a smoothing effect is seen when the WECs are placed $0.25\lambda_{peak}$ apart.

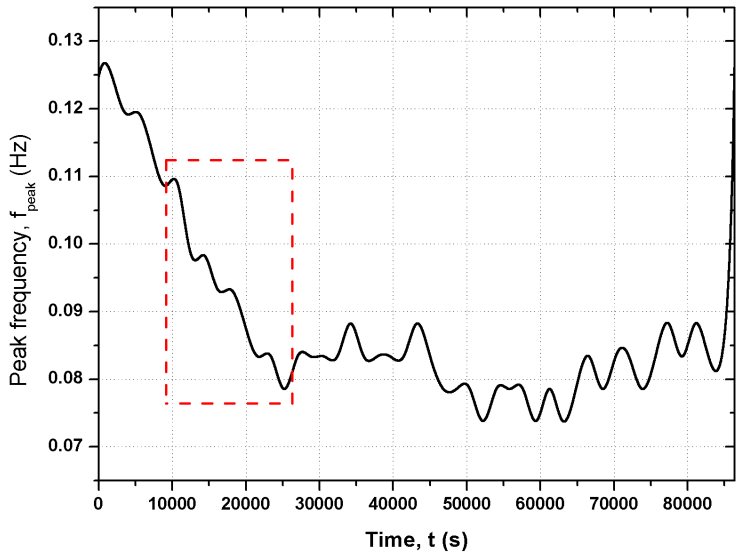

Figure 4.6: *Variation of the peak frequency over a day.*

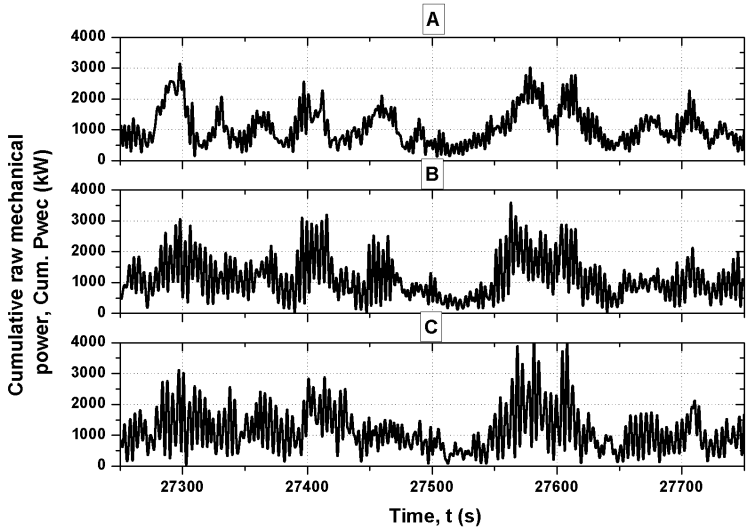

Figure 4.7: *The cumulative raw mechanical power extracted by the line of six WECs for d = (a) 0.25λ_{peak} (b) 0.375λ_{peak} and (c) 0.5λ_{peak}, when placed in a non-stationary sea.*

Spacing d	**Variance in the cumulative Pwec over 500 seconds (MW)**^{2}	**Variance in the cumulative Pwec over 5.5 hours (MW)**^{2}
$0.25\lambda_{peak}$	0.0517	0.0495
$0.375\lambda_{peak}$	0.2018	0.1266
$0.5\lambda_{peak}$	0.2757	0.1862

Table 4.3: *Variance in the cumulative Pwec, for different array spacings, of the line of six WECs modelled in a non-stationary sea*

Orientation α	**Variance in the cumulative Pwec over 500 seconds (MW)**^{2}	**Variance in the cumulative Pwec over 5.5 hours (MW)**^{2}
0°	0.0517	0.0495
30°	0.0589	0.0472
60°	0.2184	0.1232
90°	0.4766	0.3247

Table 4.4: *Variance in the cumulative Pwec, for different array orientations, of the line of six WECs modelled in a non-stationary sea*

4.4.4 Non-stationary, irregular sea - effects of array orientation

In this section, the effects of changing the orientation of the array of WECs on the smoothing in the cumulative Pwec are discussed further. It was shown earlier that some smoothing in the cumulative Pwec is seen when the array is oriented along the dominant wave direction. This was seen in the case of a stationary but irregular sea. Now, whether the smoothing seen in the cumulative Pwec is still seen when the array is simulated in a non-stationary sea is examined.

Figure 4.8 displays a similar effect to the one observed for the stationary sea case. When α= 0°, the cumulative Pwec is relatively smooth. The smoothness progressively decreases as α is increased to 90°, i.e. when the array is perpendicular to the dominant wave direction. The values of the variance for both the 500-second and the 5.5-hour simulation runs corroborate this (see Table 4.4). It can be observed that the values of the variance are very close to each other for α= 0° and α= 30°. The relatively high value of the variance for the α= 0° case is due to the fact that λ_{peak} varies, which overrides the smoothing that would have been produced because of the alignment of the array. The definition of the spreading function, where significant spreading in the waves is seen even at $\pm$ 30° from the dominant wave direction, also plays a role in producing this effect.

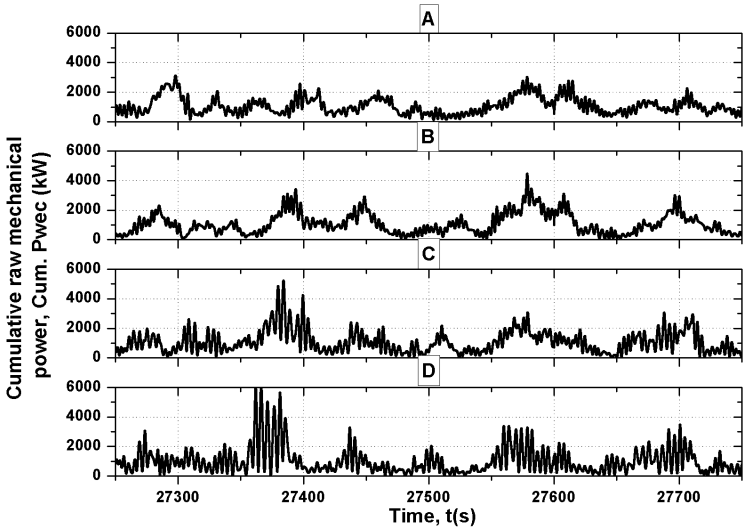

Figure 4.8: *The cumulative raw mechanical power extracted by the line of six WECs for α = (a) 0° (b) 30° (c) 60° and (d) 90°, when placed in a non-stationary sea.*

4.5 Effects of spacing and orientation on the net real power (Pfarm) generated by the line of six WECs

In the preceding section, it was shown that spacing the WECs at quarter the peak wavelength and orienting the linear array along the dominant wave direction ensured a smoother cumulative Pwec time-series. Since the main aim of this thesis is to study the electrical network impacts of connecting wave power farms, the quality of the net real power injected to the network by the array is more significant than the cumulative Pwec time-series. The voltage quality in weak, rural distribution networks is largely defined by the quality of the power fed by the DG connected to it. Hence, for the different array configurations and seas used in the preceding sections, the power smoothing seen in the net Pfarm is now analysed. The wave power farms modelled in these sections have been connected to a simple three bus electrical network, which is representative of rural distribution networks. Details of the network and its diagram were given in Section 2.6 (Figure 2.26).

Figure 4.9 shows the net real power generated by the array under the same three spacings for the stationary but irregular sea. It is seen that the fluctuations in the net Pfarm are bigger when the spacing is $0.25\lambda_{peak}$ than when the spacing is $0.5\lambda_{peak}$. This is attributed to the fact that the hydraulic system and the DFIG within each WEC behave as filters and filter out the high frequency cumulative Pwec fluctuations, seen at the $0.5\lambda_{peak}$ spacing case, more than the

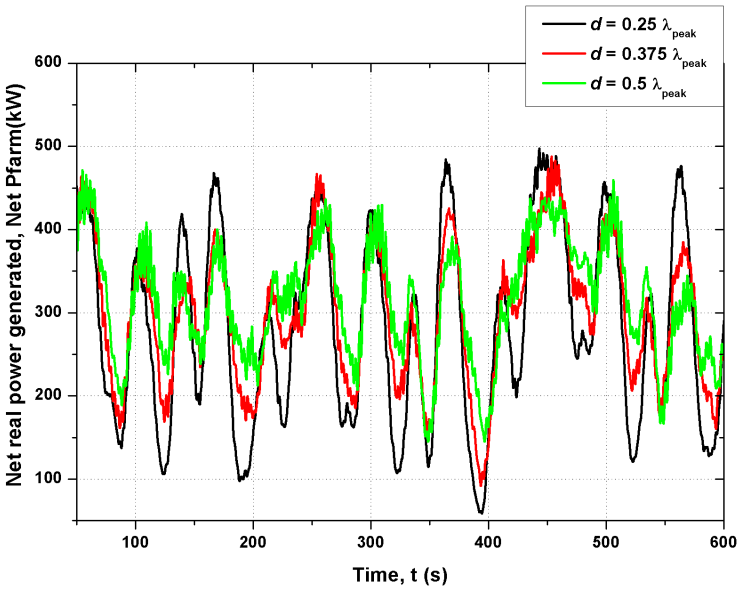

Figure 4.9: *The net real power generated by the line of six WECs, when placed in a stationary sea with $H_s = 4.4$ m and $T_z = 6.78$ s.*

Spacing d	**Variance in the cumulative Pwec (MW)^2**	**Variance in the net Pfarm (MW^2)**
$0.25\lambda_{peak}$	0.0042	1.3136×10^4
$0.375\lambda_{peak}$	0.0119	7.0647×10^3
$0.5\lambda_{peak}$	0.0299	4.8998×10^3

Table 4.5: *Variance in the cumulative Pwec and the net Pfarm, for different array spacings, of the line of six WECs modelled in a stationary sea*

low frequency variations in cumulative Pwec, seen when the spacing is $0.25\lambda_{peak}$. Increasing the spacing d from $0.25\lambda_{peak}$ to $0.375\lambda_{peak}$ and $0.5\lambda_{peak}$ was seen to augment the average real power fed to the network by approximately 6% and 11% respectively. Table 4.5 shows the variance in the net real power generated for the three spacings, which clearly shows an increased smoothing in the net real power generated when d is $0.5\lambda_{peak}$.

Figure 4.10 shows the real power fed to the network by the wave power farm for the α= 0° and α= 90° cases. The extent of the low frequency swings in the net Pfarm time-series is reduced in the α= 90° case when compared to the α= 0° case. Though significant high frequency variations in the net Pfarm time-series are seen, most of these variations will be smoothened by the use of hydraulic accumulators which is the subject of the next section. From these results it can be inferred that the smoothing in the net Pfarm increases with an increase in the orientation angle α. In this case too, the time-series of the cumulative Pwec studded with high frequency

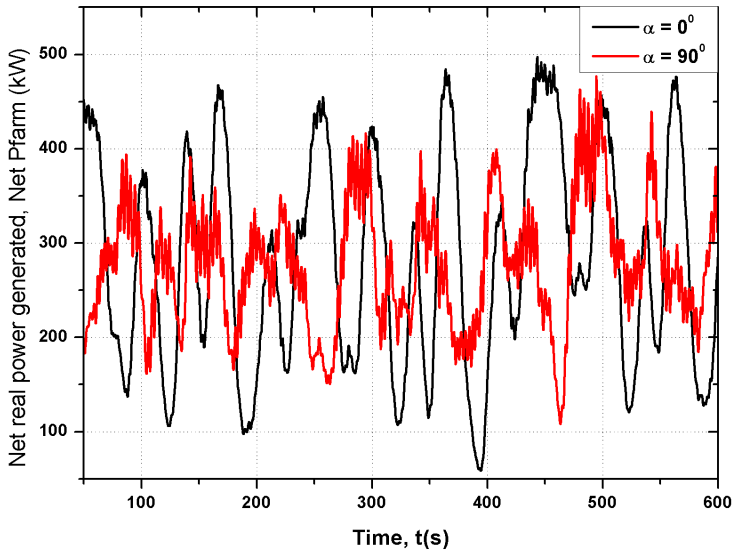

Figure 4.10: *The net real power generated by the line of six WECs, when placed in a stationary sea with $H_s = 4.4$ m and $T_z = 6.78$ s.*

Orientation α	**Variance in the cumulative Pwec (MW)^2**	**Variance in the net Pfarm (MW^2)**
0°	0.0042	1.3136×10^4
30°	0.0047	9.9861×10^3
60°	0.0348	7.3361×10^3
90°	0.0465	4.3064×10^3

Table 4.6: *Variance in the cumulative Pwec and the net Pfarm, for different array orientations, of the line of six WECs modelled in a stationary sea*

variations gives a much smoother net Pfarm time-series, as seen in the case when $d = 0.5\lambda_{peak}$. The values of the variance for the four different orientations (see Table 4.6) corroborate the visual evidence shown in the figure.

4.6 Effects of using accumulators on the net Pfarm

One of the advantages of using a hydraulic PTO system is the option of having some on-board storage in the form of accumulators. The results shown in Section 4.5 were all obtained through simulation runs in which no accumulators were used. This section explores some of the advantages of using accumulators in WECs. The effects of having accumulators on some of the results discussed in the previous section are examined here.

Increasing the size of the accumulator improves the quality of the real power generated by a WEC. This is shown in Figure 4.11 in which the real power generated by two WECs, one

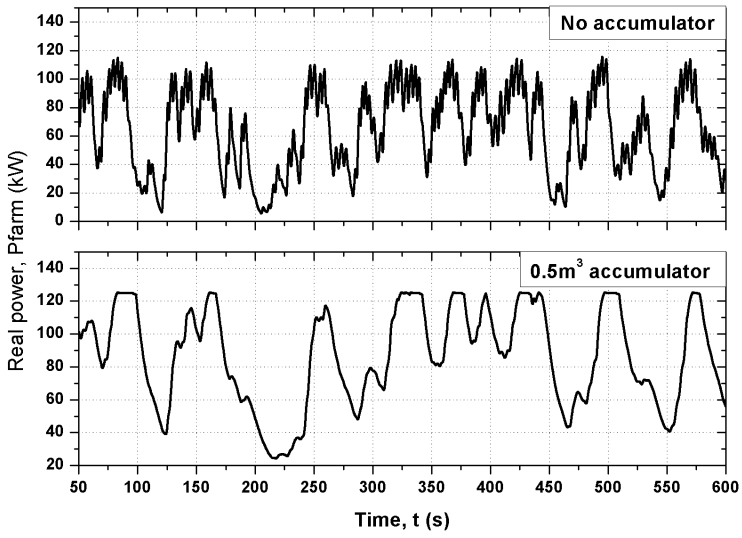

Figure 4.11: *Effects of using accumulators on the real power generated by a WEC.*

Accumulator capacities (m^3)	**Average cumulative Pwec (kW)**	**Average net Pfarm (kW)**	**Avg. net Pfarm/Avg. cumulative Pwec**
0.01	539	445	0.825
0.05	539	470	0.872
0.10	539	479	0.888
0.25	539	485	0.899
0.50	539	489	0.908

Table 4.7: *Effects of using accumulators on the average real power fed to the network*

without any accumulator and one with an accumulator of size 0.5 m^3, are shown. The WECs have been excited by the same sea state. Most of the high frequency fluctuations in the power, detected in the case when no accumulator is used, are reduced when the accumulator is used. These high frequency fluctuations in power are those caused by the wave-to-wave power variations. The lower frequency fluctuations are not addressed by the increase in the size of the accumulator. Another significant advantage of using accumulators is the augmentation of the exported power from a wave power farm. Table 4.7 shows the effects of increasing the accumulator size on the average real power exported from an array of 6 WECs.

The effects of having accumulators on the smoothing in the net Pfarm, which is obtained by appropriately spacing and orienting the array are now discussed. Figure 4.12 shows the net Pfarm time-series for the three spacings, when each WEC in the array has an accumulator of size 0.5 m^3. The average real power generated for the three cases was seen to be higher

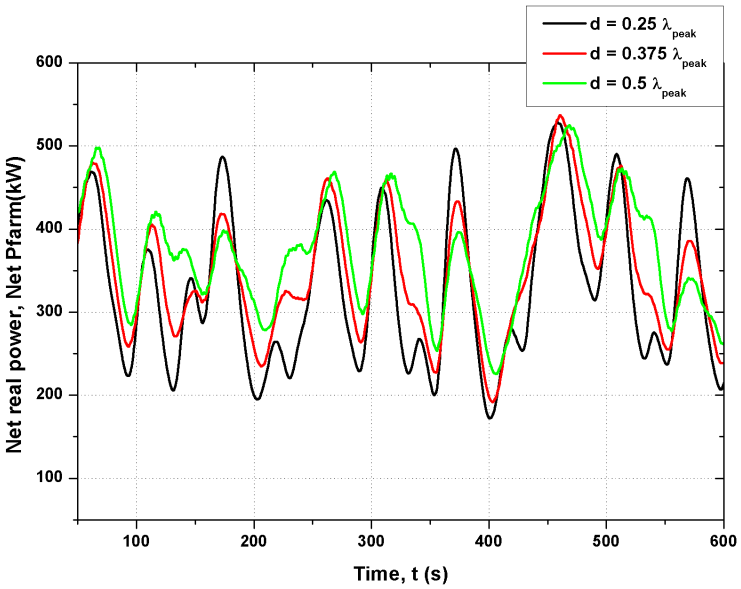

Figure 4.12: *The net real power generated by the line of six WECs with on-board storage for different array spacings, when placed in a stationary sea.*

Spacing d	**Variance in the cumulative Pwec (MW)**^{2}	**Variance in the net Pfarm (MW**^{2}**)**
$0.25\lambda_{peak}$	0.0042	8.4499×10^3
$0.375\lambda_{peak}$	0.0119	5.7587×10^3
$0.5\lambda_{peak}$	0.0299	4.7514×10^3

Table 4.8: *Variance in the cumulative Pwec and the net Pfarm, for different spacings, of the line of six WECs with on-board storage, when modelled in a stationary sea*

than when no accumulators were used (by approximately 16%, 17% and 19.5% for the d = $0.25\lambda_{peak}$, $0.375\lambda_{peak}$ and $0.5\lambda_{peak}$ cases respectively). This is an important result, which affirms that using some amount of storage in the array increases the average yield from the array. As seen in the case without accumulators, the average real power generated also increased with an increase in d from $0.25\lambda_{peak}$ to $0.375\lambda_{peak}$ and $0.5\lambda_{peak}$. An increase of approximately 6% and 14% respectively, with respect to the d = $0.25\lambda_{peak}$ case, was seen.

Table 4.8 shows the variance in the net Pfarm for the three spacings with the accumulator. As seen in the case without accumulators, the real power generated is the smoothest when the spacing is $0.5\lambda_{peak}$, as shown by the values of the variance. Comparing the values of the variance shown in the Tables 4.5 and 4.8 clearly shows the improvement in the power smoothing obtained when accumulators are used.

Figure 4.13 shows the smoothing in the real power generated by a WEC for three accumulator

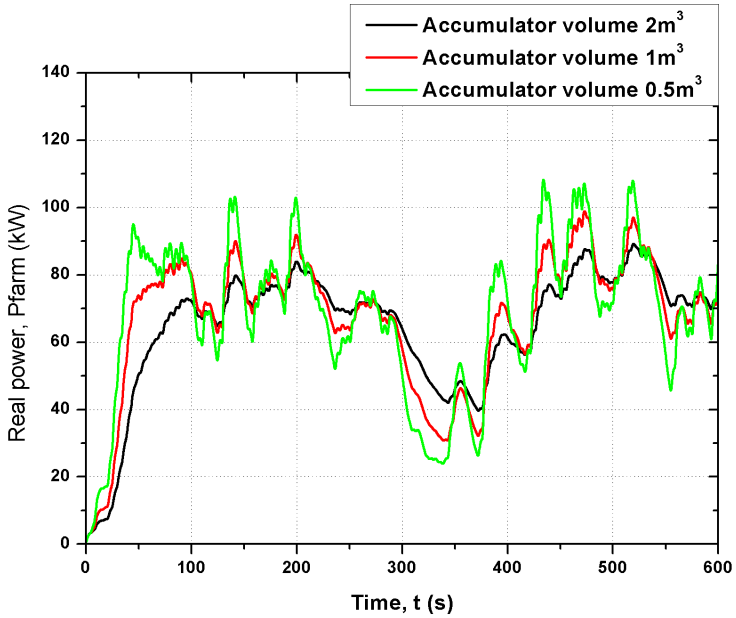

Figure 4.13: *Real power generated by a WEC for different accumulator sizes.*

sizes. There is some improvement seen in the smoothing with an increase in the accumulator size, but the improvement is not keeping with the 300% increase in the accumulator size (from 0.5 m^3 to 2 m^3). This clearly shows that any improvement in the smoothing in the net Pfarm that can be obtained by spacing the WECs appropriately, will also contribute to the overall power smoothing. Also, a trade-off between the smoothing required and the cost and space requirements for large accumulators has to be made. In the rest of this chapter, all the simulation runs have been performed with WECs having an accumulator of size 0.5 m^3 each.

4.7 8-WEC arrays - different topologies

So far in this chapter, only a line of WECs was considered to study the effects of spacing and orientation on the power output. Some of the inferences drawn from the results in the preceding sections are now tested with more realistic arrays of 8 WECs. In this section, the power smoothing introduced by appropriate spacing in three different 8-WEC array topologies is explored. The three considered topologies are shown in Figure 4.14. The spacing between the rows and columns of WECs in the array has been taken as 100 m and $0.25\lambda_{peak}$ respectively.

For the dominant wave direction shown in the figure, it becomes obvious that in the case of Array 1, since all the WECs are in coherence, the cumulative raw mechanical power will be

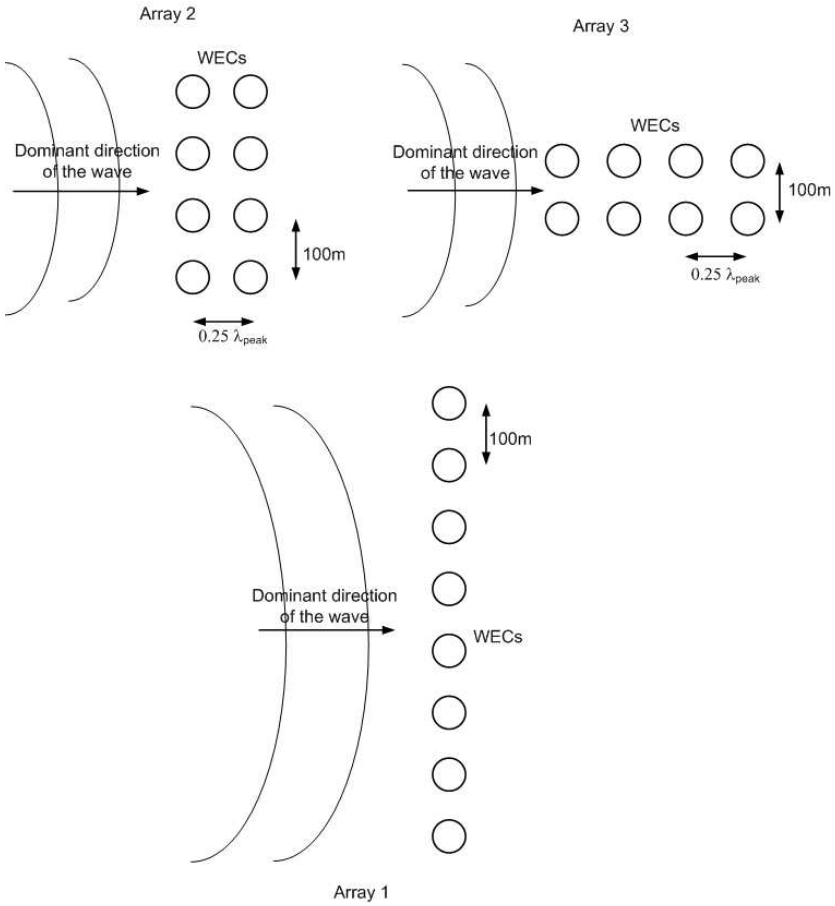

Figure 4.14: *Topologies of the arrays of 8 WECs.*

Array configuration	**Variance in the cumulative Pwec (MW)^2**	**Variance in the net Pfarm (MW^2)**
1	0.0428	1.7007×10^3
2	0.0210	3.2244×10^3
3	0.0175	3.8327×10^3

Table 4.9: *Variance in the cumulative Pwec and the net Pfarm for the three 8-WEC array topologies*

the least smooth. In Array 2, the 4 WECs constituting the first column of WECs in the array and the 4 WECs in the second column of WECs are in coherence. Since only 4 WECs are in coherence, it might be assumed that a smoother cumulative raw mechanical power output when compared to Array 1 will be obtained. This again depends on the spacing between the two columns of WECs. The spacing has been taken as $0.25\lambda_{peak}$. Array 3 has only the 2 WECs in each column in coherence with each other. Thus, the smoothest cumulative raw mechanical power output would be expected from this array configuration. The three array topologies are tested under a commonly occurring sea state found off the north west coast of Scotland. The sea state used is irregular and non-stationary with $H_s = 4.32$ m and $T_z = 6.71$ s and an average peak wavelength of 132.41 m.

Figure 4.15 shows the cumulative raw mechanical power extracted by the three arrays. As expected, the smoothness in the cumulative Pwec increases as the array configuration changes from 1 to 3. This is also confirmed by the variance in the cumulative Pwec listed in Table 4.9. Analysing the net Pfarm generated by the three arrays, which is shown in Figure 4.16, shows wider power fluctuations when Array 3 is used. Array 1 in which all the WECs are in coherence performs better than the other configurations with respect to the net real power fluctuations. This is seen in the values of the variance in net Pfarm shown in Table 4.9, with Array 1 having the lowest variance. As seen in the case with different spacings and orientations in the line of six WECs, in the case of different topologies of arrays of 8 WECs, the smoothness in the generated net Pfarm and the cumulative Pwec extracted vary inversely; i.e. smoother the generated cumulative Pwec time-series, less smooth the generated net Pfarm time-series is.

4.8 Increasing the array size - effects on power smoothing

A general belief of researchers in both the wind energy and the wave energy industry is that just increasing the number of wind/wave energy converters would solve the problem of the fluctuations in the generated power. This is true to an extent when considering wind power farms; but when examining wave power farms not only the number of devices in the farm but

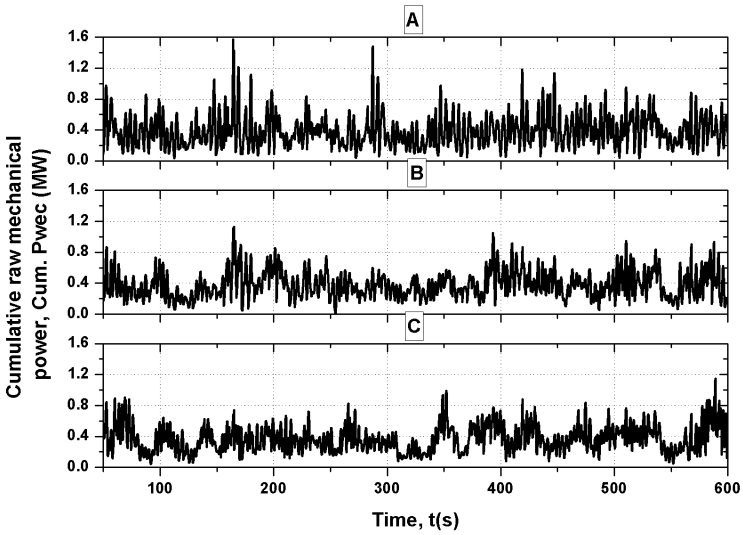

Figure 4.15: *The cumulative raw mechanical power extracted by (a) Array 1 (b) Array 2 and (c) Array 3.*

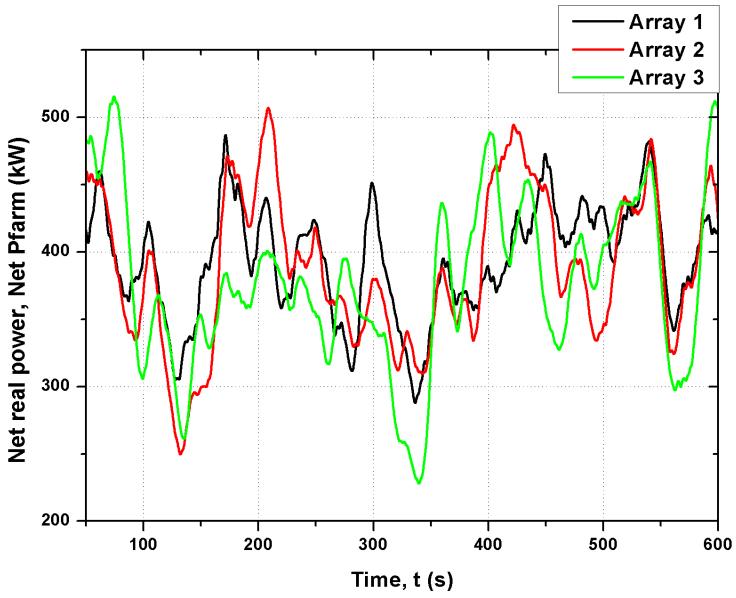

Figure 4.16: *The net real power generated by (a) Array 1 (b) Array 2 and (c) Array 3.*

Array size (MW)	**Variance in the net Pfarm (MW^2)**	**Average net Pfarm (kW)**	**Coefficient of Variance (kW)**
1	1.7007×10^3	393.9	4.3276
2	7.4109×10^3	791.0	9.3689
3	1.7222×10^4	1194.8	14.4141
4	2.7094×10^4	1608.4	16.8453
5	3.4090×10^4	2023.5	16.8470
6	4.0343×10^4	2436.3	16.5591

Table 4.10: *The average of and the variance in the net Pfarm, for different array sizes, of the 6 MW wave power farm modelled in a stationary sea with $H_s = 4.4$ m and $T_z = 6.78$ s*

also the layout of the farm influences the quality of the net real power generated. This has been investigated and the results and inferences are discussed in this section. Arrays of sizes ranging from 1 MW to 6 MW have been simulated and the effects of appropriate spacing of the columns of WECs within the array on the quality of power generated are discussed. The theory presented in the case of the simple line of six WECs has been extrapolated with the spacing between columns of WECs in the array being the variable of interest. This section also analyses the effects of increasing the size of the array on the quality of the real power generated, and whether the advantages of appropriately spacing the WECs still hold good for these larger arrays.

Starting from the 1 MW Array 1 configuration (see Figure 4.14), successive arrays with additional columns of 8 WECs each; i.e. arrays of 1 MW, 2 MW, 3 MW, 4 MW, 5 MW, and 6 MW have been considered. The six arrays are shown in Figure 4.17. The spacing between two neighbouring columns of WECs is $0.25\lambda_{peak}$ and the stationary sea state with $H_s = 4.4$ m and $T_z = 6.78$ s has been used in the first part of this section. Figure 4.18 shows the real power generated by the six arrays. It is seen that large fluctuations in the net Pfarm are seen even in the 6 MW wave power farm's case. Table 4.10 shows the variance in the net Pfarm and the average net Pfarm values for the six arrays. In absolute terms, the variance in the net Pfarm increases with an increase in the size of the array. The coefficient of variance is initially seen to increase with an increase in the array size. For farm sizes above 4 MW, the coefficient of variance is seen to plateau.

Figure 4.19 shows the cumulative Pwec and the net Pfarm time-series generated by the 6 MW array when the spacing between the column of WECs is $0.25\lambda_{peak}$ and $0.5\lambda_{peak}$. Table 4.11 lists the variance in the cumulative Pwec and the net Pfarm for the two spacings. The variance in the cumulative Pwec is approximately 2.3 times higher in the $0.5\lambda_{peak}$ spacing case when

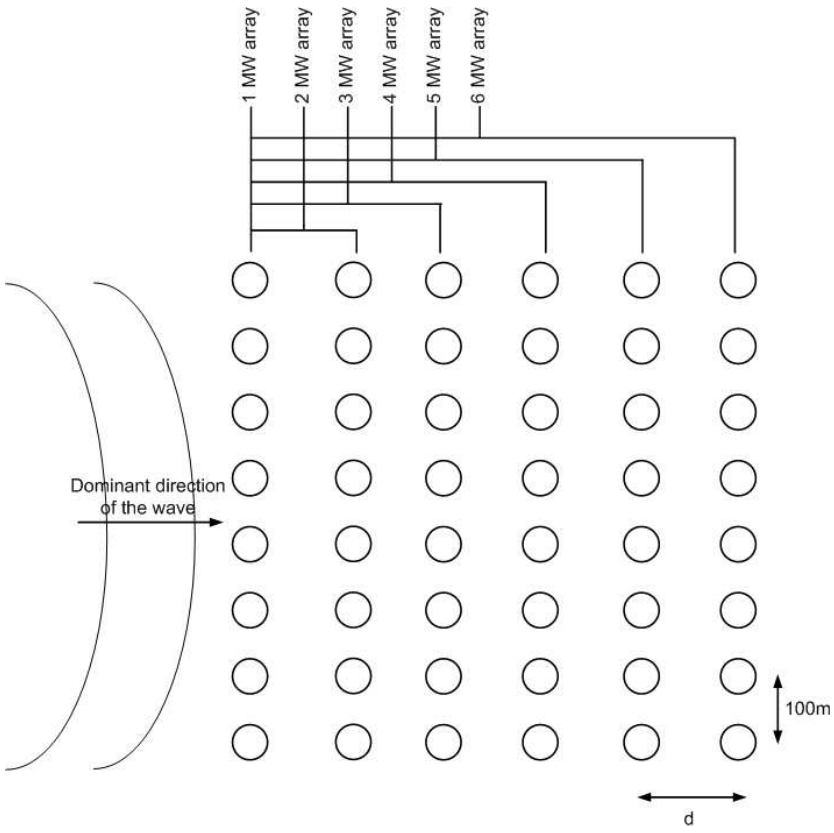

Figure 4.17: *The six arrays of WECs.*

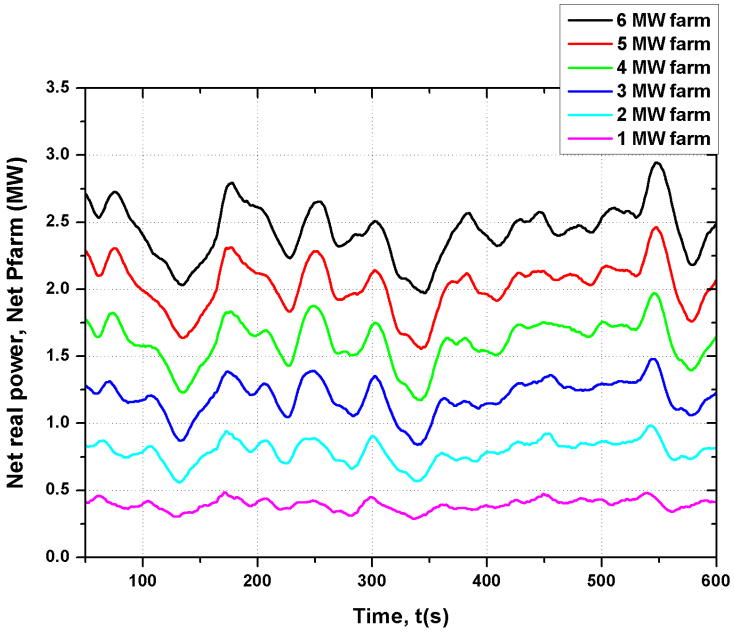

Figure 4.18: *The net real power generated by the six arrays when placed in a stationary sea with $H_s = 4.4$ m and $T_z = 6.78$ s.*

Spacing d	**Variance in the cumulative Pwec (MW)**^{2}	**Variance in th net Pfarm (MW**^{2}**)**	**Average net Pfarm (kW)**
$0.25\lambda_{peak}$	0.1069	4.0343×10^4	2436.3
$0.50\lambda_{peak}$	0.2479	2.7799×10^4	2474.3

Table 4.11: *Variance in the cumulative Pwec and the net Pfarm, for two different spacings, of the 6 MW wave power farm modelled in a stationary sea with $H_s = 4.4$ m and $T_z = 6.78$ s*

compared to the $0.25\lambda_{peak}$ spacing case. On the other hand, the net real power generated is smoother in the $0.5\lambda_{peak}$ spacing case when compared to the $0.25\lambda_{peak}$ spacing case. These results prove that the effects of spacing on the net Pfarm smoothness holds even as the size of the array increases.

The simulations performed with the stationary sea state with $H_s = 4.4$ m and $T_z = 6.78$ have been repeated using a more energetic sea state with $H_s = 12.87$ m and $T_z = 11.83$ s. The same set of array configurations has been used and the real power time-series generated by the six arrays are plotted in Figure 4.20. Table 4.12 lists the variance in the net real power and the average net real power generated by the different arrays. It becomes evident that significant power fluctuations occur even when the size of the array increases. These results are similar

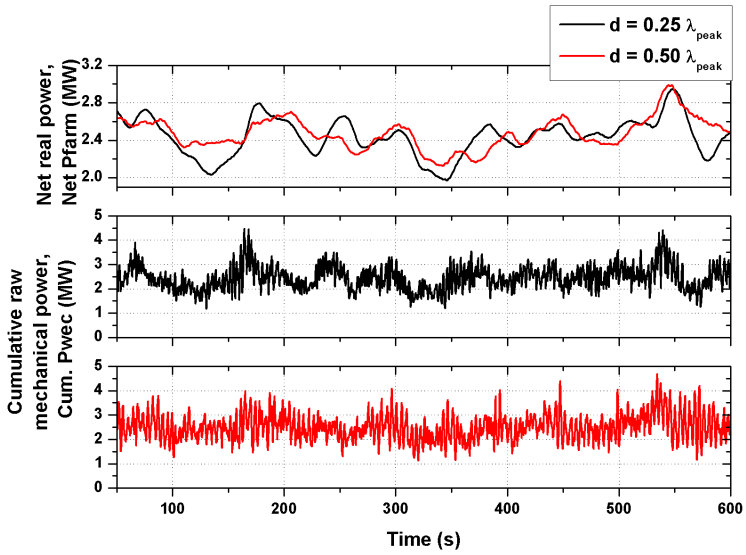

Figure 4.19: *The cumulative raw mechanical power and the net real power generated by the 48-WEC array for two different array spacings, when placed in a stationary sea with $H_s = 4.4$ m and $T_z = 6.78$ s.*

Array size (MW)	**Variance in the net Pfarm (MW^2)**	**Average net Pfarm (kW)**	**Coefficient of Variance (kW)**
1	6.7018×10^3	709.6	9.4445
2	1.7988×10^4	1425.1	12.6223
3	3.2851×10^4	2146.4	15.3052
4	5.0714×10^4	2870.7	17.6661
5	6.2302×10^4	3574.4	17.4301
6	6.5091×10^4	4264.2	15.2645

Table 4.12: *The average of and the variance in the net Pfarm, for different array sizes, of the 6 MW wave power farm modelled in a stationary sea with $H_s = 12.87$ m and $T_z = 11.83$ s*

to the observations made through the simulation runs performed with the moderately energetic sea state.

For comparing the effects of having column spacings of $0.25\lambda_{peak}$ and $0.5\lambda_{peak}$, Figure 4.21 shows the generated net Pfarm and cumulative Pwec extracted by the array of 48 WECs. The generated net real power is smoother when the column spacing is $0.5\lambda_{peak}$. The smoothness in the net real power generated is not as evident as in the sea state used previously, but still exists. Table 4.13 shows the variance in the cumulative Pwec and the net Pfarm for the two spacings. The variance in the net Pfarm is seen to be lower when the spacing between the columns of WECs is $0.5\lambda_{peak}$.

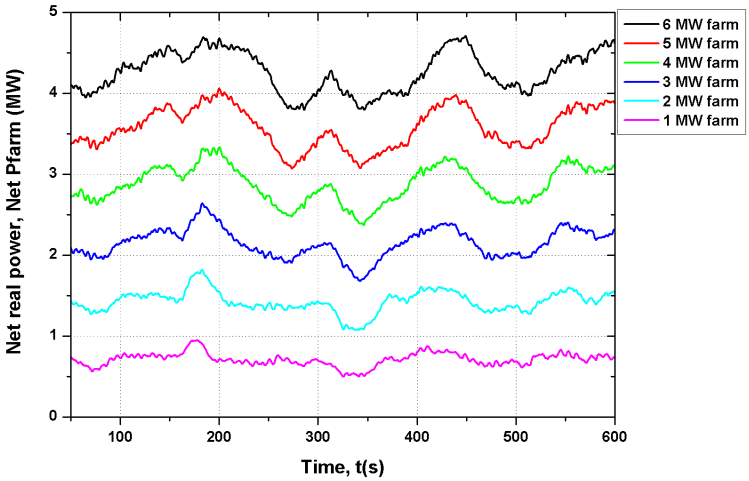

Figure 4.20: *The net real power generated by the six arrays when placed in a stationary sea with $H_s = 12.87$ m and $T_z = 11.83$ s.*

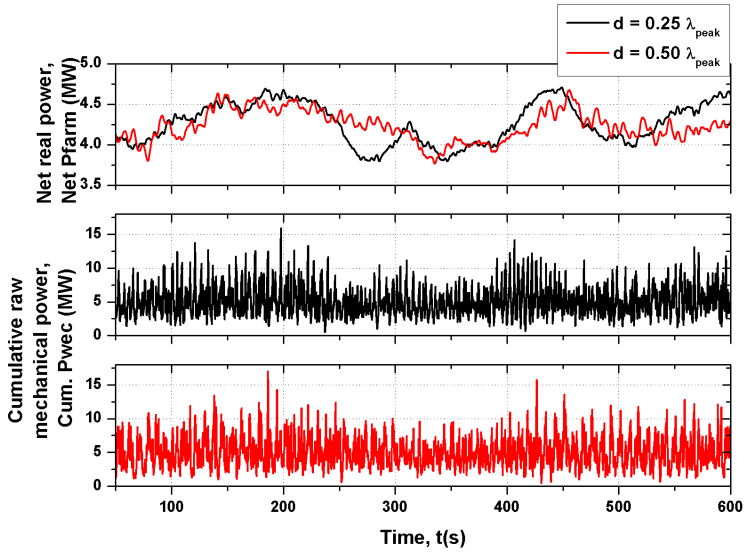

Figure 4.21: *The cumulative raw mechanical power and the net real power generated by the 48-WEC array for two different array spacings, when placed in a stationary sea with $H_s = 12.87$ m and $T_z = 11.83$ s.*

Spacing d	**Variance in the cumulative Pwec (MW)**^{2}	**Variance in the net Pfarm (MW**^{2}**)**	**Average net Pfarm (kW)**
$0.25\lambda_{peak}$	4.4739	6.5091×10^4	4264.2
$0.50\lambda_{peak}$	4.1092	3.6070×10^4	4233.8

Table 4.13: *Variance in the cumulative Pwec and the net Pfarm, for two different spacings, of the 6 MW wave power farm modelled in a stationary sea with $H_s = 12.87$ m and $T_z = 11.83$ s*

4.9 6 MW wave power farm - different spacings

In this section, the effects of changing the spacing d between columns of WECs in the 6 MW wave power farm are discussed further. The array configuration is shown in Figure 4.22. The different spacings that have been considered in this section are - $0.25\lambda_{peak}$, $0.5\lambda_{peak}$, $0.75\lambda_{peak}$, λ_{peak} and $1.25\lambda_{peak}$. The array has been simulated in a sea state with $H_s = 4$ m and $T_z = 6$ s. In the site off the north west coast of Scotland being considered in this work, this is a commonly occurring sea state. In theory, the smoothing in the cumulative raw mechanical power obtained by placing the WECs $0.25\lambda_{peak}$ apart should be seen even when the WECs are spaced at odd-numbered multiples of $0.25\lambda_{peak}$. This has been tested and the results are presented in this section.

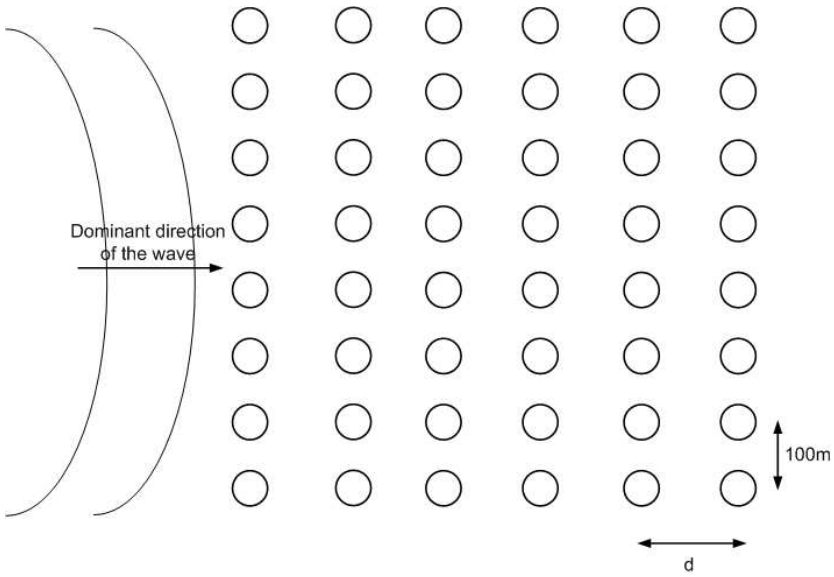

Figure 4.22: *6 MW wave power farm configuration.*

Figure 4.23 shows the cumulative Pwec and the net Pfarm generated by the 6 MW wave power farm when the columns of WECs in the array are spaced at $0.25\lambda_{peak}$ and $0.5\lambda_{peak}$. The cumulative Pwec time-series is smoother when the spacing is $0.25\lambda_{peak}$ than when the spacing is $0.5\lambda_{peak}$. The net real power generated by the farm sees wider variations when the spacing

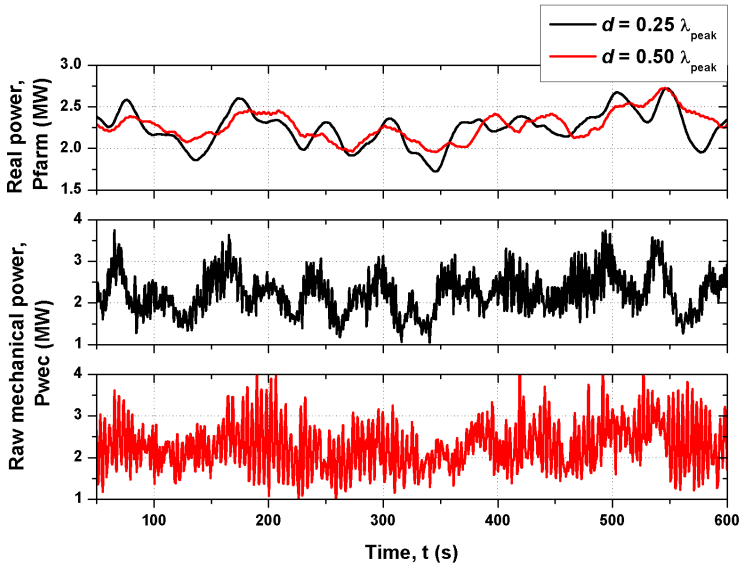

Figure 4.23: *The cumulative raw mechanical power and the net real power generated by the 48-WEC array for two different array spacings d = 0.25λ_{peak} and 0.5λ_{peak}.*

is 0.25λ_{peak} than when the spacing is 0.5λ_{peak}. These observations are as expected and as discussed earlier in this chapter. Figure 4.24 shows the reason why a smoother cumulative Pwec time-series is seen when the columns of WECs are spaced 0.25λ_{peak} apart. The figure shows the raw mechanical power extracted by two WECs in the same row but in neighbouring columns of the array. When the spacing is 0.25λ_{peak}, the peak generation by the first WEC is negated by the minimum generation by the second WEC and vice versa. This feature is seen across the array between corresponding WECs in neighbouring columns. On the other hand, when the spacing between the WECs is 0.5λ_{peak}, the raw mechanical power extracted by the two WECs is almost in phase, which produces a more variable cumulative raw mechanical power time-series.

In [131], it was proposed that the smoothing in the cumulative raw mechanical power, seen when the WECs are spaced 0.25λ_{peak} apart, would be seen when the spacing is any odd-numbered multiple of 0.25λ_{peak}. This means that a similar smoothness in the cumulative raw mechanical power extracted by the array would be seen when the columns of WECs are spaced at 0.75λ_{peak} too. To test this proposition, a simulation run of the 6 MW wave power farm in which the columns of WECs are spaced 0.75λ_{peak} apart was performed. The results obtained along with those obtained from the 0.5λ_{peak} spacing run are shown in Figure 4.25. It is seen that the visible smoothing in the cumulative Pwec, seen when the columns are spaced 0.25λ_{peak}

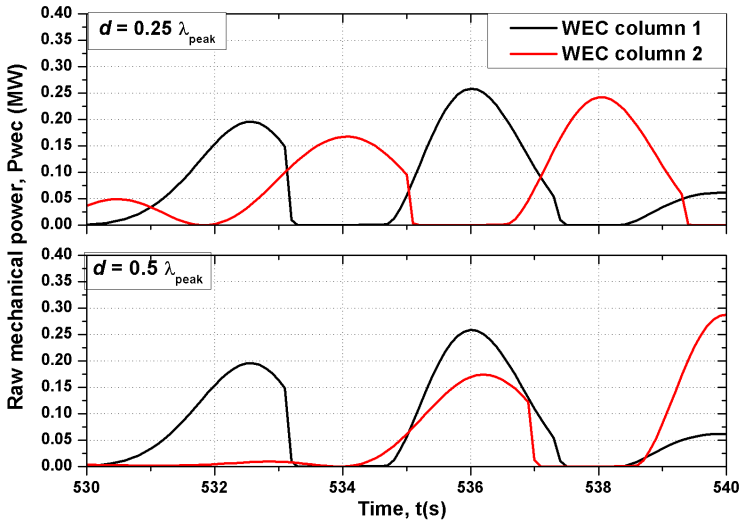

Figure 4.24: *The raw mechanical power extracted by two WECs in two neighbouring columns, occupying the same row in the array, when the spacing d = 0.25λ_{peak} and 0.5λ_{peak}.*

apart, is not seen when the spacing is 0.75λ_{peak}. From the results discussed earlier, it might be assumed that the smoothness seen in the net real power generated by the array with 0.5λ_{peak} spacing would be more than when the array spacing is 0.75λ_{peak}. Observing the net Pfarm plots in Figure 4.25 does not show a visible improvement in the smoothing when the spacing is 0.5λ_{peak}. In fact, the variance in the net Pfarm when the spacing is 0.5λ_{peak} is larger than when the spacing is 0.75λ_{peak}. Comparing the raw mechanical power extracted by two WECs of the same row and in neighbouring columns with the 0.25λ_{peak} and the 0.75λ_{peak} spacings (Figures 4.24 and 4.26) clearly shows why. When the columns of WECs are spaced 0.25λ_{peak} apart, the Pwec extracted by the two WECs are almost exactly out of phase, which ensures a relatively smooth cumulative Pwec. On the other hand, when the spacing is 0.75λ_{peak}, the Pwec extracted by the two WECs are not exactly out of phase, which accounts for the bigger variations in the cumulative Pwec. This was also seen with the other spacings (1.0λ_{peak} and 1.25λ_{peak}) that were tested. Thus, the high degree of coherence between two WECs of the same row and in two neighbouring columns seen when the spacing is 0.5λ_{peak} is not seen when the spacing increases beyond 0.5λ_{peak}.

Table 4.14 shows the variance in the cumulative Pwec and the net Pfarm for the spacings considered. For the first two cases (0.25λ_{peak} and 0.5λ_{peak}) the results were discussed earlier in this section. The discrepancy in the 0.75λ_{peak} case was also explained earlier. Observing the

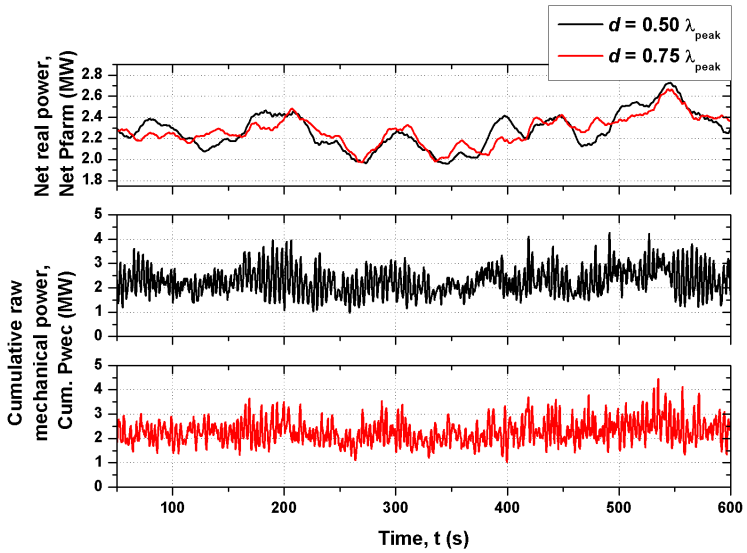

Figure 4.25: *The cumulative raw mechanical power and the net real power generated by the 48-WEC array for two different array spacings d = 0.5λ_{peak} and 0.75λ_{peak}.*

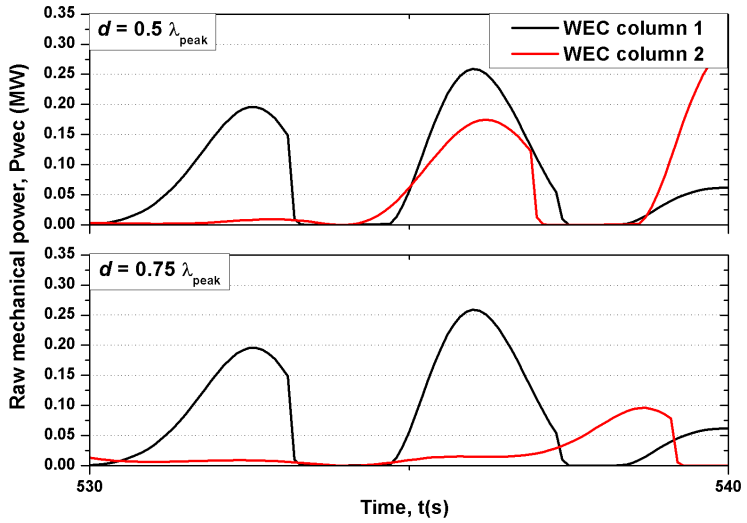

Figure 4.26: *The raw mechanical power extracted by two WECs in two neighbouring columns, occupying the same row in the array, when the spacing d = 0.5λ_{peak} and 0.75λ_{peak}.*

Spacing d	**Variance in the cumulative Pwec (MW)**^{2}	**Variance in the net Pfarm (MW**^{2}**)**
$0.25\lambda_{peak}$	0.0658	4.4032×10^4
$0.50\lambda_{peak}$	0.3103	2.8825×10^4
$0.75\lambda_{peak}$	0.2006	1.9094×10^4
$1.00\lambda_{peak}$	0.2365	1.1364×10^4
$1.25\lambda_{peak}$	0.1890	1.2953×10^4

Table 4.14: *Variance in the cumulative Pwec and the net Pfarm, for different spacings, of the 6 WM wave power farm modelled in a stationary sea with $H_s = 4$ m and $T_z = 6$ s*

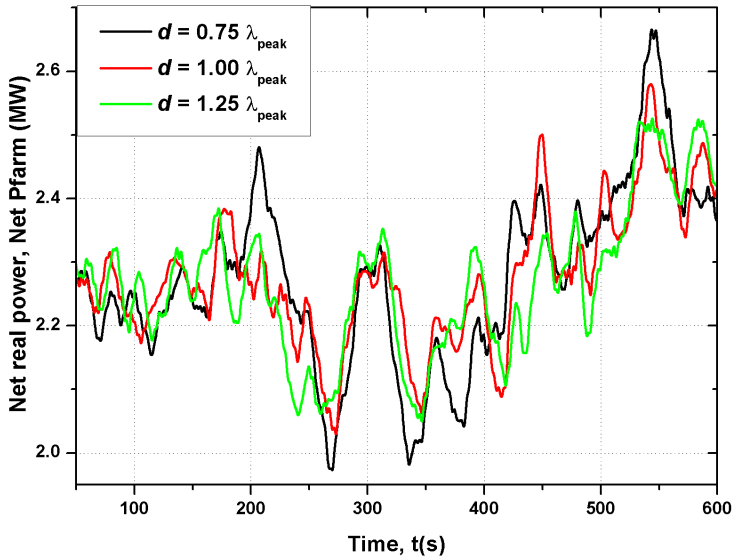

Figure 4.27: *The net real power generated by the 6 MW wave power farm for different column spacings greater than $0.5\lambda_{peak}$.*

variances in the cumulative Pwec for the $0.75\lambda_{peak}$, the $1.0\lambda_{peak}$ and the $1.25\lambda_{peak}$ cases shows that at spacings which are odd-numbered multiples of $0.25\lambda_{peak}$ the cumulative Pwec is relatively smoother when compared to the case when the spacing is a multiple of $0.5\lambda_{peak}$. But the difference in the cumulative Pwec and hence the net Pfarm smoothness that the two spacings provide reduces as the spacing increases beyond $0.5\lambda_{peak}$. Figure 4.27 shows the net Pfarm generated by the array for these three spacings, which confirm these findings. The smoothness in the net Pfarm improves with an increase in the spacing from $0.75\lambda_{peak}$ to $1.0\lambda_{peak}$. No significant reduction in the smoothing is observed when the spacing is increased from $1.0\lambda_{peak}$ to $1.25\lambda_{peak}$.

4.10 Case study - 6 MW wave power farm off the Western Isles, Scotland, UK

In this section, the results and the inferences drawn from described in the previous sections are applied in the prospective development of a real wave power farm off the north western Scottish coast. For this purpose, two years worth of data of the wave climate found off the north west coast of Scotland have been used. The data have been obtained from the Wavenet database [20].

The effects of changing the orientation of the line of six WECs with respect to the dominant wave direction were discussed earlier. It was seen that orienting the line of WECs at 90° to the dominant wave direction, such that all the WECs are in phase, produced the smoothest net real power output from the array. In the simulation runs in this section, directional spreading has been considered, but the dominant direction of the generated waves has been kept at 0°. This is keeping in view the directional features of the sea found at most sites off northern and western Scotland. Figure 4.28 shows the percentage distribution of the dominant wave direction found over the two-year period at the site being considered. For approximately 60% of the time, the dominant direction lies between 250° and 300°. Since the spreading function used has a significant spreading of up to 30° on either side of the dominant wave direction, 275° has been chosen as the dominant wave direction; i.e. the array of WECs is placed oriented with the 275° angle. Also, as more columns of WECs are added in the array, the effects that the dominant wave direction has on power smoothing reduce. This is examined is Section 4.12 of this chapter.

Figure 4.29 shows the percentage of time for which the different H_s,T_z combinations occurred at the site being considered. It is seen that for approximately 52% of the time the average zero-crossing time period T_z lies between 5 and 7 seconds. This in effect means that the wavelength corresponding to the peak frequency component in the sea is within a limited range. This wavelength is a good starting point for selecting the spacing between columns of WECs in the array.

Three different wavelengths have been considered in this section representing the three most commonly occurring time periods. They are: (a) the average wavelength of the blue cell in Figure 4.29 - 60 m (b) the average wavelength of the green cells in Figure 4.29- 115 m (c) the average wavelength of the yellow cells in Figure 4.29 - 184 m. First, the 6 MW wave power farm has been simulated with these three column spacings (the three wavelengths divided by two) with the seas most commonly found at the site being considered. After examining the

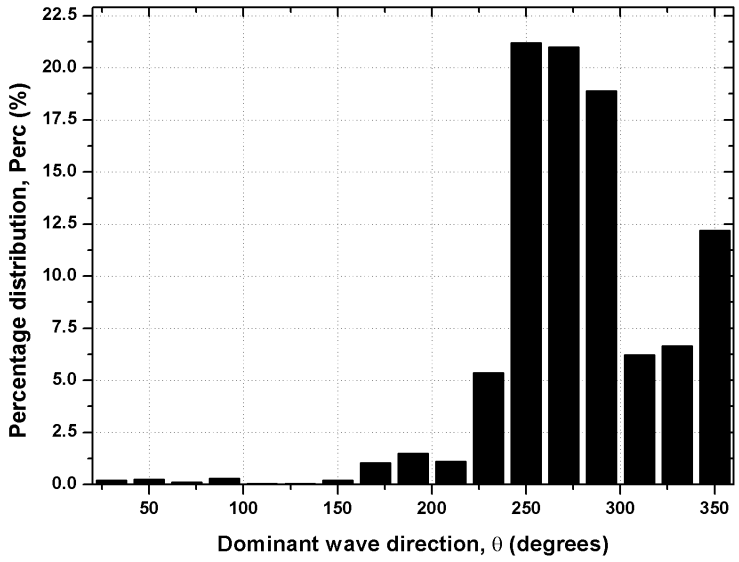

Figure 4.28: *Percentage distribution of the dominant wave direction at the site being considered.*

effects of using these spacings, the farm placed in other more energetic and rarely occurring sea states has been simulated and the effects of the chosen spacings on power smoothing have been investigated.

Sea states with H_s between 0.75-1.5 m (1 m chosen here) and T_z between 3-5 s (4 s chosen here) are weakly energetic and under these sea states the wave power farm generates approximately 100 kW on average. Since fluctuations in the power produced under such weakly energetic seas will not adversely affect the voltage quality in the electricity network, results obtained from the simulation of the array under these sea states are not discussed.

Figure 4.30 shows the net real power generated by the wave power farm when placed in a sea state with H_s between 1.5-3.0 m (2 m chosen here) and T_z between 5-7 s (6 s chosen here). For this sea state, with an average peak wavelength of approximately 112 m, the three spacings are approximately close to $0.25\lambda_{peak}$, $0.5\lambda_{peak}$ and slightly more than $0.75\lambda_{peak}$. As seen earlier, when the spacing is close to $0.25\lambda_{peak}$, wide fluctuations in the net real power generated are seen. The net Pfarm time-series is smoother in the d = 57.7 m case and relatively the smoothest when d = 92 m.

Figure 4.31 shows the net real power generated by the wave power farm when placed in a sea state with H_s between 3-5 m (4 m chosen here) and T_z between 7-9 s (8 s chosen here). For

Hs range (m)	0-0.75	0.75-1.5	1.5-3.0	3.0-5.0	5.0-7.0	7.0+
Tz range (s)						
0-3.0	0.00	0.00	0.00	0.00	0.00	0.00
3.0-5.0	0.95	8.36	3.66	0.00	0.00	0.00
5.0-7.0	0.38	9.87	33.00	9.59	0.00	0.00
7.0-9.0	0.00	1.19	9.85	13.00	2.97	0.04
9.0-11.0	0.00	0.04	0.97	2.01	2.38	1.36
11.0+	0.00	0.00	0.00	0.04	0.23	0.07

Figure 4.29: *Percentage distribution of the sea states found at the Outer Hebrides site over two years.*

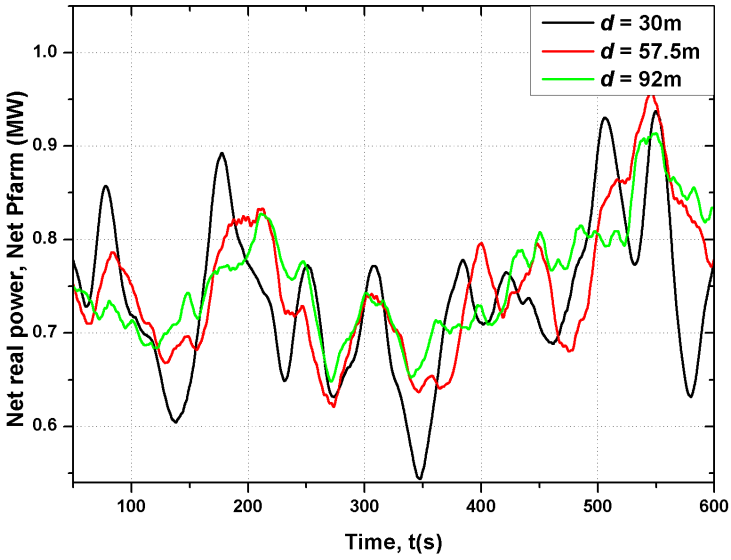

Figure 4.30: *The net real power generated by the 6 MW wave power farm for different column spacings, when placed in a sea state with H_s between 1.5-3.0 m and T_z between 5-7 s.*

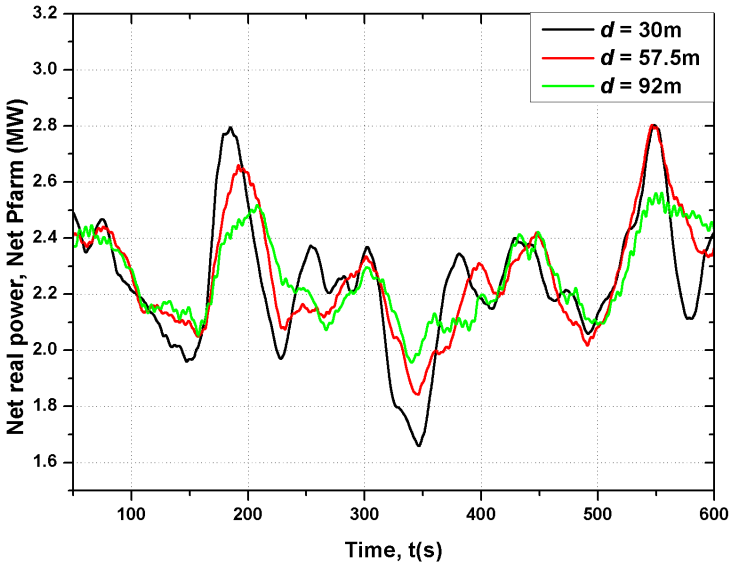

Figure 4.31: *The net real power generated by the 6 MW wave power farm for different column spacings, when placed in a sea state with H_s between 3-5 m and T_z between 7-9 s.*

this sea state, with an average peak wavelength of approximately 197 m, the three spacings are approximately close to $0.15\lambda_{peak}$, $0.3\lambda_{peak}$ and slightly more than $0.5\lambda_{peak}$. The smoothing in the real power generated is seen to improve as the spacing increases from 30 m to 92 m. These results corroborate the findings discussed earlier where it was found that for spacings less than or equal to $0.5\lambda_{peak}$, the smoothest real power would be obtained at $0.5\lambda_{peak}$.

Figure 4.32 shows the variance in the net Pfarm and the cumulative Pwec for different column spacing up to $4.0\lambda_{peak}$, when the farm is modelled in a sea state with $H_s = 4$ m and $T_z = 6$ s. As seen earlier, the net Pfarm is significantly smoother when the spacing is $0.5\lambda_{peak}$ than when it is $0.25\lambda_{peak}$. Till the spacing of $2.0\lambda_{peak}$, the same effects are seen. For example when the spacing is $1.25\lambda_{peak}$ the variance in the net Pfarm is more than when the spacing is $1.5\lambda_{peak}$. The difference is insignificant though, when compared to the variance change between say d = $0.75\lambda_{peak}$ and d = $1\lambda_{peak}$. Beyond d = $1.5\lambda_{peak}$ no such smoothing in the net Pfarm can be attributed clearly to changes in the spacing.

For the most commonly occurring sea states at the site, it was found that the spacing between the columns of WECs can be approximately 92 m for a relatively smooth net real power output. Now, for the sake of completeness, the wave power farm with spacing d = 57.5 m, 92 m and 150 m has been simulated under very highly energetic sea states from the grey cells in Figure 4.29. The figure shows that these sea states occur for less that 5% of the time at the site being consid-

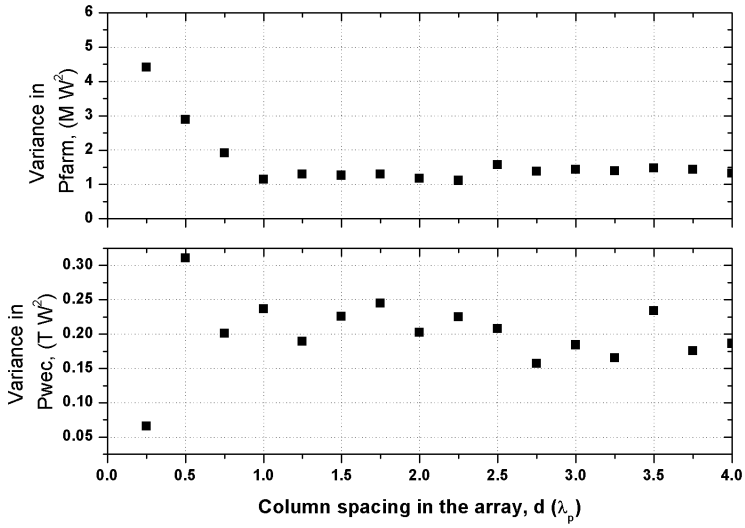

Figure 4.32: *The variance in the net Pfarm and the cumulative Pwec for the 6 MW wave power farm with different spacings up to 4.0λ_{peak}.*

ered. These runs have been performed to check the smoothing in the net real power generated by the wave power farm when the spacing between columns of WECs is increased further. For the sea state with $H_s = 6$ m and $T_z = 8$ s, the peak wavelength is 197.1 m and therefore the three spacings become approximately 0.3λ_{peak}, 0.46λ_{peak} and 0.76λ_{peak} respectively. For the sea state with $H_s = 8$ m and $T_z = 10$ s, the peak wavelength is 309.7 m and the three spacings become approximately 0.18λ_{peak}, 0.29λ_{peak} and 0.48λ_{peak} respectively.

Figure 4.33 shows the net real power generated by the 6 MW wave power farm for the three spacings when simulated in the sea state with $H_s = 6$ m and $T_z = 8$ s. As seen with the other seas tested earlier in the chapter, the smoothing in the net real power increases with an increase in the spacing. The smoothing in the net Pfarm increases with an increase in spacing from 0.3λ_{peak} (approx. 0.25λ_{peak}) to 0.46λ_{peak}(approx. 0.5λ_{peak}) and 0.76λ_{peak}(approx. 0.75λ_{peak}). Figure 4.34 shows that the net real power generated is the smoothest when the spacing between the columns of WECs in the array is close to 0.5λ_{peak}, even for sea state with $H_s = 8$ m and $T_z = 10$ s. This finding matches the results discussed earlier through which it was confirmed that for spacings less than 0.5λ_{peak}, the smoothest real power generated will be obtained when the spacing is 0.5λ_{peak}. Table 4.15 shows the values of the variance in the cumulative Pwec and the net Pfarm for these high energy sea simulation runs.

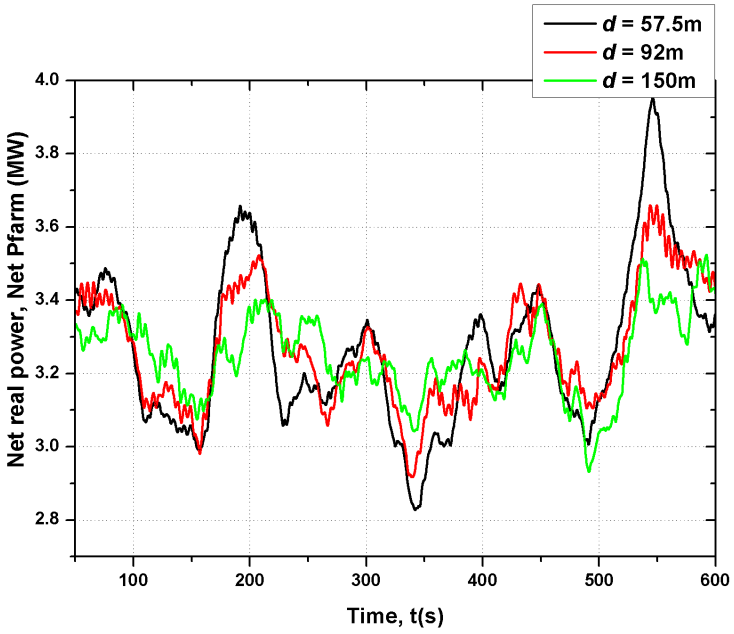

Figure 4.33: *The net real power generated by the 6 MW wave power farm for different column spacings, when placed in a sea state with $H_s = 6$ m and $T_z = 8$ s.*

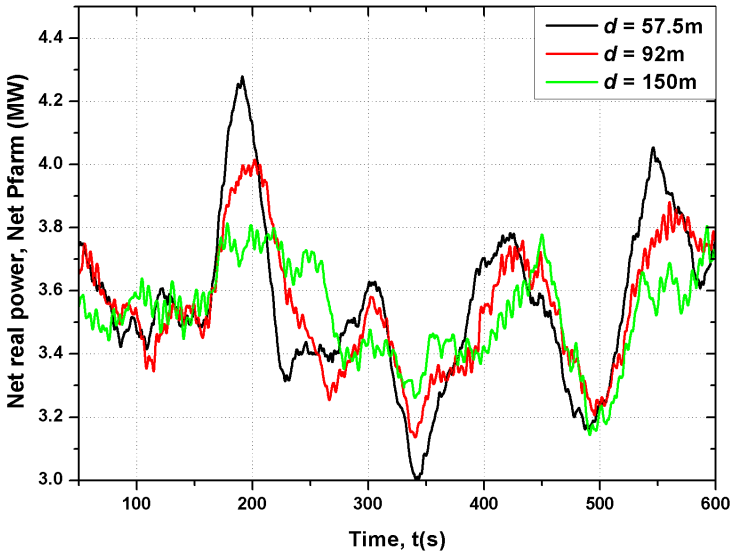

Figure 4.34: *The net real power generated by the 6 MW wave power farm for different column spacings, when placed in a sea state with $H_s = 8$ m and $T_z = 10$ s.*

Sea state	**Spacing d (m)**	**Variance in the cumulative Pwec (MW)^2**	**Variance in the net Pfarm (MW^2)**
$H_s = 6$ m and $T_z = 8$ s	57.5	0.6648	4.8227×10^4
$H_s = 6$ m and $T_z = 8$ s	92	1.2549	2.5372×10^4
$H_s = 6$ m and $T_z = 8$ s	150	0.7238	1.2787×10^4
$H_s = 6$ m and $T_z = 10$ s	57.5	0.4295	5.2455×10^4
$H_s = 6$ m and $T_z = 10$ s	92	0.9038	3.2506×10^4
$H_s = 6$ m and $T_z = 10$ s	150	0.6995	1.7986×10^4
$H_s = 8$ m and $T_z = 10$ s	57.5	1.0507	6.4751×10^4
$H_s = 8$ m and $T_z = 10$ s	92	1.9986	3.9748×10^4
$H_s = 8$ m and $T_z = 10$ s	150	1.5023	2.2302×10^4

Table 4.15: *Variance in the cumulative Pwec and the net Pfarm for different spacings for the 6 WM wave power farm modelled in different stationary sea states*

4.11 Effects of end-stops on power smoothing

In this section, the effects of having end-stops in the WEC on the power smoothing capability of arrays are discussed. This has been mainly done to explain some of the discrepancies in the variance in the cumulative Pwec, seen especially with the highly energetic sea states discussed in the previous section.

Figure 4.35 shows the cumulative raw mechanical power extracted by the 6 MW farm when simulated in a sea state with $H_s = 4$ m and $T_z = 6$ s. The time-series for the cases with and without end-stops for $0.25\lambda_{peak}$ and $0.5\lambda_{peak}$ spacings are shown. When no end-stops are used, it is seen that the cumulative Pwec is smoother when the spacing is $0.25\lambda_{peak}$ than when the spacing is $0.5\lambda_{peak}$. When end-stops are used, the cumulative Pwec time-series for the $0.25\lambda_{peak}$ case is still smoother than the $0.5\lambda_{peak}$ case. The smoothing seen is lower though, than the case without end-stops. This is because of the limit placed on the WEC's displacement by the presence of the end-stops. The limit on the WEC's displacement in turn limits the velocity of the WEC and also the power extracted.

The same effect is seen even when the farm is simulated in the highly energetic sea state with $H_s = 6$ m and $T_z = 8$ s. A significant improvement in the cumulative Pwec smoothness is seen when there are no end-stops used. With end-stops, no visible smoothness in the cumulative Pwec time-series is seen when the spacing is changed from $0.5\lambda_{peak}$ to $0.25\lambda_{peak}$. This feature reflects in some of the values of the variance listed in Table 4.15. The values of the variance in the net Pfarm in the table match the inferences drawn from this work. There are discrepancies

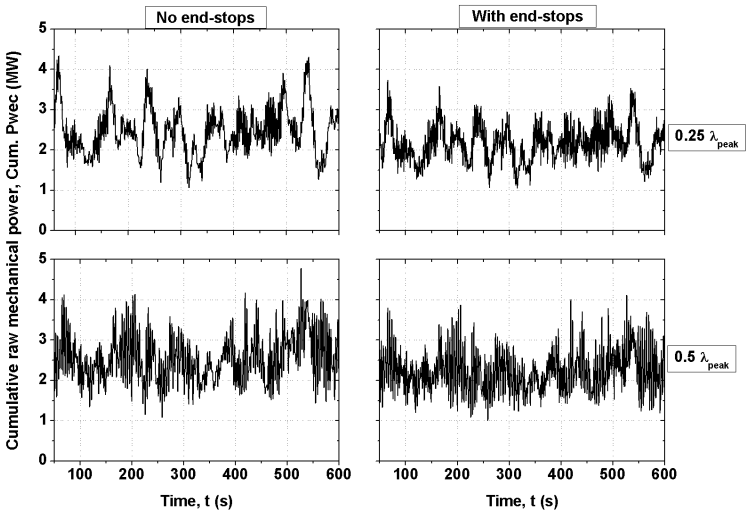

Figure 4.35: *The cumulative raw mechanical power extracted by the 6 MW wave power farm for the case with and without end-stops, in a sea state with $H_s = 4$ m and $T_z = 6$ s.*

in the values of the variance in the cumulative Pwec, which can be attributed to the use of end-stops.

4.12 Effects of the array orientation on power smoothing

In this section, the effects of changes in the dominant wave direction on the power smoothing obtained by appropriate spacing are discussed. Three different spacings - $0.25\lambda_{peak}$, $0.50\lambda_{peak}$ and $0.75\lambda_{peak}$ along the original 0° dominant wave direction have been tested. The orientation of the array with respect to the dominant wave direction is shown in Figure 4.37. The statistical work on the dominant wave direction, discussed in Section 4.10, showed that the direction remains around 275° with respect to the geographical north for approximately 60% of the time. Therefore, all the simulations performed had the array oriented at 90° to the dominant wave direction. In this section, the dominant wave direction is changed by 30° and its effects on the power smoothing obtained by appropriately spacing WECs or columns of WECs in the array are examined. The results obtained and discussed earlier showed that even when the dominant wave direction lies between $275° \pm 30°$ (between 245° - 305°), significant smoothing in the net Pfarm time-series is seen when the WECs are spaced appropriately. In this section, the analysis is extended to include the inferences drawn from the work with the 48-WEC array performed in this chapter. For this, the wave power farm has been simulated in a sea state with $H_s = 4$ m and $T_z = 6$ for two different dominant wave directions. The results obtained from this study

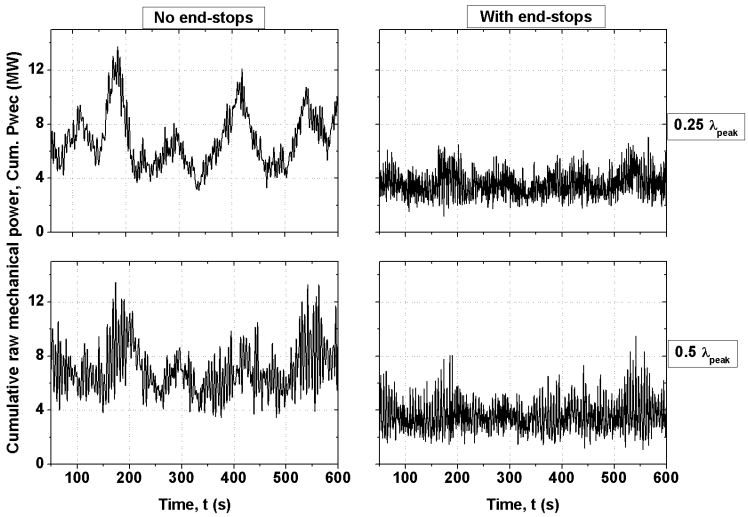

Figure 4.36: *The cumulative raw mechanical power extracted by the 6 MW wave power farm for the case with and without end-stops, in a sea state with $H_s = 6$ m and $T_z = 8$ s.*

though, will hold good even for higher and lower energy sea states.

Figures 4.38 and 4.39 and Table 4.16 show the results obtained from these simulation runs. When the spacing is $0.25\lambda_{peak}$ the cumulative Pwec extracted is the smoothest. This is confirmed in the values of the variance in the cumulative Pwec listed in Table 4.16. As discussed in Section 4.11, some of the smoothness in the cumulative Pwec is not visible because of the presence of end-stops. When considering the net Pfarm, the smoothness increases as d increases from $0.25\lambda_{peak}$ to $1.0\lambda_{peak}$. This is as expected and was described in the other sets of simulations performed.

A comparison of the values of the variance in the net Pfarm, seen when the dominant wave direction is 0° and 30°, shows a smoother net Pfarm for the 30° angle case. This can be explained through Figure 4.40. When the dominant wave direction changes from 0°, the effective spacing between the columns of WECs becomes d', which is larger than d. It was shown earlier that the smoothness in the net Pfarm increases as the spacing between the columns of WECs increases. The effective spacing between the columns of WECs increases further as the dominant wave direction increases to 60°. Therefore, a further improvement in the smoothness of the net Pfarm will be observed.

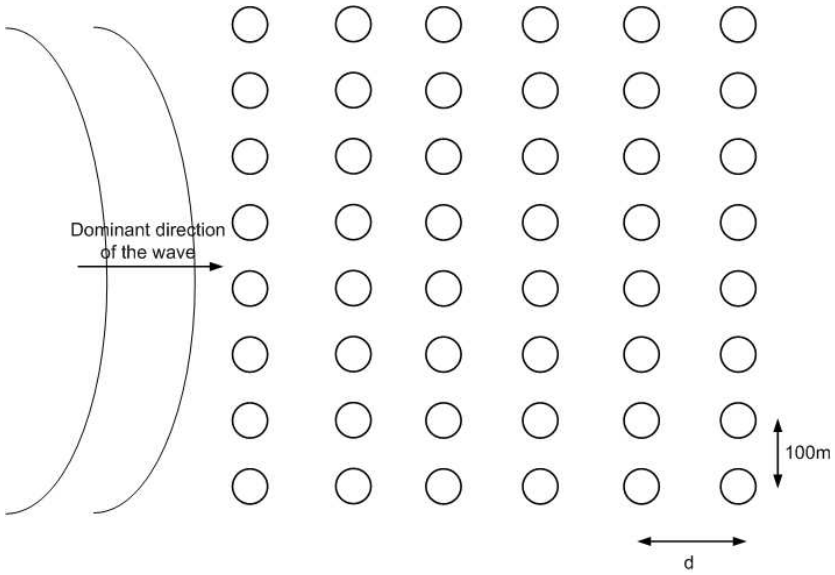

Figure 4.37: *The array orientation with the dominant wave direction.*

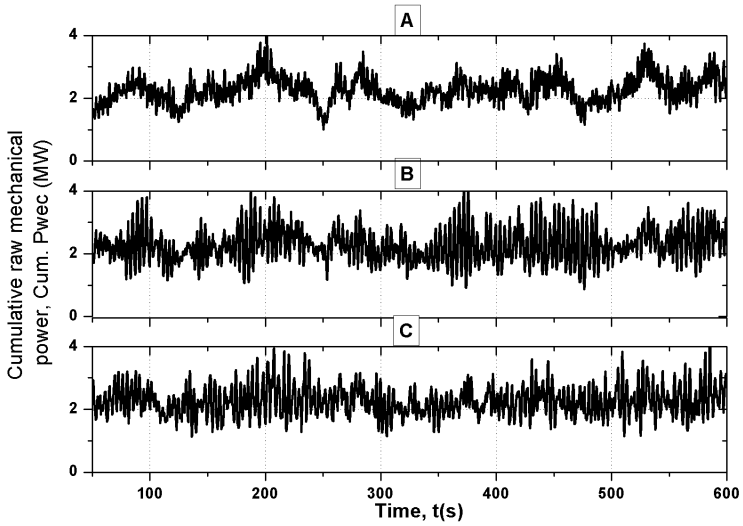

Figure 4.38: *Cumulative raw mechanical power extracted for d = (a) 0.25λ_{peak} (b) 0.50λ_{peak} and (c) 0.75λ_{peak}, when the 6 MW wave power farm is placed at 30° to the dominant wave direction.*

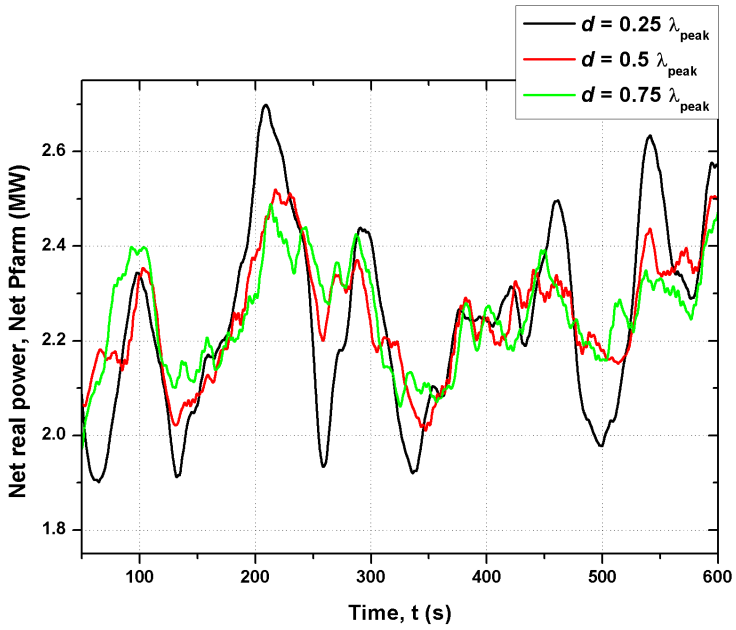

Figure 4.39: *Net real power generated for d = (a) 0.25λ_{peak} (b) 0.50λ_{peak} and (c) 0.75λ_{peak}, when the 6 MW wave power farm is placed at 30° to the dominant wave direction.*

Spacing d	**Variance in the cumulative Pwec (MW)**^{2}	**Variance in the cumulative Pwec (MW)**^{2}	**Variance in the net Pfarm (MW**^{2}**)**	**Variance in the net Pfarm (MW**^{2}**)**
	30°	0°	30°	0°
0.25λ_{peak}	0.0629	0.0658	3.9453×10^4	4.4032×10^4
0.5λ_{peak}	0.3010	0.3103	1.4969×10^4	2.8825×10^4
0.75λ_{peak}	0.2105	0.2006	1.1279×10^4	1.9094×10^4

Table 4.16: *Variance in the cumulative Pwec and the net Pfarm for different array spacings and two different dominant wave directions*

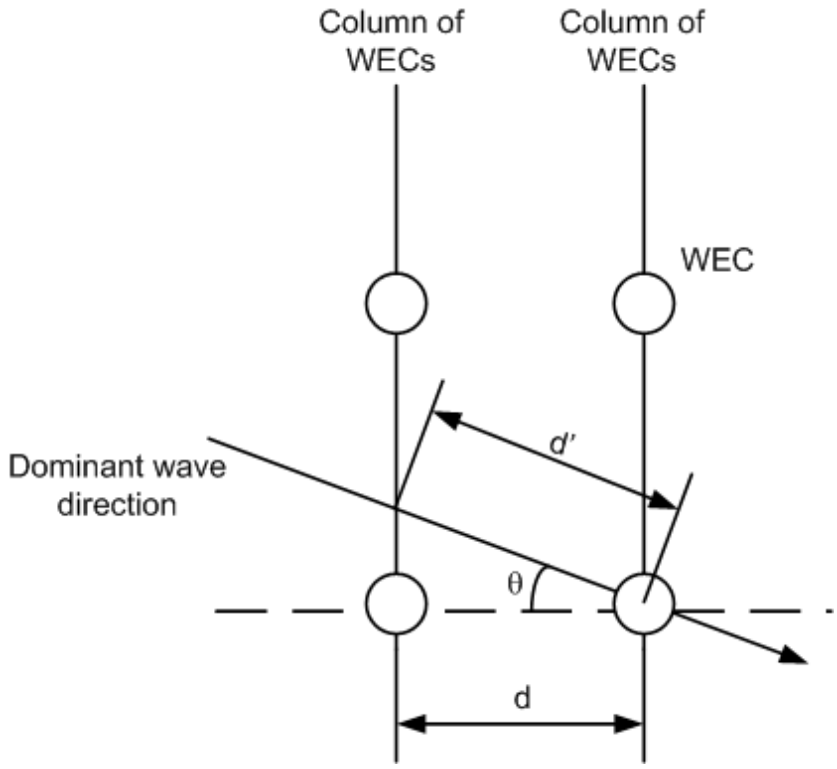

Figure 4.40: *The effects of changing orientation on column spacing.*

4.13 Summary

This chapter first looked at the smoothing in the cumulative Pwec and the net Pfarm that can be obtained by spacing WECs appropriately within a line of WECs. It was seen that when the WECs are spaced $0.5\lambda_{peak}$ apart, the net real power generated by the wave power farm is the smoothest, even though the cumulative raw mechanical power in this case is less smooth when compared to the $0.25\lambda_{peak}$ spacing case. An inverse relationship between the smoothing in the cumulative Pwec and the smoothing in the net Pfarm was seen. When investigating the best orientation of the simple line of WECs for the smoothest net real power output, it was found that placing the WECs in coherence, i.e. the line of WECs perpendicular to the dominant wave direction, produced the smoothest net real power output. Again, the cumulative Pwec was the least smooth in this case.

Having accumulators provided some amount of smoothing to the net real power output from an array. Most of the high frequency fluctuations in the power generated was removed. It was further shown that even with a 300% increase in the accumulator size (from 0.5 m^3 to 2 m^3) significant variations in the net real power generated were still present. Moreover, long term on-board storage is bulky and expensive. Therefore a trade-off has to be made between the amount

of storage to be included and the cost and space requirements of having large accumulators.

Next, the effects of increasing the farm size on the smoothness in the net real power produced were examined. It was seen that as the size of the farm increased, the absolute variance in the net Pfarm increased. This shows that the net Pfarm fluctuations cannot be removed by merely increasing the number of devices in the farm. The spacing between the WECs in the array and the orientation of the array with respect to the dominant wave direction also have roles to play. In the 6 MW wave power farm simulated, placing the columns of WECs $0.5\lambda_{peak}$ apart produced a smoother net Pfarm than when the spacing was $0.25\lambda_{peak}$. The cumulative Pwec time-series of two WECs in the same row and adjacent columns plotted in the chapter clearly showed the coherence in the raw mechanical power extracted when the spacing between the columns of WECs was $0.5\lambda_{peak}$. The smoothness in the net Pfarm time-series can be attributed to this.

In the case where the WECs are placed in a unidirectional and a purely sinusoidal sea, the effects of spacing the WECs $0.25\lambda_{peak}$ and $0.5\lambda_{peak}$ apart would exist for all odd-numbered multiples of $0.25\lambda_{peak}$ and $0.5\lambda_{peak}$. In the case of realistic mixed seas though, the smoothness in the cumulative Pwec at $0.25\lambda_{peak}$ and its odd multiples existed, but was the most prominent only up to the $0.5\lambda_{peak}$ spacing case. Beyond $1.5\lambda_{peak}$, no such visible advantage was seen when the columns of WECs were appropriately spaced. The coherence/non-coherence between the Pwec extracted by two WECs in adjacent columns and in the same row was seen to reduce as the spacing increased beyond $0.5\lambda_{peak}$. In general, larger spacings greater than $0.5\lambda_{peak}$ produced a smoother net Pfarm time-series. The multiples of $0.25\lambda_{peak}$, $0.5\lambda_{peak}$ spacing effect was significant only when spacings smaller than $0.5\lambda_{peak}$ were considered.

Next, the effects of using end-stops on the WECs on the smoothness in the net real power produced were analysed. The smoothness in the cumulative Pwec when the columns of WECs were spaced $0.25\lambda_{peak}$ apart was better when no end-stops were considered. When a physical limit on the cumulative Pwec output was made, the smoothing in the cumulative Pwec became less obvious. This was more so the case when the wave elevation was high and when the end-stops played a more important role. Having end-stops improved the smoothness in the net Pfarm with an expected reduction seen in the average real power fed to the network.

Statistical analysis of the dominant wave direction at the site off the north west Scottish isles showed that the dominant wave direction remained fairly within a $\pm 30^{\circ}$ range for approxi-

mately 60% of the time. Since an increase or decrease in the dominant wave direction from the 0° direction in effect increases the distance between two columns of WECs in the array, the smoothness in the net Pfarm improved when the dominant wave direction changed from the most commonly occurring one. Even when the dominant wave direction changed, the improvement in smoothing seen between the $0.25\lambda_{peak}$ and the $0.5\lambda_{peak}$ spacings was still seen.

From the results discussed in this chapter, it becomes evident that there is some role for appropriate spacing and orientation for smoothing the net real power generated by a wave power farm. Using on-board storage in the form of accumulators also helps smooth the net real power output. Even after spacing and orienting the WECs appropriately and using accumulators, the net real power generated from the farm has variations, which in turn causes the network voltage to vary. To smooth the network voltage it is envisaged that reactive power control in real-time will be used and the next chapter deals with the use of reactive power control to improve voltage quality.

Chapter 5
Voltage control in wave power farms

5.1 Introduction

In the UK, the best wave resources are largely found offshore from remote, rural areas where the electrical demand is low [12]. The electricity network in these areas had been arranged to supply power generated at the central generating stations to the demand in these areas. Hence, the electricity networks in these areas are of low capacity. Most of the distribution networks in rural areas taper radially, with lower X/R ratios as one reaches the outer edges of the network. This characteristic of rural distribution networks makes them weak, such that even a small variation in the power generated by any connected generator will have a significant effect on the supply quality in these areas. The varying and unpredictable nature of the ocean waves further adds to the challenge of integrating large wave power farms to these networks. Therefore, there is a need for a careful study of the impacts of integrating wave power farms in particular and distributed generators (DG) in general with weak, rural networks.

Chapter 4 showed that some smoothing in the net real power fed to the network by these wave power farms can be obtained by appropriately spacing the WECs and orienting the wave power farm. Having some storage, in the form of hydraulic accumulators, also removed some of the high frequency variations in the power produced. Further improvement in the voltage profile can be achieved using dynamic processes that take place in real-time during the operation of the wave power farm. This chapter explores the network impacts and their mitigation by further smoothing using excitation control of the connected generators.

5.2 The need for control

According to the Electricity, Safety, Quality and Continuity Regulations 2002 [122], with respect to voltage magnitudes, the nominal voltage of a load bus should be maintained within $\pm 6\%$ under all power flow conditions in an 11 kV network. The substation tap changing transformer, which supplies the radial network, is often adjusted so that the voltage at the substation is set at 1.03 p.u. This is done to compensate for the voltage drop across the radial network

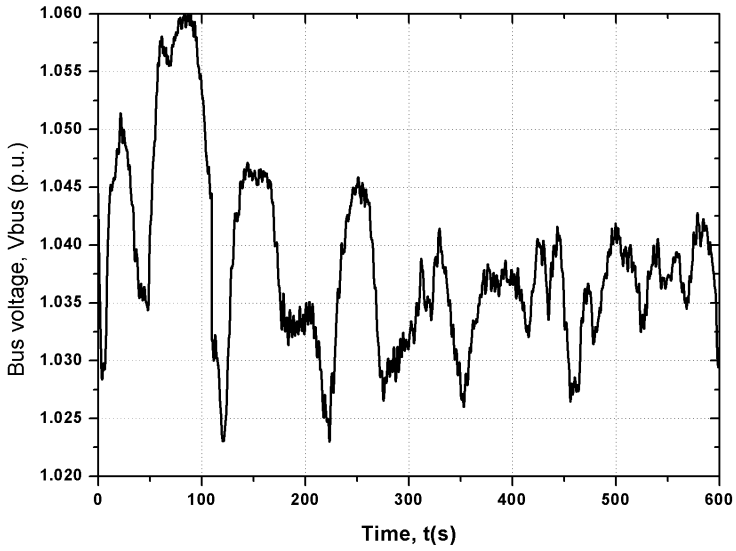

Figure 5.1: *Voltage variation at the bus where a wave power farm is connected.*

especially during periods of high demands so that the load bus voltage magnitude requirements are met.

Once the wave power farm is connected to the radial network, the excess power after the local load is supplied is fed back to the sub-transmission network. This reversal of power flow can cause voltage variations in the network which may go beyond the statutory limits. Figure 5.1 shows a sample variation of the rms-voltage magnitude at the bus where a wave power farm is connected. The voltage reaches 1.06 p.u. during certain instants in this 600-second period. The network interface protection would operate to trip the wave power farm and clear over-voltages above 1.055 p.u. that lasts longer that 500 ms. The voltage variation shown in the figure would therefore cause the wave power farm to be tripped off the network. This represents as a loss of revenue for the wave power farm developers who aim to have the farm connected to the network for as long as possible. Means must therefore be tested to keep the voltage within the permissible range.

5.3 Power flow and voltages in a two-bus system

Consider the simple two-bus network shown in Figure 5.2. Bus 1 is the infinite bus where the voltage magnitude and angle is kept fixed. Bus 2 is the load bus, in this case, with the distributed generator and the load. The real and reactive power exchanged by the load bus with the network P_B, Q_B is the difference between P_G, Q_G and P_L, Q_L. R and X represent the

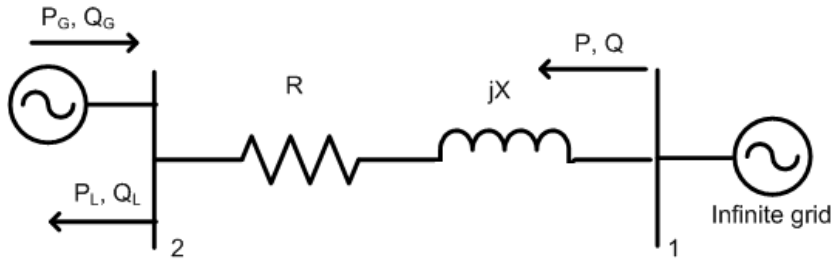

Figure 5.2: *Power flow in a simple two-bus system.*

resistance and the inductive reactance of the line.

The voltage rise or drop on the line is:

$$V_1 - \mathbf{V_2} = \frac{RP + XQ}{V_1} + j\frac{XP - RQ}{V_1}. \tag{5.1}$$

It is seen that the voltage rise or drop has a real and an imaginary component. The real part of the voltage rise/drop is $\Delta V = \frac{RP+XQ}{V_1}$, while the imaginary part of the voltage rise/drop is $\delta V = \frac{XP-RQ}{V_1}$. In distribution networks, where R is predominant when compared to X, the imaginary part of the voltage rise/drop δV is insignificant and can be neglected. The voltage rise/drop thus becomes $\Delta V = \frac{RP}{V_1} + \frac{XQ}{V_1}$. Because of the low X/R ratios in weak distribution networks, the voltage rise is dominated by the first term. This is an important consideration to be made when developing distributed generation schemes, because even a small rise in the generated power can produce large voltage changes when the $\frac{RP}{V_1}$ term dominates.

5.4 Voltage control options

Voltage control can be organised into three levels considering distinct geographical areas and time constants [132, 133]. At the primary control level, control of the electrical parameters of the network is performed locally with the aim of rapid (in a few seconds) compensation of random voltage variations. Only local information is used to decide the control signals. Regional information and hourly load changes spread over hours are used in the secondary control level. The time constant in secondary control is in the range of a few minutes. Communication channels are required to maintain the voltage in the regional network within limits. Tertiary control involves the use of system-wide information and has a time constant between tens of minutes to a few hours. It involves coordinating the different generators and the control devices connected to the network, so that they are able to maintain the voltage within limits and are able to tackle voltage variations produced by generation or demand changes or emergencies. In this chapter, local voltage control in rural distribution networks with distributed generation is discussed.

Different local voltage control strategies have been adopted, some of which are [134]:

- Control of HV/MV substation secondary voltage
- Automatic voltage control of the generator
- Inverter based control of reactive power output from the generator
- Continuous voltage/VAr control using VAr compensators (eg. STATCOM)
- Curtailment of real power generation

The first four control methods enlisted have been discussed elaborately in the literature. Their applicability for the control of wave power farms has been explored in this chapter. The conventional operation of the wave power farm as voltage following and voltage supporting machines have been tested and their drawbacks are discussed. Certain more intelligent control methods, which involve reactive power exchange between the wave power farm and the network, have also been investigated. The voltage control methods for the wave power farm discussed in this chapter are: constant voltage controller, constant power factor controller, on-load tap changing (OLTC) transformer controller, Automatic Voltage and Power Factor Controller (AVPFC) and Fuzzy Logic Power Factor Controller (FLPFC). Curtailing the active power generation [135] is a valid control option, since the aim of this study is to find means to maintain the voltage within the statutory limits. A hierarchical control scheme has been followed here, wherein real power curtailment is used only after the available reactive power capability has been exhausted [136].

In this chapter, only short time storage in the capacitors that form a part of the power electronic interface and in the hydraulic accumulators was considered. This is mainly because commercial and economical forms of long-term local electrical energy storage (e.g. supercapacitors and fuel cells) are still rudimentary [137]. The amount of energy storage required for different WECs was dealt with in detail in [138]. A very basic energy storage modelling in [139] showed the improvement in the voltage profile brought about by storage. Advances have also been made in the field of voltage control through the control of loads [140]. Demand side management through load control is envisaged to play a significant role in the distribution networks of the future [141].

These five control techniques have been first tested on a simple nine-bus system with parameters selected to represent rural networks. Figure 5.3 shows the radial distribution network to which

the wave power farm is connected. A 1 MW wave power farm has been considered with 8 WECs each rated at 125 kW. The WECs are capable of operating between 0.95 leading and 0.95 lagging power factors. The 11 kV network is connected to the edge of the 33 kV sub-transmission network (bus 1) through a system impedance of 1.2029 + 2.6435 p.u. (on a 100 MVA base). This is representative of networks in Stornoway/Harris where significant wave energy developments will be seen in the near future. The total demand connected to the 33 kV bus is 2 MW at unity power factor. The demand is divided between buses 4, 6 and 7 in the network. These buses have a maximum demand of 0.4, 1 and 0.6 MW respectively and these demands pre-date the connection of the wave power farm. The loads have been considered to be constant at 25% of the maximum demand for the simulated 600-second period. Over such time periods, the variations in the power generated from the wave power farm occurring over tens of seconds show a bigger influence on the network voltage profile when compared to demand variations which occur over tens of minutes. For longer simulations (e.g. over 24 hours), a load profile, which best describes the demand of the settlement, may be used. A simple inter-array electrical layout has been used here where each WEC is connected to an offhore hub (bus 9), where the voltage is stepped up to 11 kV. The impedance of the submarine cables connecting the individual devices to the hub has been neglected here. A 1 km long submarine power cable (2XS(FL)2YRAA 6/10 (12) kV Nexans submarine power cable [142]) carries the power from the hub to the shore. Table 5.1 gives details of the network and the equipments used. The impedance of the transformers and the overhead lines have been taken from [143] and [144] respectively.

A sea state formed by the concatenation of three different seas - (a) less energetic ($H_s = 1.27$ m, $T_z = 4.66$ s) (b) moderately energetic ($H_s = 5.82$ m, $T_z = 8.74$ s) (c) highly energetic ($H_s = 7.16$ m, $T_z = 9.82$ s), has been used for testing the applicability of these control methods on this simple network. Figure 5.4 shows the variation of H_s, T_z and $H_s^2 T_z$, which is a measure of the energy content in the sea over the 1800-second period. It must be noted that the figure does not show the wave elevation time-series. Though such a sea state may not be realistic, the concatenated sea is a good test for the robustness of the control methods. All the simulations have been run for 1800 seconds and the three sea states last for 600 seconds each. At t = 600 s the sea changes from the highly energetic state to the less energetic state and at t = 1200 s the sea changes from the less energetic state to the moderately energetic state. It is assumed that this 600-second period is short enough to keep the H_s and T_z values constant. After testing the control methods for this simple network, they have been tested on a more realistic 11 kV UK

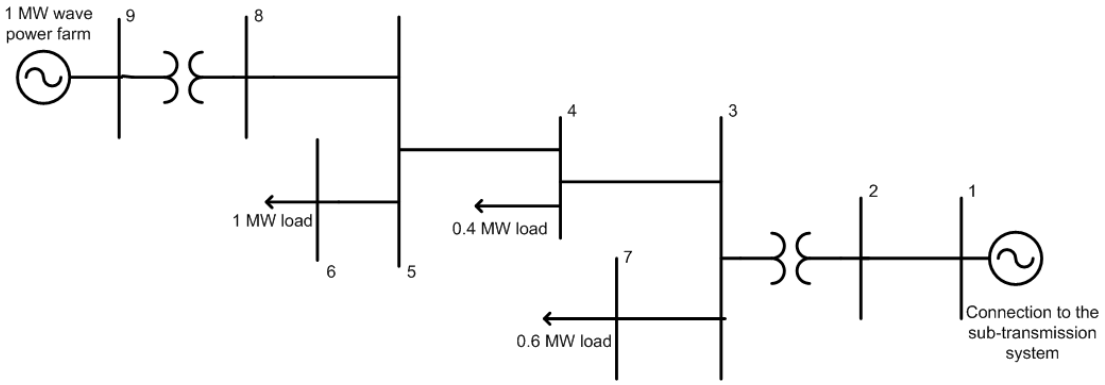

Figure 5.3: *Radial network model of a hypothetical rural distribution feeder with the wave power farm and the distributed loads.*

From bus	To bus	Equipment	R (p.u.)	X (p.u.)	B (p.u.)
1	2	System impedance	1.2029	2.6435	0.0
2	3	4 MVA, 33:11 kV OLTC transformer with 7.5% impedance	0.25	1.875	0.0
3	4	2 km of ACSR 34/6 bare conductor for overhead line	1.402	0.70	0.0
4	5	3 km of ACSR 34/6 bare conductor for overhead line	2.102	1.051	0.0
5	6	0.5 km of ACSR 34/6 bare conductor for overhead line	0.35	0.175	0.0
3	7	4 km of ACSR 34/6 bare conductor for overhead line	2.803	1.402	0.0
5	8	1 km long submarine power cable	0.49	0.1288	9.88e-5
8	9	1.5 MVA, 11:0.690 kV transformer with 5% impedance	0.6667	3.333	0.0

Table 5.1: *Network data (100 MVA base)*

distribution system with the wave power farm modelled under more realistic sea conditions.

5.4.1 Constant power factor control

Conventionally, generators connected to the distribution network have been operated at a constant power factor (normally at Unity Power Factor). This is a viable option for reliable and dispatchable distributed generators (DGs), but may cause problems when the primary energy source is variable, as in the case of wave power farms. In this section, the effects of the constant power factor operation of a wave power farm are analysed.

Figure 5.5 shows the voltage at the bus where the wave power farm is connected over the 1800-second period with the wave power farm operating at different power factors. From the

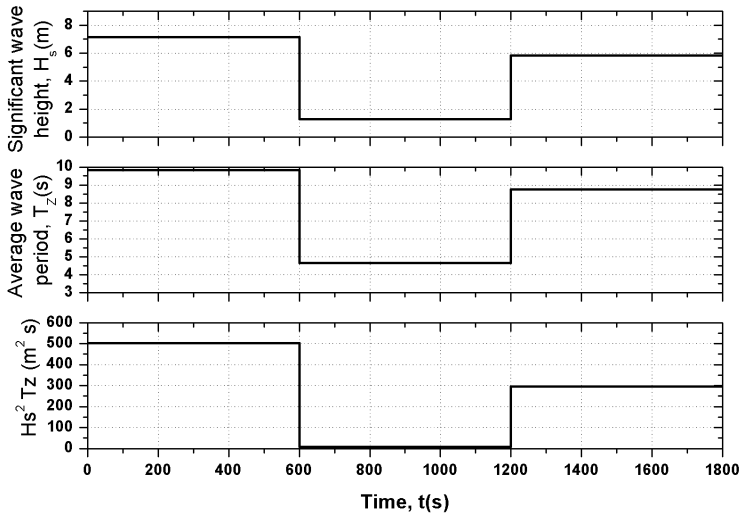

Figure 5.4: *Variation of H_s, T_z and $H_s^2T_z$ over the 1800-second simulation period.*

figure and as confirmed in practice with land based DG, the extent and the duration of the over-voltages are reduced by operating close to or below unity power factor. Figure 2.22 shows the block diagram of the power factor controller of the individual generators in the wave power farm.

The real and reactive power losses generally increase when the wave power farm absorbs reactive power (operating under leading power factor). This in turn means that the real power carrying capability of the network reduces. The increase in the losses will be significant in the case of a larger network and a larger wave power farm. Variations in the local demand can also make the use of the constant power factor operation untenable, which is exemplified through some of the simulations discussed in Section 5.5.

5.4.2 Constant voltage control

Prior to the connection of DG to the electricity networks, power was generated at central power stations mainly by synchronous machines. The machines' excitations were controlled by their automatic voltage regulators which ensured power generation at a constant voltage. The advantages of having large generators connected to the transmission network operating as voltage supporting machines and those of a smaller size in the distribution network operating as voltage following machines were enumerated in [145]. Similar conclusions were drawn in [146], where it was said that large synchronous machines in the power stations, operating at a constant voltage, ensured better voltage stability in the network. Both these publications dealt with the

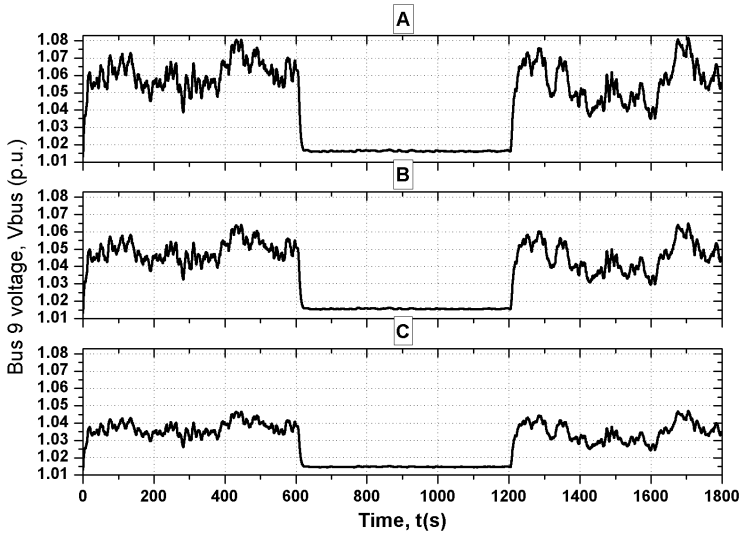

Figure 5.5: *Bus 9 voltage for different DFIG excitations (a) 0.98 lagging power factor (b) unity power factor (c) 0.98 leading power factor.*

synchronous generators at central generating stations. With distributed generators the scenario is different since they are generally smaller in size when compared to the generators in the central power stations. Operating these small generators as voltage supporting machines may cause them to be overloaded when the bus voltage changes from one extreme to the other due to system bus voltage fluctuations or demand variations. The Distribution Network Operators (DNOs) have not traditionally allowed the DGs to generate power at a constant voltage mainly due to this reason. In this section, the effects of operating the wave power farm at a constant voltage are analysed.

The 1 MW wave power farm, in Figure 5.3, has been operated such that a constant voltage, irrespective of the real power production, is maintained at bus 9. This has been performed by controlling the reactive power exchanged between the farm and the network. Figure 2.22 shows the block diagram of the automatic voltage regulator used with each generator in the model of the wave power farm.

Figure 5.6 shows the results obtained when operating the wave power farm with the voltage reference at 1.05 p.u. The power factor plotted is the operating power factor of the farm. It is observed that during the period when the sea is weakly energetic (600 s - 1200 s), the operating power factor of the wave power farm is very low, which is beyond the limits allowed by network operators. Operating the DFIGs at such low power factors also puts excessive stresses on the

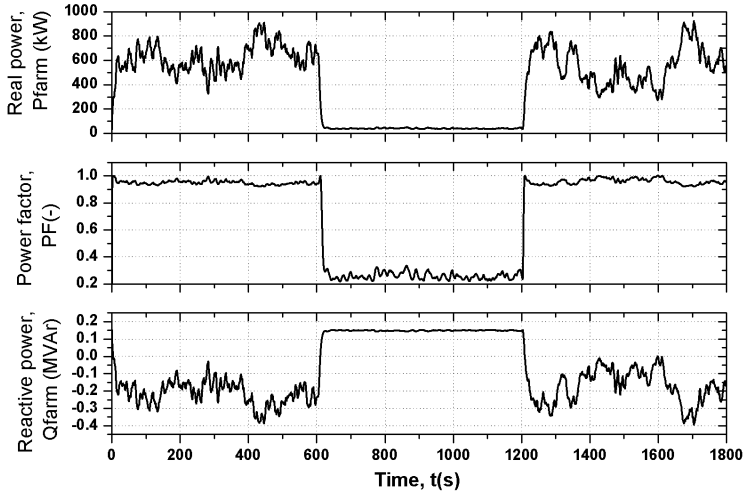

Figure 5.6: *Operation of the wave power farm in the constant voltage mode.*

machines.

When DGs operate at a constant voltage, conflicts may also arise between the controller on the DG and the substation transformer's auto-tap-changer settings. Such a scenario in which the transformer tap position changes until it reaches its extreme position is shown in Figure 5.7. Since the two controllers have not been coordinated, unnecessary tap operations are seen in the transformer. At every successive tap change, the wave power farm generates more reactive power to maintain the bus voltage constant. The need to coordinate the control of the transformer's on-load tap changer and the control of the wave power farm is thus evident and is dealt with in Chapter 6.

5.4.3 Control using the substation OLTC transformer

On-load tap changing (OLTC) transformers have been used at substations to maintain the voltage downstream of the substation above statutory limits, especially during periods when the demand is high. For effective control, these transformers have been used for voltage control accompanied by line drop compensators or reverse reactance compounding compensators [147]. The operation of such schemes in radial feeders with distributed generation was described in [148]. The optimal control of these transformers is challenging, especially when they feed parallel feeders and when the DG, connected to the network downstream, exchanges reactive power with the network. The control of the bus 9 voltage using an OLTC transformer at the substation operating in the automatic voltage control mode is discussed in this section. The

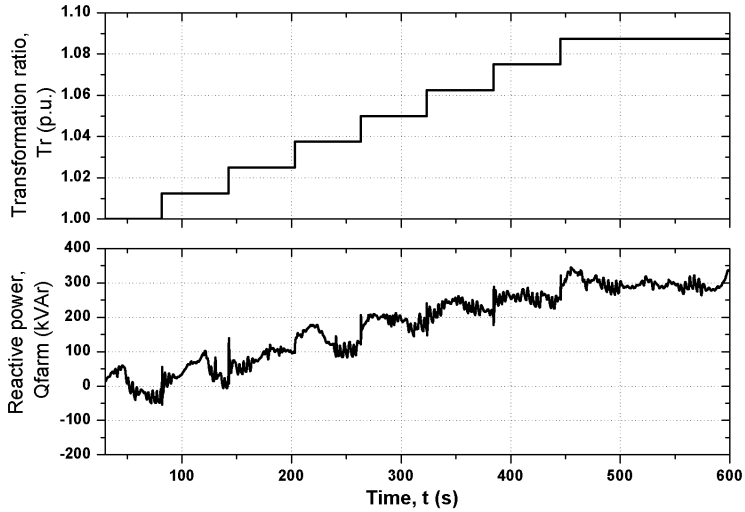

Figure 5.7: *Interactions between the constant voltage controller of the wave power farm and the substation OLTC transformer.*

Parameter	Value
V_h	1.04 p.u.
V_l	1.02 p.u.
V_{step}	0.0125 p.u.
t_d	60 s
Tap_{max}	7
Tap_{min}	-7

Table 5.2: *OLTC transformer settings*

main aim of this section is to demonstrate the inability of the OLTC transformer to operate as fast as the variations in the power generated by wave power farms. It has been assumed here that the OLTC transformer has direct access to the voltage at bus 9, which in reality would need some voltage estimation technique or communication means, which is further discussed in Chapter 6.

The conventional control of an OLTC transformer in the voltage regulation mode, described in [149, 150], has been used to model the transformer. Table 5.2 lists the OLTC settings used. The voltage deadband of the OLTC transformer has been set between V_h and V_l. To prevent unnecessary tap changes due to transient voltage variations, a time delay t_d of 60 seconds has been used. This ensures that a tap change occurs only when the voltage remains outside the voltage deadband for t_d seconds. Tap_{max} and Tap_{min} are the two extreme tap positions. The algorithm based on which the OLTC transformer operates is explained in the flowchart shown in Figure 5.8.

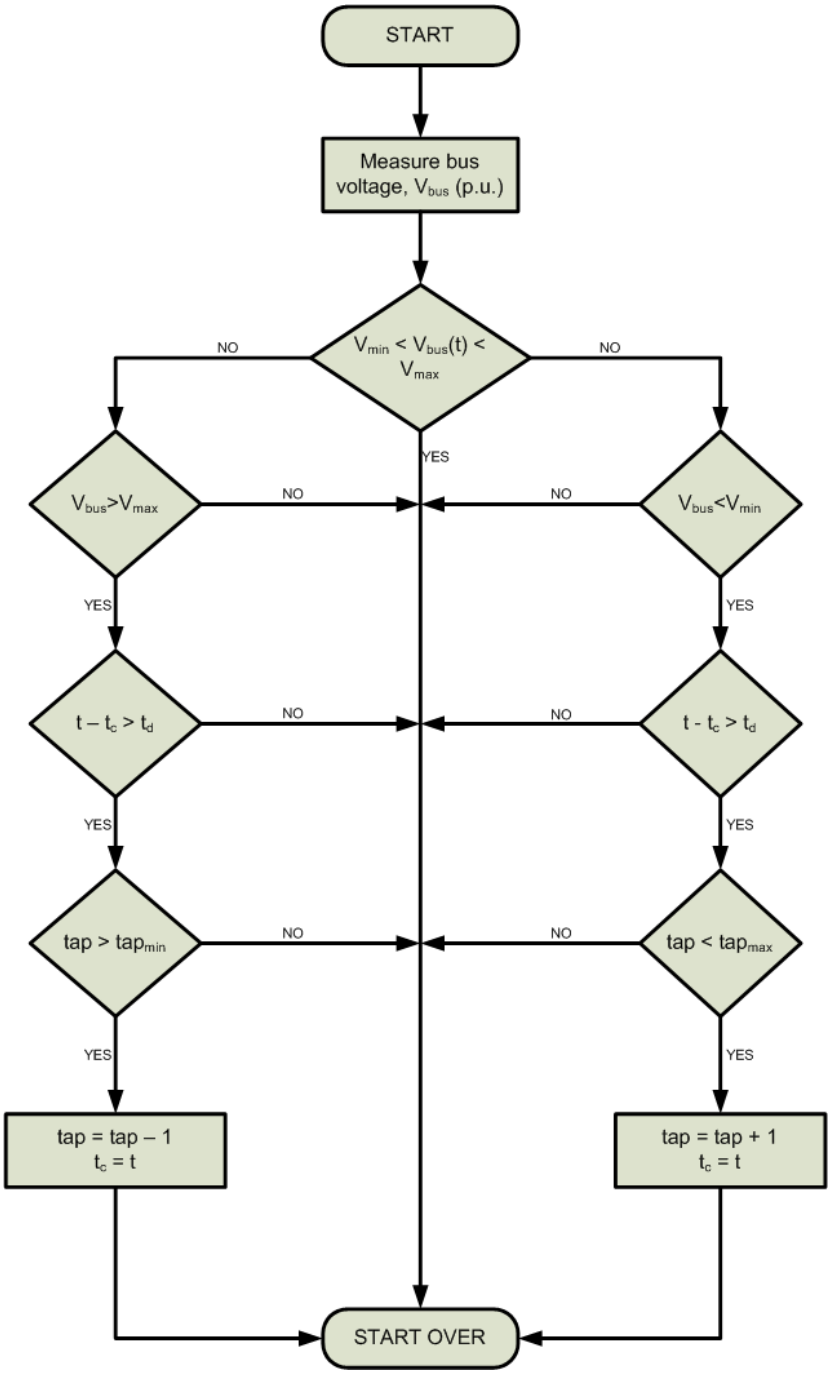

Figure 5.8: *Flowchart of the operation of an On-Load Tap Changing transformer controller.*

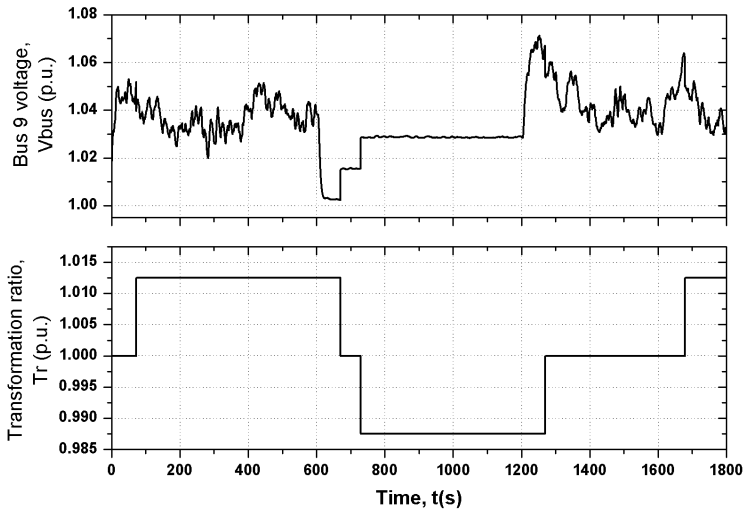

Figure 5.9: *Voltage control using the substation OLTC transformer.*

Figure 5.9 shows the changes in the tap position over the 1800-second simulation period. Since the tap is on the high voltage side of the transformer, an increase in the transformation ratio of the transformer reduces the bus 9 voltage. It is seen that the substation OLTC transformer maintains the bus 9 voltage within the statutory limits during the simulation run, except between time t = 1200 s and t = 1300 s. The wave power farm would have been tripped off the network due to this voltage violation. The presence of the time delay in the control algorithm makes the transformer operation slow when compared to the variations in the power generated by the wave power farm. From the figure it becomes evident that only coarse voltage control in certain steps is possible using OLTCs at these transformers.

Significant work has been accomplished in developing advanced controllers based on artificial neural networks and fuzzy logic for OLTC transformers [151, 152]. Even with these advanced controllers the inherent incapability of the OLTC transformers to deal with fast variations in the network voltage remains a disadvantage. OLTC transformers still have a role to play for slow, secondary voltage control. Effort will need to be made to coordinate the operation of the substation transformer and the DG downstream for optimal network operation [153, 154]. Commercial products to control OLTC transformers (SuperTAPP and GenAVC), which acknowledge the presence of the downstream DG, have been developed [155–157]. Both these products use communication means and state estimation techniques to decide the optimal tap position. Such developments and an improved voltage estimation technique that does not require any communication means are discussed in Chapter 6. Coordination between the OLTC

transformers at the secondary and the tertiary control levels have been described in [158, 159], which is not explored further in this work.

5.4.4 Automatic Voltage and Power Factor Control

Switching the DG from the voltage supporting mode to the voltage following mode and vice versa was suggested to overcome the drawbacks of the power factor and the voltage control modes [145, 147]. The Automatic Voltage and Power Factor Control (AVPFC) was developed as a hybrid of these two modes [160]. The developed controller has been concept-tested on models of hydro power plants and wind farms [161, 162]. The proposed control method was seen to augment the amount of DG that could be connected to networks [163]. Experimental and simulation based studies on the applicability of the AVPFC controller (though not called so) with synchronous generators and DFIGs prove the practical viability of the hybrid controller [164, 165]. Its applicability with wave power farms and the improvement in the supply voltage quality obtained by using the controller have been studied and the results obtained are discussed in this section.

In the AVPFC method, the wave power farm may be allowed to operate either in the constant power factor mode or in the constant voltage mode depending on the current sea conditions. Figure 5.10 shows the algorithm used in deciding whether the wave power farm operates in the voltage control or the power factor control mode at any instant of time. Measurements of the bus 9 voltage V and the operating power factor of the wave power farm PF, which can be obtained from real and reactive power measurements, are required to select the operating mode. In the flowchart, V_l and V_h represent the lower and the upper voltage limits of the controller and PF_{ref} is the reference power factor, which is the operating power factor of the wave power farm when operating in the constant power factor mode. V_d and PF_d are respectively the voltage and the power factor deadbands. Table 5.3 details the AVPFC mode selection rules, which can be understood from the voltage vector diagram of a two-bus system shown in Figure 5.11. From these, it is understood that when the voltage and the power factor are within limits, the wave power farm operates in the constant power factor mode. When a voltage violation occurs, the wave power farm operates in the constant voltage mode with either V_l or V_h as the reference, as the case might be. A time delay t_d has been included in the controller to prevent hunting between the two control modes.

Table 5.4 lists the AVPFC voltage and power factor set points used for the simulation in this

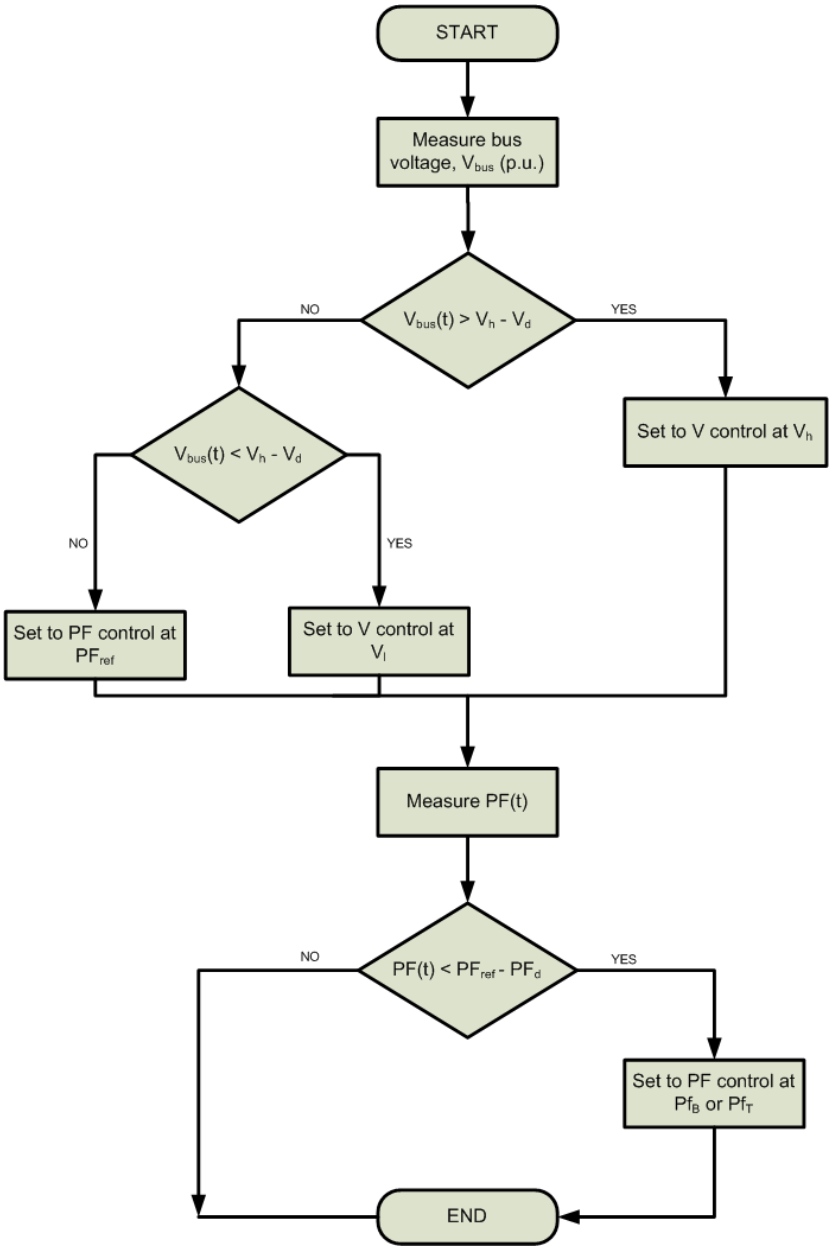

Figure 5.10: *Flowchart of the operation of an Automatic Voltage and Power Factor controller.*

	$V \leq V_l$	$V_l < V < V_h$	$V_h \leq V$
$PF \leq PF_B$	V_l	PF_{ref}	PF_{ref}
$PF_B < PF < PF_T$	V_l	PF_{ref}	V_h
$PF_T \leq PF$	PF_{ref}	PF_{ref}	V_h

Table 5.3: *AVPFC mode selection rule set*

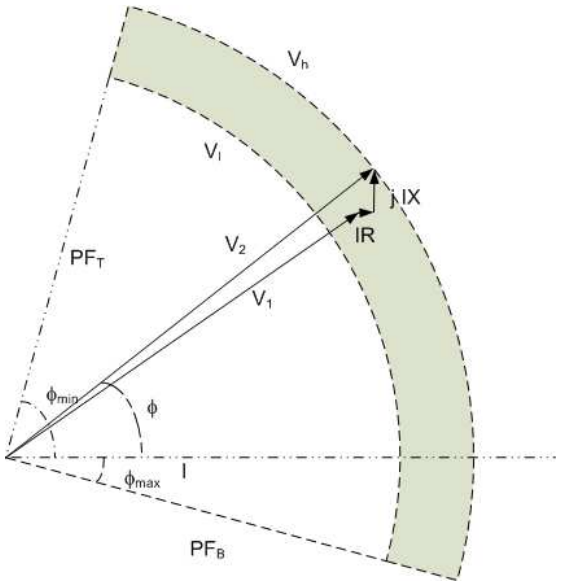

Figure 5.11: *Voltage vector diagram of a two-bus system.*

Parameter	Value
V_l	0.97 p.u.
V_h	1.05 p.u.
V_d	0.0025 p.u.
PF_B	0.9975 (lag)
PF_T	0.9975 (lead)
PF_{ref}	UPF

Table 5.4: *AVPFC parameters*

section. A time delay t_d of 10 seconds was chosen keeping in mind the average time period of the waves. Figure 5.12 shows the AVPFC control signal and the voltage and power factor measured at bus 9 when the wave power farm is controlled using this method. As seen in the figure, both the voltage and the power factor are within the statutory limits for the entire run. The AVPFC method ensures the connection of the wave power farm to the grid much longer than the other methods discussed earlier in the section. Thus, this hybrid controller has advantages over both the constant voltage and the constant power factor operation of the wave power farm.

The operation of this controller can be varied by changing the set points and the time delay of the controller. Some of the set points (e.g. the power factor set points) are selected after studying the network to which the wave power farm will be connected and the demand variations seen at the site, while the farm operators have discretion in selecting certain others (e.g. time delay). The selection of the different set points for a 4 MW wave power farm connected to a realistic network is discussed in Section 5.5.

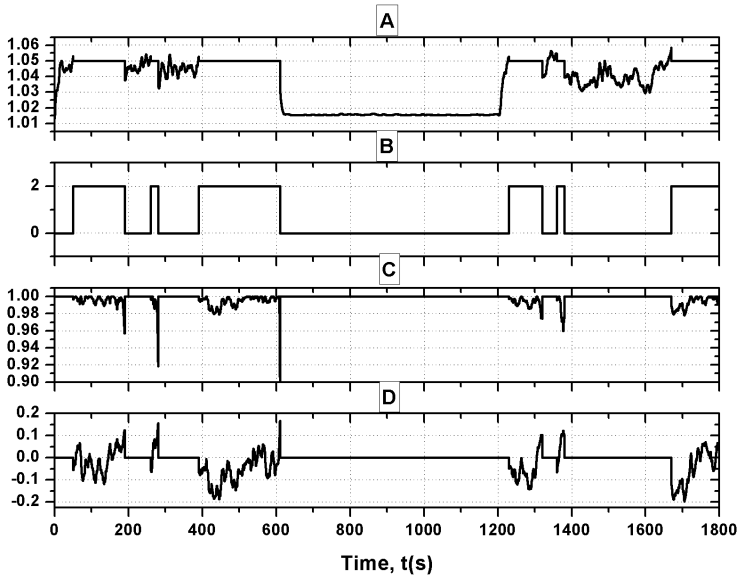

Figure 5.12: *Operation of the wave power farm, connected to the nine-bus system, with the AVPFC controller. (a) Bus 9 voltage (p.u.) (b) voltage / power factor control signal (2 - voltage control, 0 - power factor control), (c) power factor (-) (d) reactive power generated (MVAr).*

5.4.5 Fuzzy Logic Power Factor Control

Many fuzzy logic based applications for power systems are found in the literature [166]. In wind energy conversion, fuzzy logic controllers have been extensively researched for controlling the PWM converters through which variable speed generators are connected to the electricity network. Some of the work in this area was to track the maximum power point during variable speed operation [167, 168]. Fuzzy logic based excitation controllers for synchronous generators are also found in the literature [169, 170]. In most of these papers the aim was to regulate voltage. The Fuzzy Logic Power Factor Controller presented in this section is similar to these, in that, the reactive power output from the DFIGs is controlled. Some of the recent publications on fuzzy logic applications in power systems dealt with system-wide voltage regulation and voltage/VAr control. In these works, optimisation of the use of OLTC transformers, SVCs, etc., in electricity networks was performed using fuzzy theory [171, 172]. A fuzzy logic controller for controlling the reactive power generated from wind generators was described in [160]. The fuzzy logic controller developed in this section builds upon the work discussed in [160] by making the developed controller less network-specific. This section describes the working of the Fuzzy Logic Power Factor Controller (FLPFC) developed to control the voltage

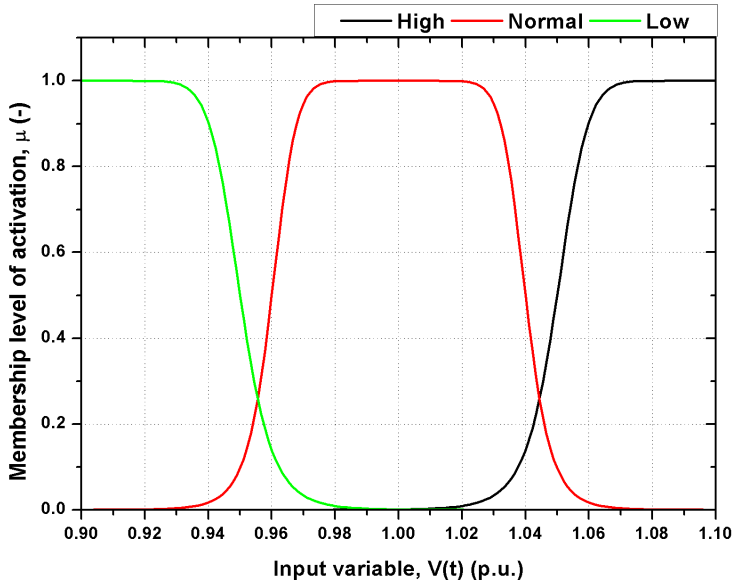

Figure 5.13: *Input membership functions for $V(t)$.*

at the bus where the wave power farm is connected. The controller is a hybrid between the constant power factor and the constant voltage controllers.

A Mamdani-type fuzzy logic controller [173], with the terminal voltage $V(t)$ and the difference between the terminal voltage and the voltage limit ΔV as inputs, has been developed. The increase in voltage from V_h = 1.03 p.u. or the decrease in voltage from V_l = 0.97 p.u., i.e. ΔV, with respect to V_h or V_l, is the second input to the controller. $V(t)$ varies over the range [0.9,1.1] p.u. while ΔV varies over the range [-0.02,0.02] p.u. Three linguistic variables define the terminal voltage $V(t)$: LOW, NORMAL and HIGH. Generalised bell shaped input membership functions have been used for $V(t)$ and are described by: $f(x;a,b,c) = \frac{1}{1+\left|\frac{x-c}{a}\right|^{2b}}$, where a, b and c are parameters, with parameter c denoting the centre of the curve. The input membership functions for the terminal voltage $V(t)$ used in this work are shown in Figure 5.13. The parameter vector $[a,b,c]$ for the three linguistic variables used were $[0.05,5,0.9]$,$[0.05,5,1]$ and $[0.05,5,1.1]$.

Nine linguistic variables define the change in voltage ΔV: HIGH NEGATIVE (HN), MEDIUM NEGATIVE (MN), LOW NEGATIVE (LN), VERY LOW NEGATIVE (VLN), NORMAL (N), VERY LOW POSITIVE (VLP), LOW POSITIVE (LP), MEDIUM POSITIVE (MP), HIGH POSITIVE (HP). Triangular input membership functions have been used for ΔV and are described by: $f(x;a,b,c) = max(min(\frac{x-a}{b-a}, \frac{c-x}{c-b}), 0)$, where a, b and c are parame-

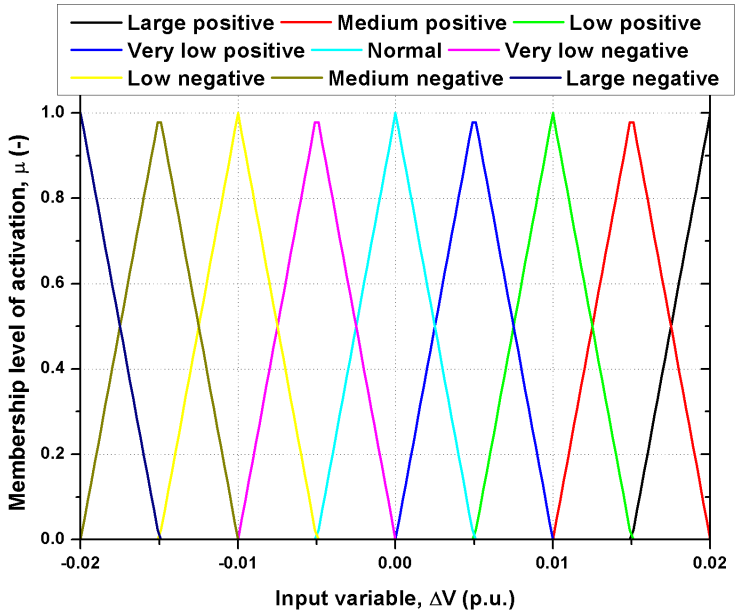

Figure 5.14: *Input membership functions for* ΔV.

ters. The parameters a and c locate the lower vertices of the triangle and the parameter b locates the peak. The input membership functions for ΔV are shown in Figure 5.14. The parameter vector $[a, b, c]$ for the nine linguistic variables used were $[-0.025, -0.02, -0.015]$, $[-0.02, -0.015, -0.01]$, $[-0.015, -0.01, -0.005]$, $[-0.01, -0.005, 3.469e{-}018]$, $[-0.005, 0, 0.005]$, $[-3.469e-018, 0.005, 0.01]$, $[0.005, 0.01, 0.015]$, $[0.01, 0.015, 0.02]$ and $[0.015, 0.02, 0.025]$. A large number of membership functions have been used to improve the sensitivity of the controller and to reduce the losses in the network by the unnecessary operation of the wave power farm at lower power factors than required.

For any $V(t)$ and ΔV, the output for the fuzzy controller is the change in the power factor ΔPF required to maintain the voltage within limits. The linguistic variables, the membership functions and the range of ΔPF are the same used with the input variable ΔV.

The fuzzy rule set used in this work consists of the following rules:

1. IF (ΔV IS HN) AND ($V(t)$ IS NOT NORMAL) THEN (ΔPF IS HN)
2. IF (ΔV IS MN) AND ($V(t)$ IS NOT NORMAL) THEN (ΔPF IS MN)
3. IF (ΔV IS LN) AND ($V(t)$ IS NOT NORMAL) THEN (ΔPF IS LN)
4. IF (ΔV IS VLN) AND ($V(t)$ IS NOT NORMAL) THEN (ΔPF IS VLN)

5. IF (ΔV IS N) AND ($V(t)$ IS NOT NORMAL) THEN (ΔPF IS N)
6. IF (ΔV IS VLP) AND ($V(t)$ IS NOT NORMAL) THEN (ΔPF IS VLP)
7. IF (ΔV IS LP) AND ($V(t)$ IS NOT NORMAL) THEN (ΔPF IS LP)
8. IF (ΔV IS MP) AND ($V(t)$ IS NOT NORMAL) THEN (ΔPF IS MP)
9. IF (ΔV IS HP) AND ($V(t)$ IS NOT NORMAL) THEN (ΔPF IS HP)

It becomes evident from the rules that a change in power factor is sought only when the terminal voltage is not NORMAL. The membership function for the linguistic variable NORMAL can be modified as per the allowed voltage range to be used. In the present case (see Figure 5.13), no change in the power factor is issued when the terminal voltage is between approximately 0.97 and 1.03 p.u. Only when the terminal voltage goes beyond the limits set by the membership function for the linguistic variable NORMAL, will the controller output ΔPF be non-zero. In later sections, the operation of the FLPFC with different allowed voltage ranges has been analysed and the set points used have been listed in the appropriate sections.

To explain how the fuzzy controller functions, an example is described now. Assume at an instant of time the terminal voltage goes to 1.05 p.u. Thus $V(t) = 1.05$ p.u. and $\Delta V = 0.02$ p.u. These are the inputs to the controller. For these inputs, only the last rule is relevant and is the only one examined here. The first step is to determine to what degree each input fits into one or more of the linguistic variables. This process is called fuzzification. Figure 5.15 shows how the controller operates when rule nine is relevant. The first sub-figure, associated with ΔV, shows that the membership level of activation for ΔV is HIGH POSITIVE is $\mu_1 = 1$. Similarly, the membership level of activation for $V(t)$ is HIGH is $\mu_2 = 0.5$, as seen in the second sub-figure. The membership function for the linguistic variable NORMAL is not shown in the second sub-figure because all the rules give an output only when $V(t)$ is NOT NORMAL. The figure also demonstrates the operation of the fuzzy operator that works with these two fuzzified inputs. In this work, the AND operator has been used, which has been implemented by the minimum (min) method [174]. The membership level of activation for the output ΔPF is HIGH POSITIVE is therefore $min(\mu_1, \mu_2) = 0.5$, which is shown in the third sub-figure.

In a fuzzy system, decisions are based on the outputs obtained from testing all the rules. These outputs must therefore be combined and this process is called aggregation. The maximum (max) method has been used to aggregate the outputs from all the rules. In the example being

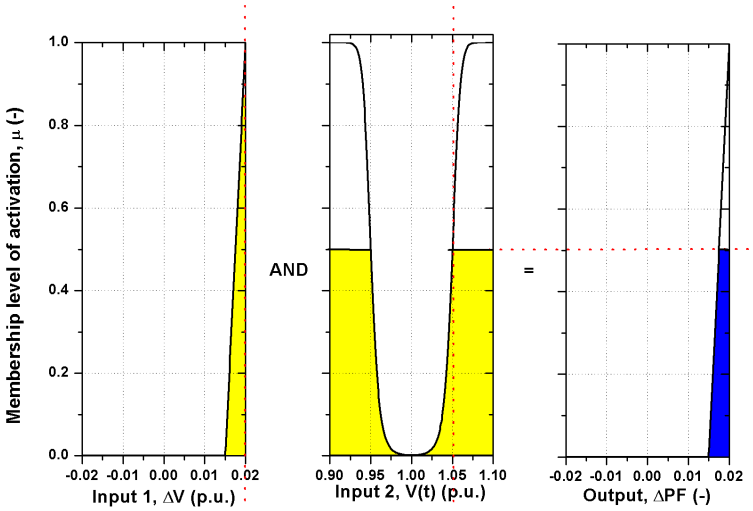

Figure 5.15: *The fuzzification process for rule 9.*

considered here, only the ninth rule gives an output. Otherwise, the outputs of all the rules would have had to be aggregated. The result of the aggregation is shown in Figure 5.16. The centroid of the resulting area is calculated (a process called defuzzification) and used as the output of the controller. The defuzzified result denotes the required change in power factor. The centroid of the area is represented in the figure by the vertical red line. The change in power factor $\Delta PF = 0.0182$ would have been issued by the controller for the inputs used in this example.

Figure 5.17 shows the fuzzy inference system output, which is the relationship between the change in voltage ΔV and terminal voltage $V(t)$, and the change in power factor ΔPF required to deal with the voltage change. Figure 5.18 shows the block diagram of the controller with the DFIG and its volt/VAr controller.

Figure 5.19 shows the voltage and the power factor measured at bus 9 when the wave power farm is controlled using the FLPFC method for $V_h = 1.05$ p.u. and $V_l = 0.96$ p.u. It is seen that the power factor setting changes every time the voltage goes beyond the upper voltage limit. A magnified version of the same figure is given in Figure 5.20 where only one second of the operation is shown. At time t = t_1, a small reduction in the operating power factor of the farm is issued by the controller since the terminal voltage is above 1.05 p.u. It is seen that the reduction in the power factor is not sufficient to keep the voltage below 1.05 p.u. and, due to this, at time t = t_2 a further reduction in the operating power factor is issued. The voltage is below 1.05 p.u. at the next time step. At times t = t_3 and t_4, further reductions in the operating power factor of

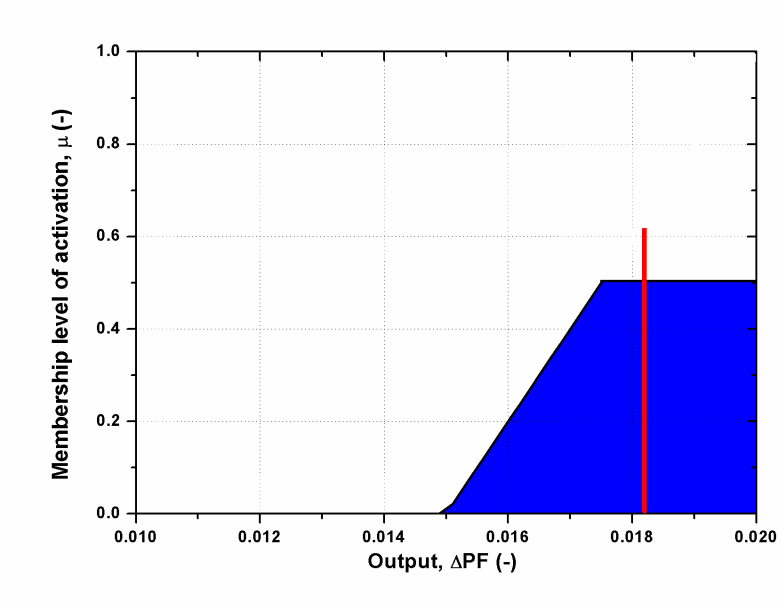

Figure 5.16: *The aggregation and the defuzzification process for rule 9.*

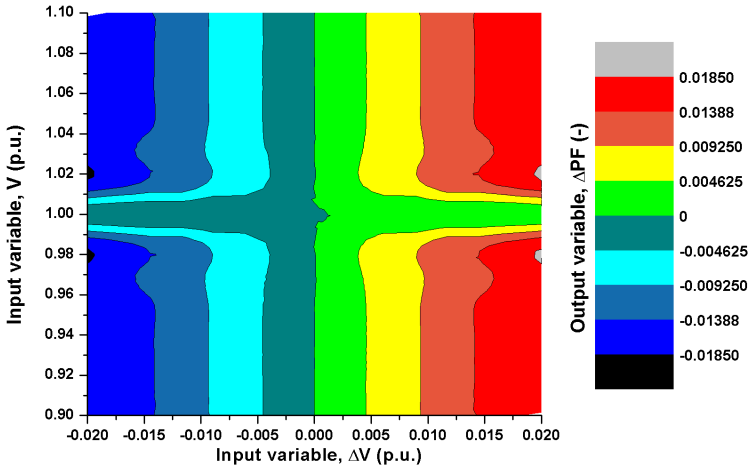

Figure 5.17: *Fuzzy inference system output surface.*

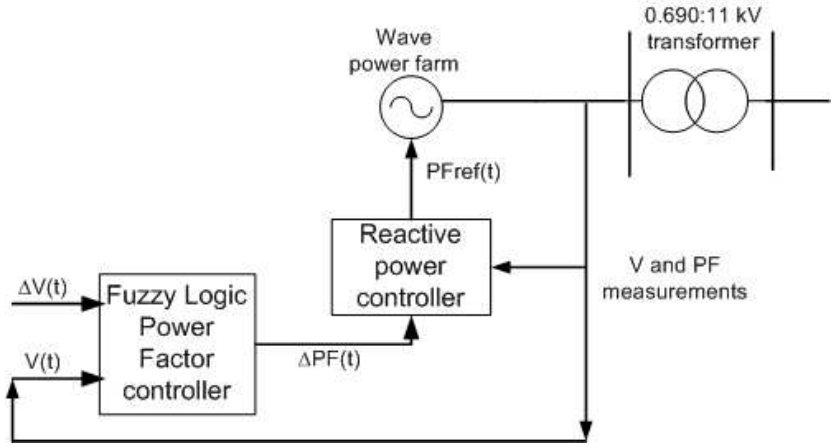

Figure 5.18: *FLPFC block diagram.*

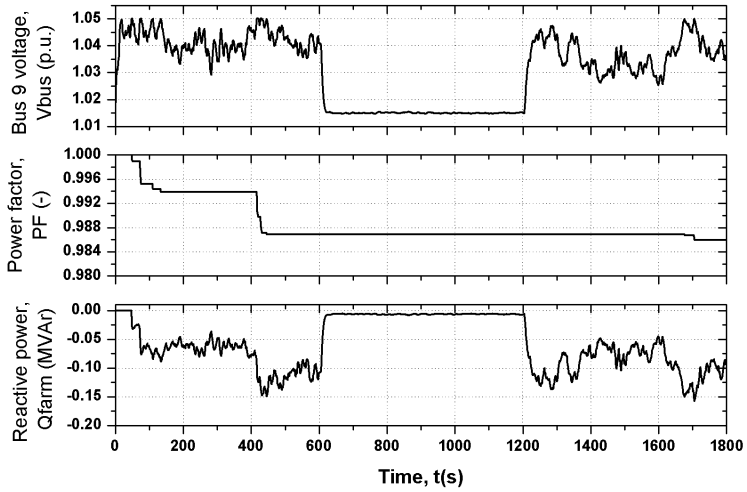

Figure 5.19: *Operation of the wave power farm, connected to the nine-bus system, with the FLPFC controller.*

the farm are issued to keep the voltage below the upper limit.

Some control over the operation of the FLPFC controller is possible by changing the allowed voltage and power factor range. The developed controller can also be used with other reactive power compensating devices (e.g. STATCOMs) in the network. Both these are explored further later in this chapter.

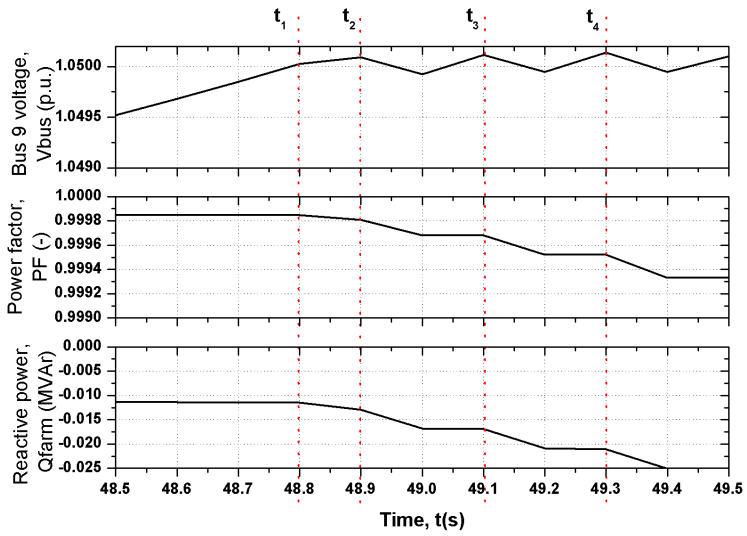

Figure 5.20: *Operation of the wave power farm, connected to the nine-bus system, with the FLPFC controller (magnified).*

5.5 Control of a 4 MW wave power farm connected to a generic UK distribution network

In this section, the effects of connecting a 4 MW wave power farm (with 32 WECs) to a generic 11 kV UK distribution network [175] have been analysed. Some modifications have been made to the network to make it suitable for a single line equivalent power flow solution. All the lines have been taken as three phase transposed lines. The loads have been taken as balanced three phase loads. Figure 5.21 shows the network model. The 4 MW wave power farm is connected to bus 56 (an offshore hub) and is represented by a generator in the figure. The voltage is stepped-up to 11 kV at the hub (transformer between buses 55 and 56) and the power is sent onshore using a 1 km long submarine cable (2XS(FL)2YRAA 6/10 (12) kV Nexans submarine power cable [142]).

The total load connected to the network is 2.384 MW and 0.475 MVAr. Bus 1 in the figure is connected to the sub-transmission network through the system impedance measured at bus 1. Details of the line parameters and the loads used in this network are given in the Appendix A. The voltage at bus 53 is maintained at 1.03 p.u. to compensate for the voltage drop across the radial feeder when the demand is high. An OLTC transformer would normally be used for this purpose. To isolate and study the effects of the different control methods discussed so far in this chapter, the tap position of the OLTC transformer is assumed to be automatically adjusted

to maintain the voltage at bus 53 at 1.03 p.u. at all times.

Typical values for the parameters H_s and T_z found in the seas off the north west coast of Scotland have been obtained from the Wavenet database [20]. Data obtained from the site for two years between February 2009 and February 2011 have been used to select representative seas over the four seasons. Figure 5.22 shows the cumulative probability distribution of the energy ($H_s^2 T_z$) in the seas during the four seasons. The figure clearly shows that the UK waters are more energetic during the winters (December to February) when compared to the summers (June to August). The cumulative probability distribution of the energy in the sea during autumns (September to November) and springs (March to May) lie in between the two curves for summers and winters.

The wave power farm has been modelled in four different sea states representing four different energy levels. The four H_s, T_z combinations used are (a) $H_s = 12.21$ m, $T_z = 11$ s (b) $H_s = 7.16$ m, $T_z = 9.04$ s, (c) $H_s = 5.82$ m, $T_z = 8.05$ s and (d) $H_s = 1.27$ m, $T_z = 4.49$ s. The mean power generated by the wave power farm when placed in the 4 different sea states are 3.79 MW, 3.30 MW, 2.44 MW and 1.60 MW respectively. Figure 5.23 shows the time-series of the real power generated by the wave power farm when simulated in these four sea states. The sea states modelled are non-stationary and irregular over the 10-minute period. The four sea states are hence referred to as sea states A, B, C and D. At the site under consideration, sea state A only occurs during winters. The other three sea states can occur during any of the four seasons.

Figure 5.24 shows the variation in the winter demand in the rural areas of north western Scotland over a day [176]. Analysing a longer data set would clearly show the daily, weekly, and seasonal characteristics of the demand variation. Figure 5.25 shows the probability distribution function of the demand over the four seasons. The demands are higher during the winters and lower during the summers. In this work, the maximum and minimum demands have been respectively taken as 100% (winter maximum) and 25% (summer minimum) of the total loads connected to the buses. Since the simulations discussed in this section have only been performed for 600-second periods, the demand has been kept constant. This is justified since the variations in the generated power from the wave power farm far exceed the variations in the demand over 10-minute periods.

Conventionally, an analysis of the network under extreme operating conditions (maximum gen-

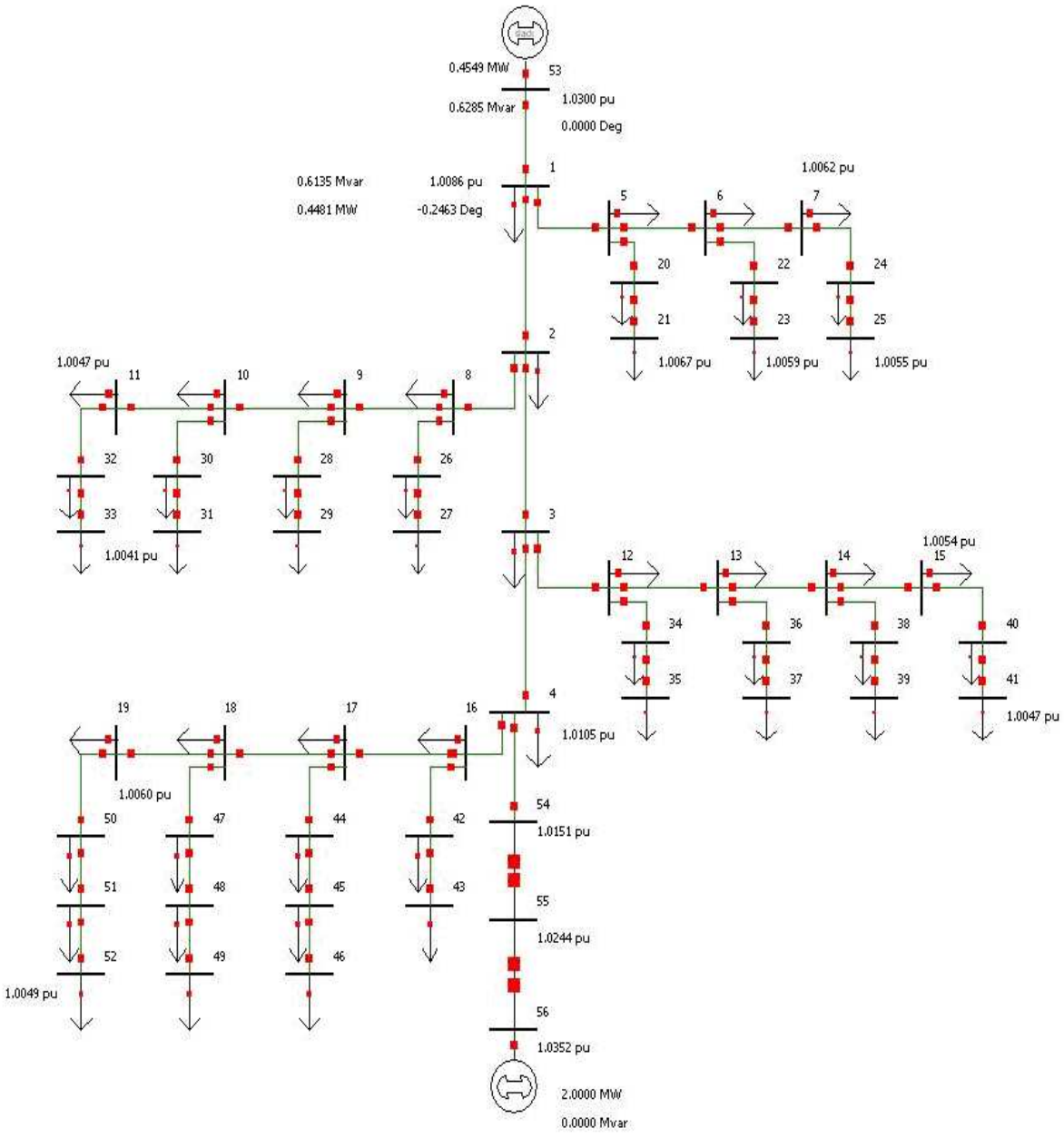

Figure 5.21: *Generic 11 kV UK distribution network.*

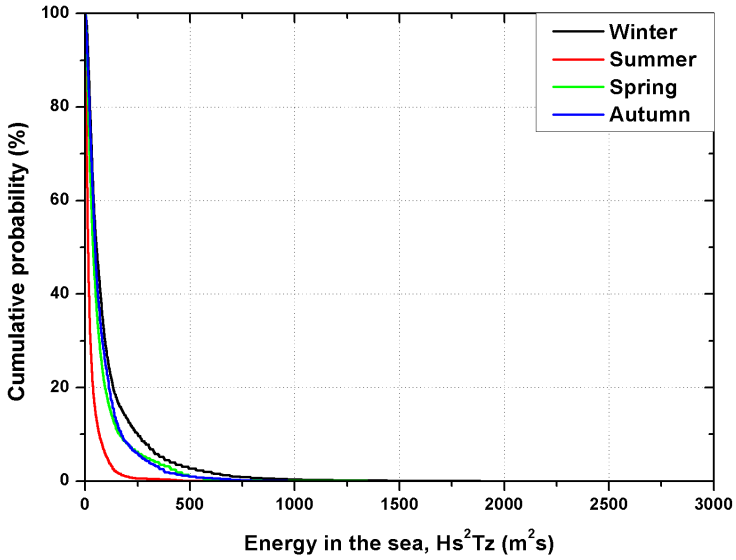

Figure 5.22: *Cumulative probability distribution of the energy ($H_s^2 T_z$) in the sea over the four seasons.*

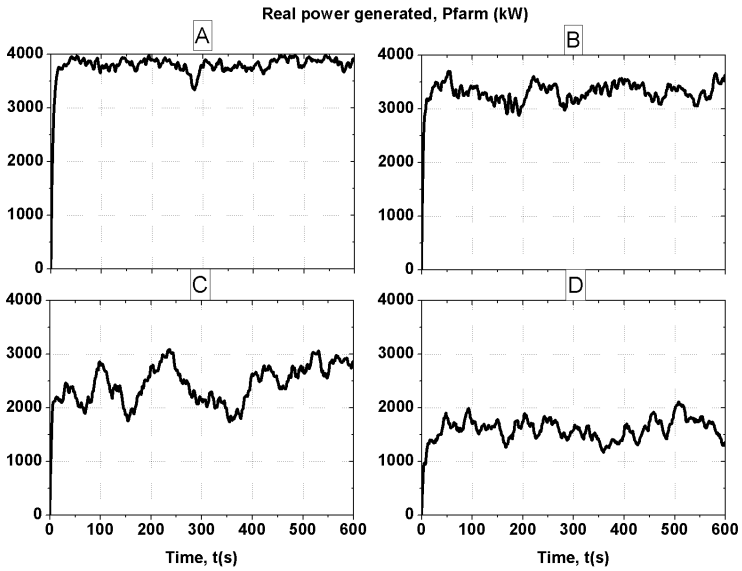

Figure 5.23: *Real power generated by the wave power farm when placed in the four different sea states. (a) Sea state A with $H_s = 12.21$ m, $T_z = 11$ s (b) sea state B with $H_s = 7.16$ m, $T_z = 9.04$ s, (c) sea state C with $H_s = 5.82$ m, $T_z = 8.05$ s and (d) sea state D with $H_s = 1.27$ m, $T_z = 4.49$ s.*

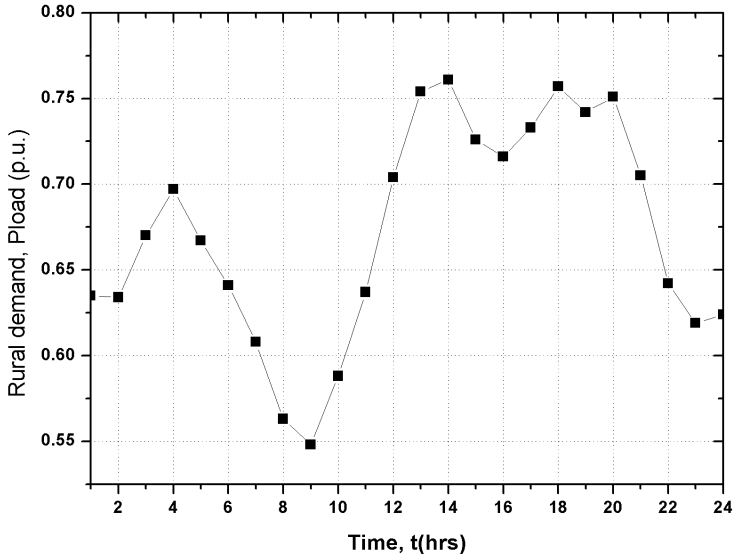

Figure 5.24: *Sample daily demand variation in the UK.*

eration, minimum load; minimum generation, maximum load) is performed to evaluate the effects of any new added generation on the network. Figure 5.26 shows the voltage profile of the network under the two extreme operating conditions. When generating 4 MW, the wave power farm supplies all the loads connected to the network. The excess power, after the loads are supplied, is fed back to the sub-transmission network (represented by bus 53 in the network diagram). Voltage violations, defined by [122], are seen at various buses. These violations may cause the wave power farm to be tripped off the network causing significant loss of revenue to wave power farm developers.

Without any control applied to the wave power farm, the upper voltage limit of 1.05 p.u. would be reached at bus 56 by a generation of 1.075 MW (under the minimum demand case). Any sustained generation above this value will cause the generator to be tripped off the network. In the following sections, the augmentation in the net real power fed to the network by the use of the AVPFC and the FLPFC methods are discussed.

5.5.1 Benefits of the wave power farm

Before the wave power farm was connected, the real and reactive power losses in the network when supplying all the connected loads were 99 kW and 171 kVAr respectively. Figure 5.27 shows the real and reactive power losses in the network, under maximum demand, for different real and reactive power generation by the wave power farm. The real and reactive power flow

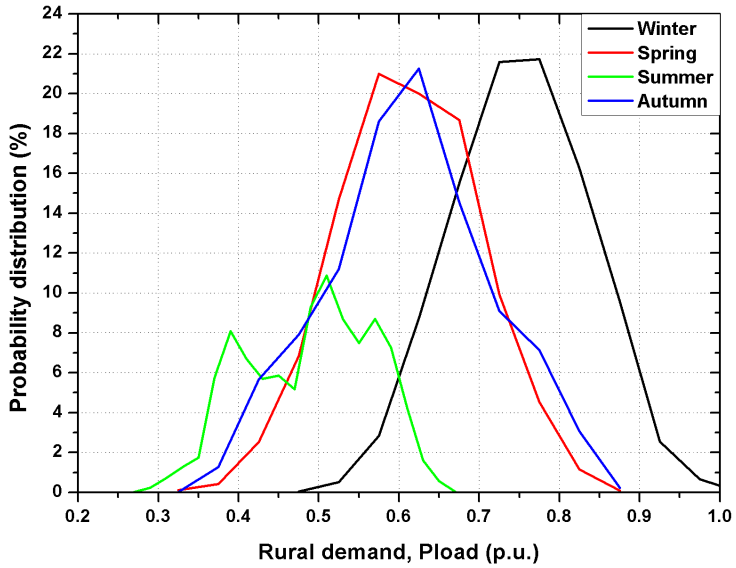

Figure 5.25: *Probability distribution of demand over the four seasons in the UK.*

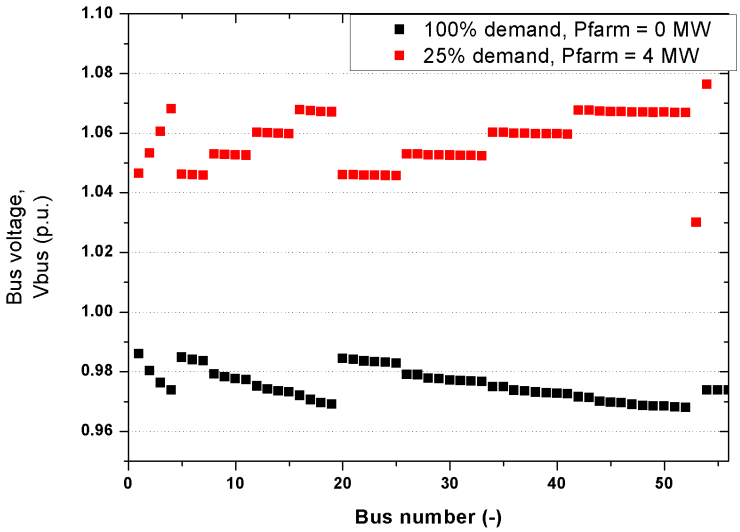

Figure 5.26: *Voltage profile across the network for the two extreme operating conditions.*

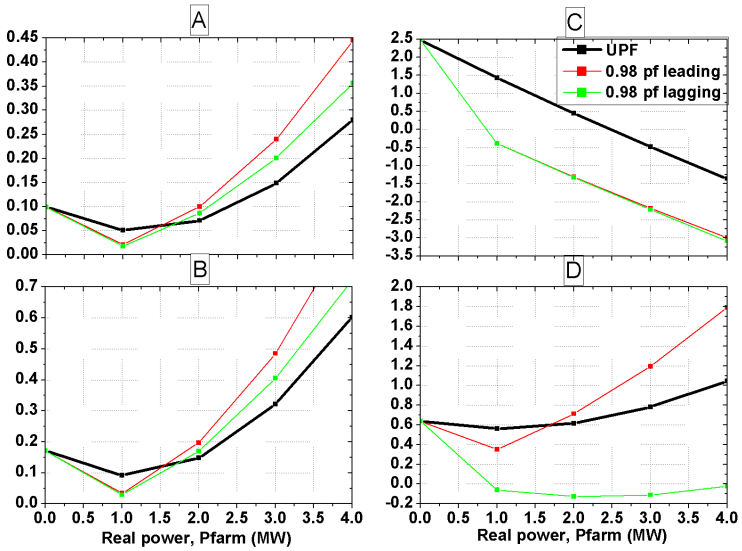

Figure 5.27: *(a) Real power loss (MW) and (b) reactive power loss (MVAr) and the measured (c) real power flow (MW) and (d) reactive power flow (MVAr) at the substation for different wave power farm outputs.*

measured at the substation for varying generation are also shown in the figure. With an increase in the wave power farm size, the real power fed from the sub-transmission network (sub-figure (c)) reduces until it reaches the stage where the excess power generated by the farm is fed back to the sub-transmission network.

5.5.2 AVPFC control of the wave power farm

In this section, the results of the simulation runs completed where the AVPFC controller has been used to control the wave power farm connected to the generic 11 kV distribution network are discussed. As mentioned earlier, the primary aim of using the control method is to ensure the connection of the wave power farm to the network for the longest possible time without any voltage violations occurring. This section also discusses how the different parameters of the AVPFC algorithm - t_d, V_h, V_l, PF_{ref}, PF_T and PF_B - are selected based on simulation runs.

Figure 5.28 shows the voltage envelope at bus 56 when the control of the farm switches from the constant power factor mode to the constant voltage mode for three different time delays when the wave power farm is simulated in sea state C. Over-voltage protection would trip the wave power farm off the network when an over-voltage occurs for more than 500 ms. This being the case, a time delay of less than 500 ms (e.g. 300 ms) becomes the obvious choice. Due to the inherent nature of the net real power generated from wave power farms and the nature of the

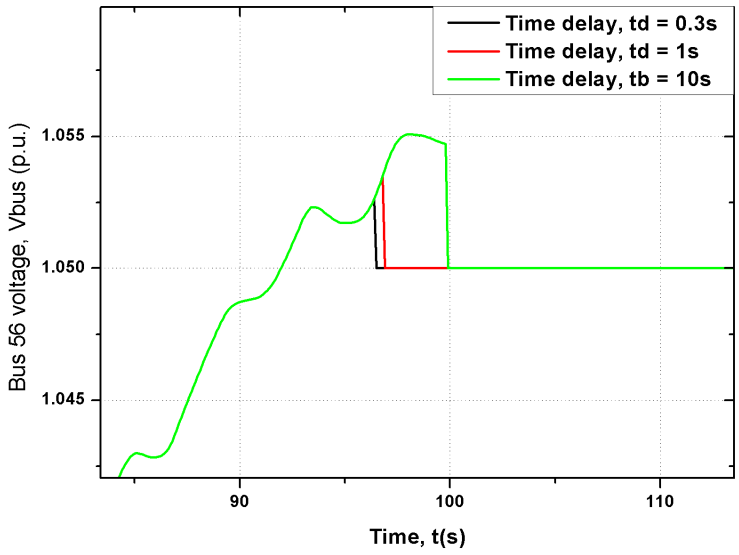

Figure 5.28: *Voltage magnitude envelope during a control mode change for different time delays.*

network and the distributed demand, even after 10 seconds after the voltage goes beyond the upper limit of the deadband (1.0525p.u.) the voltage does not go beyond the statutory limits. Additionally, at times, DNOs operate their over-voltage or under-voltage protection devices only after voltage violations are seen for 6 seconds or more [177]. Due to these two reasons, a time delay of 10 seconds has been chosen for the simulation runs that follow in this section.

To choose the power factor set point of the controller, the operation of the wave power farm during periods of minimum demand has been analysed. Figure 5.29 shows the amount of reactive power the wave power farm needs to exchange with the network to maintain a constant voltage of 1.05 p.u. (the upper voltage limit of the AVPFC controller) for different real power generation scenarios. Up to 1 MW output, the wave power farm operates at a lagging power factor to maintain the voltage constant. As the real power generated increases further, the leading power factor reduces till the generation is approximately 4 MW. Further increase in the real power generated increases the leading power factor. The minima of the power factor curve shown in the figure lies when the wave power farm generates 4 MW. To maintain the bus 56 voltage at 1.05 p.u., with the wave power farm generating 4 MW, the farm will need to absorb 0.8833 MVAr from the network. This essentially means that the wave power farm will need to operate at a leading power factor of 0.9765. Since this value corresponds to the minima of the power factor curve, the power factor limit of the controller has been set at 0.975 lead

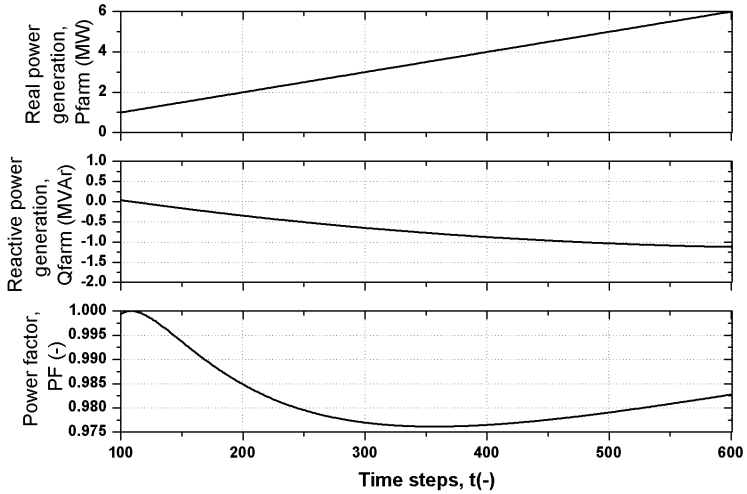

Figure 5.29: *The operation of the wave power farm maintaining a constant voltage of 1.05 p.u. with different real power generation.*

and lag. If a higher power factor set point is chosen, unnecessary switching between the two control modes will be seen. Also, depending on the time delay chosen, over-voltages may be seen during periods when the wave power farm operates at a constant power factor.

Using a similar approach, choosing a voltage set point of 1.055 p.u. for the constant voltage mode requires a power factor limit of approximately 0.979 lead and lag. Choosing this limit might force the use of a smaller time delay because the voltage buffer between the upper limit of the AVPFC bandwidth and the upper statutory limit reduces. For this network and wave power farm size, the upper voltage limit V_h of 1.05 p.u. has been chosen. During periods of high demand before the wave power farm was connected to the network, the voltage at the extremities of the network used to reach 0.9737 p.u. Considering this, the lower voltage set point of the controller has been set at 0.97 p.u.

Figures 5.30 and 5.31 show the results when the wave power farm operates with the AVPFC controller using the parameters selected previously in this section. The wave power farm has been simulated under the sea state A and two different loading scenarios (25% and 100% of the maximum demand) have been used. The spike in voltage seen at the start of the simulation is because of the initial condition of the wave power farm (the generated power is 0 MW at time t = 0 s). Since the increase in the power output from the wave power farm is gradual, occurring over tens of seconds, such voltage or power factor spikes will not be seen in reality unless the local load trips. Under both the loading conditions, it is seen that the wave power farm operates

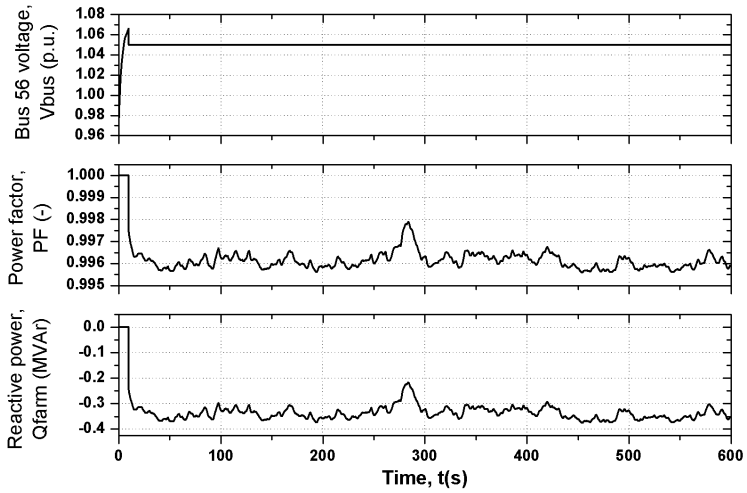

Figure 5.30: *Operation of the wave power farm with the AVPFC controller; in sea state A, connected to the UK 11 kV generic network, with 1 p.u. load and bus 53 voltage = 1.03 p.u.*

in the constant voltage mode. The operating power factor of the wave power farm is different in the two cases. While the power factor is on average 0.996 leading in the 100% demand case, it is on average 0.976 leading in the 25% demand case. Figure 5.32 shows the results of the AVPFC operation when the bus 53 voltage is maintained at 1.00 p.u. For the 25% demand case, during highly energetic seas (sea state A), the wave power farm operates at a constant voltage. The average power factor during the 600-second period is approximately 0.994 leading. Using 0.994 as the power factor limit of the AVPFC controller means that a much smaller power factor change takes place during control mode switching. This option is better from the voltage stability point of view in the network. The scope for improving the controller's operation by adjusting the substation OLTC transformer's tap position based on the energy content of the sea is discussed in Chapter 6.

The results discussed in this section confirm that the control parameters of the AVPFC controller are site specific. Optimal values of these parameters, based on the size of the wave power farm, the distribution network the farm is connected to, the loads, the reactive power capability of the electrical machines, etc., need to be established. Whether the wave power farm warrants the use of additional reactive power compensators (e.g. SVCs, STATCOMs) will also need to be analysed. These compensators will need to be controlled and coordinated with the controller of the wave power farm.

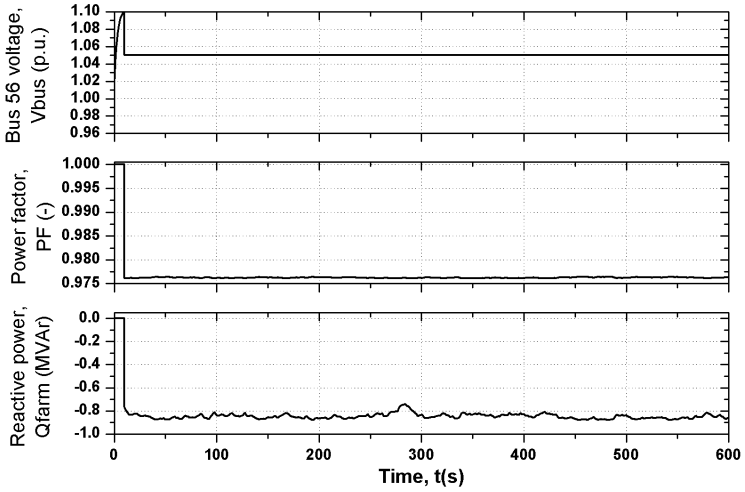

Figure 5.31: *Operation of the wave power farm with the AVPFC controller; in sea state A, connected to the UK 11 kV generic network, with 0.25 p.u. load and bus 53 voltage = 1.03 p.u.*

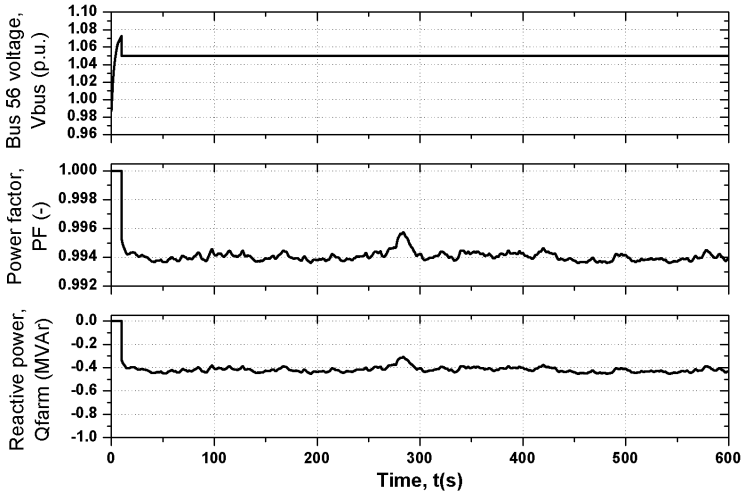

Figure 5.32: *Operation of the wave power farm with the AVPFC controller; in sea state A, connected to the UK 11 kV generic network, with 0.25 p.u. load and bus 53 voltage = 1.00 p.u.*

5.5.3 FLPFC control of the wave power farm

The FLPFC controller has been used to control the wave power farm connected to the generic 11 kV distribution network. As mentioned earlier, the primary aim of using the control method is to ensure the connection of the wave power farm to the network for as long as possible and to maximise production without any voltage violations occurring. Two different voltage deadbands have been tested and a power factor limit of 0.95 lead and lag has been used in the simulations.

Figure 5.33 shows the operation of the wave power farm using the FLPFC controller for the 25% demand case, with the farm simulated in sea state D. The power factor, and hence the reactive power the wave power farm exchanges with the network, changes at every instant when the voltage envelope reaches 1.05 p.u. The wave power farm thus operates as a voltage following machine, but operates at a power factor which is selected based on the energy content of the sea and the demand.

Figure 5.34 shows the operation of the wave power farm at a lagging power factor set by the FLPFC controller for the 100% demand case with the farm simulated in sea state D. The voltage at the bus where the wave power farm is connected is less than 1.01 p.u. for the first few seconds of the simulation. Even though such power variations will not be seen over such short periods of time in reality, the current case shows the operation of the wave power farm at a lagging power factor. It is seen that the FLPFC controller makes the wave power farm operate at approximately 0.95 lagging power factor during the first 40 seconds. When voltage excursions beyond 1.05 p.u. are seen, the wave power farm is made to operate at higher lagging power factors.

One of the main advantages of using the FLPFC over the AVPFC method is that it is less network, load, and wave power farm size specific. Using such intelligent controllers are more advantageous when compared to the conventional 'fit and forget' method of control. The results discussed here clearly show that for selecting the power factor and the voltage limits for the AVPFC and the FLPFC methods, the worst case operating conditions still need to be considered.

5.5.4 Reactive power control using Static Synchronous Compensators (STATCOMs)

Static VAr Compensators (SVCs) and Static Synchronous Compensators (STATCOMs) have been used in the transmission network to maintain the network voltage profile within limits

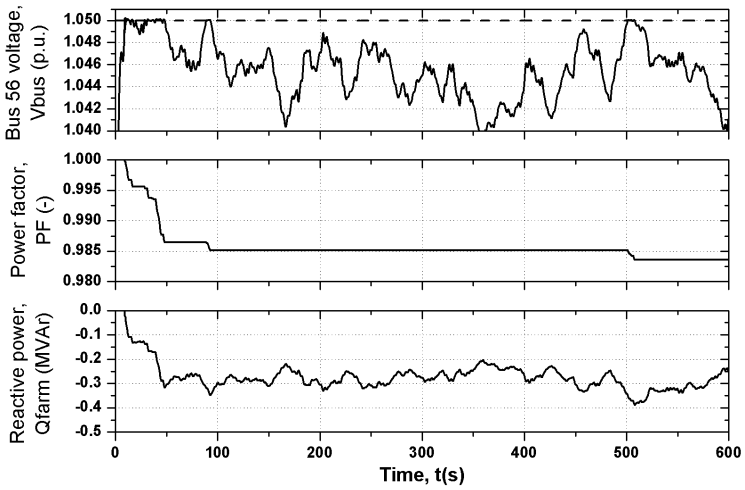

Figure 5.33: *Operation of the wave power farm with the FLPFC controller; in sea state D, connected to the UK 11 kV generic network, with 0.25 p.u. load and bus 53 voltage = 1.03 p.u.*

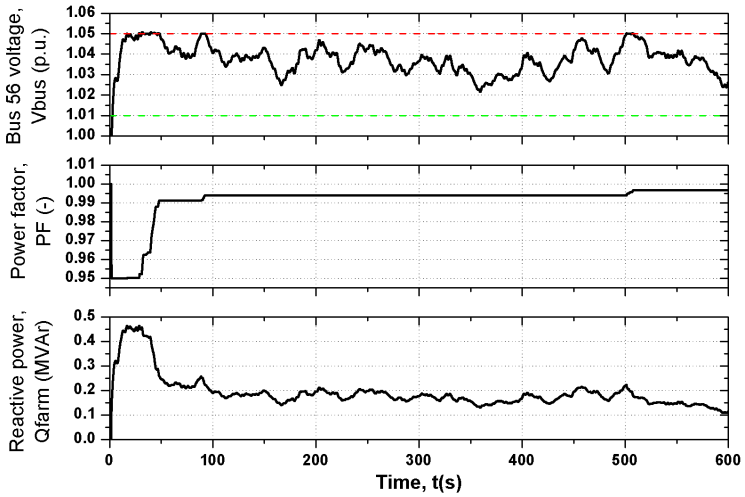

Figure 5.34: *Operation of the wave power farm with the FLPFC controller; in sea state D, connected to the UK 11 kV generic network, with 1 p.u. load and bus 53 voltage = 1.00 p.u.*

[178]. With the addition of significant amounts of generation from renewable sources, the compensators have been used accompanying the DGs to reduce voltage fluctuations introduced by the DGs [179, 180]. The use of such compensators with some real power storage was suggested for wave power farms using Oscillating Water Columns (OWCs) in [181]. In this section, the preliminary use of these compensators is to avoid the over-stressing of the DFIGs caused by an excessive generation or absorption of reactive power. The flexibility provided by STATCOMs over SVCs to accommodate variable generation in the network was documented in [182]. Therefore, STATCOMs were chosen for this work. This section explores how voltage and power factor control is possible using STATCOMs. The modelled STATCOM is connected to the same bus at which the wave power farm is connected. The simulations in this section have been performed with the wave power farm excited by the sea state A with the demand at 25% of the maximum demand.

Figure 5.35 shows the equivalent circuit of the STATCOM used for the simulations [181, 183]. The AC source represents the capacitor banks and the shunt reactors along with the voltage source converter. The output voltage of the STATCOM (V_s) is controlled to get the required reactive power absorption/generation. The operation of the STATCOM is described as follows [183]:

- If the voltage V_s is less than V_k, the STATCOM absorbs reactive power
- If the voltage V_s exceeds V_k, the STATCOM generates reactive power
- If V_s = V_k, there is no exchange of reactive power

STATCOM losses have been ignored in this work since they are less than 1.5% of the equipment rating [179]. Assuming an ideal STATCOM with no real power loss, the following equation yields information of the reactive power exchange with the network [183]:

$$Q_{STATCOM} = \frac{|V_k|^2 - |V_k|.|V_s|}{X_s}. \tag{5.2}$$

Figure 5.36 shows the bus 56 voltage when the STATCOM's voltage V_s is set at 1.01 p.u. The figure also shows the reactive power exchanged between the STATCOM and the network. Figure 5.37 shows the bus 56 voltage when V_s is fixed at 1.03 p.u.

The FLPFC method, described earlier, can be applied to control STATCOMs accompanying wave power farms. The FLPFC controller controls the reactive power exchanged between the

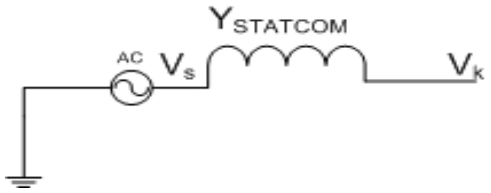

Figure 5.35: *Equivalent circuit of the STATCOM.*

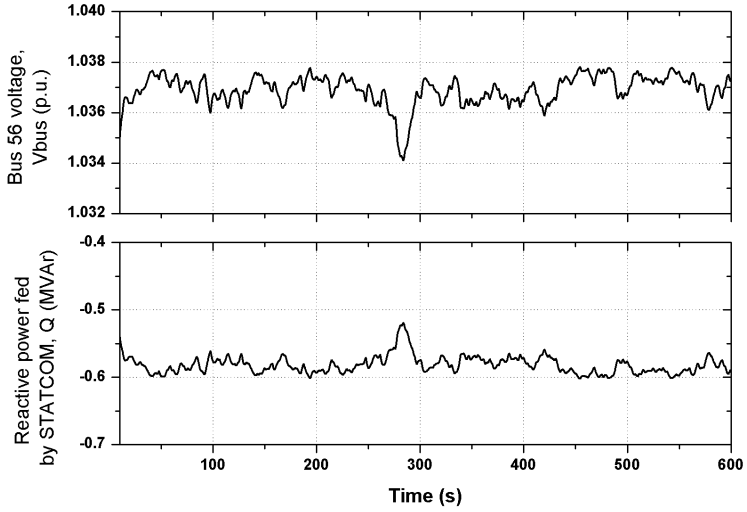

Figure 5.36: *Operation of the wave power farm with the STATCOM, with V_s = 1.01 p.u.*

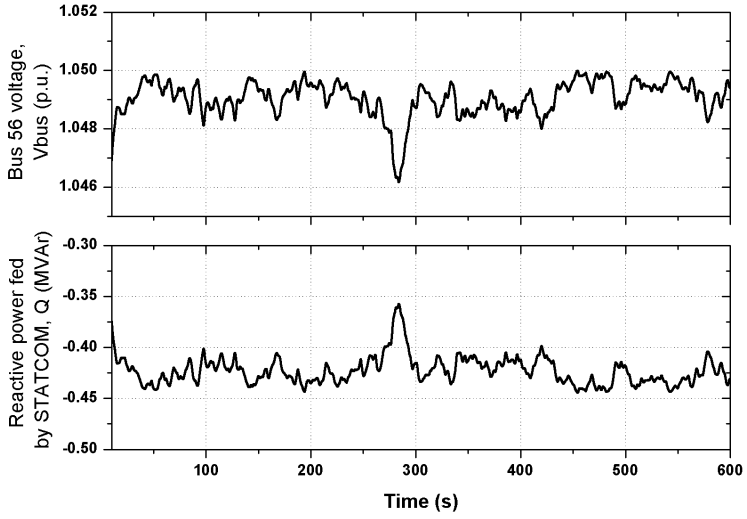

Figure 5.37: *Operation of the wave power farm with the STATCOM, with V_s = 1.03 p.u.*

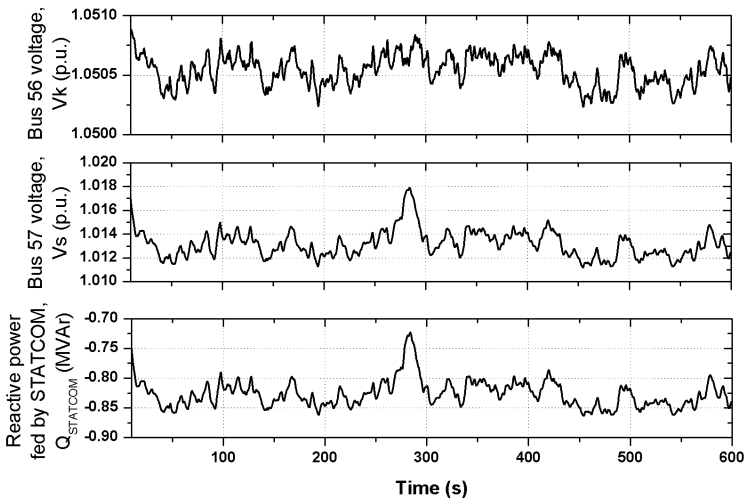

Figure 5.38: *Operation of the wave power farm with the STATCOM maintaining the bus 56 voltage between 1.049 p.u. and 1.051 p.u.*

STATCOM and the network. In this case, the FLPFC acts on the power factor (and hence the reactive power) set point of the STATCOM. Figures 5.38 and 5.39 show the operation of the STATCOM, controlled by the FLPFC method, when it is asked to maintain the bus 56 voltage within certain prescribed ranges. In Figure 5.38 the STATCOM maintains the voltage at bus 56 between 1.049 p.u. and 1.051 p.u., while in Figure 5.39 the STATCOM maintains the voltage between 1.01 p.u. and 1.05 p.u.

5.6 Individual and group control of WECs

So far in this chapter, it was assumed that all the WECs in the farm are controlled together, in effect, working like a single machine connected to the electrical network. The operating power factor and the voltage seen at the bus where the wave power farm is connected were taken as the input control variables, based on which the operating mode of all the DFIGs in the farm was decided. In reality, the volt/VAr controllers on the DFIGs, in many cases, will only have access to the local power factor and voltage. They will need to make the decision regarding the control mode based on these variables alone. When the individual controllers in the wave power farm do not communicate with each other, their operation may be significantly different from the cases discussed till now in this chapter. In this section, different individual and group control options are analysed. The pros and cons of using these control options are examined in detail. All the simulations in this section have been performed with the wave power farm excited by a stationary but irregular sea state with $H_s = 6.03$ m and $T_z = 8.52$ s.

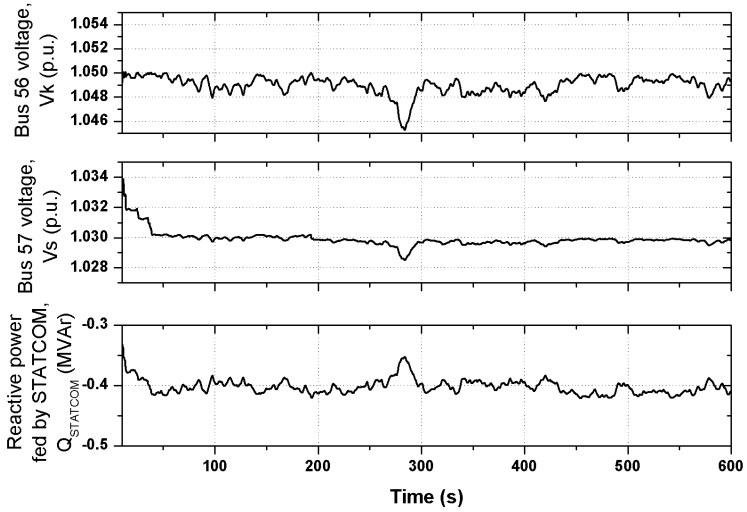

Figure 5.39: *Operation of the wave power farm with the STATCOM maintaining the bus 56 voltage between 1.01 p.u. and 1.05 p.u.*

5.6.1 Electrical proximity of the generators

Figure 5.40 shows the model of the hypothetical rural distribution feeder used for the simulations discussed in this section. The power generated by the individual WECs at 440 V or 690 V is stepped up to 11 kV using offshore transformers. The power is then taken onshore by 1 km long submarine cables. Each WEC in the figure is rated at 125 kW. The electrical demand at bus 3 has been taken to be constant over the simulated time periods in the simulation runs discussed in this section.

Figure 5.41 shows the voltage measured at buses 12-19 over a 100-second period. It is seen that even with the impedance between the WECs and bus 3 and the difference in the real power generated (see Figure 5.42) by the individual WECs, the voltages seen at these buses are exactly the same. This can be attributed to the small size of the WECs used in the farm and the fact that no reactive power was exchanged by the WECs with the network. The figure thus speaks of the close electrical proximity of the WECs in the current farm layout. Since the WECs see the same voltage, methods of controlling the DFIGs within the farm using individual quadrature droops [184] can not be applied here. When reactive power is exchanged by the WECs, the voltages will be slightly different at each bus and this is further examined later in this section.

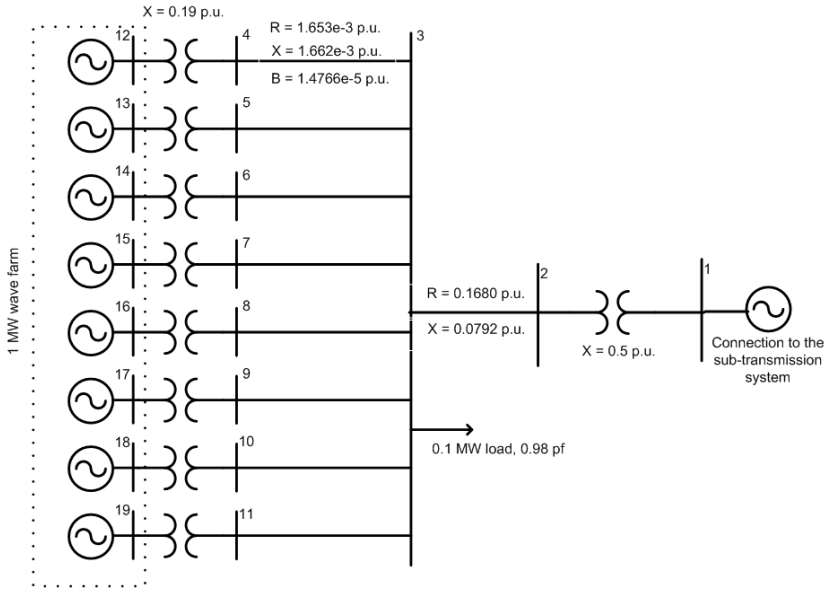

Figure 5.40: *Electrical network model of a wave power farm connected to a hypothetical rural distribution feeder (2 MVA base).*

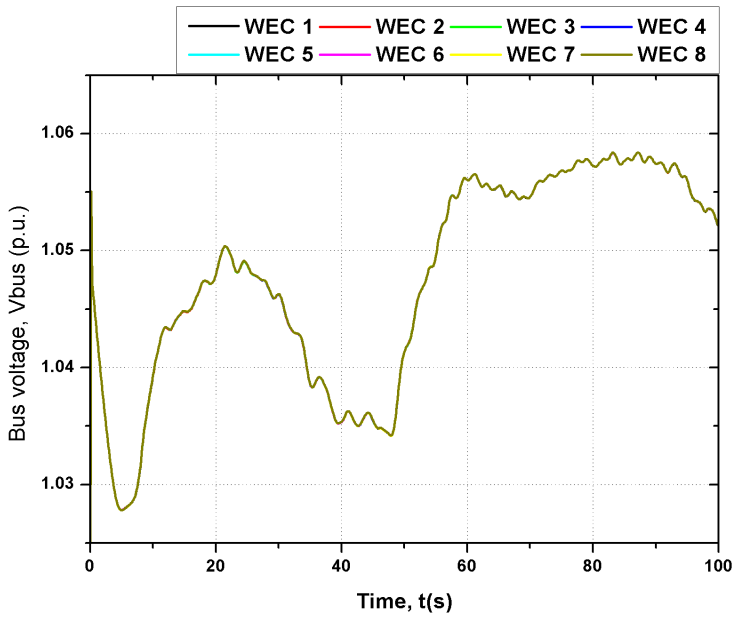

Figure 5.41: *Voltage profiles at buses 12-19.*

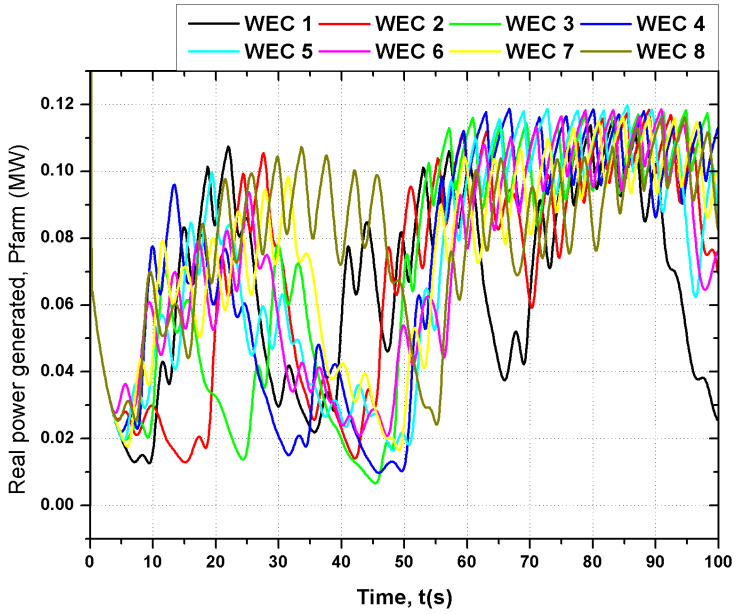

Figure 5.42: *Real power generated by the 8 WECs in the 1 MW farm.*

5.6.2 Individual controllers that do not communicate

In this section, it has been assumed that the AVPFC controller on each WEC operates on its own, without considering the operating mode and status of the other controllers in the farm. In other words, the controller on a WEC (e.g. the WEC connected to bus 12 in Figure 5.40) uses only the voltage and power factor measured at the bus it is connected to (here bus 12) to make the decision on its operating mode. All the eight WECs in the farm have such controllers that do not communicate with each other. The AVPFC controller set points used in this section are $V_h = 1.05$ p.u., $V_l = 1.05$ p.u. and $t_d = 1$ s. The power factor set point chosen for the individual controllers is 0.975.

Figure 5.43 shows the AVPFC control signal, the voltage and power factor measured at the corresponding buses (12-19) and the reactive power exchanged by the WECs with the network, when the wave power farm is controlled using individual controllers that do not communicate with each other. These quantities for three WECs, connected to buses 12, 15 and 19, are shown in the figure. Since the WECs are in close electrical proximity and thus see almost the same voltage, all the eight controllers go into the voltage control mode at the same instant of time.

All the WECs that are in the voltage control mode share the reactive power, required to keep the voltage fixed, equally. Due to this and the different real power generated by each WEC, the

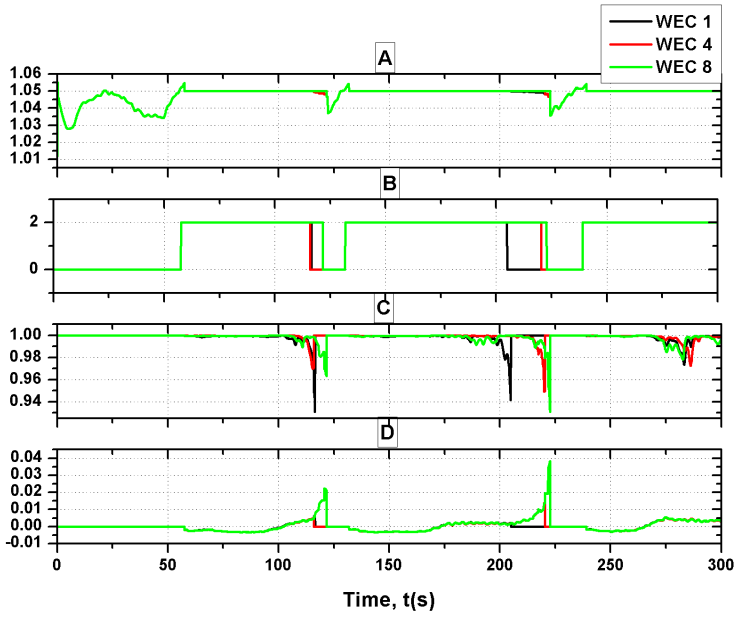

Figure 5.43: *Operation of the wave power farm with individual AVPFC controllers that do not communicate. (a) Voltage at buses 12, 15 and 19 (p.u.) (b) voltage / power factor control signal (2 - voltage control, 0 - power factor control) (c) power factor (-) (d) reactive power generated (MVAr).*

operating power factor of the WECs are different and therefore the instants of time at which the WECs return to the power factor control mode are different. When one or more WECs move from the voltage control mode to the power factor control mode, the reactive power shared by the remaining WECs in the voltage control mode increases. For example, between time 200 s and 250 s in the figure, it is seen that WEC 1 reaches the power factor limit and goes into power factor control mode before WEC 4. Among the three WECs considered here, WEC 8 goes into the power factor control mode last. Between the time WEC 1 and WEC 8 go into the power factor control mode, WEC 8 operates in the voltage control mode. It is seen that the reactive power exchanged (generated here) between WEC 8 and the network increases with every WEC going into the power factor control mode. This puts additional stresses on the DFIGs still in the voltage control mode. This control, therefore, is not sufficient since some DFIGs in the farm may reach the excitation limit placed.

5.6.2.1 One WEC operating with the AVPFC controller

Instead of having a controller on all the WECs, only one of the WECs has been controlled by the AVPFC method here. All the other WECs operate in power factor control at UPF as voltage

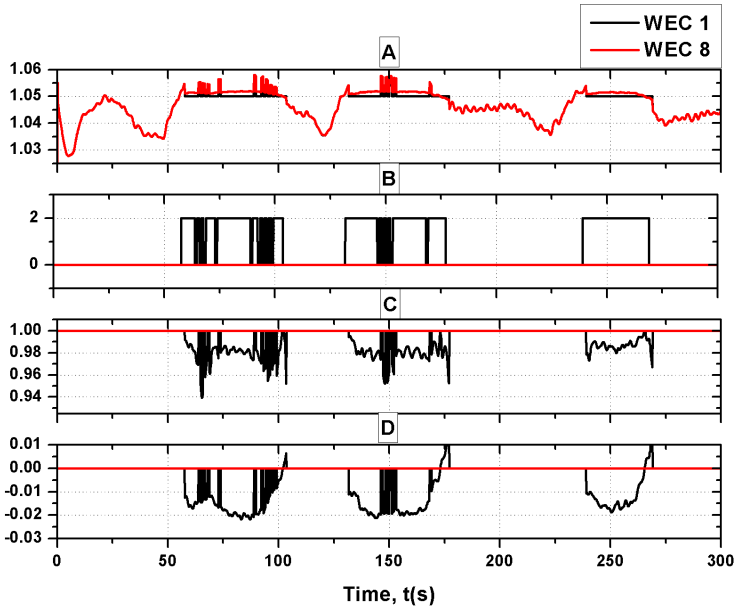

Figure 5.44: *Operation of the wave power farm with WEC 1 controlled by an AVPFC controller. (a) Voltage at buses 12 and 19 (p.u.) (b) voltage / power factor control signal (2 - voltage control, 0 - power factor control) (c) power factor (-) (d) reactive power generated (MVAr).*

following machines. Figure 5.44 shows the AVPFC control signal of WEC 1, the voltage and power factor measured at buses 12 and 19 and the reactive power exchanged by WEC 1. As expected, WEC 1 deals with much more reactive power in this case. Between 50 s and 100 s in the figure, there are durations when the control mode keeps switching. Spikes in the voltage reaching 1.057 p.u. are seen, which would trip the farm off the network. These spikes occur every time WEC 1 reaches the power factor limit and moves back to the power factor control mode. When in this mode, since the voltage is still above the upper voltage limit, WEC 1 returns to the voltage control mode after another time delay.

5.6.2.2 Two WECs operating with the AVPFC controller

Having two WECs controlled by the AVPFC method improves the control of the wave power farm, when compared to the case when only one WEC is controlled. This is seen in Figure 5.45, where the sharing of the reactive power requirement by the two WECs during the voltage control mode prevents unnecessary switching between the control modes and the voltage spikes associated with it (as seen in Figure 5.44). Since only two WECs share the reactive power exchanged with the network, the probability of the WECs being taken off the farm (see Sec-

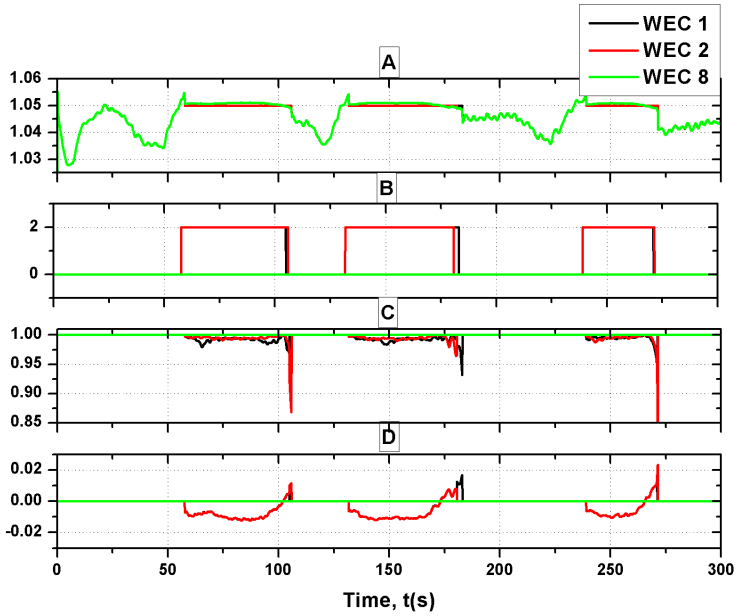

Figure 5.45: *Operation of the wave power farm with WEC 1 and WEC 2 controlled by AVPFC controllers. (a) Voltage at buses 12, 13 and 19 (p.u.) (b) voltage / power factor control signal (2 - voltage control, 0 - power factor control) (c) power factor (-) (d) reactive power generated (MVAr).*

tion 5.6.5) is high, especially when the farm is excited by highly energetic seas. Taking off one of the controlled WECs (due to excessive generation from the farm) would further burden the remaining controlled WEC when in the voltage control mode. The results discussed in this section and the preceding section show that the onus of maintaining voltage and/or power factor has to be distributed among the WECs in a farm to make full use of the capability of the intelligent AVPFC controller.

In both Figures 5.44 and 5.45, the voltage seen at buses 12 and 19 are not the same when the farm operates in the voltage control mode. This is due to the reactive power exchanged by WECs 1 and 2 and the reactive impedance between buses 12-19 and bus 3.

5.6.3 Individual controllers that communicate

In the preceding section, some of the issues that arise when the individual controllers on the WECs do not communicate with each other were discussed. The main problem occurred when the WECs moved from the voltage control mode to the power factor control mode. Since this switching of modes did not happen at the same time in all the WECs, the WECs still in the voltage control mode had to deal with excessive reactive power generation/absorption to maintain

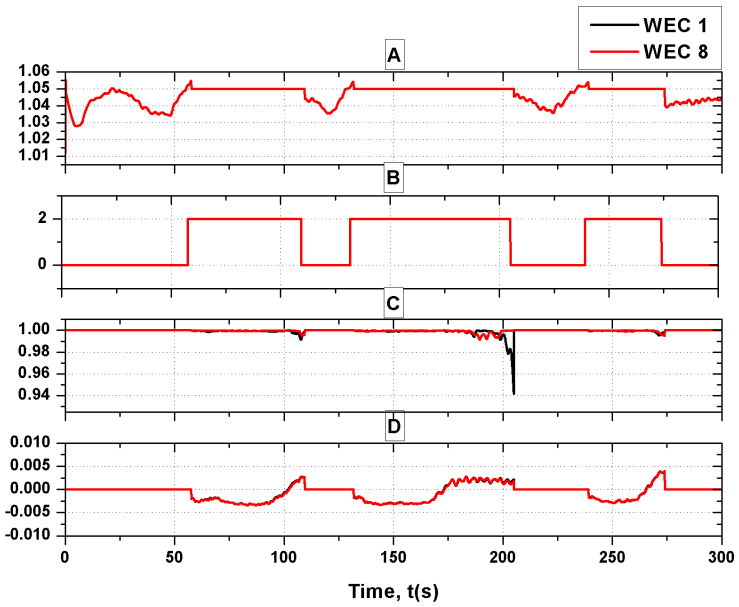

Figure 5.46: *Operation of the wave power farm with individual AVPFC controllers that communicate. (a) Voltage at buses 12 and 19 (p.u.) (b) voltage / power factor control signal (2 - voltage control, 0 - power factor control) (c) power factor (-) (d) reactive power generated (MVAr).*

a constant voltage. The advantages of letting the individual controllers communicate with each other have been studied and the results are discussed in this section. The AVPFC algorithm has been slightly modified to accommodate the interactions between the controllers on the WECs. Some means of communication between the individual controllers is also required.

The individual controllers still work based on the input variables measured at their respective buses (buses 12-19). The only change made to the AVPFC control algorithm is that all the WECs are forced back to the power factor control mode when the power factor limit is reached by any one of the WECs. This essentially means that a control hierarchy exists with an additional controller above the individual controllers. The improvement in the wave power farm operation when this change in incorporated is seen in Figure 5.46. All the WECs share the reactive power requirement equally throughout the time period irrespective of the control mode of the WECs, since all the WECs now come into and go out of the power factor control mode together. The additional controller does not play any role during the switching to the voltage control mode. This is due to the close electrical proximity of the WECs which ensures that all the WECs enter the voltage control mode together even without the additional controller.

5.6.4 Power factor set point for constant voltage controller

In Sections 5.6.2 and 5.6.3, all the WECs in the voltage control mode shared the reactive power requirement equally, and therefore, their operating power factors depended on their instantaneous real power production. For the same reactive power generation/absorption, the WEC with the lowest real power production had the lowest operating power factor. For example, in the case described in Figure 5.46, at t = 109.5 s when the farm moves into the power factor control mode, only one of the WECs (WEC 2, connected to bus 13 in Figure 5.40) had reached the power factor limit of 0.975. At that instant of time, the WEC was generating only 9.62 kW of real power, which was the lowest in the farm. It is because WEC 2 reached the power factor limit, the other WECs were forced into the power factor control mode by the additional controller described in the preceding section. This happened even when the other WECs were producing power at power factors well within the power factor limit, which means that the reactive power capability of the farm was not being used completely.

In this section, a different control option has been used wherein a supervisory controller, with access to and knowledge of the voltage and the operating power factor of the farm at bus 3, decides the operating control mode of all the WECs in the farm. In the network shown in Figure 5.40, bus 3 is onshore. Bus 3 may be an offshore hub in larger array developments. In the power factor control mode, the supervisory controller constrains the individual controllers to operate at UPF. When the voltage at bus 3 goes beyond the upper or the lower voltage limit, the farm is forced into the voltage control mode. When in this mode, the supervisory controller constantly issues the operating power factor of the farm to maintain the voltage at 1.05 p.u. or 0.97 p.u., as needed.

The supervisory controller that has been used is the FLPFC controller described in Section 5.4.5. When the bus 3 voltage goes beyond 1.05 p.u., the FLPFC controller aims to maintain the voltage between 1.0495 p.u. and 1.0505 p.u. by issuing to the individual controllers of the DFIGs the operating power factor of the farm. The power factor limit of the supervisory controller was set at 0.9975 (leading and lagging). Figure 5.47 shows the AVPFC control signal of WECs 1 and 8, the voltage and power factor measured at buses 12 and 19 and the reactive power exchanged by the two WECs. It is seen that all the WECs operate at the same power factor that is issued by the FLPFC controller. This means that the reactive power contributed by each WEC is in proportion to the generated real power at any instant of time. Comparing Figures 5.46 and 5.47, shows the difference in the operating power factor of the WECs with and without the

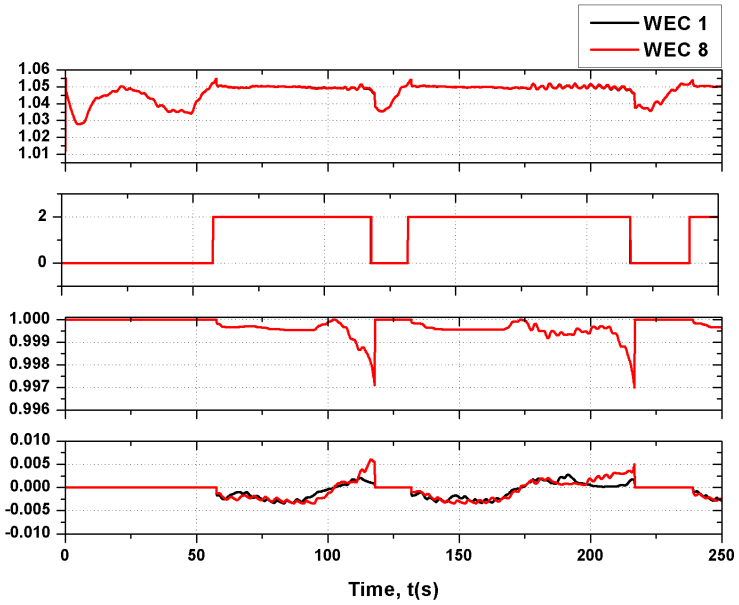

Figure 5.47: *Operation of the wave power farm with individual AVPFC controllers that operate at the same power factor. (a) Voltage at buses 12 and 19 (p.u.) (b) voltage / power factor control signal (2 - voltage control, 0 - power factor control) (c) power factor (-) (d) reactive power generated (MVAr).*

supervisory controller. In the current case, the WECs have to deal with much smaller power factor changes.

5.6.5 Constraining WECs off the network during periods of excessive generation

In all the simulation runs discussed so far, there was never a case for constraining a WEC off the network due to excessive generation by the wave power farm. This is an option that has to be considered when the seas are excessively energetic and when, even with the maximum allowed reactive power generation/absorption by the WECs, the voltage cannot be maintained at the lower/upper voltage limit. This section explores and compares different individual and supervisory control strategies that can be used to remove generators from the network. Both partial constraint or power shedding are possible in a wave power farm. The former is accomplished by proper adjustment of the hydrodynamic parameters (through control of the hydraulic PTO), while the latter involves removing WECs from the network during periods of excessive generation. Different WEC control methods involving the control of the hydraulic PTO have been pursued as a part of the SuperGen Work Stream 7 at Lancaster University. Dr. David Forehand and Dr. Aristides Kiprakis, at the University of Edinburgh, have also developed a

bi-directional wave-to-wire model of the wave power farm, wherein control of the DFIGs in the farm controls the damping coefficients of the PTO and hence the power extracted by the WEC from the sea. In this thesis, the damping coefficients of the PTO of the WECs have been selected for maximum power extraction and only power shedding has been considered.

An additional clause has been added to the initial AVPFC algorithm (see Figure 5.10) to remove generators during periods of excessive generation. According to the clause, a WEC is removed from the network when the operating leading power factor of the WEC reaches the limit. On the other hand, the WEC is forced into the power factor control mode when the WEC operates at the lagging power factor limit, as seen in Figure 5.46.

In the simulations that follow in this section, the size of each WEC, and hence the farm, has been increased. This has been accomplished by removing the real power generation limits that are normally placed on the WECs. This simulation run has been performed to show the effects of taking generators off the network with the same sea state used so far in this section. The power factor limit of the AVPFC controller has also been reduced to 0.9975 (leading and lagging) for the case with the supervisory controller.

5.6.5.1 The case with individual controllers

The disadvantages of having individual controllers on the WECs, which do not communicate with each other, were discussed in Section 5.6.2. The discussion there was regarding the switching from the voltage control mode to the power factor control mode, which occurs when the WECs reach the lagging power factor limit. The work has been extended to also include generator constraints.

The main issue seen earlier when individual controllers were used was that all the WECs did not return to the power factor control mode simultaneously. This resulted in the WECs still in the voltage control mode having to produce excessive amounts of reactive power. A similar scenario would be seen in the case when a WEC is taken off the grid due to excessive generation. As mentioned earlier, this would happen when the WEC reaches the leading power factor limit. Once one WEC is taken off, the remaining WECs will need to increase their share of the reactive power absorbed to maintain a constant voltage. This might in turn push another WEC to the leading power factor limit, tripping that WEC off the network. A chain-reaction might follow, resulting in the whole farm being removed from the network.

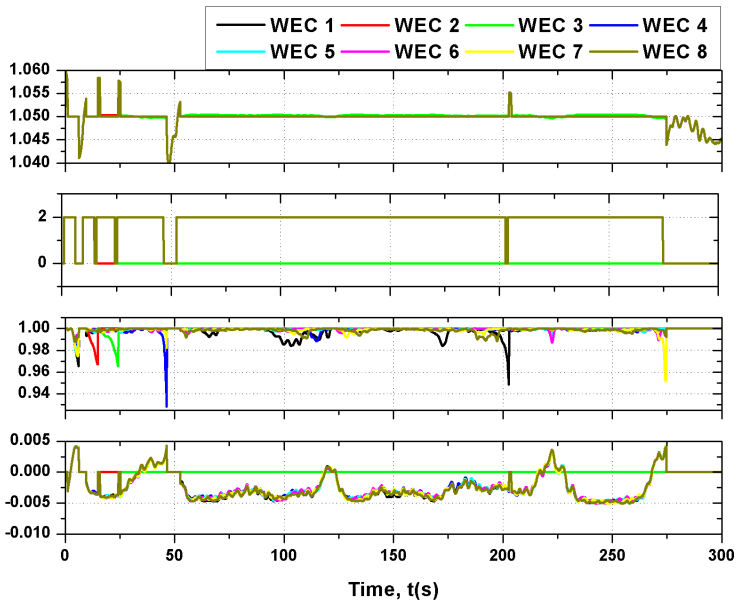

Figure 5.48: *Operation of the wave power farm with the WEC constraint option, with individual controllers that communicate. (a) Voltage at all buses (12-19) (p.u.) (b) voltage / power factor control signal (2 - voltage control, 0 - power factor control) (c) power factor (-) (d) reactive power generated (MVAr).*

When the individual controllers can communicate (as in Section 5.6.3), all the WECs are constrained to the power factor control mode when one of the WECs reaches the leading power factor limit and is taken off. The operation of the farm with individual controllers that communicate is shown in Figures 5.48 and 5.49. In Figure 5.49, it is seen that two WECs are taken off the network within the first 25 seconds of the simulation run. At the instants when the two WECs are taken off, spikes are seen in the bus 3 voltage (see Figure 5.48). These voltage spikes can be attributed to the fact that the controllers on the WECs still connected to the network are forced into the power factor control mode, when one of the WECs is taken off the network.

Another reason why these voltage spikes are seen is that the WEC generating the least amount of real power operates at the lowest power factor as explained earlier. This is the case when all the WECs absorb the same amount of reactive power. Therefore, the WEC taken off the network is not the most significant contributor to the voltage rise problem. These results clearly show the necessity of a supervisory controller, like the one discussed in Section 5.6.4, to overcome these shortcomings of WECs having individual controllers.

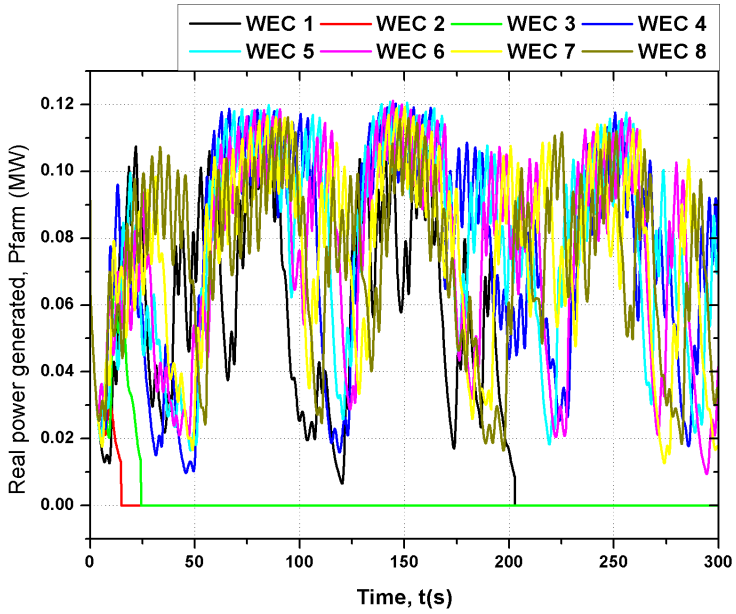

Figure 5.49: *The real power production by the 8 WECs in the farm, showing the WECs being constrained off the network; with individual controllers that communicate.*

5.6.5.2 Supervisory controller for taking off WECs

As discussed earlier, the supervisory controller uses the measurements made at bus 3 to decide on its future course of action. The advantages of this approach were discussed in the case when there was a need to move from the voltage control to the power factor control mode. In this section, the operation of the supervisory controller in the WEC constraint decision making process is described.

The simulation runs described in this section use the same supervisory controller described in Section 5.6.4, with the additional WECs constraint functionality. The results with the supervisory controller (see Figures 5.50 and 5.51) are very similar to the results seen in Figures 5.48 and 5.49 with the individual controllers that communicate. In Section 5.6.2, some of the drawbacks of having individual controllers that do not communicate were examined and as a solution to these the necessity of having controllers that communicate with each other was proposed. This additional control layer ensured that all the WECs went into the power factor control mode once the lagging power factor limit was reached by any one of the WECs. A drawback of this proposed modification was seen in Figure 5.48, where voltage spikes were seen at instants when WECs were taken off the network. Voltage spikes are again seen, in the first 25 seconds is Figure 5.50, at instants when two WECs are taken off the network.

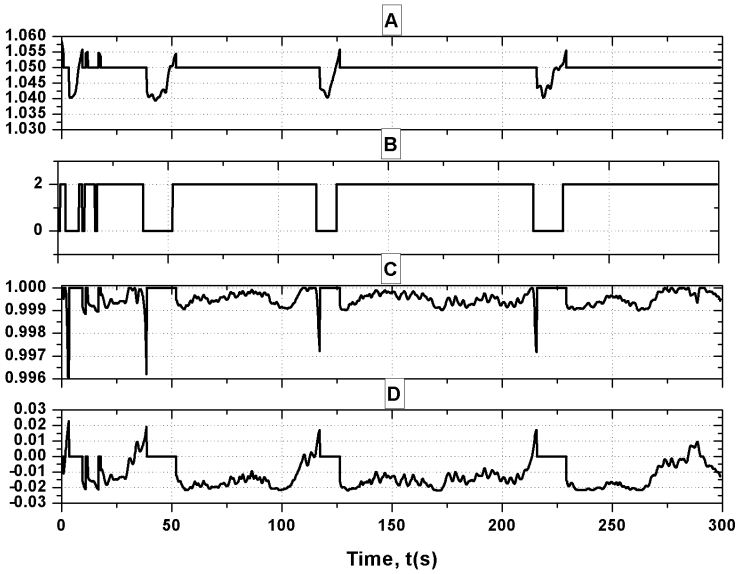

Figure 5.50: *Operation of the wave power farm with the WEC constraint option, with the supervisory controller. (a) Voltage at bus 3 (p.u.) (b) voltage / power factor control signal (2 - voltage control, 0 - power factor control) (c) power factor (-) (d) reactive power generated (MVAr).*

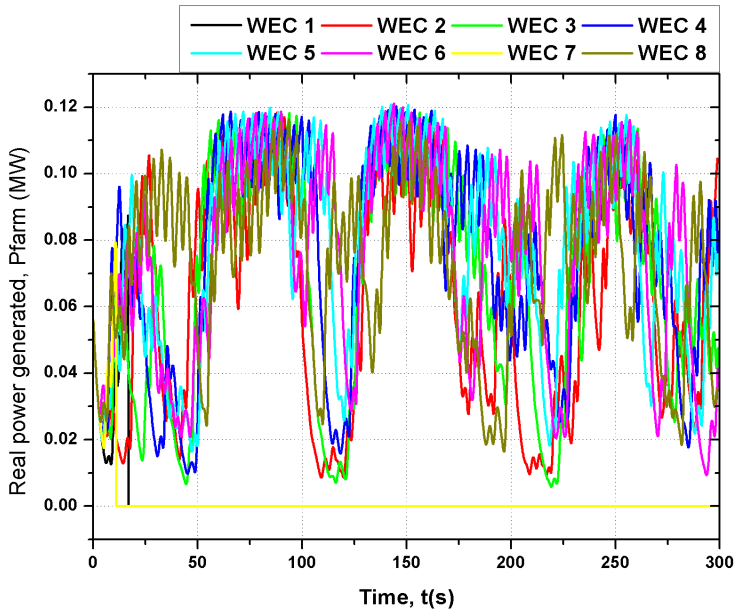

Figure 5.51: *The real power production by the 8 WECs in the farm, showing the WECs being constrained off the network; with the supervisory controller.*

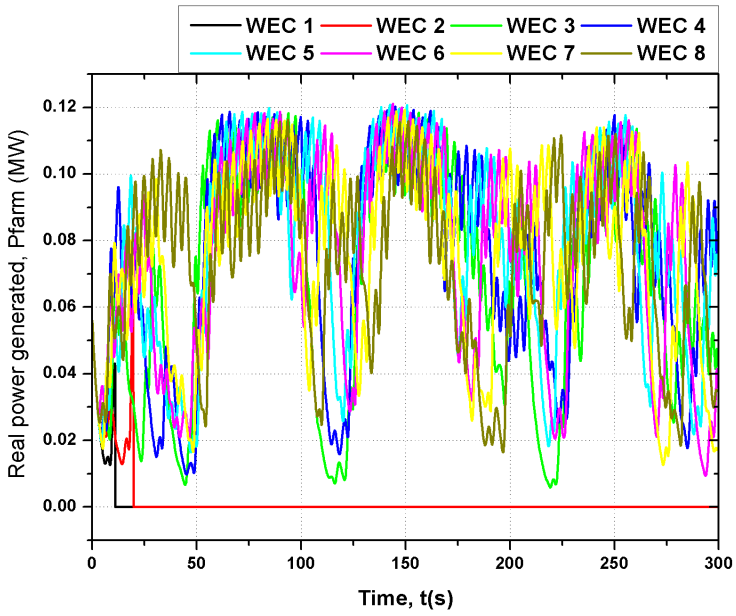

Figure 5.52: *The real power production by the 8 WECs in the farm, showing the WECs being taken off the network; with the new supervisory controller with no priority generation shedding.*

5.6.5.3 New supervisory controller

Forcing all the WECs into the power factor control mode, when one of the WECs reached the power factor limit, was necessary when individual controllers worked only with the local power factors. This was incorporated to avoid any excessive reactive power generation/absorption by the WECs and to avoid the occurrence of a chain-reaction on the removal of one or more WECs from the network. With the new supervisory controller described in this section, this feature is no longer required. The supervisory controller allows the WECs to continue in the voltage control mode even after one or more WECs are taken off the network. It returns to the power factor control mode only when the lagging power factor limit of the farm is reached.

Figures 5.52 and 5.53 show the operation of the new supervisory controller when the WECs are taken off, not taking into account their individual real/reactive power generation or power factors. In other words, when the first leading power factor limit is reached by the farm, WEC 1 is taken off the network. The second time the leading power factor limit is reached, WEC 2 is taken off the network and so on. No voltage spikes or unnecessary switching between the control modes are seen in this simulation run with the new supervisory controller.

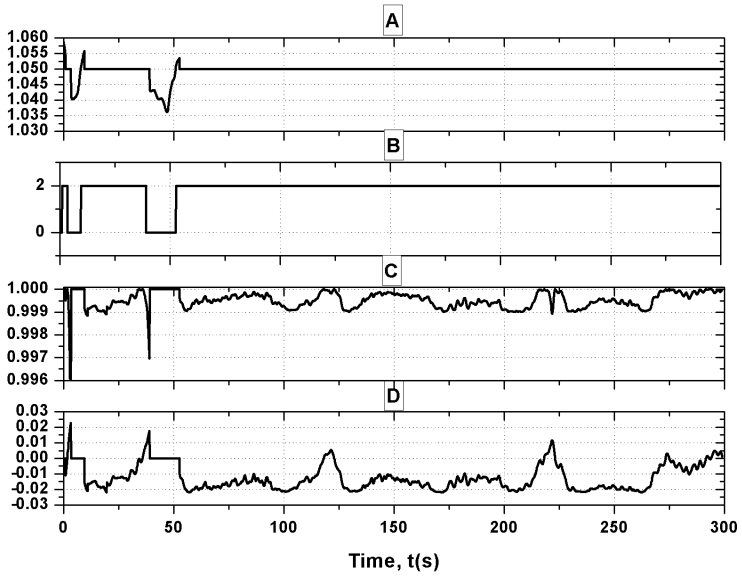

Figure 5.53: *Operation of the wave power farm with the WEC take off option, with the new supervisory controller with no priority generation shedding. (a) Voltage at bus 3 (p.u.) (b) voltage / power factor control signal (2 - voltage control, 0 - power factor control) (c) power factor (-) (d) reactive power generated (MVAr).*

Figures 5.54 and 5.55 show the operation of the supervisory controller when the WECs are taken off depending on the magnitude of the real power generated by each WEC. At the instant of time when the leading power factor limit is reached, the WEC which is contributing most towards the net real power generation of the farm is taken off the network first. In the previous case (see Figure 5.52), WECs 1 and 2 were taken off the network, while in this case (see Figure 5.54) WECs 7 and 1 were taken off the network. Again, no voltage spikes or unnecessary switching between the control modes are seen in this simulation run with the supervisory controller.

Figures 5.52 and 5.54 compare the operation of the supervisory controller with and without priority generation shedding. In both these cases, two WECs were constrained off the network. The average net real power generated by the farm in the two cases is almost the same and no significant advantage using the priority generator shedding is seen.

From these results, the advantages of having the new supervisory controller become evident. All the simulations in the thesis, apart from the ones in this section, have been performed using the supervisory controller. In essence, all the WECs within the wave power farm have been controlled together as slaves, with the supervisory controller acting as the master.

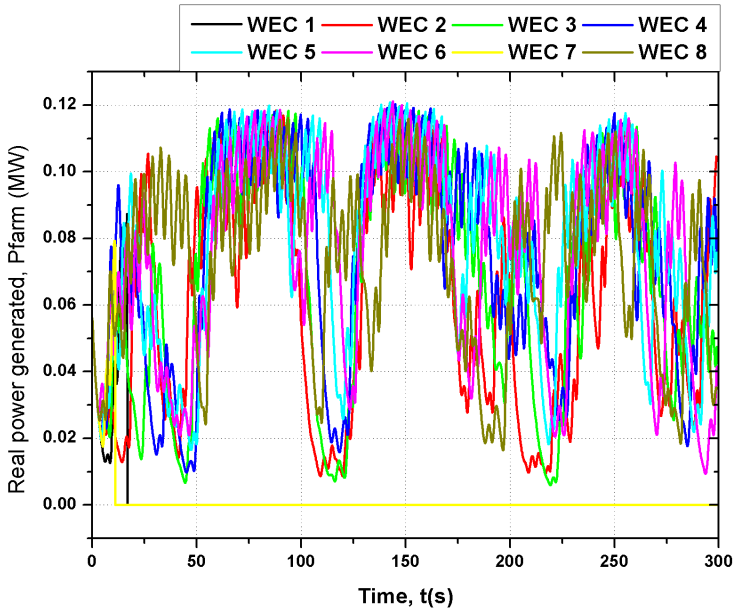

Figure 5.54: *The real power production by the 8 WECs in the farm, showing the WECs being taken off the network; with the new supervisory controller with priority generation shedding.*

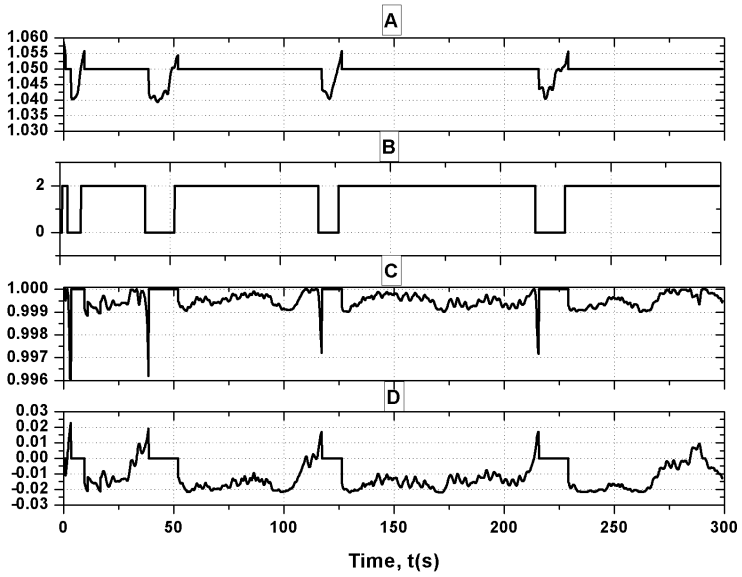

Figure 5.55: *Operation of the wave power farm with the WEC take off option, with the new supervisory controller with priority generation shedding. (a) Voltage at bus 3 (p.u.) (b) voltage / power factor control signal (2 - voltage control, 0 - power factor control) (c) power factor (-) (d) reactive power generated (MVAr).*

5.7 Control of a 4 MW wave power farm connected to the 33 kV Stornoway/Harris distribution network

Section 5.5 described the procedure used to select the voltage and power factor limits and the time delay of the AVPFC and the FLPFC controllers for optimal performance. The 4 MW farm, in that section, was connected to a generic UK distribution network. The network used was largely passive between the source and the generator and had only distributed loads.

In this section, the 4 MW wave power farm is connected to the Stornoway/Harris distribution network [176]. This area off Outer Hebrides will see wave power developments in the near future. The network is more active with a number of OLTC transformers and a wind farm (3 MW capacity at Arnish Moor) and a hydro power plant (1.2 MW capacity at Chilostair). The network is shown in Figure 5.56. The 4 MW wave power farm is connected to the 11 kV BARVAS1A bus. The OLTC transformers between BARVAS3B and BRAVAS1A buses have been rated appropriately for the new farm connection. The procedure described in Section 5.5 has been used to determine the set points of the controllers used in the simulation runs discussed here. Some transmission and distribution network operators allow only a $\pm 3\%$ variation from the nominal voltage. Keeping this in mind, the upper and lower voltage limits have been taken as 1.03 p.u. and 0.97 p.u. respectively and the power factor limit has been taken as 0.975 (leading and lagging) for the simulations discussed in this section.

Simulation runs over 500 seconds have been performed for different loading and generating conditions. The outputs from the wind and the hydro power plants and the demand have been taken to be constant during the simulation time. The transformation ratios of all the OLTC transformers have been calculated from power flow runs completed before hand with the same demand conditions. Under the conditions mentioned so far, the simulated network is still passive. Two cases, where the OLTC tap changer changes its tap position and 50% of the load connected to the BARVAS1A bus is lost suddenly, have been used as tests of the AVPFC and the FLPFC controllers in more active networks. For the simulation runs in this section, the wave power farm has been simulated in the sea state D (see Figure 5.23) and the 25% demand case has been used.

Figure 5.57 shows the operation of the wave power farm with the AVPFC controller when the tap ratio of the transformer changes. At time t = 300 s the transformation ratio of the OLTC transformer between BARVAS3B and BARVAS1A changes from 0.9435 to 0.9385 p.u. The

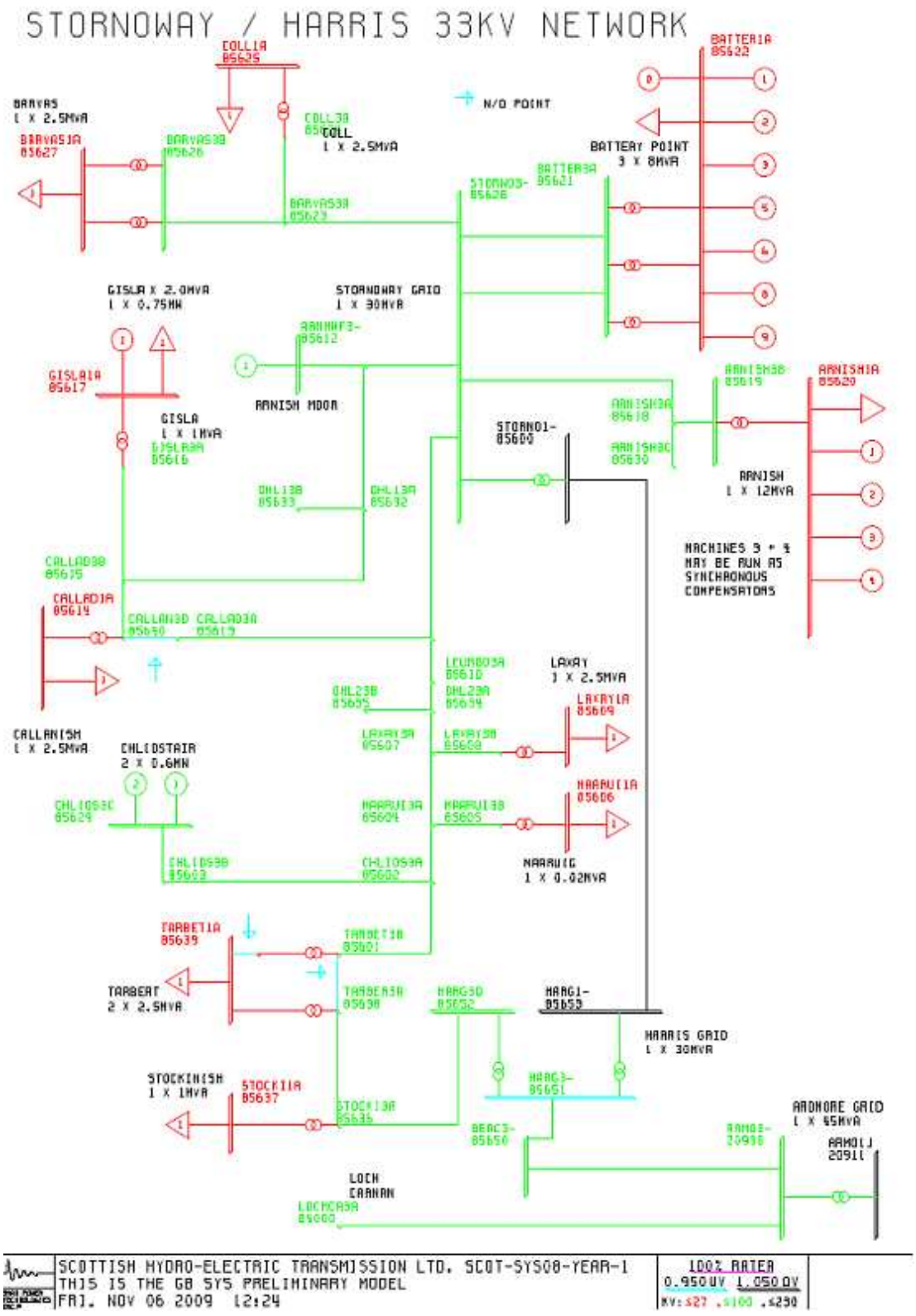

Figure 5.56: *Stornoway/Harris 33 kV network.*

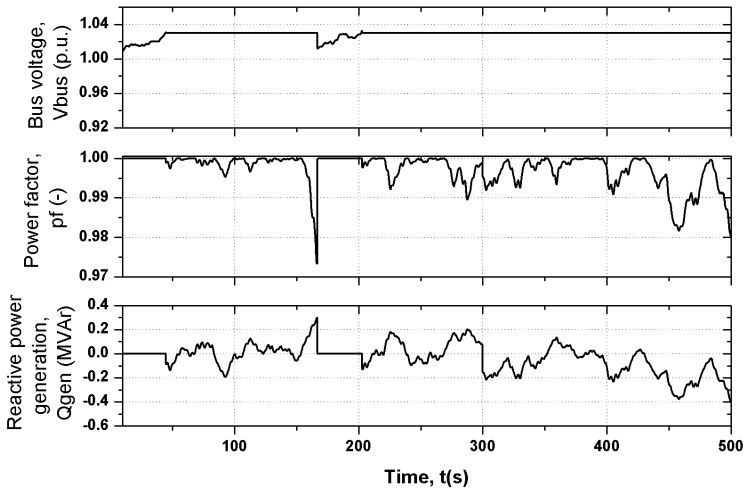

Figure 5.57: *Operation of the wave power farm with the AVPFC controller when a tap change occurs.*

wave power farm was operating in the voltage control mode till that instant. At the instant the tap change occurs, a sudden increase in the reactive power absorbed by the farm is seen. Since the power factor limit of the controller is not reached, the farm continues in the voltage control mode. Had the power factor limit been reached, one of the WECs would have had to be constrained off the network.

The operation of the wave power farm with the AVPFC controller when 50% of the load connected to the BARVAS1A bus is suddenly lost (at time t = 300 s) is shown in Figure 5.58. The wave power farm was operating in the power factor control mode till time t = 300 s. Due to the sudden rise in the voltage seen with the loss of load, the farm is constrained to operate in the voltage control mode. This shows the capability of the AVPFC controller to circumvent some of the issues seen in the network.

Figures 5.59 and 5.60 show the operation of the wave power farm, under the same sea and demand conditions like above, controlled by the FLPFC method. The voltage limits of the FLPFC controller has been modified from those used in Section 5.5.3. The upper and lower voltage limits used here were 1.03 p.u. and 0.97 p.u. respectively. In Figure 5.59, at time t = 290 s, the transformation ratio of the OLTC tap transformer changes from 0.9435 to 0.9385 p.u. A sudden reduction in the operating power factor of the farm is issued by the FLPFC controller, which helps to maintain the voltage under 1.03 p.u. An increase in the reactive power absorbed by the farm is seen at this instant. In Figure 5.60, a significant increase in the voltage is seen

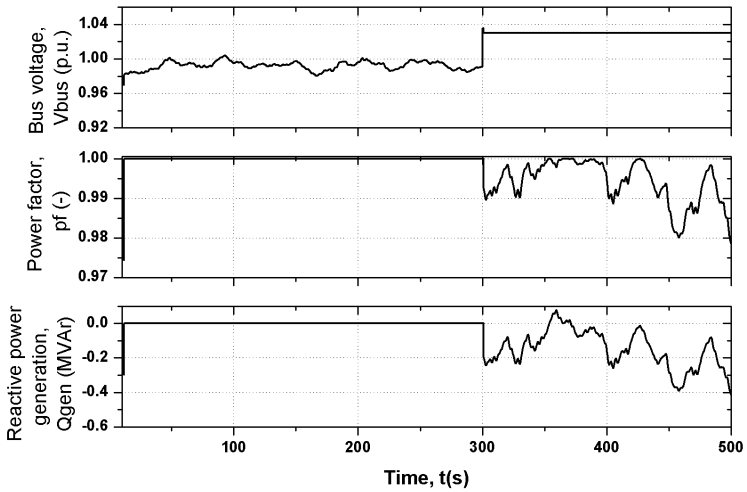

Figure 5.58: *Operation of the wave power farm with the AVPFC controller when a sudden loss of load occurs.*

when 50% of the load is suddenly lost. The wave power farm was operating at UPF till the load loss. With the load loss, the FLPFC controller forces a reduction in the operating power factor of the farm to maintain the voltage within the allowed limits.

In this section, the performance of the AVPFC and the FLPFC controllers in more active networks was tested. Both the controllers have some capability to overcome certain network issues (like loss of load). For more severe issues, the operation of the farm may eventually need to be constrained and the WECs may need to be taken off the network.

5.8 Benefits of using the intelligent controllers

In this section, the savings that can be made using the AVPFC method for controlling a 6 MW wave power farm over a period of one year has been analysed. A site off the north western coast of Scotland has been chosen and the sea data [20] and the demand data [176, 185] have been obtained. This area has been identified by wave energy developers as a potential site for the development of wave power farms [186]. The limited capacity of the electrical network in this area is one of the major constraints for new distributed generation (DG) developments here [187]. Normally, the DG developers are required to upgrade the network before their generators can be connected. Any significant reinforcement of the network is expensive and time consuming. The Scottish potential for renewable power may not be fully utilised to meet the stringent 2020 targets due to these constraints. Using the intelligent controllers developed in this work defers the required network upgrades. The additional income generated through

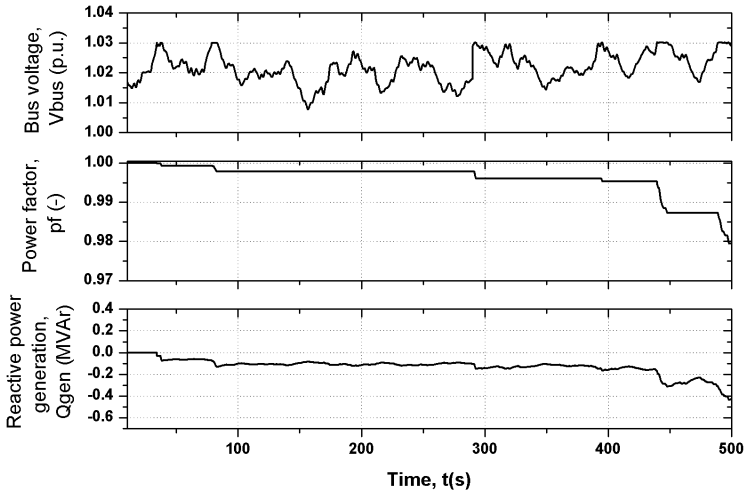

Figure 5.59: *Operation of the wave power farm with the FLPFC controller when a tap change occurs.*

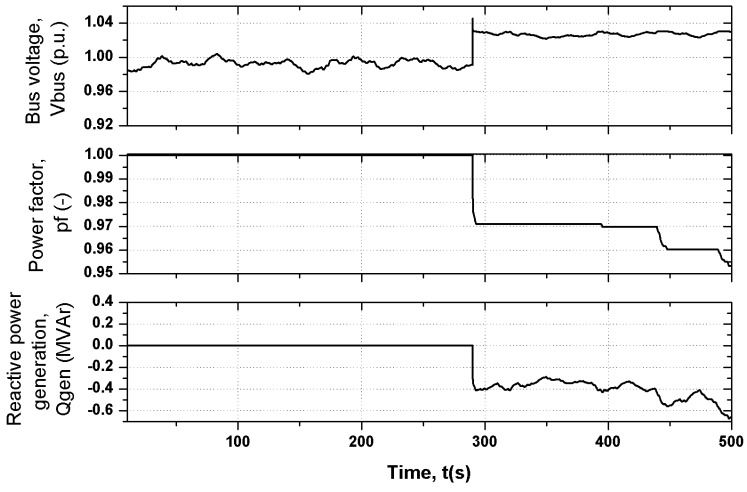

Figure 5.60: *Operation of the wave power farm with the FLPFC controller when a sudden loss of load occurs.*

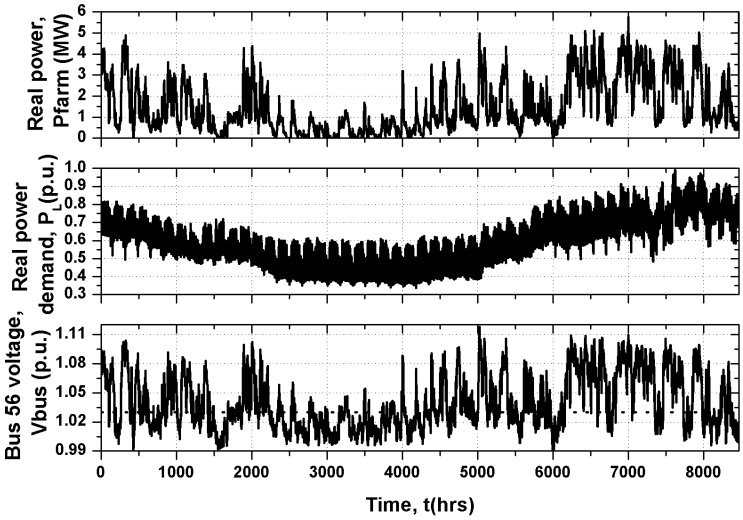

Figure 5.61: *The real power generation by a 6 MW farm, the demand variation and the voltage variation over a year.*

the avoidance of network upgrades has not been quantified in this work. The income generated by the energy yield alone has been considered.

The model of the wave power farm has been simulated for a year using one-hour averaged power generation and demands. The wave data between February 2011 and February 2012 have been used, while the demand data during the same months but in 2002-2003 have been used. Since the yearly demand patterns show a very strong correlation, the use of the older demand data is sufficient to show the advantages of using the AVPFC method with the wave power farm.

Figure 5.61 shows the variation in the power generated by the 6 MW farm and the demand variation at the site over the year. The voltage variations at the bus to which the farm is connected are also shown. UPF operation of the wave power farm has been used to generate these results. It is seen that for approximately 52% of time during the year the voltage at bus 56 lies above the 1.03 p.u. limit. This in effect means that without the option of voltage control and power constraining, the wave power farm would have been allowed to generate power only for approximately six months that year.

Figure 5.62 shows the variation in the power generated by the 6 MW farm and the demand variation at the site over a winter month (February 2011), when the sea was extremely energetic. In this case, voltage violations are seen for more than 76% of the time, which means that the

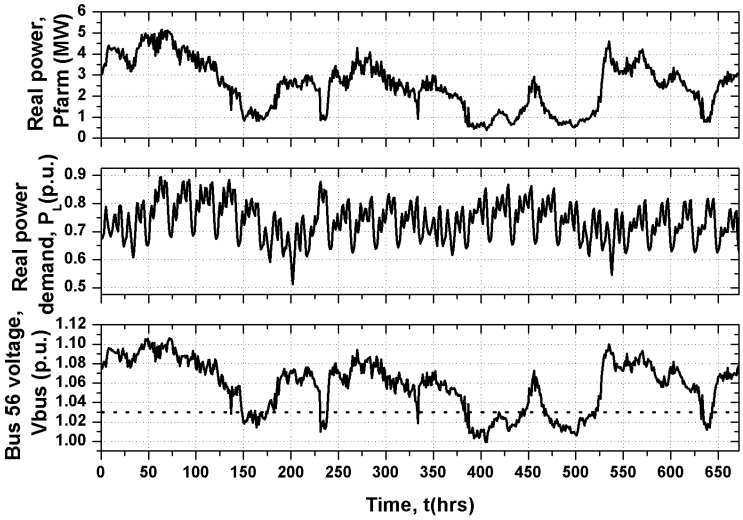

Figure 5.62: *The real power generation by a 6 MW farm, the demand variation and the voltage variation over two and half weeks in February 2011.*

farm would have been tripped off the network for all but seven days in February 2011 without voltage control or power constraining. A similar analysis performed for December 2011 when the sea was extremely energetic showed that the farm would have been connected to the network for only three days that month. This clearly shows the advantages, from the energy production point of view, of the intelligent voltage controllers.

The operation of a 6 MW wave power farm over a three-year period has been analysed to understand the benefits of using the intelligent volt/VAr controllers. Wave data from 23 February 2009 to 12 February 2012 and demand data from 23 February 2001 to 12 February 2004 were used to make this assessment. The wave data between September 2010 and November 2010 were not available and therefore the number of hourly data points in the year two simulation runs was less than the other two years. Three control strategies have been compared on the basis of both the additional energy and income production. DNOs normally require the connected DG to constrain the real power generated to maintain the voltage within the allowed limits. This is one of the strategies tested here. The second option is where there is no controller and when the wave power farm G59 interface (with an automatic restarter) operates to trip the farm off the network whenever the voltage goes beyond the voltage limits. The third strategy involves the use of the AVPFC method with the supervisory controller. Figures 5.63 shows the operation of the wave power farm over a month. The demand variation between 0.5 - 0.85 p.u. is usual in autumns/springs when the seas can be very energetic, as is the case shown in the figure. With

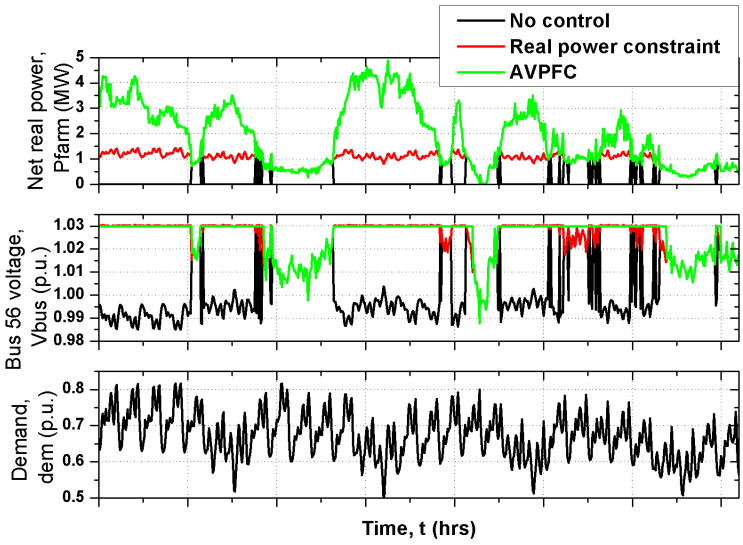

Figure 5.63: *The real power generation by a 6 MW farm, the demand variation and the voltage variation over a year using the three control strategies.*

the wave power farm operating without any control, it is tripped off the network for extended periods during the month to avoid voltage violations. Constraining the real power keeps the voltage within limits, but limits the power generated and energy yield of the farm. The farm is seen to operate at a constrained capacity (approx. 1 MW) much below it rated capacity (6 MW). Using AVPFC ensured that both the voltage is maintained within limits and all the generated power is fed to the network.

The net energy production over the three-year period, when the three strategies were used, are given in Table 5.5. The percentage of time for which the wave power farm had to be tripped off the network or the real power generation had to be constrained during the three-year period is also given. It is observed that the wave power farm would have been off the network for more than six months between February 2011 and 2012 due to extremely energetic seas had the AVPFC controller not been used. Over the three-year period too this value is significant, and for close to five months every year the generation-demand conditions would trip the wave power farm off the network. Relaxation of the voltage limits set by the DNO will allow the connection of a larger farm to the network, which will cause all the voltage magnitude issues seen in the case of the 6 MW farm discussed here. Using the intelligent controllers will make the farm size selection more flexible.

Between two successive hourly instants of time, the instantaneous power generated by the farm

	Average energy production (MWh)	**Percentage of time (%)**
Year 1		
Without control	2965	
Real power control	6237	35.39
AVPFC control	9337	
Year 2		
Without control	2622	
Real power control	4809	27.75
AVPFC control	6899	
Year 3		
Without control	2151	
Real power control	6839	51.92
AVPFC control	12779	
Gross		
Without control	7738	
Real power control	17885	38.80
AVPFC control	29015	

Table 5.5: *Additional energy production*

was found to be greater than the average for approximately 50% of the time. This means that if the power, averaged over an hour, caused voltage violations, then for at least 50% of that hour voltage violations would be seen in reality. To assess the impact of the remaining 50% of the hour on the supply voltage magnitude, a series of simulation runs where the average power over an hour was taken to be the minimum power generated for the particular sea state were performed. It was found that during only 6.57% of the entire three-year period were voltage violations avoided when the average power generation, for the different sea states, was taken to be the minimum instantaneous power. Assuming an equal probability of occurrence for all powers between the minimum instantaneous power and the average power (over the 50% period within an hour), it was found that the percentage of time for which voltage violations were seen reduced to 33.47% for year 1, 26.40% for year 2 and 50.29% for year 3. The difference between these values obtained after the correction for instantaneous power and those shown in Table 5.5 are insignificant. Also, applying this correction will not change the energy yield significantly.

It is seen that by constraining the real power the wave power farm was kept connected to the network throughout the three-year period. With the AVPFC controller though, the energy production was 62% more than when only real power control was used. This is economically advantageous to wave power farm developers. Every extra MWh produced brings extra Renewables Obligation Certificates (ROCs) to the developers. The Scottish government has recently reviewed the ROC bands and has increased the ROCs/MWh for wave power farms to 5 ROCs

[188] (from the previous value 2 ROCs [189]). For the energy produced shown in Table 5.5, using real power constraining as a strategy alone would bring the developer 50735 more ROCs over the three-year period when compared to the case when the farm is allowed to be tripped off the network. With AVPFC control though, the number of ROCs gained would increase by a further 55650 for the three-year period. According to the current buy-out rates of ROCs (£40.71 per ROC) [190], the additional ROCs gained would be valued approximately at £4.3M (without any control being applied, the income would have been £1.57M). The net additional income gained by the developers can be even higher (approx. £4.8M) because of the auctioning system based on which ROCs are traded [191].

5.9 Summary

In this chapter, the effects of connecting wave power farms to weak, rural electricity networks were explored. Though there are many benefits gained through the newly added distributed generators, especially those dependent on renewable sources, there are constraints that the supply quality limits place on them. The focus in this chapter was on the fluctuations in the rms-voltage magnitude introduced by the injection of wave power. Weak networks, like the ones considered here, are particularly affected by the varying generation from wave power farms. Control options for primary voltage control were discussed.

The operation of the wave power farm either at a constant voltage or power factor were thoroughly explored. Some of the evident drawbacks of using these conventional control options were discussed. Voltage control using OLTC transformers showed the problems associated with the time delay, which proved that the substation transformer was suitable only for coarse, secondary control. The advantages of using intelligent control methods, like the AVPFC and the FLPFC, were demonstrated. In both these methods, reactive power generated/absorbed by the farm was used as the control variable. Using these intelligent controllers ensured the connection of the wave power farm to the network for much longer than when the conventional control methods were used. More importantly, the voltage was also kept below statutory limits. The different operating conditions the DFIGs in the farm were put into by the intelligent controllers were well within the reactive power capability of the DFIGs used in the farm [192]. By using the intelligent controllers expensive network upgrades can also be avoided.

Different group and individual control strategies with an AVPFC controller on each WEC were compared and tested in this chapter. The disadvantages of having individual controllers that

did not communicate with each other were established. Due to the close electrical proximity of the WECs within the array, the WECs in the farm could be controlled as a single device. It was established that having a master/supervisory controller in the farm, with access to the operating power factor and voltage of the farm, was necessary for optimal use of the reactive power capability of the farm. In the case of power shedding too, the farm with a supervisory controller performed much better than the case where the individual controllers on the WECs did not communicate with each other.

The succeeding chapter investigates the effects of controlling the wave power farm locally on the other voltage control devices in the network and discusses how the different controllers can be coordinated for optimal voltage control.

Chapter 6
Voltage estimation at the far end of a rural distribution feeder

6.1 Introduction

Until now, the focus of the work reported was on optimising the operation of the wave power farm to avoid the varying nature of the power generated from causing voltage violations in the network to which the farm is connected. A significant part of this thesis examined voltage fluctuations due to the connection of wave power farms and looked at means by which these fluctuations can be reduced. In Chapter 4, means of reducing the fluctuations in the power generated and hence the voltage were suggested that involved spacing and orienting the WECs differently within the wave field. It was found that even after appropriately placing the WECs within the wave power farm, significant fluctuations in the power profile still remained. To ensure the prevention of voltage violations and the continued connection of the farm to the electricity network, voltage and power factor control mechanisms for the farm were introduced and tested in Chapter 5. In that chapter, the focus was on primary voltage control using reactive power control of the connected wave power farm. Intelligent volt/VAr controllers like the AVPFC and the FLPFC were also described. Distribution networks generally have other voltage and power factor control elements like the OLTC transformer at the substation, which might not work effectively with the connection of the wave power farm. This is specially the case if these intelligent controllers of the farm are not coordinated with the control of the onshore control elements.

This chapter looks at a means of estimating the downstream voltage from the substation OLTC transformer. The voltage estimator can be used to predict the voltage at the bus where the wave power farm is connected, through measurements made at the substation. Before explaining the estimation method, power flow runs have been performed to show its necessity. Other benefits that may be accrued by using the information gained from the estimation are also discussed. The voltage estimation method developed, uses real and reactive power measurements made at the substation prior to the connection of the wave power farm. A demand prediction method is

described in this chapter, which returns the real and reactive power demand at the substation at future instants of time. The demand prediction algorithm is a simple one, which uses past values of the measured demand and values of the demand from historical archives to make a one-step-ahead prediction. Hourly spaced data, obtained from [176, 185], have been used to train a wavenet network, which is then used to predict the demand. Three models using different sets of past and current data have been developed for the prediction and are compared in this chapter. The performance of two nonlinearity estimators available in the system identification toolbox of MATLAB/Simulink is also compared. The percentage errors in the predicted demand have been fitted to normal distributions and the mean and standard deviation of the percentage errors have then been used in the voltage estimation method described later in the chapter.

Once the predicted real and reactive power flows at the substation are available, real-time measurements of the voltage, real power and reactive power at the substation along with the predicted demand values are used to estimate the voltage at the bus where the wave power farm is connected. A neural network has been trained with the data obtained from offline power flow simulations, which estimates the voltage at the bus under consideration. This work shows that the voltage estimation method by itself has a high accuracy and can be used instead of state estimation techniques or full power flow simulation runs. The only uncertainty in the estimation is introduced by the imprecision in the demand prediction.

The main advantage of the method developed is that no communication means or new measurement devices are required to make the estimation. Simple one-hidden-layer neural networks have been used and the method developed can be implemented in standard microcontrollers or microprocessors. The developed voltage estimation method has then been applied to identify the control mode of a wave power farm, controlled by the Automatic Voltage and Power Factor Control (AVPFC) method, connected to a generic 11 kV distribution network.

6.2 Need for voltage estimation

In this section, the need for effective voltage estimation at the substation is discussed. The voltage estimation is performed with the aim of coordinating the controllers of the WECs within a wave power farm and the substation OLTC transformer. The operation of the AVPFC and FLPFC methods and the control of the OLTC transformer were discussed in detail in the previous chapter.

To study the interactions between the controllers of the substation OLTC transformer and the

wave power farm, only a simple two-bus system (see Figure 2.26) has been used initially. The issues that would be seen when the two uncoordinated controllers interact will normally worsen as the complexity of the radial distribution network increases (for example when there are laterals drawn out from the main radial feeder). The OLTC transformer between buses 2 and 3 controls the voltage at the bus where the wave power farm is connected. The transformer is used as a voltage regulator. More complex networks might need the transformer to operate as a load drop compensator (LDC).

When an OLTC transformer is used as an LDC, current measurements made at the site of the transformer are used to estimate the voltage at the load centre [150]. The transformer's tap position is determined once the voltage estimate is known. The LDC settings for the resistive and reactive compensation R_{set} and X_{set} need to be decided before the LDC can be used. Once the settings are decided, the LDC is found to work satisfactorily for cases when the OLTC transformer deals with unidirectional power flows (towards the end of the radial feeder). The presence of a DG operating at a constant power factor will require the settings of LDC to be changed to account for the presence of the DG. When the DG is controlled using more intelligent controllers (like the AVPFC and the FLPFC methods), the LDC will not be able to accurately estimate the voltage changes caused by the varying amounts of reactive power exchanged by the DG with the network. When the real and the reactive power outputs from the DG vary, which will be the case when intelligently controlled wave power farms are connected to the network, the R_{set} and X_{set} will need to be varied continuously to give a good estimate of the voltage downstream of the substation. Therefore, a means to estimate the voltage at the bus where the wave power farm is connected becomes important. Additionally, knowledge of this voltage provides an opportunity to coordinate the operation of the OLTC transformer and the wave power farm based on some optimisation criterion (eg. reduction of losses, lowering the number of tap changes, etc.). The interactions between the controllers have been studied using simulation runs in which the wave power farm is modelled in a 1800-second sea state (see Figure 5.4 for H_s, T_z details).

6.2.1 Interactions between the wave power farm controlled by the AVPFC method and the substation OLTC transformer

Section 5.5.2 explained the procedure that would be used to select the different voltage and power factor set points of the AVPFC controller based on the demand patterns seen at the site and the size of the wave power farm. To accommodate the export of maximum real power

AVPFC parameter	OLTC setting
V_h = 1.05 p.u.	V_{nom} = 1.03 p.u.
V_l = 0.97 p.u.	V_h = 1.04 p.u.
PF_B = 0.9975 (lag)	V_l = 1.02 p.u.
PF_T = 0.9975 (lead)	$Tap_{max/min}$ = $\pm$7
T_d = 10 s	T_d = 60 s

Table 6.1: *The AVPFC parameters and the OLTC transformer settings*

generation by the wave power farm, the voltage set point is normally chosen to be close to the allowed upper voltage limit (1.05 p.u. or 1.055 p.u.). The substation OLTC transformer would normally be set such that the voltage at its secondary is 1.03 p.u. This is done to prevent low voltage violations occurring at the load-end of the network during periods of high demand, before the connection of the DG downstream. The set points of the AVPFC controller and the controller of the OLTC transformer used in the first simulation run are listed in Table 6.1. The operation of the two controllers with these set points is shown in Figure 6.1. It is seen that during periods when the sea is energetic (0-600 seconds and 1200-1800 seconds) and when the farm tends to operate in the constant voltage mode for considerable periods, a large number of tap changes occur. This is because the nominal voltage set points of the AVPFC controller and controller of the OLTC transformer are different. These unnecessary tap changes would eventually wear out the tap changing mechanism.

The unnecessary tap changes seen in the case just discussed can be avoided by setting the controller of the OLTC transformer to have a wider allowed voltage range when compared to the controller of the wave power farm. Such voltage set points are shown in Table 6.2, where the voltage range of the OLTC transformer overlaps that of the farm's controller. The nominal voltage of both the controllers is 1.03 p.u. The deadband of the AVPFC controller is +0.02 p.u and -0.06 p.u., whereas the deadband of the OLTC controller is +0.03 p.u. and -0.07 p.u. respectively. Since the time delay and the deadband of the OLTC transformer are larger than and overlap the AVPFC's time delay and the deadband, the OLTC tap changes occur only when the AVPFC controller cannot deal with certain voltage/ power factor conditions. In the simulation, no tap change occurs because no voltage violations are seen (see Figure 6.2). Thus, by proper selection of the AVPFC controller's set points, unnecessary tap operations may be avoided.

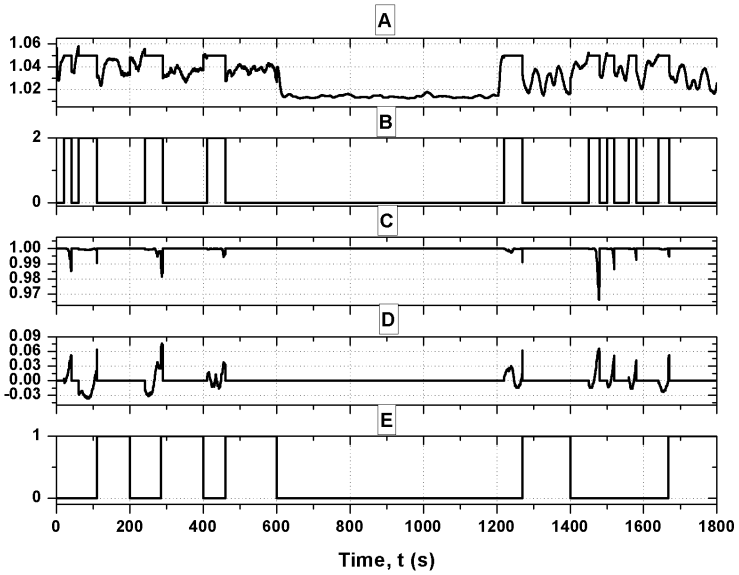

Figure 6.1: *Interactions between the uncoordinated substation OLTC transformer and the AVPFC controller of the wave power farm showing (a) bus 3 voltage (p.u.), (b) voltage / power factor control signal (2 - voltage control, 0 - power factor control), (c) power factor (-) (d) reactive power generated (MVAr) and (e) tap position (0 is the nominal position)(-).*

AVPFC parameter	**OLTC setting**
V_h = 1.05 p.u.	V_{nom} = 1.03 p.u.
V_l = 0.97 p.u.	V_h = 1.06 p.u.
PF_B = 0.9975 (lag)	V_l = 0.96 p.u.
PF_T = 0.9975 (lead)	$Tap_{max/min}$ = $\pm$7
T_d = 10 s	T_d = 60 s

Table 6.2: *The optimal AVPFC parameters and the OLTC transformer settings*

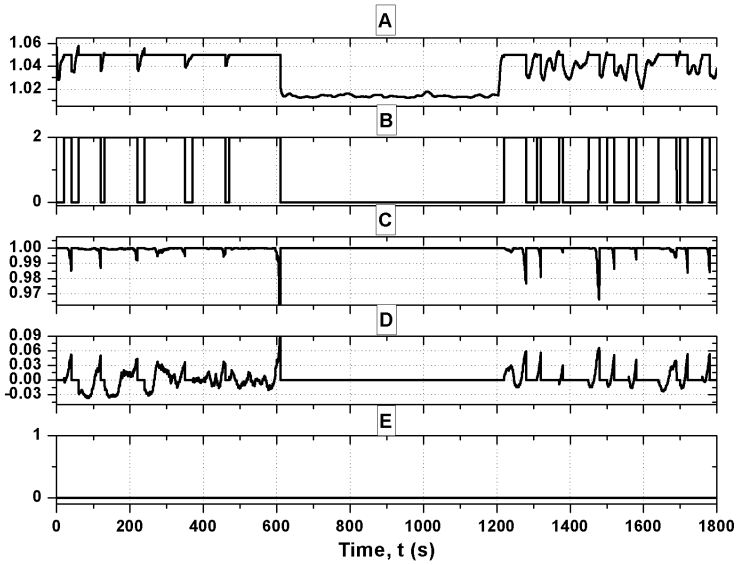

Figure 6.2: *Interactions between the coordinated substation OLTC transformer and the AVPFC controller of the wave power farm showing (a) bus 3 voltage (p.u.), (b) voltage / power factor control signal (2 - voltage control, 0 - power factor control), (c) power factor (-) (d) reactive power generated (MVAr) and (e) tap position (0 is the nominal position)(-).*

6.2.2 Interactions between the wave power farm controlled by the FLPFC method and the substation OLTC transformer

The problems associated with the controller of the farm interacting with the controller of the OLTC transformer are more significant when the farm operates at a constant voltage. This is the case when the AVPFC method is used to control the farm and was discussed in the preceding section. Since the farm's control using the FLPFC method is essentially operation at a power factor decided by the controller, no major increase in the number of tap operations are seen even when the optimal voltage set points (Table 6.2) are not used. This is shown in Figure 6.3 for the controller set points shown in Table 6.3. No tap changes are seen during the 1800-second simulation run. This is because even though the voltage goes above 1.04 p.u. a few times, the violation occurs for less than the time delay of the OLTC transformer. For a different sea state though, OLTC tap operations may have been seen, which can be avoided by using the the OLTC voltage set points listed in Table 6.2.

It was shown in this section that the selection of the set points of the two controllers in question has an influence on the performance of the whole system. Coordinating the two controllers

FLPFC parameter	**OLTC setting**
V_h = 1.05 p.u.	V_{nom} = 1.03 p.u.
V_l = 1.01 p.u.	V_h = 1.06 p.u.
	V_l = 0.96 p.u.
	$Tap_{max/min}$ = $\pm$7
	T_d = 60 s

Table 6.3: *The FLPFC parameters and the OLTC transformer settings*

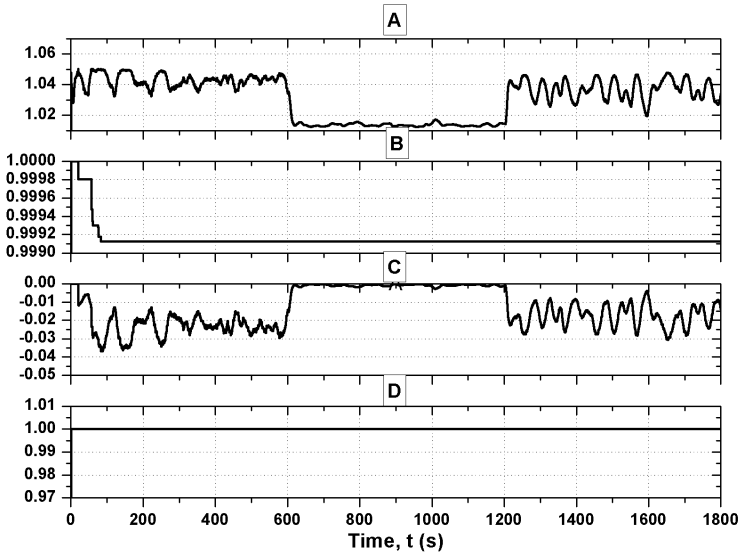

Figure 6.3: *Interactions between the uncoordinated substation OLTC transformer and the FLPFC controller of the wave power farm showing (a) bus 3 voltage (p.u.), (b) power factor (-) (c) reactive power generated (MVAr) and (d) tap position (0 is the nominal position)(-).*

provides a means to optimise the performance of the network. Such a means to coordinate the two controllers is discussed in this chapter. The technique developed relies on historical data collected at the substation to make accurate estimations of the voltage at the bus where the wave power farm is connected. In this section so far, a simple two-bus system has been considered where the controller of the OLTC transformer has exact measurements of the voltage at the bus where the wave power farm is connected. This estimation is simple for the two-bus system because the secondary terminal of the OLTC transformer is connected to the same bus as the wave power farm. This would not be the case in realistic networks. For proper coordination, a voltage estimate will be needed, but no straightforward method is available for this purpose. Some techniques discussed in literature, which could be adapted for this purpose, are compared and discussed in the next section.

One of the advantages of the estimation technique proposed in this chapter is that no additional measurements need to be made in the network and no means of communication between the wave power farm and the substation are required. The estimation technique developed can be used to coordinate and find the optimal operating set points of different voltage and power factor control elements found in the distribution system today.

6.3 Existing techniques

Before adopting the voltage estimation strategy discussed in this chapter, a specific study of the related literature was performed. The focus of the literature survey was not only on voltage estimation techniques, but also other methods that could be modified and used for estimating voltages in distribution networks.

Analytical expressions for the voltage along radial distribution feeders were derived in [193–195]. In [193], the emphasis was on controlling the DG connected to the distribution network using the derived voltage expression. The radial feeder was assumed to have uniformly distributed loading and generation, which is not the case in practice. In [194], the expression developed can be used only if the real and reactive power injection of the DG to the network is known. This is the case for controllable and dispatchable DG (CHP, diesel generator sets, etc.), but cannot be used when the power generation is varying in nature. A similar analysis was presented in [195] where the voltage along parallel feeders can be evaluated. Again in this publication, the real and reactive power injected by the DG is to be known beforehand. According to the goals set out at the outset of this chapter, the voltage estimation technique that

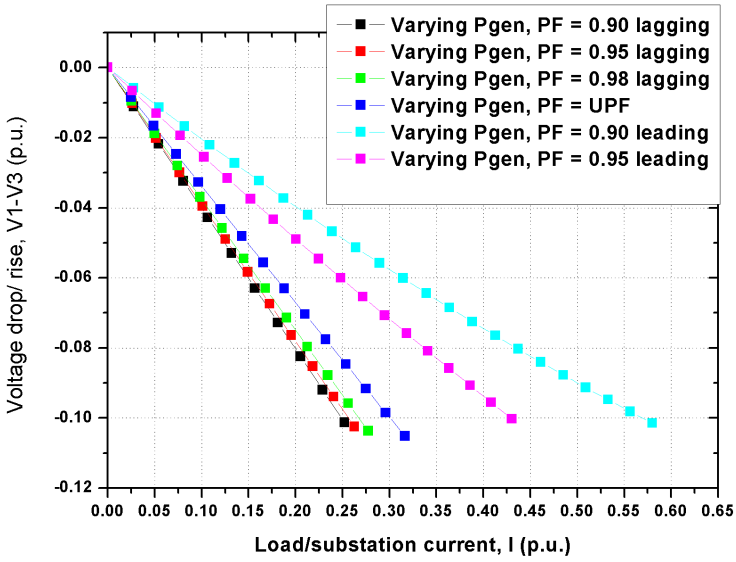

Figure 6.4: *The relation between different levels of real and reactive power generation from the wave power farm and the current measured at the substation.*

will be used to coordinate the control of two or more volt/VAr control elements in the distribution network should not need any real-time measurements of the power generated by the wave power farm. The estimation should ideally be performed through local measurements made at the substation and by using archives of historical load data measured at the substation, provided these are available.

A volt/VAr control strategy to be used at distribution substations was presented in [196]. In the method presented, the current measurement at the substation and the effective impedance Z_{eff} of the feeder are used to determine the voltage drop. In the publication, Z_{eff} was taken to be purely real. The IEEE 34-bus system [197] was chosen for their analysis and the network did not have any generator connected. The same procedure suggested in the paper was tested with the addition of a DG to the IEEE 34 bus network. It was found that the suggested method could still be used when the DG operated at a constant power factor. When controlling the wave power farm using the AVPFC or the FLPFC method, the operating power factor of the farm varies depending on the energy in the sea. Therefore, the method suggested in [196] cannot be used to estimate the downstream voltage. Figure 6.4 shows the change in voltage along a feeder for different real and reactive power generation by the DG connected to the network shown in Figure 2.26. The figure clearly shows that the proposed method cannot be used in the case of a wave power farm controlled by the AVPFC or the FLPFC methods.

Another approach was tried in which the system impedance from two voltage and current measurements at the wave power farm was calculated and used to estimate the current tap position of the substation OLTC transformer [198]. In this approach, both the real and imaginary parts of the voltages, currents and the system impedance were used in the calculations. This procedure again proved to be ineffective as the calculated system impedance changed depending on the real and reactive power generated by the farm and the demand at the different buses.

A method to reduce any radial distribution network to a two-bus system with an equivalent impedance and an equivalent load was described in [199]. Expressions for the real and reactive power through each branch in the network and the voltage at every bus of the network were derived. This approach can only be applied with purely radial networks, which will not be the case in reality. A similar approach was described in [200], where expressions used to derive the equivalent impedance were given. In this approach, the apparent power fed to each bus is to be known before the equivalent impedance is calculated. In the case of a wave power farm, the apparent power fed to the network by the farm varies and thus such a reduction procedure cannot be applied. This approach was further extended in [201–203] to accommodate more complex radial distribution feeders. In both these papers, a novel method for solving the load flow in radial distribution networks was examined. Both these approaches required the real and reactive power injection from the last bus in the laterals for solution. This means that some communicating means to send the information regarding the measured quantities to the substation was required. The use of such communication and measurement requirements at the wave power farm will be avoided by using the voltage estimation method developed in this chapter.

Different state estimation techniques have been developed and are discussed in [204–206]. State estimation techniques have been used in commercially developed products like GenAVC developed by Senergy Econnect [207]. Most of the state estimation applications to distribution networks involve some measurements and pseudo measurements being made and communicated. The power injected at buses, currents through lines, voltages at buses, etc., are generally the estimated variables. For the voltage estimation method developed in this work only historical demand data and the real and reactive power measurements made at the substation are required. Therefore, the full state estimation procedure used in these publications will not be required. The full state estimation procedure is mathematically laborious. The neural network fitting based method, developed in this work, can be implemented relatively easily in micro-

controllers.

The SuperTaPP n+ system [156, 208], developed by Fundamentals Ltd. [209], uses a method of separating the generation and the load components of the substation current using current measurements made before and after the DG is connected to the network. Since only the current magnitude is used in the calculations shown in these publications, it is obvious that the system will not be effective when the DG exchanges reactive power with the network. The method was mainly developed to improve the performance of the LDC, when a DG is connected to the network downstream of it. The application of the SuperTAPP n+ system, for substations feeding parallel feeders, was also demonstrated in a real distribution network and the results were discussed in [210]. The method presented in this chapter is an improvement to the methodology used in the SuperTAPP n+ device.

6.4 Load forecasting

For the voltage estimation method presented in this chapter, an estimate of the load patterns observed at the substation is required. This section describes a simple one-step-ahead load forecasting method which will be used in conjunction with the voltage estimation method.

Load forecasting has for long been used in the planning and operation of electrical utilities. Short-term (up to one day), medium-term (a day to a year) and long-term (a year to 10 years) load forecasts have been used for planning and devising control mechanisms for electric power systems. The focus in this section will be on short-term load forecasts. A range of different techniques have been used for making these forecasts, some of which are [211]:

- Similar day approach - where from a database a similar day is chosen and the load is forecasted depending on what was seen on that day;
- Regression method - in which a relationship between the load pattern and certain variables like the weather, the day type, etc., is found and then used to forecast loads;
- Time-series approach - where variations (yearly, monthly, weekly and daily) in the demand pattern are recognised and are used to forecast loads;
- Neural networks [212] - which can be used to model nonlinear relationships between different independent variables and the demand;
- Rule-based systems [213, 214] - which use heuristic rules to make demand forecasts;

- Fuzzy logic [215–217] - which is another technique of mapping inputs to outputs, where the inputs and the outputs take certain qualitative ranges and not just the Boolean logic truth values of zero and one;
- Support vector machines - these are techniques used for classification and clustering, which can also be used for load forecasting;

  A list of references for short-term load forecasting using the different methods listed above is available in [218].

In the current work, the focus will be on a one-step-ahead load forecast, which is performed using an approach in which both time-series analysis and neural networks are used. Data of the demand at a substation in the Stornoway/Harris 33 kV distribution network have been used in this work. The data consist partly of measurements from the substation and partly of demand generated based on the measurements made. The data has been collated over three years (2001-2003). The data consists of hourly real power measurements. Since the data only has real power measurements, the estimation of the real power at the substation alone has been performed in this chapter. The same procedure developed here may be used to get estimates of the reactive power flow at the substation too.

System identification has been examined earlier in Chapter 3 as a means to map the input-output relationship of systems. In the same fashion as elucidated in that chapter, nonlinear exogenous models of the historical demand and the one-step-ahead demand have been developed. The models used here are only use the current and past demand to predict the next demand. Therefore, the models are different from the NARX models developed in Chapter 3, where even past outputs were used in the regressor set.

Different sets of the demand data have been used to develop these models. The performances of the models developed, in predicting the one-step-ahead demand, have then been compared and the results are presented in this section. The demand prediction techniques developed in this work use only past values of the demand. No other variables like temperature, humidity, etc., which are commonly used in load forecasting methods [219] have been used. The load forecasting technique discussed in this work will form the first part of the voltage estimation method which is discussed in Section 6.5. The electrical demand/load variation has daily, weekly, monthly, and yearly patterns, which can be used to predict the future demand. This section explores how these variations can be modelled and then used to predict the future

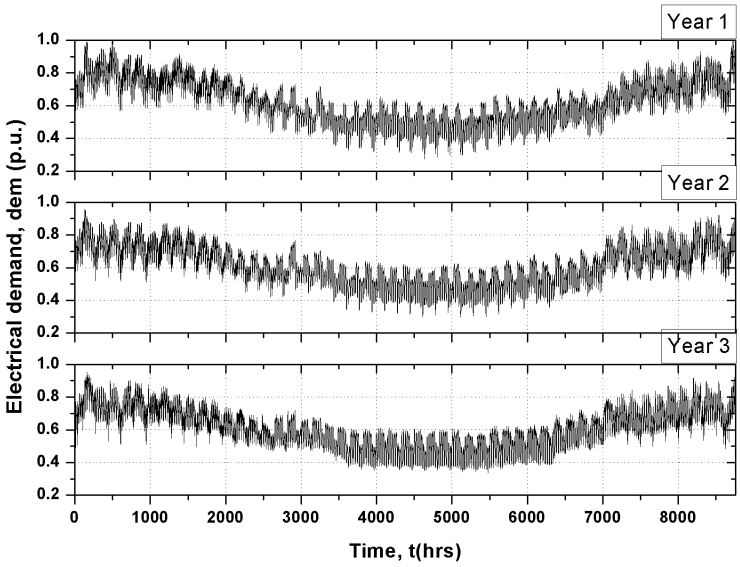

Figure 6.5: *The electrical demand pattern at the Isle of Lewis over three years.*

demand patterns.

6.4.1 Correlation between the annual demand patterns

Figure 6.5 shows the variation in the real power flow measured at a substation in the Stornoway distribution network over a period of three years. Very prominent similarities in the annual demand profiles can be observed from the figure. Relatively lower demands are seen during the summer months and higher demands are seen in the colder months. The characteristics of the weekly demand profile can also be seen with dips in the demand during the weekends. Figure 6.6 shows the demand pattern over the same month in the three years. There are similarities in the demand pattern seen, which have been used here to predict the future real power demand at the substation.

Figure 6.7 shows the correlation between the real power demands of year 1 and year 2. A regression coefficient of 0.945 was obtained between these two quantities. The system identification process used for the one-step-ahead load prediction needs to try and model the discrepancies from the linear fit seen in the figure. Figure 6.8 shows the residual in the year 2 demand values, with respect to the corresponding year 1 demand values. It is seen that the values of the residual are not dependent on the magnitude of the year 1 demand. The aim of the system identification process thus is to reduce the value of this residual through proper modelling.

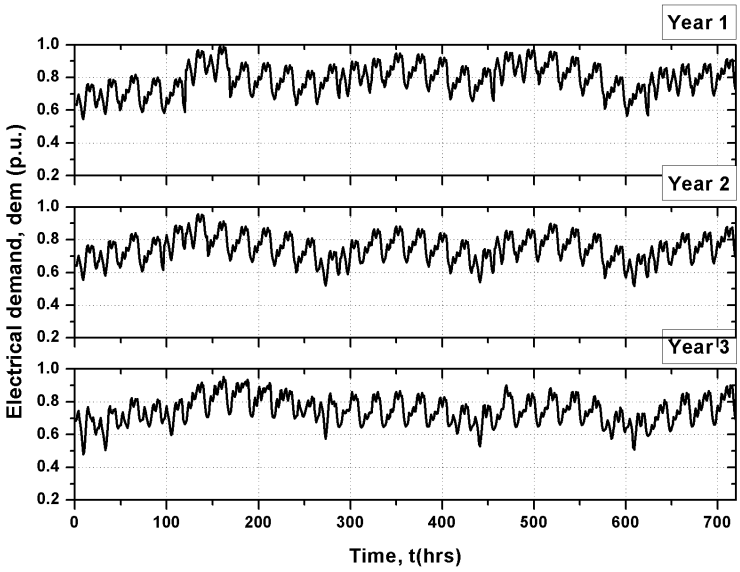

Figure 6.6: *The electrical demand variation over a month at the Stornoway distribution network.*

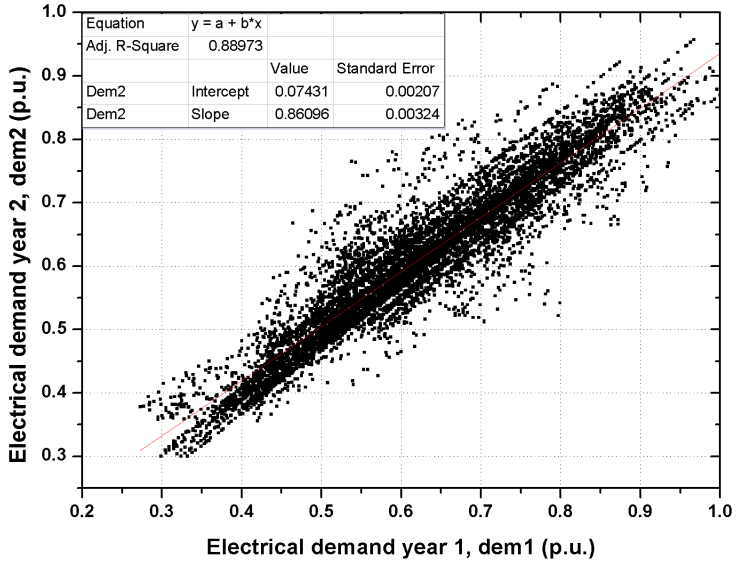

Figure 6.7: *Correlation between the demand seen in year 1 with the demand seen in year 2.*

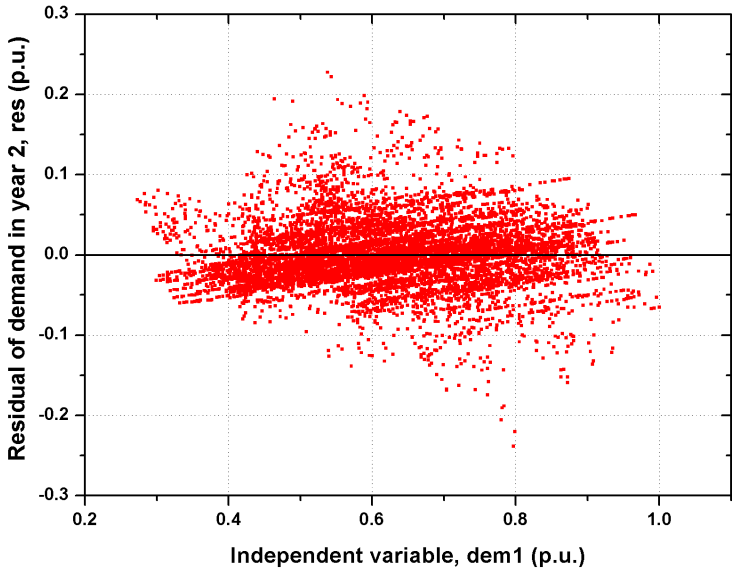

Figure 6.8: *Residual in the demand of year 2 with respect to the corresponding year 1 demand.*

6.4.2 System identification for one-step-ahead demand prediction

Three nonlinear exogenous models have been developed to predict the demand patterns. The averaged hourly demand data measured over three years have been used to train and construct the models and also to validate them. Three different regressor sets have been used to train the neural network and the performance of the models constructed using these regressor sets has been compared.

In model 1, to predict the demand at the current time t_i, the demand at time t_{i-1}, t_{i-2} and t_{i-3} and the demand at time t_i, t_{i-1} and t_{i-2} of the preceding year have been used as inputs. That is, the corresponding demand seen during the previous year on a similar day is used to predict the next demand of the current year. This model tries to model the similarities in the demand pattern over years. In model 2, to predict the demand at the current time t_i, 25 previously measured demand values have been used. This model in effect uses the daily patterns in the demand profile. In model 3, the demand at time t_i has been estimated based on the current day's demand at t_{i-1} and the demand at time t_i and t_{i-1} of the previous day. This modelling approach is similar to the one found in [220]; the difference being the nonlinear mapping function used here. It is observed that model 1 would require maximum amount of stored data, since the corresponding demand values from the previous year are required. On the other hand, both models 2 and 3 require almost the same amount of stored data (demand of the previous day/ 25

past demand values).

6.4.3 Performance of the demand predictor

6.4.3.1 Comparison between the wavenet and the treepartition nonlinearity estimators

For the estimation, two nonlinearity estimators - the wavenet network and the treepartition network - have been tested. Both these nonlinearity estimators have inherent characteristics which make them react differently to the training set. The demand prediction models constructed using the two nonlinearity estimators have been compared and the results are discussed in this section. Wavenet neural networks have been extensively described and discussed in Chapter 3. The theory behind wavenet networks is not discussed further here.

Treepartition networks create partitions of the regressor space defined by a binary tree and fit the input to the output in these partitions using piecewise linear functions or simple regression models [119, 221]. In the System Identification toolbox in MATLAB, the number of such partitions (or units) is determined iteratively. The theory of regression and classification trees is available in [222] and these trees form an important part of data mining studies in computer science.

Figure 6.9 shows the estimated and the measured demand pattern of year 2 over a 100-hour period, when the wavenet and the treepartion nonlinearity estimators were used for constructing model 1. The predicted demand shows a good fit to the measured demand for most periods during the 100 hours. A wavenet network with 51 units and a treepartition network with 1023 units were used and a fit of 90.21% and 92.05% were respectively obtained. The figure also shows the distribution of the percentage error for the estimation achieved using both the networks. For most periods the percentage error is less than $\pm 5\%$. The percentage error distribution shown in the figure has a mean of 0.03055% and a standard deviation of 2.1291 for the wavenet network and 0.0545% and 1.6164 for the treepartition network. Models 2 and 3 also showed a better fit to the validation data and a lower standard deviation for the estimation achieved using the treepartition network.

Figure 6.10 shows the spread of the residual over the range of year 2 demand values. Comparing this figure with the residual spread shown in Figure 6.8 shows the improvement in the demand prediction made using model 1 with the treepartition network, when compared to using only the correlation of the measured demand values of year 1 to make the prediction.

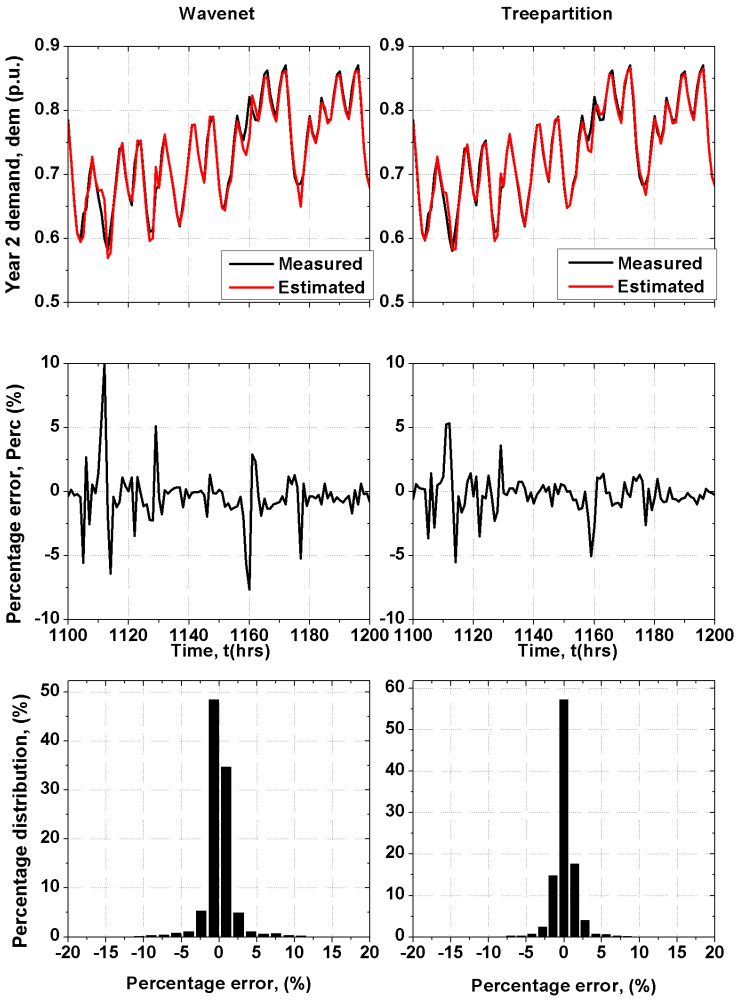

Figure 6.9: *Comparison of the wavenet and the treepartition network for the one-step-ahead demand prediction using model 1.*

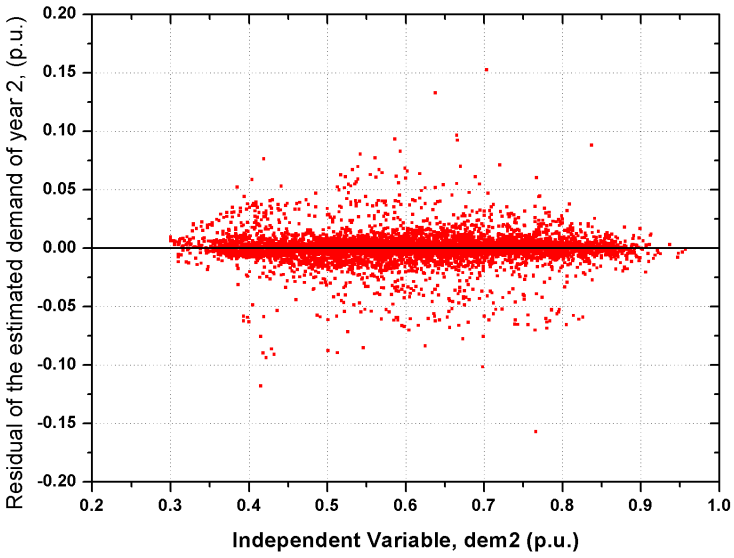

Figure 6.10: *Residual in the estimated demand with respect to the measured year 2 demand, using model 1 with the treepartition network as the nonlinearily estimator.*

6.4.3.2 Comparison between models 1, 2 and 3 for estimating year 3 data with the treepartition network

The results in Figures 6.9 and 6.10 were obtained when the demand values of year 2 were predicted. Since a time-delayed year 2 demand pattern was used to train the model, estimating the year 2 demand may not be a good validation test for the model developed. In this section, the performance of the three models in estimating the one-step-ahead year 3 demand is compared.

Figure 6.11 shows the percentage distribution of the percentage errors obtained when estimating the year 3 demand using the three models. In all the three cases, the percentage error values are less than $\pm 5\%$ for most of the predicted demands. The average percentage error and the standard deviation obtained using the three models are respectively 0.0038%, 0.0705%, 0.0425% and 2.5838, 2.6574, 2.0628. The maximum percentage error in the estimated demand is approximately 20%, which occurs very rarely. As expected, the estimation of the year 2 demands, discussed in the previous section, is comparatively better than the estimation of the year 3 demands. This is attributed to the fact that the year 2 data was a part of the training data used to train the treepartition network used when constructing the three models.

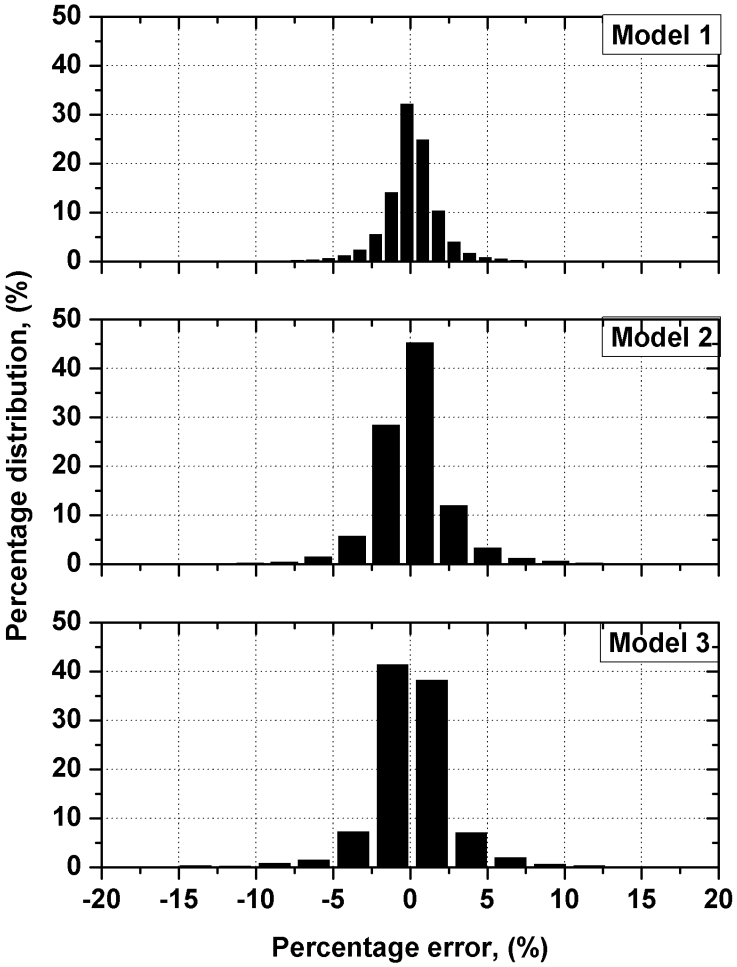

Figure 6.11: *Comparing models 1, 2 and 3 when the model is trained with the data from year 1 and 2 to predict the year 3 demand.*

6.4.3.3 Comparison between the models generated using the 1-year and the 2-year training data set for year 3 demand prediction

In all the results shown so far in this section, only the year 1 data and the time-delayed year 2 data have been used as inputs to train the network. The year 2 data was the output and a relationship between the year 2 data and the input data was modelled. In this section, the effects of increasing the size of the training set are examined. For this, data from the first two years (year 1 and year 2) have been used for the estimation of the year 3 demands. Time delayed demand data of year 3 have also been used as one of the inputs during the training process.

Figure 6.12 shows the same results as in Figure 6.11, but when the model has been developed using the larger training set. The tails of the percentage distribution in this figure are steeper and the maximum percentage error values are lower compared to the results shown in Figure 6.11. The mean and the standard deviation for the three models constructed using the 2-year data are respectively 0.0545%, 0.1345%, 0.0454% and 1.6155, 2.6452, 2.7436. These values were obtained when the model was constructed using treepartition networks.

6.4.3.4 Validation

The load forecasting method developed in this section is not meant to replace other load forecasting techniques which are in use today, most of which include more variables in their prediction analysis and hence may give more accurate results. The method developed shows that even the simple load prediction technique discussed here gives a good estimate. The simplicity and the accuracy with which the demand prediction is completed here, makes the suggested method attractive for use especially in rural substations where complex load forecasting solutions using measured values of weather conditions may not be practical. One of the main advantages of this suggested method is that only past values of the demand are used in making the estimate.

A time-series of randomly generated percentage errors, obtained from the probability distribution of the percentage errors in the estimated demands, will be added to the actual demand profile to obtain the forecast of real power flow at the substation. This assumption has been used in the voltage estimation technique discussed in the next section. It will be shown that the voltage estimation methodology works satisfactorily even when using the simple load forecasting method discussed here. With better demand forecasts, the voltage estimates will improve.

This section described three models which can be used to predict the one-step-ahead demand

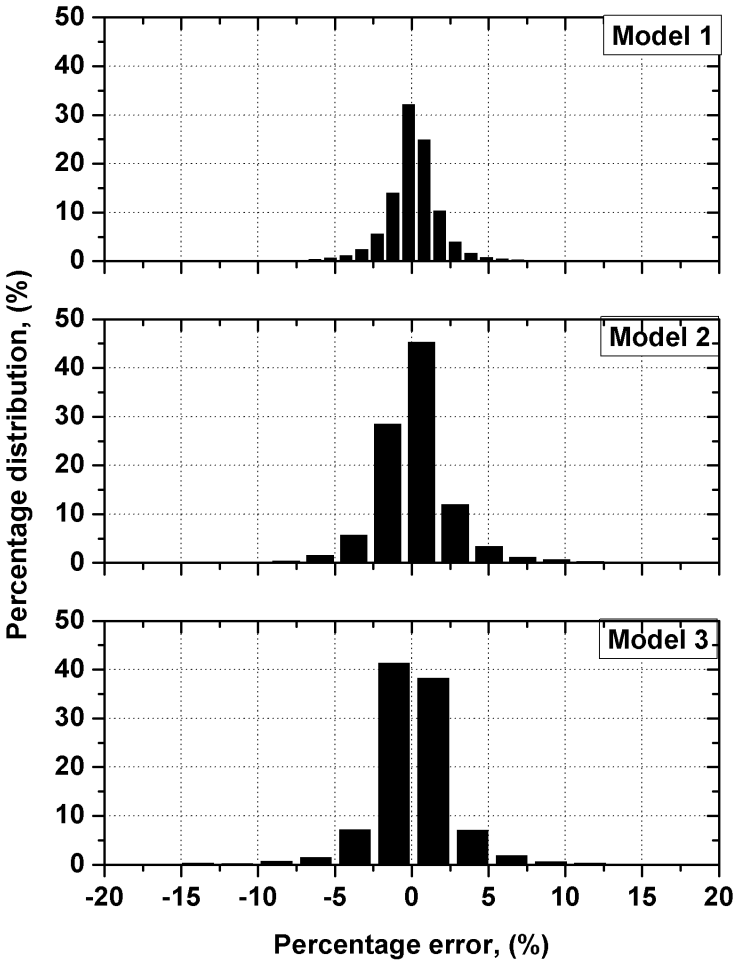

Figure 6.12: *Comparing models 1, 2 and 3 when the model is trained with a larger data set (collected over two years).*

pattern using past values of the demand. The performance of the three models was compared. Both wavenet and treepartition networks were used and their performance compared. The treepartition network gave lower values of standard deviation and maximum percentage errors for the data sets and hence was chosen to generate the results discussed in the following sections. A significant difference in the performance was not seen when the three models, built using three different regressor sets, were compared. All the models constructed produced an error of less than 5% for most of the time during which they were tested. The maximum percentage error seen was approximately 20%, which occurred very rarely.

6.5 Voltage estimation

The need to coordinate the control of the different voltage and power factor controllers in the distribution network was discussed earlier in the chapter. Some of the gains obtained through the coordination of the control elements were also mentioned there. As an example, the coordination of the control of the substation OLTC transformer and the volt/VAr controller of the wave power farm was briefly examined. It was found that unless the two controllers were coordinated, there would be unnecessary tap changes in the substation OLTC transformer and also a probability of voltage set point runaway. The drawbacks of the LDC system used to control OLTC transformers, especially when a new generator is connected downstream of it, was also touched upon. Some means is therefore necessary to remove the DG's effects on the power flow for the LDC to operate as expected. Additional benefits can be gained if the added knowledge about the control mode or voltage at the far end of the feeder can be used to modify the control of the substation OLTC transformer based on some optimisation criterion.

The preceding section looked at a simple demand prediction technique, which predicts the one-step-ahead real power flow at the substation using past values of the flow. It was mentioned that the demand prediction technique presented would be used in conjunction with a voltage estimation methodology, which is the subject of this section. A voltage estimation method is described here which can be used to obtain information about the operation of the wave power farm at the substation. The generic UK 11 kV rural distribution system, shown in Figure 5.21, has been used to validate the method. A 4 MW wave power farm is connected to bus 56 in the network. As mentioned earlier, the aim of this work is to sense the bus 56 voltage at the substation (bus 53). This method uses no communication lines and only measures the real and reactive power and the voltage at the substation to make an estimate of the voltage at bus 56. These are measurements that are normally made at substations and hence no additional

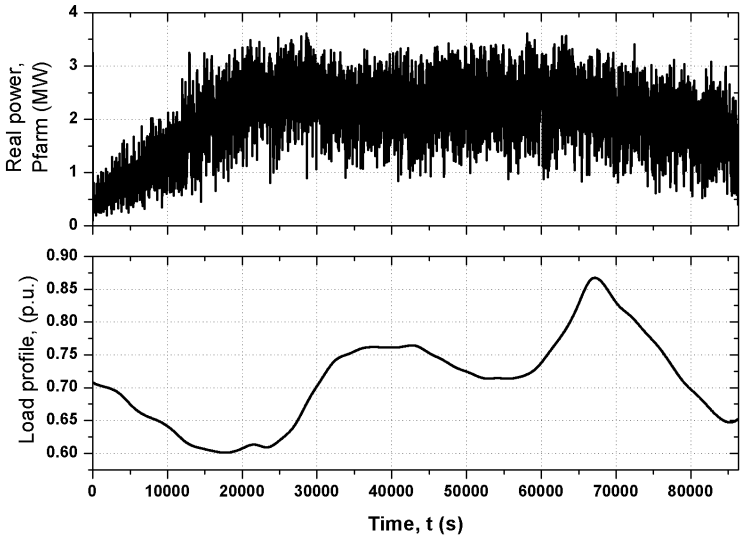

Figure 6.13: *The real power generated and the demand profile over a day.*

measurements will need to be made. An archive of historical real and reactive power flow at the substation prior to the connection of the wave power farm is required for using this method. The data may be obtained from offline simulations of the network or from archives of measured data.

6.5.1 The methodology

The relationship between the real and reactive power and the voltage at the substation and the voltage at the bus where the wave power farm is connected is nonlinear. This relationship has been modelled in this work by training neural networks with historical data.

Figure 6.13 shows the variation in the real power generated by a 4 MW wave power farm over a day. The load profile over a winter day is also shown in the figure. Figure 6.14 shows the results of the power flow solution, performed over a day, both before and after the connection of the wave power farm to the network. The changes in the measured values brought about by the connection of the wave power farm have been used here to estimate the voltage at the bus where the wave power farm is connected. The simulation in this section and the results in Figure 6.14 have been obtained with the substation voltage kept constant at 1.03 p.u. and the wave power farm operating at UPF. Since the method uses only measurements made at the substation, the developed method is independent of the load profiles used at each bus and the varying nature of the power produced by any generator connected to the network.

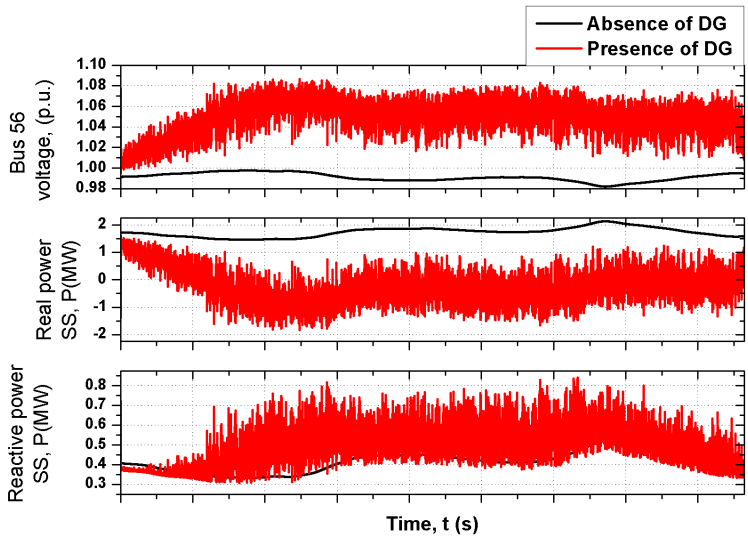

Figure 6.14: *The real and reactive power measured at the substation and the bus 56 voltage profile over a day.*

A training data set with 120,000 sets of real power, reactive power, substation voltage, and voltage at bus 56, both before and after the connection of the wave power farm, were obtained through power flow runs. 100 randomly generated loads (between 0.25-1 p.u.), 100 randomly generated real power outputs from the connected wave power farm (between 0-6 MW) and 12 power factors from 0.95 to UPF (both leading and lagging) were used in these power flow runs. The training data set thus had values of the real power and the reactive power generation and the loads across the range normally found in the network. In the simulation runs used to obtain the training data, all the loads have been assumed to have the same profile, which is valid in the case of rural networks [223]. A test case in which half the loads have randomly generated profiles has also been tried and the results are presented later in this chapter.

The Neural Network toolbox [111] available in MATLAB has been used to estimate the voltage. The theory of neural networks and their training was discussed in detail in Section 3.3.3. Figure 6.15 shows the structure of the neural network used in this study. As mentioned earlier, the real and reactive power flow and the voltage at the substation, both before and after the connection of the wave power farm, are the inputs to the neural network. The hidden layer of the neural network consists of 20 neurons. The hyperbolic tangent sigmoid transfer function has been used as the activation function of the neurons in the hidden layer and is shown in Figure 6.16. The outputs of the neurons in the hidden layer are linearly summed in the output layer. The weights and the biases of the hidden layer and the output layer are selected during

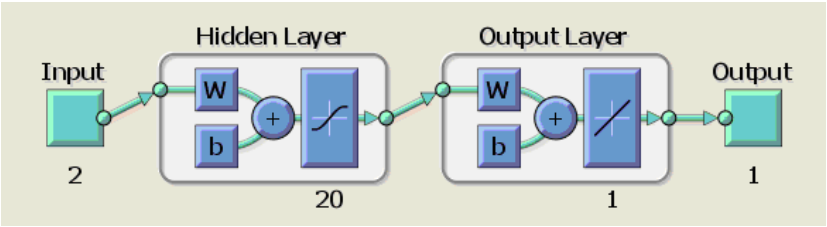

Figure 6.15: *Structure of the neural network used for the voltage estimation.*

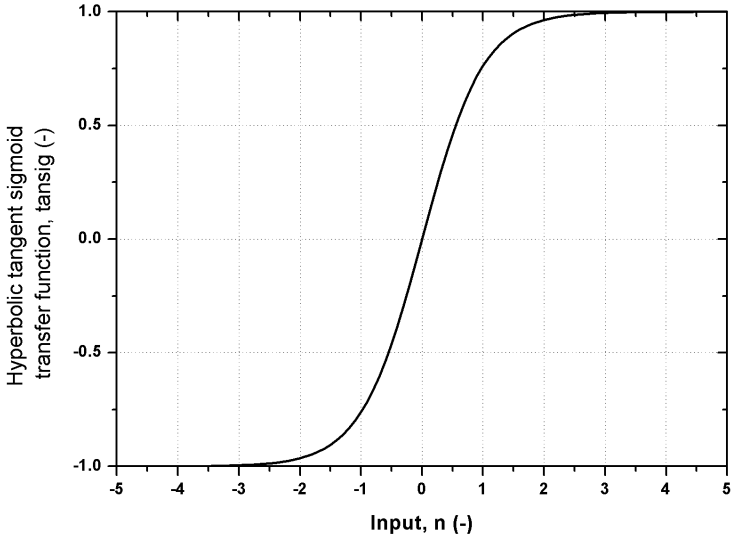

Figure 6.16: *The hyperbolic tangent sigmoid transfer function.*

the training of the network using the Levenberg-Marquardt algorithm (see Section 3.3.4 for details of learning in neural networks). The output of the network is the rms-voltage magnitude at the bus where the wave power farm is connected. After training the network with the data, plotting the target values with the output from the network gave a regression coefficient of 0.99998, which means that the neural network almost exactly models the relationship between the variables in consideration. The regression plots are shown in Figure 6.17.

6.6 Voltage estimation methodology validation

6.6.1 Loads conforming to generic profile

In this section, the voltage estimation method established in the preceding section is validated using simulation runs in which actual time-series of the real and reactive power generated by the wave power farm have been used. The time-series of the real power generated by the wave power farm, under different sea conditions, have been obtained through 100-second simulation

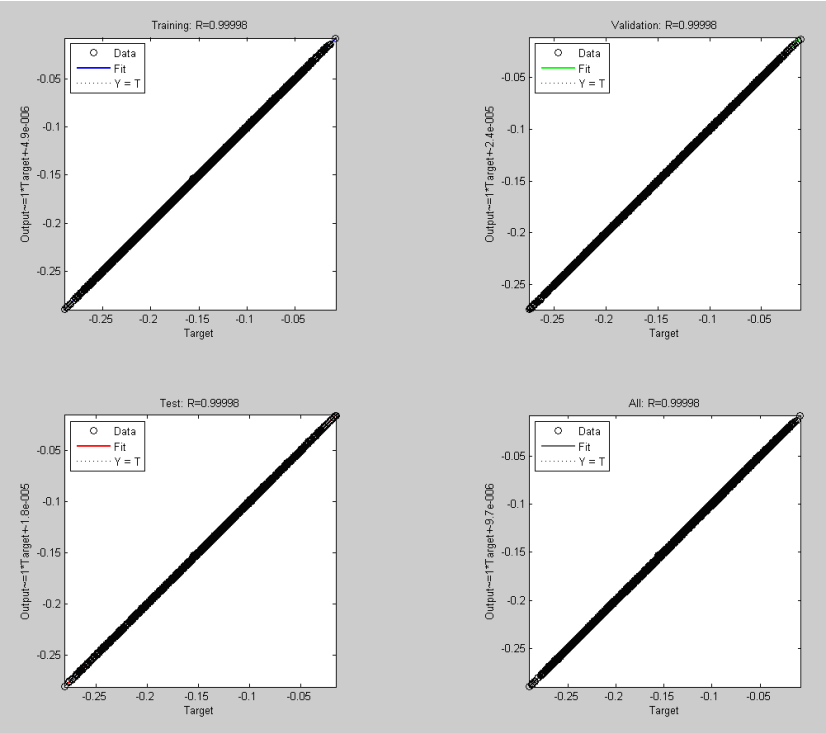

Figure 6.17: *The regression coefficients obtained from the neural network based fitting.*

runs (1000 data points). The different sea states used are listed in Table 6.4. These time-series of real power, under different wave power farm operating power factors and varying demand in the network, have been fed to the distribution network at bus 56. Power factors spaced at 0.01 from 0.95 to 1 (both lagging and leading) and electrical demands from 0.25 to 1 p.u. spaced at 0.05 p.u. have been used in the validation process. Thus, 192192 sets of data points have been used to validate the voltage estimation method for each of the 9 sea states used. In this section, only the voltage estimation method is validated using the different sets of data and it has been assumed that the real and reactive power flow at the substation, before the wave power farm is connected, has been predicted with an accuracy of 100%. The effects of having demand estimates with different accuracies will be dealt with in the next section.

Table 6.4 shows the results of the validation performed for all the sea states used. The percentage error listed in the table is the error between the voltage obtained through power flow runs and the estimated voltage. It is seen that the maximum, minimum and average percentage errors are extremely small. The values of the standard deviation of the percentage errors for the nine sea states used are also small.

Figure 6.18 shows a snapshot of the results for the $H_s = 4$ m, $T_z = 8$ s sea state. The actual voltage at the bus where the farm is connected, obtained from the power flow solution, and the

Sea state (H_s (m), T_z (s))	**Standard deviation of percentage errors**	**Maximum percentage error(%)**	**Minimum percentage error(%)**	**Average absolute percentage error(%)**
1 m, 4 s	0.0025	0.0068	-0.0038	0.0026
1 m, 6 s	0.0024	0.0057	-0.0053	0.0021
2 m, 6 s	0.0020	0.0011	-0.0095	0.0034
2 m, 8 s	0.0019	0.0005	-0.0097	0.0037
4 m, 6 s	0.0036	0.0083	-0.0082	0.0029
4 m, 8 s	0.0037	0.0100	-0.0082	0.0030
6 m, 8 s	0.0053	0.0133	-0.0100	0.0051
6 m, 10 s	0.0050	0.0133	-0.0094	0.0048

Table 6.4: *Errors in the estimated voltage*

voltage estimated using the neural network constructed in the previous section are shown in the figure. A close match between the two is seen. In the 200 instants of time plotted, the maximum residual observed is 0.0001 p.u. and the maximum percentage error seen in 0.01%. Figure 6.19 shows the percentage distribution of the percentage errors for all the validation tests performed. It is observed that the percentage error is less than 0.01% for the entire time-series used.

Another validation run has been performed in which the wave power farm is simulated under the sea state A (see Section 5.5). The operating power factor of the wave power farm has been changed every 60 seconds (shown in Figure 6.20). The electrical demand of the network has been randomly varied between 0.25 and 1 p.u. at every instant of time. The actual and the estimated voltage obtained through this run are plotted in the figure along with the residual and the percentage error. The maximum absolute percentage error seen is approximately 0.033%. The values of the percentage error seen in this run are higher than those seen in Figure 6.18, since in the previous case the same power factors used to train the neural network were used in the validation. In the present case, the power factors in the same range have been randomly chosen.

6.6.2 Loads not conforming to the generic profile

The loads connected to all the buses in the preceding section followed the same generic load profile. This selection is justified being a rural distribution feeder. Changing the load profile of certain loads might make the voltage estimation method ineffective. In this section, it will be shown that the voltage estimation method developed does not depend on the individual load profiles. Only the profiles of the real and reactive power flow and the voltage at the substation are required. For proving this, a simulation run has been completed in which half the loads connected to the different buses are given values randomly generated. The remaining loads

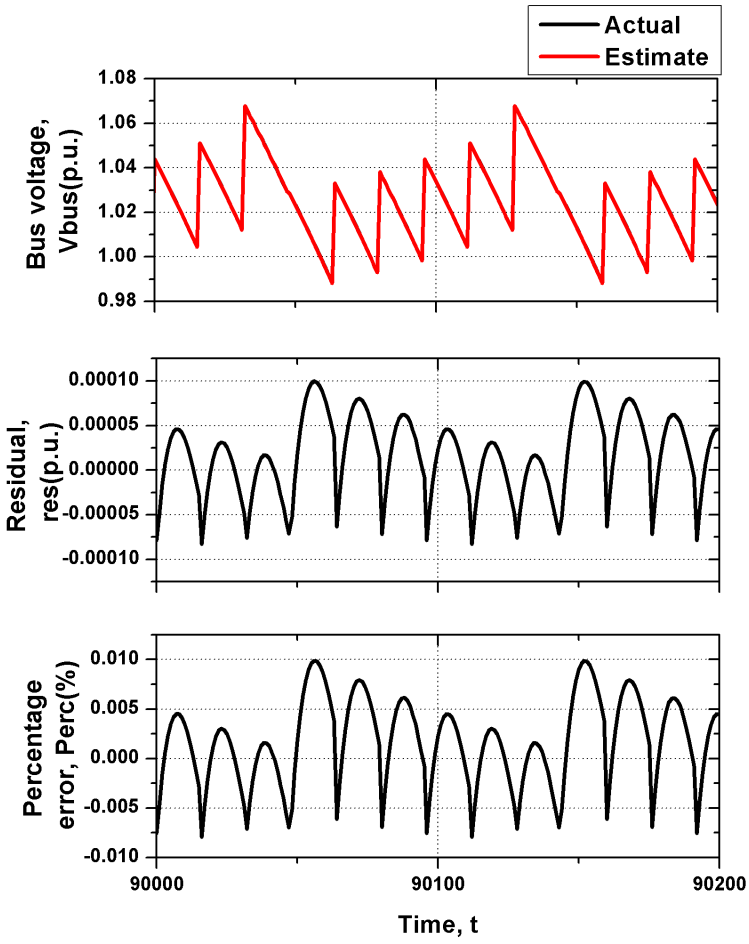

Figure 6.18: *Snapshot of the estimated and the actual voltage with the residual and the percentage error for the case with conforming loads*

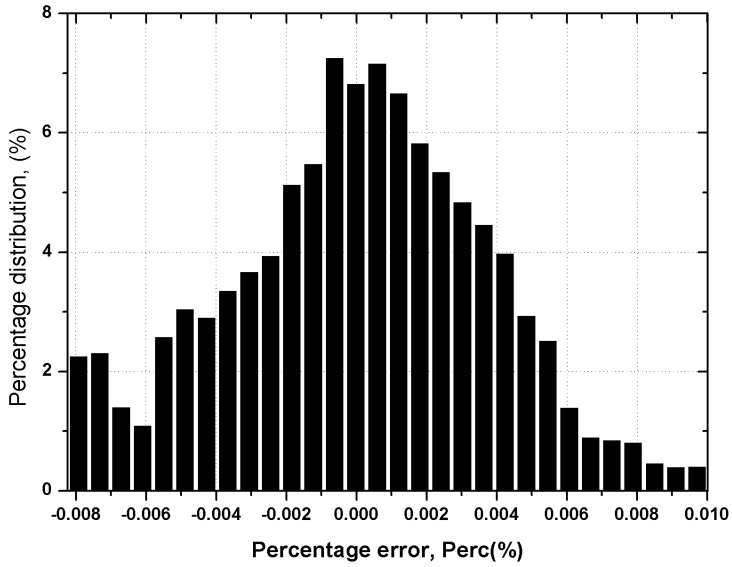

Figure 6.19: *Percentage distribution of the percentage errors obtained in the validation tests performed with conforming loads.*

conform to the generic load profile. Ten randomly selected values of the real power generation by the wave power farm (between 0 and 6 MW), the loading of the network and five randomly selected values of the operating power factor of the farm were used to validate the estimator. Therefore, the data set used for non-conforming loads had 500 data points.

Figure 6.21 shows the estimated and the actual voltage and the residual and the percentage error obtained in this run. It is seen that the range of residuals and percentage errors are similar (though relatively higher) to those obtained with the conforming loads. This proves that the voltage estimation method depends only on the profile of the measurements made at the substation and not on the individual load profiles, which is one of the advantages of using this voltage estimation method.

6.7 Full system validation

In the preceding section, the voltage estimation method developed in this chapter was tested on data sets assuming that accurate demand estimates of the real and reactive power flows at the substation, without the wave power farm, were known. In this section, the effects of different demand forecast accuracies on the voltage estimate made are examined. It has been assumed that the forecast demand (prior to the connection of the wave power farm) is equal to the actual demand plus a random number at any instant of time [224]. The random numbers used have

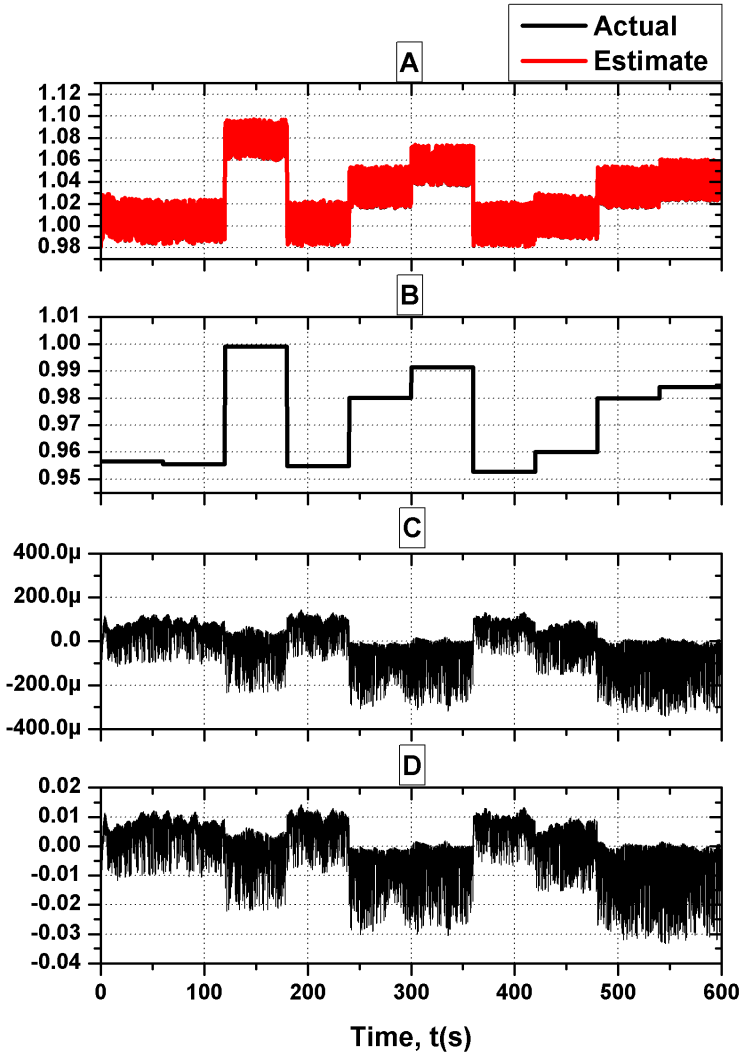

Figure 6.20: *(a) The estimated and the actual voltage (p.u.), (b) the randomly generated power factors (-), (c) the residual (p.u.), and (d) the percentage error (%) for the case with conforming loads.*

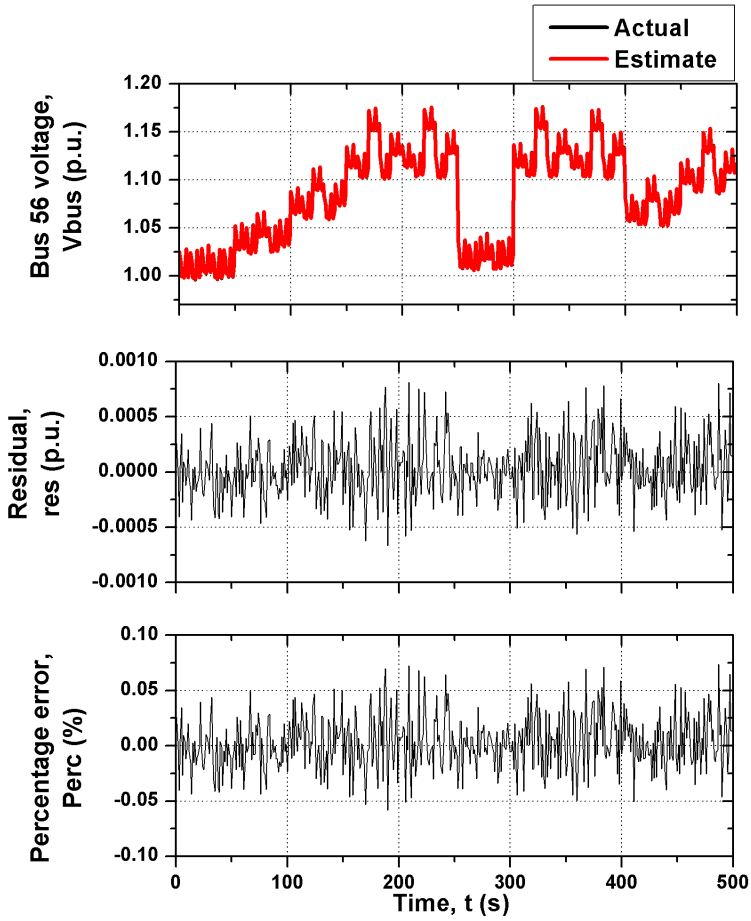

Figure 6.21: *The estimated and the actual voltage (p.u.), the residual (p.u.), and the percentage error (%) for the case with non-conforming loads.*

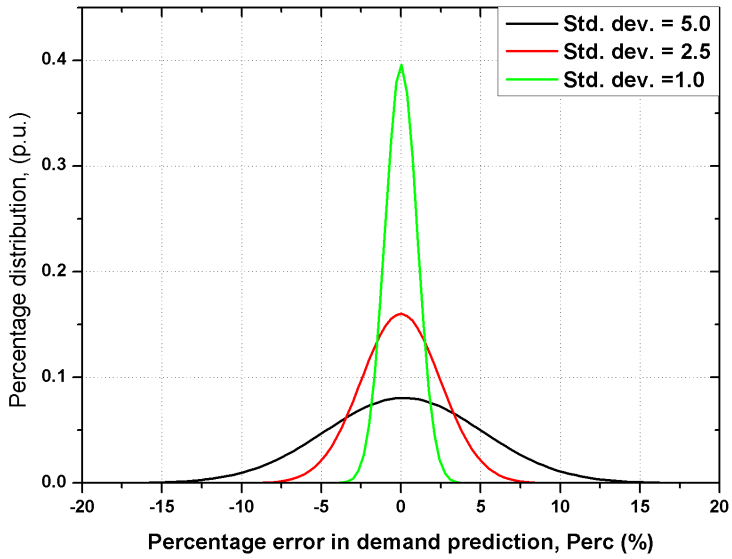

Figure 6.22: *The normal distribution of percentage errors in the demand prediction for different standard deviations.*

been generated using normal error distributions like the ones shown in Figure 6.12. This models the effect of using a demand predictor as the first step of the voltage estimation process. The mean and the standard deviation of the distribution give an idea of the extent of percentage errors seen. The real and reactive power demands at the substation have been taken separately and percentage errors, generated from a normal distribution with mean 0% and standard deviations 1, 2.5 and 5, have been added to the actual demand to model the inaccuracies in the demand prediction. The distribution functions for the different standard deviations used to generate the percentage error in the demand prediction are shown in Figure 6.22. The effects of the error range, measured by the standard deviation, on the precision of the voltage estimation have been analysed and the results are discussed here.

Figure 6.23 shows the variation in the real and the reactive power generated by the wave power farm, the random operating power factor (changing once every 60 seconds), and the electrical demand (changing every time-step) used for testing the performance of the voltage estimator.

In the first validation run, which is the worst case scenario, both the real and reactive power estimates have randomly generated errors at every instant of time obtained from the distribution with a standard deviation of 5. Figure 6.24 shows the estimated and the actual voltage, the residual and the percentage error over the 600-second simulation time. The values of the percentage error in the estimated voltage are less than 1.0% during the entire run. Figure 6.25

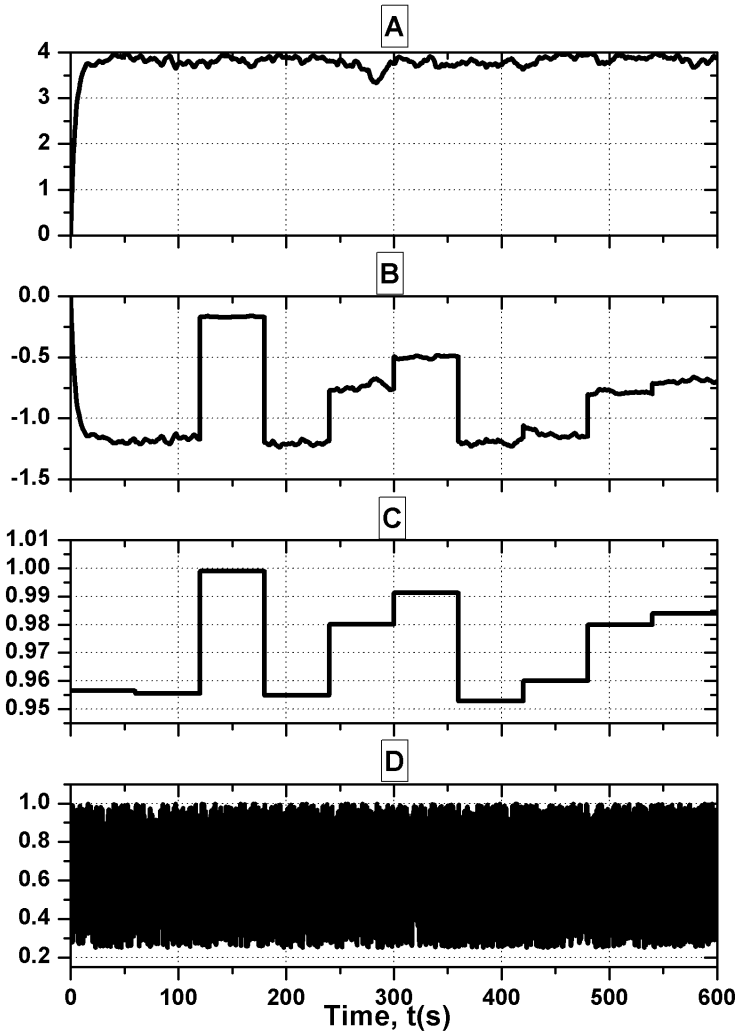

Figure 6.23: *The data used to validate the full voltage estimator system: (a) the real power generated (MW), (b) the reactive power generated (MVAr), (c) the operating power factor (-) and (d) the demand variation over the 600-second period (p.u.).*

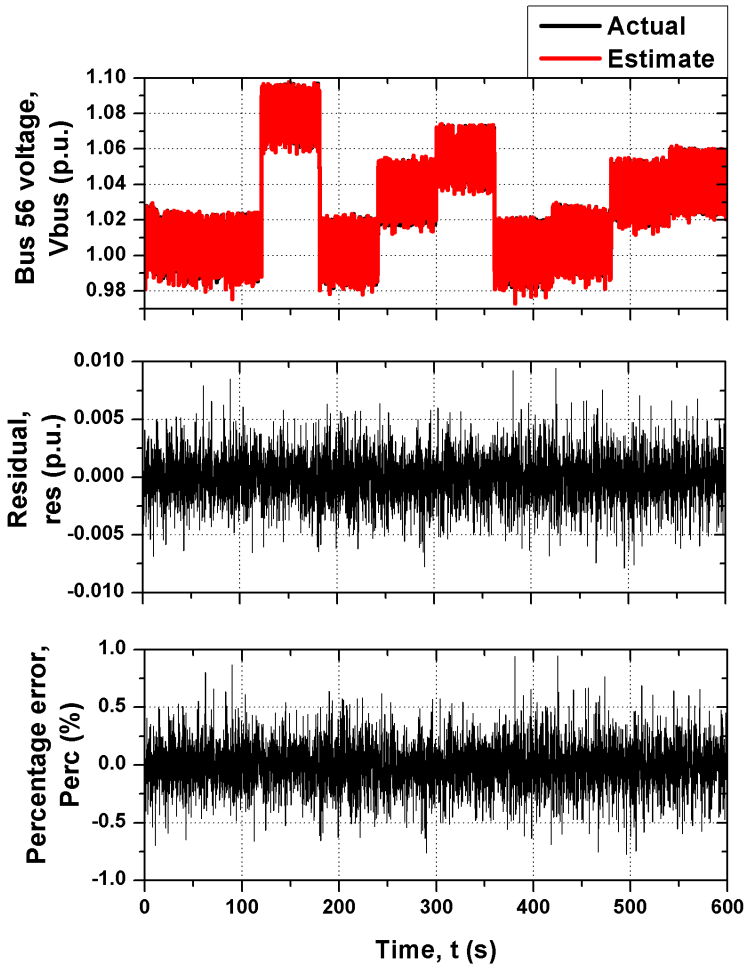

Figure 6.24: *The estimated and the actual voltage with the residual and the percentage error obtained from the full system validation, with the standard deviation of the demand prediction error = 5.*

shows the percentage distribution of the percentage error in the estimated voltage. For more than 95% of the time, the value of the percentage error lies less than 0.5%.

The same validation test has been then performed with the demand prediction errors generated using the normal distribution with a standard deviation of 2.5. This is in the range of standard deviations seen in the demand prediction work discussed earlier in this chapter. The results are shown in Figure 6.26 and the percentage distribution of the percentage error in the estimated voltage is shown in Figure 6.27. As expected, the values of the percentage error and the residual are smaller when compared to the case when the errors in the demand were generated using a distribution with standard deviation 5. The percentage error is less than $\pm 0.4\%$ during the entire run. The distribution of the percentage error shows that the values of the percentage error in the

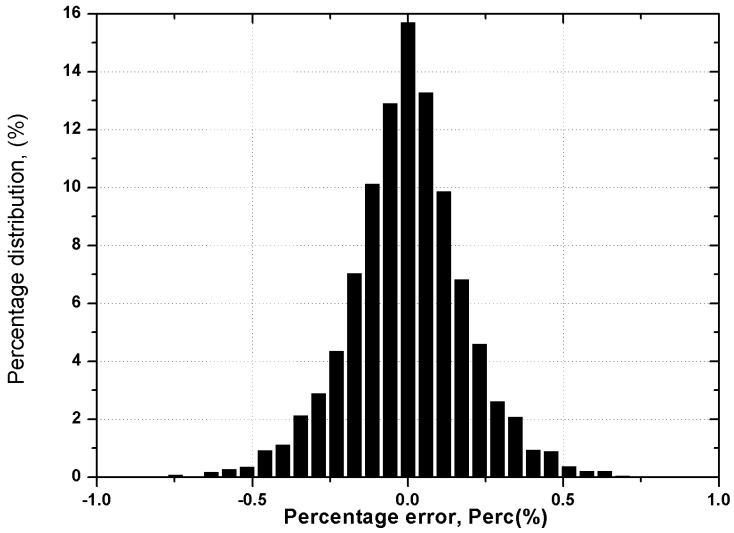

Figure 6.25: *Percentage distribution of the percentage error in the estimated voltage obtained through the full system validation, with the standard deviation of the demand prediction error = 5.*

Standard deviation of the demand prediction error	**Mean absolute percentage error (%)**	**Standard deviation of the voltage estimation error**
1.0	0.0296	0.0390
2.5	0.0730	0.0972
5.0	0.1446	0.1906

Table 6.5: *Errors in the estimated voltage obtained through the full system validation for different standard deviations*

estimated voltage are less than $\pm 0.2\%$ for a large part of the simulation time.

Table 6.5 shows the improvement in the voltage estimation with the improvement in the demand prediction accuracy. A linear relationship between the two is seen and is as expected because the precision of the voltage estimation methodology only depends on the accuracy of the demand forecast.

6.8 Voltage estimation application

In this section, the voltage estimation method validated in the previous section has been applied to coordinate the control of the substation OLTC transformer and the AVPFC controller of the wave power farm connected to bus 56 in the generic UK 11 kV distribution system. The AVPFC simulation runs used in this section have already been analysed in Section 5.5.2 and the current

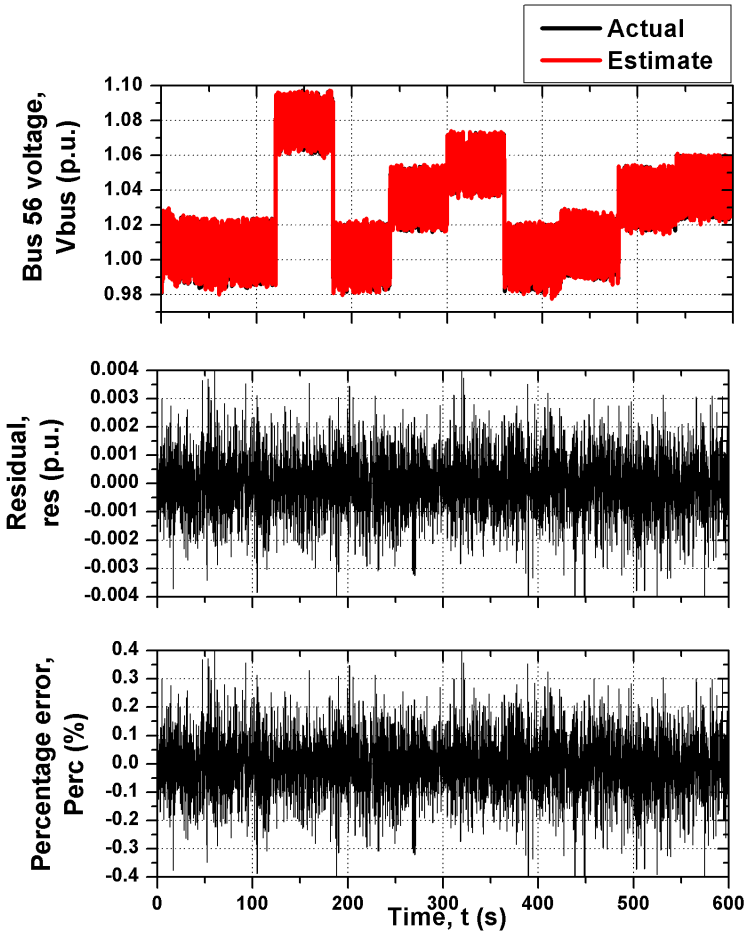

Figure 6.26: *The estimated and the actual voltage with the residual and the percentage error obtained from the full system validation, with the standard deviation of the demand prediction error = 2.5.*

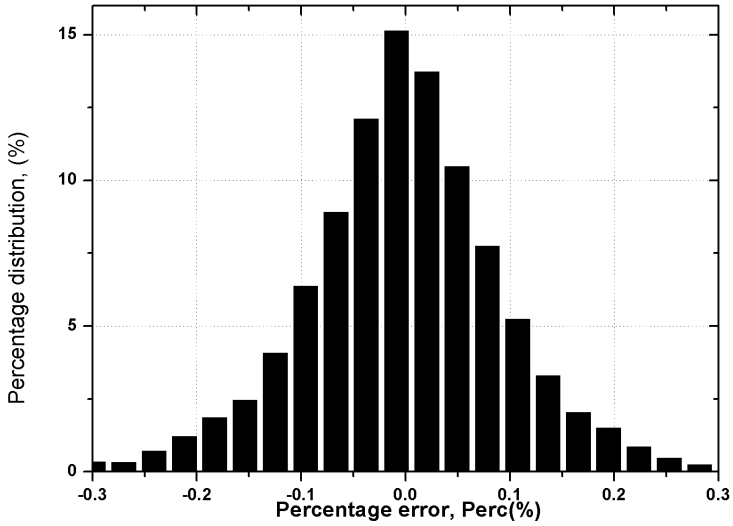

Figure 6.27: *Percentage distribution of the percentage error in the estimated voltage obtained through the full system validation, with the standard deviation of the demand prediction error = 2.5.*

emphasis is to portray the applicability of the voltage estimation method. The following set points have been used for the AVPFC controller: $V_l = 0.97$ p.u., $V_h = 1.05$ p.u., $PF_{ref} = 1$, $PF_{B/T} = 0.975$ (lead and lag), $T_d = 10$ s; with the wave power farm simulated is the sea state C (see Section 5.5).

In the first test in this section, the voltage estimation has been performed under the assumption that the demand prediction has an accuracy of 100%. The estimated and the actual voltage time-series are plotted in Figure 6.28. A very close match between the two is seen, which proves the applicability of the voltage estimation method for coordinating voltage and power factor control in distribution networks.

Figure 6.29 shows the estimated and the actual voltage, with the residual and the percentage error, when the percentage errors in the demand prediction have been generated using a distribution with a standard deviation of 5. The maximum value of percentage error in the estimated voltage seen in this case is less than 1%. The precision of the voltage estimation improves with an improvement in the accuracy of the demand forecast. Figure 6.30 shows the same results when the percentage error in the demand prediction have been generated using a distribution with a standard deviation of 2.5, which is more realistic. The maximum percentage error in this case is approximately 0.375%. Literature shows more accurate demand prediction methods with prediction errors that can be represented by normal distributions with standard deviations

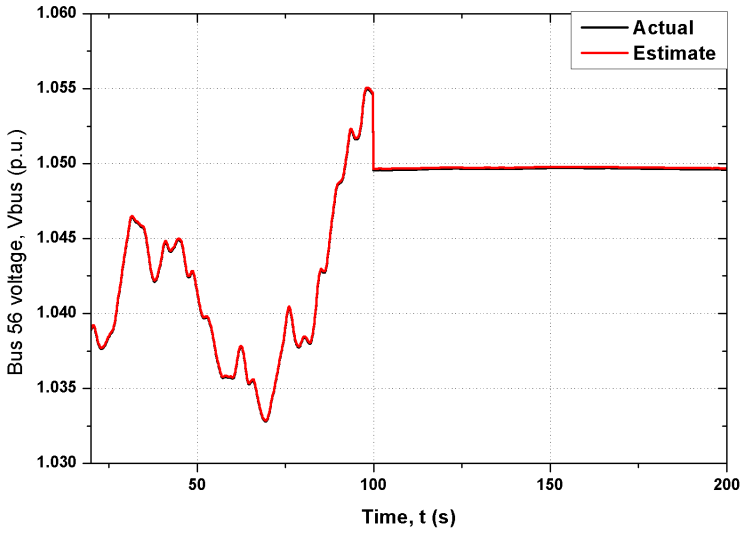

Figure 6.28: *The estimated and the actual voltage time-series for 200 seconds, with 100% accurate demand estimates.*

of less than 1 [225]. With such demand prediction errors, the precision of the voltage estimation will improve even further.

6.9 Summary

This chapter investigated issues that will need to be tackled when using intelligent volt/VAr control techniques with newly added distributed generators. Some of these issues between uncoordinated controllers of the substation OLTC transformer and the wave power farm, like unnecessary tap changes and voltage set point runaways, were discussed in this chapter. Through these examples discussed early in the chapter, the need to estimate voltage downstream of the substation becomes evident.

As the first part of the voltage estimation, the real and reactive power and voltage measurements at the substation, taken prior to the connection of the wave power farm, were needed. The collected data were then used to predict the one-step-ahead power flow at the substation. A wavelet neural network, trained with the demand data obtained from archives, was used to make the demand prediction. The neural network models the relationship between the past values of the demand at the substation and the one-step-ahead demand. Three nonlinear exogenous models and two nonlinearity estimators were tested for the demand prediction and their performance was compared. The developed model was not meant to replace other load forecasting algorithm available in literature and was used to portray a simple forecasting technique

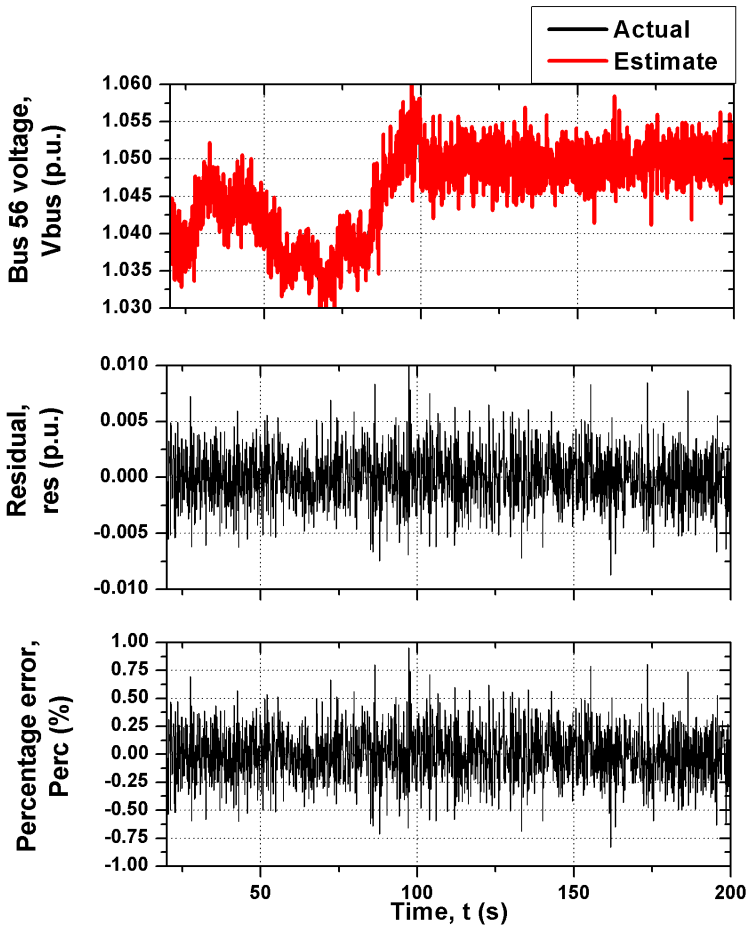

Figure 6.29: *The estimated and the actual voltage time-series for 200 seconds, with a standard deviation of the demand prediction error = 5.*

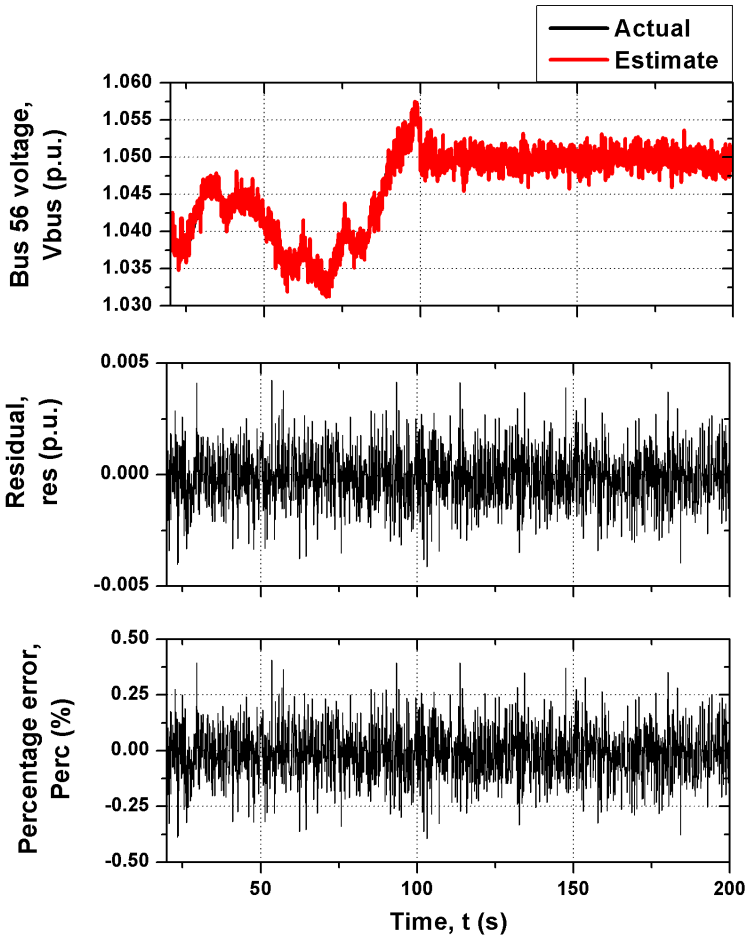

Figure 6.30: *The estimated and the actual voltage time-series for 200 seconds, with a standard deviation of the demand prediction error = 2.5.*

to be used in conjunction with the voltage estimation method. The demand predictor only made one-step-ahead forecasts. Predictions over longer periods will require more regressors and also the incorporation of other independent variables.

The one-step-ahead predicted demand was one of the inputs of the voltage estimator. The difference in the predicted and the real-time measurement of the power flow at the substation is used to estimate the voltage at the bus under consideration. Inaccuracies in the demand prediction, which affects the voltage estimation process, were generated using distributions of the demand prediction errors obtained earlier. Data obtained from offline simulations of a UK 11 kV distribution network were used to train neural networks, which were then used to calculate the voltage downstream of the substation transformer. The developed voltage estimation method was tested with different real power time-series, load profiles and power factors. A good match between the estimated and the actual voltages were seen in all the cases tested.

There are three distinct benefits of using the voltage estimation method presented in this chapter. The first one is the optimal usage of the volt/VAr control elements in the network. Estimating the voltage at the bus where the wave power farm is connected makes the functioning of the LDC schemes effective, since actual operating data (also called pseudo measurements in the field of power system state estimation) are available now. This is the second main benefit of using the voltage estimation technique. The third significant benefit of the method lies in the possibility of optimising the operation of the wider distribution network on the basis of the information available. The operation of the OLTC transformer and the controller of the wave power farm can be controlled based on different optimisation criteria; e.g. reduction of losses in the network, etc.

In this chapter, a method by which the voltage at the bus where a DG is connected in the distribution network can be estimated from upstream was suggested. It is envisaged that the developed method will become more important and more effective as the traditional distribution networks are replaced by smarter networks with more measurements made in real-time.

Chapter 7
Comprehensive assessment of voltage control means and quantification of voltage fluctuations

7.1 Introduction

Until now in this thesis, different strategies to minimise voltage fluctuations introduced in the network by the connection of wave power farms were discussed. Chapter 4 examined the effects of spacing and orienting WECs differently within a farm on the smoothing in the net real power generated. Intelligent controllers for further voltage smoothing by excitation control of the DFIGs within a farm were described in Chapter 5. The focus there was to avoid the wave power farm being tripped off the network due to voltage violations.

Voltage violations (including voltage swells and dips) are classified as network events, which are quantified based on the number and duration of their occurrences. Such events are quantified using different indices like the System Average Interruption Frequency Index and the Customer Average Interruption Duration Index [226]. Recent interest in studying the economic impacts of voltage disturbances has arisen [227–230], again focussing on interruptions and voltage dips alone. With an increasing penetration of varying generation from renewable sources in the electricity network, the focus may need to move away from network events alone.

Existing power quality measurement standards (eg. [231]) treat slow voltage variations using 10-minute rms-voltage values. They specify the voltage quality requirements using statements like "all 10 minute mean rms values of the supply voltage shall be within the range of $\pm 10\%$" etc. It is generally accepted that as long as the voltage is within this range any equipment connected to the network will not be adversely affected. Moreover, it is assumed that the voltage excursions during the 10-minute period may be of any nature as long as the 10-minute rms remains within the specified limits.

Rapid voltage changes (voltage step changes occurring over a few seconds) are dealt with sep-

arately in the standard. Flickermeters are mentioned as a means of measuring extremely fast variations in the rms-voltage magnitude occurring in the seconds to sub-second time-scales. Variations in the power generated from wave power farms occur over time-scales in the range from 3 seconds to 10 minutes and the the network voltage variations introduced by these farms cannot be quantified either using 10-minute averages or using flicker indices. Other indices to quantify voltage variations in these time-scales have been suggested in publications [149, 232–235], but these indices have not found widespread use. Therefore, a need to introduce additional quantities to measure voltage variations that occur over this range of time-scales is required.

Voltage fluctuations can cause non-flicker consequences, which have been mentioned in Section 3.5 of [236]. Also, long-term exposure of the equipment connected to the network to voltages different from their design value may impact the lifetime of equipment [237]. There is no clear indication of the tolerance of the equipment against changes in the voltage. This has been studied to an extent in the case of lighting loads, but no study of the potential impacts of voltage variations on industrial loads, for example, has been undertaken [237]. With the increasing penetration of generation from renewable energy sources and the susceptibility of equipment to long-term voltage variations, it might become necessary to quantify these variations and to study their economic impacts.

A number of indices that are available in the literature to quantify fluctuations in the rms-voltage magnitude are reviewed in this chapter. Some of these indices have been modified to make them more suitable for assessing the different volt/VAr control options discussed in Chapter 5. New indices have also been suggested and the performance of these indices, as a measure of voltage quality, is compared. With respect to the work presented in this thesis, the ‘goodness’ of the different control means presented in the thesis are assessed. Using the indices presented in this chapter, both the extent and the persistance of voltage fluctuations are quantified. Such quantification may be used as the yardstick in accomplishing different smart voltage management techniques across distribution networks.

7.2 Indices

This section describes some of the voltage fluctuation quantification indices which may be used to assess voltage control means and to quantify voltage fluctuations. How the indices have been calculated and how already existing indices have been modified to quantify the ‘goodness’ of the rms-voltage time-series are also explained. Two new indices for quantifying voltage

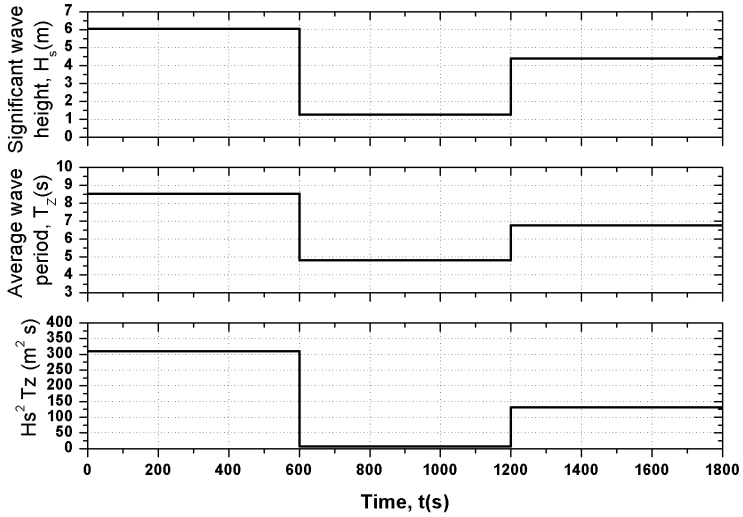

Figure 7.1: *Variation of H_s, T_z and $H_s^2 T_z$ over the 1800-second simulation period.*

fluctuations are also presented.

The voltage fluctuation indices have been calculated for different volt/VAr control methods used with wave power farms. A 1 MW wave power farm connected to bus 9 in the network, shown in Figure 5.3, has been analysed. The effects of connecting the wave power farm to the network, at the different load buses, have been assessed. The wave power farm has been controlled in the constant power factor mode, the constant voltage mode, and using the AVPFC and the FLPFC methods. Secondary voltage control through the substation OLTC transformer has also been assessed. The wave power farm has been simulated in a 1800-second concatenated sea state (see Figure 7.1) and the rms-voltage magnitude fluctuations during the three time periods - during highly energetic, weakly energetic and moderately energetic seas, have been assessed separately. The three time periods have been denoted as time intervals 1, 2 and 3 in the discussed results.

7.2.1 Cumulative probability function - index (CPF-index)

The Cumulative Probability Function-index (CPF-index) overcomes one of the issues of using the flicker severity index to quantify voltage fluctuations. The flickermeter uses a series of filters to model the eye-brain unit's response to fluctuations in luminance. Because of these filters, the standard flickermeter only captures luminance fluctuations in the frequency range 0.5-30 Hz [238]. Even within this range, the flickermeter is most sensitive to voltage fluctuations with frequency between 3.5 Hz - 8.8 Hz. Analysing the real power time-series generated by wave power

farms shows that the changes in the generated power are much slower, over periods of tens of seconds. The voltage fluctuations caused by such real power excursions therefore cannot be detected by flickermeters. The CPF-index removes the eye-brain unit's response to luminance fluctuations and thus provides a more objective index when compared to flickermeters. Though the main drawback of using traditional flickermeters is negated, the new index is by no means a replacement for the standard flicker severity index P_{st}.

The cumulative probability function (CPF) of the rms-voltage magnitude is used to calculate the CPF-index. The CPF is evaluated by subdividing the rms-voltage into a number of classes or levels [239]. The cumulative probability $p(l)$, of a time domain signal, that a particular class l has been exceeded over a period of time T is [240]:

$$p(l) = (total\, time\, when\, signal\, level\ > l)/T. \tag{7.1}$$

Since the CPF curves cannot be represented by standard distribution functions, a multipoint method is used to characterise any CPF curve. Using this method, the CPF-index is defined by:

$$CPF - index = \sqrt{K_1 P_{0.1} + K_2 P_1 + K_3 P_3 + K_4 P_{10} + K_5 P_{50}}, \tag{7.2}$$

where K_1 to K_5 are the weighting coefficients and P_k is the CPF curve level with an assigned probability of being exceeded [239]; i.e. $P_{0.1}$ is the level exceeded by only 0.1% of the observation period. All the weights K have been given the value of 0.2, such that the CPF-index is equal to 1 when the voltage is either 1.06 p.u. or 0.94 p.u. during the entire period under examination. Different values may be given to these weights to assign different scales of importance to different voltage levels.

Plots of the cumulative probability functions (CPF) are shown in Figures 7.2 and 7.3. These show diagrammatically the extent of voltage excursions and their persistence for the different control options used at the different buses in the network. Figure 7.2 clearly shows the advantages of using the intelligent control options like the AVPFC and the FLPFC for controlling the wave power farm. In both these cases the voltage at bus 9 exceeds the 1.05 p.u. limit placed by the controllers only for an extremely small percentage of time. Figure 7.3 shows the CPF of the voltage seen at all the buses in the network when then FLPFC controller is used. The voltage quality (in terms of the rms-voltage magnitude) improves farther away from the bus where the wave power farm is connected, as is shown by the reduction in the range of the rms-voltage magnitude seen. The five percentiles used to calculate the index are also shown in the two figures. Table 7.1 shows the values of the CPF-index for the different control methods used.

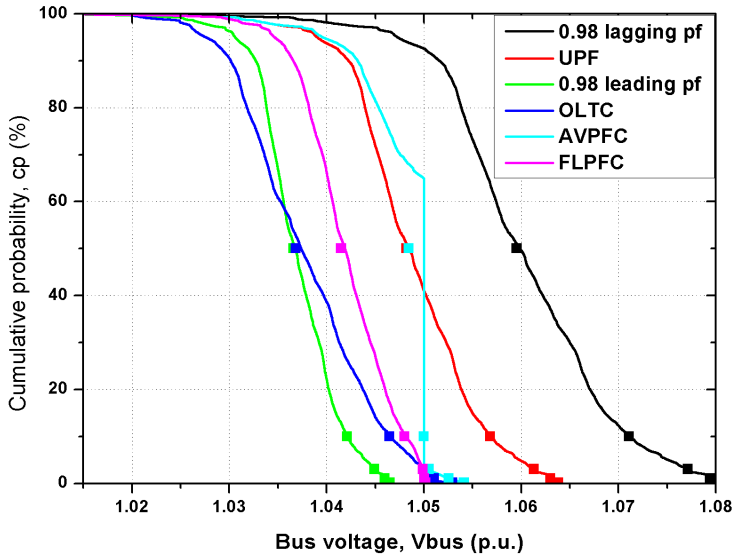

Figure 7.2: *Cumulative probability functions of the bus 9 voltage when the different control methods are applied (time interval 1).*

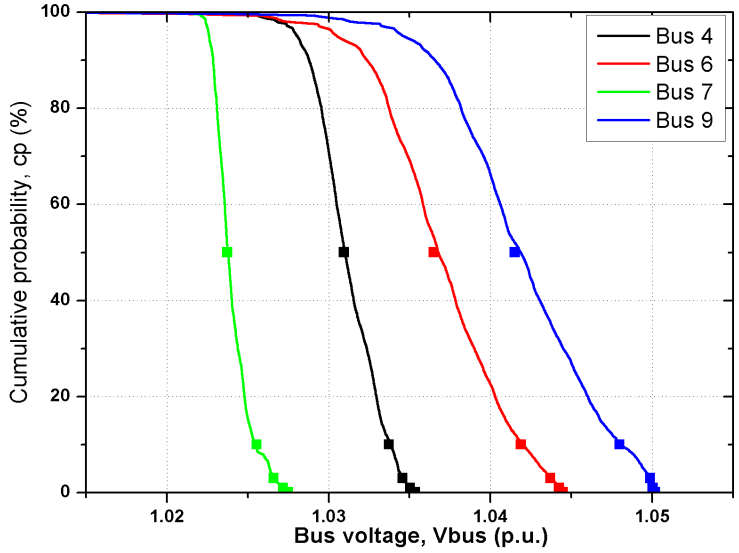

Figure 7.3: *Cumulative probability functions of the voltage at buses 4, 6, 7, and 9 when the FLPFC controller is used (time period 1).*

Control method	CPF-index
0.98 lagging PF	1.0361
UPF	1.0289
0.98 leading PF	1.0214
OLTC	1.0235
AVPFC	1.0252
FLPFC	1.0237

Table 7.1: *CPF-index values*

7.2.2 Voltage fluctuation index

The average change in the rms-voltage magnitude between each time-step in an rms-voltage time-series can be used as a simple index to quantify voltage fluctuations [148]. The index has been named the voltage fluctuation index (VFI) and is defined as follows:

$$VFI = \frac{\sum_{i=2}^{N} |V_i - V_{i-1}|}{N-1}, \tag{7.3}$$

where i refers to an instant of time and N is the total number of such instants being considered. In this work, N has been taken as 6000, which denotes a sampling time of 0.1 seconds over a simulation period of 600 seconds.

The VFI may be used to quantify fluctuations in the rms-voltage magnitude at a particular bus under consideration. The global voltage index, which is a modified form of the VFI, may be used to assess the rms-voltage quality across a network [241].

The VFI calculated for the voltage time-series obtained by simulating the wave power farm, controlled by the different methods in the three sea states, are given in Figure 7.4. As seen earlier, the operation of the farm at lagging power factors worsens the voltage fluctuation problem seen in the network. This is corroborated by the high values of the VSI seen when the wave power farm operates at 0.98 lagging power factor. The VSI obtained when operating the farm at a constant voltage (ideally equal to 0) has not been plotted in the figure due to their extremely low values. The time period between 600 and 1200 seconds shows lower VFI values when compared to the other time periods due to the lower variations in the energy content of the sea. The advantage of using the VFI is that both the magnitude and the number of voltage fluctuations, occurring in the time duration under consideration, are accounted for. The voltage variations occurring over different time-scales can also be quantified using the VFI, by averaging the rms-voltage over the time-scale and using the averaged values as V_i in Equation 7.3. By following this procedure for different time-scales, the average variation in the rms-voltage magnitudes over a range of time-scales can be obtained.

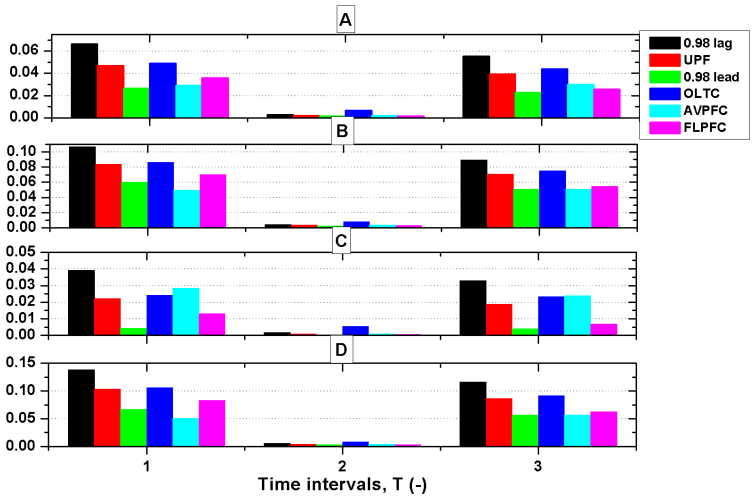

Figure 7.4: *Voltage fluctuation indices at buses 4, 6, 7, and 9 when the different controllers are used over the three time periods.*

7.2.3 Localised spectral analysis (Energy index ratio)

Windowed Fourier transform and wavelet methods were compared earlier in Chapter 3. They can be used for spectral analysis of time varying signals and can be used to identify information both in the time and the frequency domains. A wavelet based technique for localised spectral analysis of an rms-voltage time-series was described in [242]. The developed method was used to assess the impacts of increasing the penetration of solar photovoltaics in distribution networks through curves plotted, which show the different frequency components at different instants of time. In this chapter, the aim was to develop indices which can be used to assess the quality of the rms-voltage and therefore an approach of obtaining the time-frequency information from signals using the Windowed Discrete Fourier Transform has been adopted.

The Discrete Fourier Transform (DFT) [243] is defined by:

$$X(k\Delta\omega) = \sum_{n=0}^{N-1} x(n\Delta t)\, exp(-j\, k\Delta\omega\, n\Delta t), \tag{7.4}$$

where $0 \leq n < N-1$ and $0 \leq k < N-1$ and $X(k\Delta\omega)$ is the magnitude of the DFT at frequency $\omega = k\Delta\omega$, N is the transform length or the number of samples used for the DFT and $x(n)$ is the discrete (sampled) version of the continuous signal $x(t)$ under consideration. A moving-windowed DFT (with 4096 (2^{12} samples) each) has been used in this work, so that time-localised spectral data are obtained. Each window thus corresponds to approximately 7 minutes of data sampled every 0.1 seconds. The windowing function is moved by one time-step

and the DFT is calculated until the end of the signal. Smaller window lengths were also tested for calculating the DFT, but using 4096 samples as the window length gave a higher frequency resolution. In this work, since the focus is on the fluctuations in the voltage with respect to its mean value, the DFT of the rms-voltage time-series subtracted from the mean rms-voltage over the period being considered has been used to obtain the frequency domain information from the rms-voltage signal.

Once the moving windowed DFT is evaluated, the power spectral density (PDS) of the rms-voltage signal is calculated using

$$PSD = S(k) = 2\frac{|X(k)|^2}{F_s N}. \tag{7.5}$$

where F_s is frequency at which the time domain signal has been sampled. Since the DFT of the rms-voltage subtracted from the mean rms-voltage over every window has been used, the PSD calculated from the DFT essentially shows the power in the rms-voltage fluctuations about the mean value.

The energy in a time domain signal can be obtained by integrating the PSD over frequency using

$$E = \sum_{k=1}^{N/2} S(k)\Delta f, \tag{7.6}$$

This energy quantifies the energy contained in the rms-voltage fluctuations about the mean rms-voltage. To better compare the different control methods used for voltage and power factor control of wave power farms, the ratio between the energy in the voltage fluctuations introduced by a particular control method and that introduced in a base case has been used as the index and this index has been named the Energy Index Ratio (EIR). The UPF operation of the wave power farm has been chosen as the base case in this work. Lower the EIR, better the supply voltage quality is.

As discussed earlier, the PSD of the rms-voltage signal, over all the windows used, are required before the EIR can be calculated. Figure 7.5 shows the PSD of the rms-voltage time-series when the AVPFC method is used to control the wave power farm. The figure shows the results after the DFT is obtained from the first window starting at time t = 0 s. The EIR calculated, for the different control methods and the three sea states, for the voltage time-series seen at bus 9 are given in Figure 7.6. As has been mentioned earlier, the EIR has been calculated relative to the UPF operation of the wave power farm (the EIR of the UPF operation is therefore 1.0).

Since the UPF operation of the farm has been taken as the base case, the EIR over the three time periods for the lagging and the leading power factor cases remains constant (at 1.7, 1.0 and 0.4 for the lagging, UPF and the leading cases respectively). This can be explained by the fact that operating at the farm at different constant power factors gives a similar shape to the rms-voltage envelope. Depending on the power factor, the rms-voltage envelope is either pushed up or down from that of the UPF case. During the first 600-second period, controlling the wave power farm using the AVPFC method gives relatively low values of the EIR because, during this period, the farm operates at a constant voltage for most of the time. During the period between 1200 and 1800 seconds, the EIR is high for the AVPFC case because of an increase in the number of switchings between the control modes. When the farm is controlled by the FLPFC method, the EIR values lies between the values seen in the 0.98 leading and the UPF cases. This is because, when thus controlled, the wave power farm in essence operates at a leading power factor between 0.98 and UPF. The step voltage changes that occur when the OLTC transformer is used for voltage control in the network produces higher EIR values during all the time periods, when compared to the other voltage/power factor control methods. During the second time period, two voltage step changes (due to two tap changes) produced a very high EIR value, which was approximately 50 times higher than the UPF case.

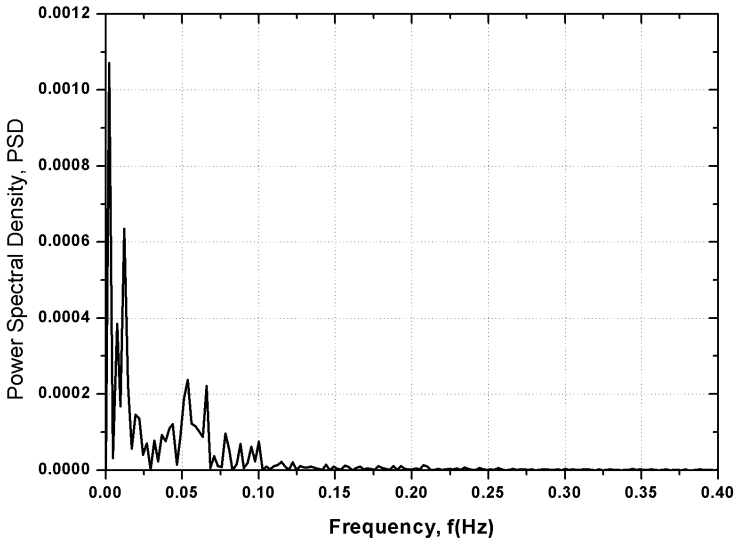

Figure 7.5: *The power spectral density (PSD) of the voltage fluctuations when the wave power farm is controlled by the AVPFC method.*

Capacity and availability factors are two indices commonly used by power systems engineers to assess the economic impact of power plants. The former is defined as the ratio of the actual

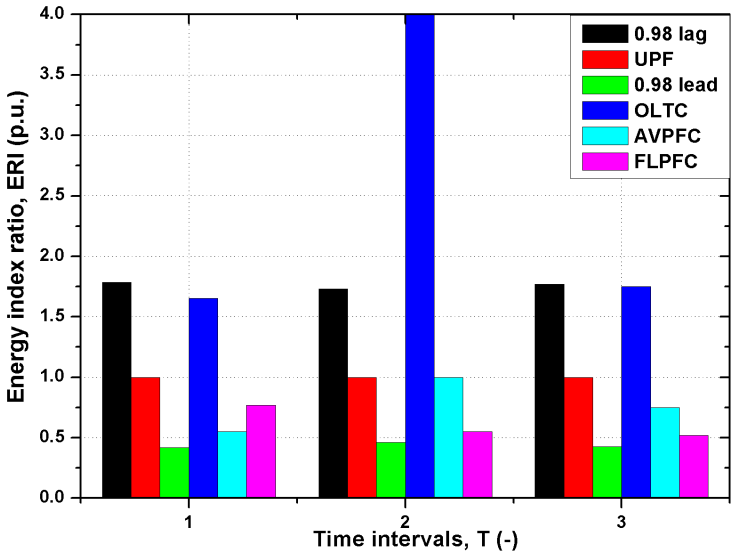

Figure 7.6: *Energy index ratio at bus 9 when the different controllers are used over the three time periods.*

output of a power plant over a period of time to its output if it had operated at its rated capacity, while the latter is defined as the ratio of the amount of time that the power plant is able to produce electricity over a certain period to the time period considered. For all the control methods tested in this work, except the 0.98 lagging power factor case, the availability factor was 100%, with 0.94 p.u. $< V_{bus} <$ 1.06 p.u as the limit. The capacity factor for all the cases, except the 0.98 lagging power factor case, was approximately 33%. Since the aim of the primary voltage control is to keep the voltage within the statutory limits, the operation of the wave power farm at 0.98 lagging power factor would generally not be considered.

7.3 Summary

There are two main reasons for developing the voltage quality indices, examined in this chapter, covering the voltage variations occurring over time-scales between 3 seconds and 10 minutes: increasing penetration of generation from renewables with their variation occurring in this range of time-scales and the susceptibility of equipment to voltage variations in this range of time-scales. Quantifying such voltage fluctuations still does not have any widely accepted index, nor have there been regulations dealing with these fluctuations. This chapter introduced some indices to quantify the extent and persistance of voltage fluctuations occurring over the specified time-scales. These were: the CPF-index, the voltage fluctuation index (VFI) and the energy

index ratio (EIR). These indices were calculated for the different wave power farm control options tested under different sea states.

The sensitivity of flickermeters to voltage fluctuations within a certain range of frequencies was overcome through the use of the CPF-index, in which the absolute value of voltage is used to calculate the index. The CPF curves also gave a visual indication of the extent of voltage fluctuations and their persistence. The VFI is a simple index which is a measure of the average change in the rms-voltage magnitude over certain durations of time. The VFI measured over different time-scales provided both the time and frequency domain information of the rms-voltage signal.

The ERI uses advances in spectral techniques to quantify the energy in the fluctuations in an rms-voltage time-series. Both time and frequency domain information of the fluctuation were obtained with respect to the base case, making it better for comparing the different control methods. The magnitude of the ERI obtained were spread more than the other indices tested earlier, making it the most sensitive index to rms-voltage fluctuations.

The new indices proposed in this chapter can be used to quantify the effects of using the methods, suggested in Chapters 4 and 5, to improve the quality of voltage with respect to voltage fluctuations. More than using the absolute values of the proposed indices, the indices can be used as a means to compare voltage fluctuations when different physical placements and volt/VAr control strategies are used. The latter was discussed in detail in this chapter. This work will also be important when making network impact assessments of new DG connections and in scenarios where active voltage management across the network is aimed for. With improvements in metering equipment and their large-scale use, the implementation of schemes for measuring and quantifying voltage fluctuations and assessing voltage control means may become practical in the near future.

Chapter 8
Discussion and conclusions

8.1 Chapter overview

This chapter discusses the significant conclusions that may be drawn from the research presented in the thesis. A chapter-wise summary of the work discussed in this thesis is first listed. The research outcomes and benefits of the work completed and the contributions to knowledge in the field of control and network integration of wave power farms are then presented. This chapter concludes by providing the scope for further academic and industrial research.

8.2 Thesis summary

Chapter 1 gave an introduction to the work. The general research setting in which this work commenced was discussed. Characteristics of the wave resource available in the UK and the distribution network to which most wave power farms would be connected were reviewed. An overview of the SuperGen Marine Energy Reseach consortium and how this project fitted with the wider research objectives of the consortium were given. The chapter concluded with the thesis statement and the contribution to knowledge expected out of the research.

The wave-to-wire model of the wave power farm based on doubly-fed induction generators, built in MATLAB/Simulink, was introduced in **Chapter 2**. The chapter first dealt with the modelling of irregular, non-stationary and multi-directional sea states using spectral means. The wave elevation time-series were generated using the Inverse Discrete Fourier Transform (IDFT) and were the inputs to the wave-to-wire model. Later, the time domain model of the hydrodynamics of a wave energy converter (WEC) developed from the basic equation of motion was presented. Then, the different options for the power take-off (PTO) and the hydrodynamic control of the WEC were discussed and the option chosen for this work was elaborately explained. Finally, the model of the generator, the power electronic converters and their control were presented; with a brief mention of the electrical network layout within the farm. This model provided the basis for examining the effects of connecting wave power farms to the electricity network. A system identified model of the wave power farm, based on the detailed

model, was then developed in the next chapter, which made analysing large farms quick and efficient.

Chapter 3 studied a new modelling framework based on system identification used to model wave power farms. Data obtained from the simulation of the detailed model, presented in Chapter 2, were used to train wavelet neural networks, which were then used instead of the detailed model. The chapter started with a brief description of the different characteristics of dynamic models centred on linear black-box models. How linear black-box models can be used for output prediction was mathematically clarified. The theory of linear models was then extended to include nonlinear black-box models. Following this, the theory behind wavelet transforms, neural networks, and wavelet neural networks, necessary to understand the development of system identified models, were discussed. Next, the various steps involved in the development of the nonlinear autoregressive exogenous (NARX) model of the WEC were presented. The developed model of the WEC was thoroughly validated for different sea states by comparing the performance of the detailed model with the NARX model. Lastly, the NARX model of the individual WEC was cloned to construct models of wave power farms, which were again validated using the detailed model for different sea conditions. This, for the first time, demonstrated the use of wavelet neural networks to model wave energy converters and wave power farms. The detailed physical model of the WECs was replaced by this input-output based model, with only an acceptable loss of accuracy. The system identified model allowed the simulation of farms with a large number of WECs for longer periods of time, which would not have been possible with the detailed model. The system identified model was extensively used in the simulations discussed in the next chapter.

An analysis of the effects of changing the spacing between the WECs within an array on the smoothing in the power generated by the array was performed in **Chapter 4**. The chapter started with a simple array of 6 and 8 WECs in a line and examined how the spacing between the WECs and the orientation of the array with respect to the dominant wave direction affects the quality of the raw mechanical power extracted by the array. The analysis was then further extended to investigate the smoothing introduced in the net real power generated by an array. The quality of the net real power generated by three different array topologies of an array with 8 WECs was then compared. Later, the consequences of increasing the array size on power smoothing were discussed. Finally, the spacing and orientation effects in a realistic 6 MW wave power farm on power smoothing were examined. A statistical study of the characteristics

of the sea state found off the Outer Hebrides was also presented, which puts the study presented in this chapter into context.

Chapter 5 introduced the need for real-time control of the generated reactive power to keep the voltage in the electricity network within limits. The conventionally used voltage and power factor control methods were discussed and their drawbacks were evidenced. Two new voltage and power factor controllers - the Automatic Voltage and Power Factor controller (AVPFC) and the Fuzzy Logic Power Factor controller (FLPFC) - were presented. The different control methods were first tested on a 1 MW wave power farm connected to a simple nine-bus network. Later, the performance of the intelligent control methods were tested on a more realistic farm connected to a generic 11 kV distribution network in the UK. How the different demand, farm size and network specific set points of the developed controllers need to be chosen were presented. A case where a STATCOM is used for voltage/VAr control was discussed and its control using the developed intelligent control algorithm was explained. The next section of the chapter discussed various individual and group control strategies to be used within the wave power farm. The advantages of coordinating the intelligent controllers on the individual WECs, through the use of a supervisory controller, were established. Another scenario where WECs had to be constrained off the network due to excessive generation was also discussed. How the supervisory controller could be used for this purpose was identified. The use of these intelligent controllers on wave power farms connected to more active networks were then tested. For this, a 4 MW wave power farm connected to the Stornoway/Harris 33 kV distribution network was used. The significant improvement in the production from the farm was also quantified. Using the intelligent controllers brought increased revenues to the farm developers and avoided expensive network upgrades. This chapter established the hierarchy of the volt/VAr control strategy that needs to be used on wave power farms for improving the voltage quality. It was for the first time that the intelligent controllers, discussed earlier, were used individually on WECs to study how they interact with each other and a overall control strategy was proposed to make the most of the intelligent control.

The interactions between the control of the wave power farm and other voltage control elements in the distribution network were explored in **Chapter 6**. The focus was on the functioning of the substation OLTC transformer. Issues that might arise due to uncoordinated control were first discussed. Some of the options of coordinating the control were then reviewed. Then, the demand pattern seen at a substation in the 33 kV Stornoway/Harris distribution network was

statistically analysed to extract behavioural information from it. This was achieved using neural networks trained using the system identification toolbox in MATLAB, and a one-step-ahead demand predictor was constructed. Three versions of the demand predictor were described and their performance compared. The percentage errors obtained in the validation runs of the demand predictor were characterised using normal distributions. A voltage estimation method, using the predicted demand values, was then established. The voltage estimation method with and without the demand predictor was validated. Finally, the estimation method was applied to identify the operating mode of a wave power farm connected to a generic 11kV distribution network in the UK from an upstream substation. This showed that a means to coordinate the working of two volt/VAr control devices on the network can be accomplished without the use of any new communication means.

In **Chapter 7**, means of assessing the impacts of using the different control methods on the voltage quality were suggested. Three indices, two of which are already in use and some which have been adapted from the literature, were described and then tested on the six voltage and power factor control methods discussed in Chapter 5. This identified suitable indices to assess the performance of the control methods discussed in the earlier chapters.

8.3 Contribution to knowledge

During the research, many useful findings and new methods to overcome some of the issues of connecting wave power farms to the network were introduced. The key contributions to knowledge are now described.

8.3.1 System identification for modelling wave power farms

System identification, as a tool for modelling wave power farms, was introduced in Chapter 3. The detailed wave-to-wire model of the wave power farm developed was used to train wavelet neural networks. These neural networks modelled the relationship between the wave elevation time-series (input) and the real power generated by a WEC (output). The most important advantage of using the system identified model over the detailed model was the savings made in simulation time and computing resource, without a significant reduction in the precision and the time-resolution. Using such models will be useful when simulating larger networks with a large number of distributed generators. This novel work, presented in the thesis, can also readily be extended to include other generator types and primary energy sources.

8.3.2 Benefits of using accumulators

Using accumulators with the hydraulic PTO system removed most of the high frequency fluctuations seen in the real power generated by a WEC. The low frequency variations in the generated power still existed. Even a 300% increase in the accumulator size did not proportionally improve the power quality. Therefore, it was found that using accumulators alone would not be sufficient to ensure the required voltage quality.

8.3.3 Benefits of a spacing of $0.5\lambda_{peak}$ or more in a wave power farm

It was found that spacing the WECs within an array at $0.5\lambda_{peak}$ produced a much smoother time-series of the net generated real power when compared to the case where the spacing was $0.25\lambda_{peak}$. Opposite results were seen when the cumulative raw mechanical power was analysed instead. This result held good for simple array topologies and also when the array size increased. The odd-numbered-multiples-of-quarter-wavelength spacing effect was more evident between the $0.25\lambda_{peak}$ and the $0.5\lambda_{peak}$ spacings. This effect reduced as the spacing between the WECs or columns of WECs increased beyond $0.5\lambda_{peak}$. It was seen that increasing the spacing beyond $0.5\lambda_{peak}$ produced a much smoother net real power time-series. A change in the dominant wave direction only improved the smoothing in the real power produced, since the effective distance between the WECs or the columns of WECs increased due to the geometry resolving differently. This work has implications for the packing and the layout of wave power farms. Most farms are normally sparsely spaced owing to mooring requirements and for providing easy access to the individual WECs. The work discussed here proves that having sparsely spaced farms, with the spacing between WECs greater than 0.5 times the predominant wavelength at a site, is better from the power smoothing point of view.

8.3.4 Peak wavelength and dominant direction characteristics of ocean waves

The characteristics of the wave climate (mainly the peak wavelength and the dominant wave direction), which affect the power smoothing obtained by appropriate spacing, were studied for a site off the Outer Hebrides. This area is being considered as a potential site for wave power farms. The study showed that the dominant wave direction at the site is almost constant for more that 60% of the three years during which the data were collected. During this period, certain mean time periods (and hence wavelengths) showed a much higher probability of occurring. These behavioural characteristics of the seas found off the Outer Hebrides allow the use of appropriate spacing and orientation for power smoothing. Once spaced based on the historical

wave climate at a site, significant power smoothing was obtained. In the case of a farm with 48 WECs (6 MW capacity), the variance in the net real power generated for the most commonly occurring sea state when the spacing between the columns of WECs was $0.25\lambda_{peak}$ was 1.5 times higher than the variance when the spacing was $0.5\lambda_{peak}$. The variance of the $0.25\lambda_{peak}$ case was almost 4 times the variance when the spacing was λ_{peak}.

8.3.5 Use of intelligent voltage and power factor control methods

Using the Automatic Voltage and Power Factor Controller (AVPFC) or the Fuzzy Logic Power Factor Controller (FLPFC) was found to be advantageous when compared to the conventionally used generator control options. Using these controllers ensured the connection of the wave power farm to the voltage constrained network for longer, thus increasing yield. It was also found that the voltage and power factor set points of the controllers were network and demand specific. The use of these controllers with other reactive power sources (STATCOMs) was also demonstrated, which proved their generic nature. The FLPFC controller was found to be less site-specific when compared to the AVPFC controller.

8.3.6 Supervisory controller for wave power farms

The operation of the wave power farm and the intelligent controllers, discussed above, assumed that all the WECs in the farm were controlled together. This work was extended in this thesis, with the WECs controlled individually using the AVPFC method. It was shown that when these individual controllers did not communicate with each other, the full capability of AVPFC method was not used. The performance of farm with the intelligent controllers improved immensely when a supervisory controller (master controller) was used, which indicated to the individual controllers (slaves) which control mode - power factor or voltage - to operate in. It can be inferred from this work that some means of communication between the WECs and the onshore or offshore hub would be required to make the most of these intelligent controllers.

Wave power developers need to have extensive instrumentation and communication means (SCADA systems) to control the WEC and check the operation of the WEC onshore [244]. These SCADA systems, which are already present, can be used for the communication required between the WECs in a farm and for the supervisory controller described in this work. The savings listed in the chapter are purely due to intellectual property and are obtained by making the already available system smarter. No additional instrumentation/control facilities are required for implementing these intelligent controllers and implementing these give very

high economic returns.

8.3.7 WEC constraint strategy

During periods of highly energetic seas, it might be found that operating all the WECs at the lowest leading power factor alone is not sufficient to keep the voltage within limits. Under such extreme cases the WECs would need to be constrained off the network. Different individual and group control strategies for taking off the WECs were considered in this work. In this case too, WEC constraint initiated by a supervisory controller, that has knowledge of the contribution of each WEC to the voltage problem, was found to be the optimal means. The use of this WEC constraining strategy ensured that the G59 trip at the interface of the wave power farm with the network was not activated. Even under extremely energetic seas, the wave power farm, with a fewer number of WECs, would continue to operate and produce power rather than be tripped off the network.

8.3.8 Interactions between the controller of the wave power farm and the substation OLTC transformer

With the wave power farm controlled by the intelligent controllers, interactions between the control of the farm and that of the substation OLTC transformer were seen. This was the case especially when the wave power farm operated in the constant voltage mode. When uncoordinated, these interactions caused a greater number of tap operations in the substation transformer, which caused excessive reactive power being exchanged between the network and the farm. By selecting the voltage and power factor set points of the controller of the farm based on the set points of the substation transformer (thus coordinating the two controllers), such negative interactions were avoided. This coordination ensured that the volt/VAr controller of the farm helped overcome smaller variations in the voltage (primary voltage control), while the OLTC transformer dealt with the slower variations in the steady state voltage (secondary voltage control).

8.3.9 One-step-ahead demand predictor

Analysing the demand pattern over three years showed daily, weekly, monthly and annual behavioural characteristics in the demand. Such characteristics were modelled and these models were used to predict the future demands. Three system identified models for predicting the one-step-ahead real power demand at a rural substation were tested. The main advantage of

the models developed was that only past demand data were used to predict the results. All the models constructed produced an error of less than 5% for most of the time during which they were tested. The maximum percentage error seen was approximately 20%, which occurred very rarely. Accurately predicting the demand was useful for the voltage estimation technique that was discussed in the work. Predicting the demand also reduces the number of actual measurements that may need to be made for voltage estimation methods.

8.3.10 Voltage estimation using neural networks

A neural network based voltage estimation technique was developed, which uses the real and reactive power measurements at the substation transformer to make an estimation of the voltage downstream at the bus where the wave power farm is connected. The estimation of the voltage was performed by comparing the real-time real and reactive power flow at the substation with the predicted power flows at the substation prior to the connection of the wave power farm. The precision of the developed method was found to be wholly dependent on the accuracy of the demand prediction made. One of the main advantages of the suggested method is its simplicity when compared to power systems state estimation methods. Such voltage estimation techniques are important in rural distribution networks where, without any addition of measurement devices or communication means, the effects of the connected DG on the network can be studied. Using the information gained from such voltage estimation techniques, the operation of the network can also be optimised.

8.3.11 Quantifying voltage fluctuations

Indices to quantify fluctuations in the rms-voltage magnitude were introduced. Some of the traditional means, like using the flicker severity index and the voltage fluctuation index, were modified to better suit the purpose. New indices, like the energy index ratio and the CPF-index, were introduced. These indices overcome the inapplicability of the traditional indices to quantify the effects of the different wave power farm control strategies on the supply voltage quality. The performance of these indices to assess the rms-voltage quality for different operating scenarios of the wave power farm was compared. The energy index ratio, which is a localised spectral index, performed better than the other indices suggested.

8.4 Potential impact of the study and beneficiaries of this work

The development of the system identification based modelling framework for modelling wave power farms can be used to model other renewable energy sources and generator types. This is especially the case when the modelling aims to study the impacts of connecting a large number of these generators to the power system. High-resolution system identified models, which can be simulated very quickly, can be used to model a high penetration of marine or wind energy converters in large power systems. Such systems will find use in academic and other research circles involved in DG modelling.

The work, which analysed the relation between the physical placement of the WECs within the array and power smoothing obtained, will be useful for wave power farm developers. In addition to the work on power smoothing, the importance of studying the quality of the real power, and hence the voltage, has been established through the work. The statistical work on the directional aspect of the waves and the mean time period (and hence wavelength) of the waves is particularly significant, since the work performed was with the data obtained from the sea off the Outer Hebrides, which is one of the largest potential sites for wave power development in the UK. Very similar sea characteristics would be seen off the Orkneys where significant wave power developments are planned in the Crown Estate leases.

The AVPFC and the FLPFC methods, which have already been tested on wind energy converters and hydro-electric systems, have been used with wave power farms which prove their effectiveness. By using these controllers, the DNOs will be able to provide wider network access to wave power farms in particular and DG in general. The allowed increase in the amount of generation from renewable energy sources, which will follow the widespread use of the control methods, will benefit the farm developers and the DNOs. Increasing the penetration of renewables will help countries meet the stringent emission reduction targets too.

The demand predictor and the voltage estimator developed can improve the functioning and simplify commercially available systems like the GenAVC [207] and the SuperTapp n+ [209]. The developed method introduces an additional level of control and can be used at rural substations without any new addition of measuring devices or communicating means. Having such systems also aids the farm developers because bigger farms may now be connected to the same network once the new method is used. Using the newly developed estimation method also improves the reliability of the distribution network. The probability of issues like a voltage roll-up

would be minimised and the wave power farm would be connected to the network for longer thus increasing its yield. Using system identification for demand prediction is also an area of research, which will interest network operators who need good estimates of futuristic demand conditions.

The voltage fluctuation indices can be taken as the measure for active management of voltages across networks, especially with a high penetration of renewables. They can also be used to study the effects of wide voltage variations on different equipments connected to the network. They will find use in drawing up frameworks for regulation of rms-voltage magnitudes.

8.5 Suggestions for further work

The work on the smoothing in the real power generated and the physical placement of WECs was only performed for heaving WECs. Means to use the spatially sinusoidal nature of ocean waves to our advantage, when other WEC types are used, will need to be studied.

The use of system identification for modelling distributed generators needs to be studied further. Again, in this work, the NARX equivalent models of a heaving WEC was developed. NARX equivalent models of other WEC types may also be developed.

The statistical study of the dominant wave direction and the mean time period used data collected at a site off the Outer Hebrides over a period of three years. A similar study of the seas off the Orkneys should be performed to demonstrate that the results presented here will hold good at the Orkneys too.

The system identification method for demand prediction can be further improved by increasing the number of variables used for the prediction; to include those like temperature, etc., which are conventionally used in demand prediction methods.

Only radial feeders were considered in Chapter 6 to show the working of the voltage estimation algorithm and because many DG connections would be made in such sections of the electricity network. Since the voltage estimation method uses only current and past measurements made at the substation, the method would work even when there are multiple parallel feeders at the substation. In these networks, loads connected to the different buses would still follow a profile and the demand at the substation can be predicted with sufficient historical data. If the parallel feeders are interconnected, then the real and reactive power measurements on the isolated feeders will need to be used in the estimation. In more complex meshed networks more

measurements/predicted quantities may be needed to make good voltage estimates.

Additionally, the proposed voltage estimation method can only be used under normal operating conditions of the network. Efforts need to be made to sense emergencies in the network. One way of doing this could be to compare the current demand values from measurements with older information. If the current measurements differ widely from the expected values, it can be inferred that the network is not operating normally and that the voltage estimates will not be reliable.

The voltage estimation method may be used to optimise the performance of the distribution network. For example, the developed technique may be used to set the substation OLTC transformer's tap position, considering the operation of the wave power farm, to reduce losses or the number of tap position changes.

8.6 Overall thesis conclusions

One of the main issues of connecting the varying power generated by wave power farms is the fluctuations in the voltage that will be seen in the network. In the UK, the areas with a large wave energy resource are supplied by weak distribution networks. In such networks, even small variations in the power fed by the farm can cause significant changes in the voltage seen in the network. The traditional control methods used for dispatchable and controllable power generating sources, such as power factor and voltage control, may not be sufficient for optimal operation of the connected wave power farms. This was shown through simulations of the distributed network with different sized wave power farms connected to it. Two intelligent control algorithms - the Automatic Voltage and Power Factor Control and the Fuzzy Logic Power Factor Control - were tested to control the wave power farm. Using these algorithms ensured the connection of the wave power farm to the network for longer and also ensured that the number and the persistence of the violations in the rms-voltage magnitude reduced. The developed voltage control algorithms were able to prevent voltage violations caused both by the high generation and low demand and the low generation and high demand scenarios. The suggested algorithms also required much smaller amounts of reactive power exchange between the farm and the network than when the constant voltage control method was used. Significant additional income was generated by the increased energy yield and the avoidance of expensive network upgrades.

The advantages of using these advanced voltage and power factor controllers for local and pri-

mary voltage control became evident through the simulation results discussed. Coordination between the controller of the farm with the other voltage control devices in the network, such as the substation on-load tap changing transformer, should also be studied to extend these advantages for wider optimal control across a network. One of the methods of doing so is to sense the voltage at the bus where the farm is connected at the substation. For this, the behavioural patterns in the demand need to be learned and the future demand patterns must be predicted from past measurements of the demand. The voltage downstream of the substation transformer may be estimated using the predicted data, which can further be used to optimise the coordination between the two controllers.

The proposed intelligent farm control algorithms and the method to coordinate the primary control of the farm with the secondary control devices can be used to augment the amount of DG that can be connected to the network, without the use of any new measurement devices or communication links.

8.7 Thesis

The thesis statement expressed in Section 1.3 was that: appropriately placing the wave energy converters within a wave power farm and the use of intelligent voltage and reactive power control algorithms applied to the farm should significantly reduce the voltage fluctuations introduced in the network by the farm and help keep the network voltage within statutory limits. Further, means to coordinate the control of the wave power farm and the other voltage control elements in the distribution network can be devised to ensure that they complement each other. The work presented here proves the above statement by analysing the effects of the placement of WECs on the smoothness of the net real power generated. This study showed that appropriately spacing the WECs or the columns of WECs in a farm produced a much smoother net real power time-series. To improve the voltage quality and to avoid voltage violations, it was found that the smoothing obtained using appropriate placement was to be complemented by real-time reactive power control of the farm. Intelligent voltage and power factor control algorithms were tested and their use improved the quality of the network voltage. Coordinating the control of the farm with other voltage and power factor control devices in the network, through the use of the developed demand predictor and the voltage estimator, gives a chance to use the wave power farm to benefit the wider network.

References

[1] P. Frankl and C. Philibert, "Critical role of renewable energy to climate change mitigation," presented at COP15 International Energy Agency Day Side Event, Copenhagen, Denmark, 2009. [Online]. Available: http://www.iea.org/

[2] "Marine energy technology roadmap," The UK Energy Research Centre and Energy Technologies Institute, Tech. Rep., 2010.

[3] EWEA. (2011) The European Wind Energy Association. [Online]. Available: http://www.ewea.org/

[4] WWEA, "World wind energy report 2010," World Wind Energy Association, Tech. Rep., 2011.

[5] BWEA, "UK offshore wind: Staying on track," British Wind Energy Association, Tech. Rep., 2008.

[6] "Renewables 2010: Global status report," Renewable energy policy network for the 21st century, Tech. Rep., 2010.

[7] "Renewables 2011: Global status report," Renewable energy policy network for the 21st century, Tech. Rep., 2011.

[8] A. Falcao, "Wave energy utilization: A review of the technologies," *Renewable and Sustainable Energy Reviews*, vol. 14, pp. 899–918, 2010.

[9] A. Clement, P. McCullen, A. Falcao, A. Fiorentino, F. Gardner, and K. Hammarlund, "Wave energy in Europe: current status and perspectives," *Renewable and Sustainable Energy Reviews*, vol. 6, pp. 405–431, 2002.

[10] (2011) Pelamis wave power. [Online]. Available: http://www.pelamiswave.com/

[11] (2011) About Wavehub. [Online]. Available: http://www.wavehub.co.uk/

[12] "Atlas of UK marine renewable energy resource," Department for Business, Enterprise and Regulatory Reform, Tech. Rep. 135, 2008.

[13] (2011) Supergen. [Online]. Available: http://www.supergen-marine.org.uk/

[14] H. Saadat, *Power System Analysis*. New York, USA: McGraw-Hill, 2007.

[15] D. I. M. Forehand, "An automatic and efficient time-domain, hydrodynamic wave energy converter array model," in *Proc. of the European Wave and Tidal Energy Conf.*, Southampton, 2011.

[16] R. H. Stewart, *Introduction To Physical Oceanography*. Department of Oceanography, Texas A&M University, 2008.

[17] J. Willard J Pierson and L. Moskowitz, "A proposed spectral form for fully developed wind seas based on the similarity theory of S A Kitaigorodskii," *Journal of Geophysical Research*, vol. 69, no. 24, pp. 5181–5190, 1964.

[18] D. E. Hasselmann, M. Dunckel, and J. A. Ewing, "Directional wave spectra observed during JONSWAP 1973," *Journal of Physical Oceanography*, vol. 10, pp. 1264–1280, 1980.

[19] D. J. T. Carter, "Estimation of wave spectra from wave height and period," Institute of Oceanographic Sciences, Tech. Rep., 1982.

[20] (2011) Wavenet. [Online]. Available: http://www.cefas.co.uk

[21] I. R. Young, "Seasonal variability of the global ocean wind and wave climate," *International Journal of Climatology*, vol. 19, pp. 931–950, 1999.

[22] M. A. Donelan, J. Hamilton, and W. H. Hui, "Directional spectra of wind-generated waves," *Philosophical Transactions of the Royal Society of London. Series A, Mathematical and Physical Sciences*, vol. 315, no. 1534, pp. 509–562, 1985.

[23] G. Chen, B. Chapron, R. Ezraty, and D. Vandemark, "A global view of swell and wind sea climate in the ocean by satellite altimeter and scatterometer," *Journal of Atmospheric and Oceanic Technology*, vol. 19, pp. 1849–1859, 2002.

[24] O. Faltinsen, *Sea Loads on Ships and Offshore Structures*. Cambridge, UK: Cambridge University Press, 1999.

[25] (2011) Faqs. [Online]. Available: http://www.oceanpowertechnologies.com/

[26] E. Bouws, H. Gunther, and W. Rosenthal, "Similarity of the wind wave spectrum in finite water depth: 1. Spectral form," *Journal of Geophysical Research*, vol. 90, no. C1, pp. 975–986, 1985.

[27] S. A. Kitaigordskii, V. P. Krasitskii, and M. M. Zaslavskii, "On Phillips' theory of equilibrium range in the spectra of wind-generated gravity waves," *Journal of Physical Oceanography*, vol. 5, pp. 410–420, 1975.

[28] E. Bouws, H. Gunther, W. Rosenthal, and C. L. Vincent, "Similarity of the wind wave spectrum in finite water depth: Part 2: Statistical relations between shape and growth stage parameters," *Ocean Dynamics*, vol. 40, no. 1, pp. 1–24, 1985.

[29] W. H. Michel, "Sea spectra revisited," *Marine Technology*, vol. 36, no. 4, pp. 211–227, 1999.

[30] WAFO-group, "WAFO - a Matlab Toolbox for analysis of random waves and loads - a tutorial," 2000.

[31] C. G. Soares, Z. Cherneva, and E. M. Antao, "Steepness and asymmetry of the largest waves in storm sea states," *Ocean Engineering*, vol. 31, no. 8-9, pp. 1147–1167, 2003.

[32] ——, "Characteristics of abnormal waves in north sea storm sea states," *Applied Ocean Research*, vol. 25, pp. 337–344, 2004.

[33] (2011) Surgedrive. [Online]. Available: http://www.aquagen.com.au/

[34] (2011) Key features. [Online]. Available: http://wavebob.com/

[35] (2011) Anaconda. [Online]. Available: http://www.checkmateseaenergy.com/

[36] (2006) OWC Pico Power Plant. [Online]. Available: http://www.pico-owc.net/

[37] (2005) Wave Dragon. [Online]. Available: http://www.wavedragon.net/

[38] (2005) Working principle. [Online]. Available: http://www.waveenergy.no/WorkingPrinciple.htm

[39] (2010) The renewable energy challenge. [Online]. Available: http://www.kineticwavepower.com/

[40] (2011) Wave developers. [Online]. Available: http://www.emec.org.uk/

[41] H. Eidsmoen, "Simulation of a slack-moored heaving-buoy wave-energy converter with phase control," Norwegian University of Science and Technology, Tech. Rep., 1996.

[42] (2011) Aegir dynamo. [Online]. Available: http://oceannavitas.com/

[43] (2010) Power pod. [Online]. Available: http://www.tridentenergy.co.uk/

[44] J. Falnes, *Ocean Waves and Oscillating Systems*. Cambridge, UK: Cambridge University Press, 2002.

[45] A. A. E. Price, "New perspectives on wave energy converter control," Ph.D. dissertation, University of Edinburgh, 2009.

[46] J. Falnes, "On non-causal impulse response functions related to propagating water waves," *Applied Ocean Research*, vol. 17, no. 6, pp. 379–389, 1995.

[47] P. C. Vicente, A. F. Falcao, L. M. C. Gato, and P. A. P. Justino, "Dynamics of arrays of floating point-absorber wave energy converters with inter-body and bottom slack-mooring connections," *Applied Ocean Research*, vol. 31, no. 4, pp. 267–281, 2009.

[48] J. Fitzgerald and L. Bergdahl, "Including moorings in the assessment of a generic offshore wave energy converter: A frequency domain approach," *Marine Structures*, vol. 21, no. 1, pp. 23–46, 2008.

[49] A. A. E. Price, C. J. Dent, and A. R. Wallace, "On the capture width of wave energy converters," *Applied Ocean Research*, vol. 31, no. 4, pp. 251–259, 2009.

[50] M. Eriksson, R. Waters, O. Svensson, J. Isberg, and M. Leijon, "Wave power absorption: Experiments in open sea and simulation," *Journal of Applied Physics*, vol. 102, pp. 084 910–1–5, 2007.

[51] W. E. Cummins, "The impulse response function and ship motions," *Schiffstechnik*, vol. 47, no. 9, pp. 101–109, 1962.

[52] *WAMIT User Manual*, 2008. [Online]. Available: http://www.wamit.com/

[53] R. W. Yeung, "Added mass and damping of a vertical cylinder in finite-depth waters," *Applied Ocean Research*, vol. 3, no. 3, pp. 119–133, 1981.

[54] Y. Drobyshevski, "Hydrodynamic coefficients of a floating, truncated vertical cylinder in shallow water," *Ocean Engineering*, vol. 31, pp. 269–304, 2004.

[55] M. E. McCormick and D. R. B. Kraemer, "Long-wave approximations of the added mass and radiation damping of a heaving, vertical, circular, cylindrical in waters of finite depth," *The Journal of Ocean Technology*, vol. 1, no. 2, pp. 58–66, 2006.

[56] M. Eriksson, J. Isberg, and M. Leijon, "Hydrodynamic modelling of a direct drive wave energy converter," *International Journal of Engineering Science*, vol. 43, pp. 1377–1387, 2005.

[57] H. Yavuz, T. J. Stallard, A. P. McCabe, and G. A. Aggidis, "Time series analysis-based adaptive tuning techniques for heaving wave energy converter in irreregular seas," *Journal of Power and Energy*, vol. 221 Part A, no. 1, pp. 77–90, 2007.

[58] H. Yavuz, A. McCabe, G. Aggidis, and M. B. Widden, "Calculation of the performance of resonant wave energy converters in real seas," *Engineering for the Maritime Environment*, vol. 220, no. Part M, pp. 117–128, 2006.

[59] J. Falnes, "Optimum control of oscillation of wave energy converters," Universitetet i Trondheim, Tech. Rep., 1993.

[60] ——, "Principles for capture of energy from ocean waves - phase control and optimum oscillation," Dept. of physics, NTNU, Tech. Rep., 1997.

[61] N. J. Baker, "Linear generators for direct drive marine renewable energy converters," Ph.D. dissertation, University of Durham, 2003.

[62] M. A. Mueller and N. J. Baker, "Direct drive electrical power take-off for offshore marine energy converters," *Journal of Power and Energy*, vol. 219, no. 3, pp. 223–234, 2005.

[63] ——, "Modelling the performance of the vernier hybrid machine," *IEE Proceedings in Electrical Power Applications*, vol. 150, no. 6, pp. 647–654, 2003.

[64] E. Spooner and L. Haydock, "Vernier hybrid machine," *IEE Proceedings in Electrical Power Applications*, vol. 150, no. 6, pp. 655–662, 2003.

[65] N. J. Baker, M. A. Mueller, and E. Spooner, "Permanent magnet air-cored tubular linear generator for marine energy converters," in *Proc. of 2nd Intl. Conf. on Power Electronics, Machines and Drives*, Edinburgh, UK, 2004.

[66] M. A. Mueller and N. J. Baker, "Low speed reciprocating permanent magnet generator for direct drive wave energy converters," in *Proc. of Intl. Conf. on Power Electronics, Machines and Drives*, Bath, UK, 2002.

[67] E. Spooner and M. A. Mueller, "Comparative study of linear generators and hydraulic systems for wave energy conversion," School of Engineering, University of Durham, Tech. Rep., 2001.

[68] *Bladder Accumulators*, 2002. [Online]. Available: http://www.hydacusa.com/

[69] A. F. d. O. Falcao, "Modelling and control of oscillating body wave energy converters with hydraulic power take off and gas accumulator," *Ocean engineering*, vol. 34, no. 14-15, pp. 2021–2032, 2007.

[70] G. Bacelli, J. C. Gilloteaux, and J. Ringwood, "State space model of a hydraulic power take off unit for wave energy conversion employing bondgraphs," in *Proc. of the World Renewable Energy Conference*, Glasgow, UK, 2008.

[71] (2011) Digital Displacement Technology. [Online]. Available: http://www.artemisip.com/

[72] G. S. Payne, A. E. Kiprakis, M. Ehsan, W. H. S. Rampen, J. P. Chick, and A. R. Wallace, "Efficiency and dynamic performance of digital displacement hydraulic transmission in tidal current energy converters," *Journal of Power and Energy*, vol. 221, no. A, pp. 207–218, 2006.

[73] M. Ehsan, W. H. S. Rampen, and S. H. Salter, "Modeling of digital displacement pump motors and their application as hydraulic drives for non uniform loads," *Journal of Dynamic Systems, Measurement, and Control*, vol. 122, no. 1, pp. 210–215, 2000.

[74] (2011) Hydraulics and pneumatics. [Online]. Available: http://www.hydraulicspneumatics.com/

[75] G. S. Payne, U. B. P. Stein, M. Ehsan, N. J. Cladwell, and W. H. S. Rampen, "Potential of digital displacement hydraulics for wave energy conversion," in *Proc. of the 6th European Wave and Tidal Energy Conference*, Glasgow, UK, 2005, pp. 365–371.

[76] I. Boldea, *Variable speed generators*. CRC Taylor and Francis, 2006.

[77] J. A. Baroudi, V. Dinavahi, and A. M. Knight, "A review of power converter topologies for wind generators," *Renewable Energy*, vol. 32, pp. 2369–2385, 2007.

[78] P. K. S. Khan and J. K. Chatterjee, "Three phase induction generators: A discussion on performance," *Electric Machines and Power Systems*, vol. 27, pp. 813–832, 1999.

[79] D. S. Henderson, "Synchronous or induction generators ? - the choice for small scale generation," in *Proc. of the Intl. Conf. on Opportunities and Advances in Intl. Electric Power Generation*, Durham, UK, 1996.

[80] P. C. Krause, O. Wasynczuk, and S. D. Sudhoff, *Analysis of Electric Machinery and Drive Systems*. Ney Jersey, USA: IEEE Press, 2002.

[81] A. M. Trzynadlowski, *Control of Induction Motors*. Academic Press, 2001.

[82] B. K. Bose, *Modern Power Electronics and AC Drives*. Prentice Hall PTR, 2002.

[83] J. Morren, S. de Haan, and J. A. Ferreira, "Model reduction and control of electronic interfaces of voltage dip proof DG units," in *Proc. of the IEEE Power Engineering Society General Meeting*, Denver, Colorado, 2004.

[84] J. G. Slootweg, S. de Haan, H. Polinder, and W. Kling, "Modeling new generation and storage technologies in power system dynamics simulations," in *Proc. of the IEEE Summer Meeting*, Chicago, 2002.

[85] A. Babarit, "Impact of long separating distances on the energy production of two interacting wave energy converters," *Ocean Engineering*, vol. 37, no. 8-9, pp. 718–729, 2010.

[86] A. Babarit, B. Borgarino, P. Ferrant, and A. Clement, "Assessment of the influence of the distance between two wave energy converters on energy production," *IET Renewable Power Generation*, vol. 4, no. 6, pp. 592–601, 2010.

[87] A. Janczak, *Identification of Nonlinear Systems Using Neural Networks and Polynomial Models*. Berlin, Germany: Springer-Verlag, 2005.

[88] L. Ljung and T. Glad, *Modeling of Dynamic Systems*. New Jersey, USA: Prentice Hall, 1994.

[89] L. Ljung, *System Identification: Theory for the user*. New Jersey, USA: Prentice Hall, 1987.

[90] S. Haykin and B. V. Veen, *Signals and Systems*. Kingsport, USA: John Wiley and Sons, 1999.

[91] J. Sjoberg, Q. Zhang, L. Ljung, A. Benveniste, B. Deylon, P.-Y. Glorennec, H. Hjalmarsson, and A. Juditsky, "Nonlinear black-box modeling in system identification: A unified overview," *Automatica*, vol. 31, no. 12, pp. 1691–1724, 1995.

[92] L. Ljung and T. Soderstrom, *Theory and Practice of Recursive Identification*. Cambridge, USA: MIT Press, 1983.

[93] L. Ljung, "Perspectives on system identification," *Annual Reviews in Control*, vol. 34, no. 1, pp. 1–12, 2010.

[94] J. R. R. Vasquez, R. R. Perez, J. S. Moriano, and J. R. P. Gonzalez, "System identification of steam pressure in a fire-tube boiler," *Computers and Chemical Engineering*, vol. 32, no. 12, pp. 2839–2848, 2008.

[95] Y. W. Lee and T. L. Chang, "Application of NARX neural networks in thermal dynamics identification of a pulsating heat pipe," *Energy Conversion and Management*, vol. 50, no. 4, pp. 1069–1078, 2009.

[96] N. Patcharaprakiti, K. Kirtikara, V. Monyakul, D. Chenvidhya, J. Thongpron, A. Sangswang, and B. Meunpinij, "Modeling of single phase inverter of photovoltaic systems using Hammerstein-Weiner nonlinear system identification," *Current Applied Physics*, vol. 10, no. 3 (Supplement 1), pp. S532–S536, 2010.

[97] F. Alonge, F. D'Ippolito, F. M. Raimondi, and S. Tumminaro, "Nonlinear modeling of DC/DC converter using the Hammerstein's approach," *IEEE Transactions on Power Electronics*, vol. 22, no. 4, pp. 1210–1221, 2007.

[98] J. Choi, B. H. Cho, H. F. VanLandingham, H. Mok, and J. Song, "System identification of power converters based on black-box approach," *IEEE Transactions on Circuits and Systems - I: Fundamental Theory and Applications*, vol. 45, no. 11, pp. 1148–1158, 1998.

[99] V. T. Kontargyri, A. A. Gialketsi, G. J. Tsekouras, I. F. Gonos, and I. A. Stathopulos, "Design of an artificial neural network for the estimation of the flashover voltage on insulator," *Electric Power Systems Research*, vol. 77, no. 12, pp. 1532–1540, 2007.

[100] E. Pisoni, M. Fariina, C. Carnevale, and L. Piroddi, "Forecasting peak air pollution levels using NARX models," *Engineering Applications of Artificial Intelligence*, vol. 22, no. 4-5, pp. 593–602, 2009.

[101] M. Espinoza, J. A. K. Suykens, R. Belmans, and B. D. Moor, "Electric load forecasting - using kernel-based modelling for nonlinear system identification," *IEEE Control Systems Magazine*, pp. 43–57, 2007.

[102] S. Mallat, *A Wavelet Tour of Signal Processing*. New York: Academic Press, 1999.

[103] R. Polikar, *The Wavelet Tutorial*, 2001. [Online]. Available: http://users.rowan.edu/ polikar/wavelets/wttutorial.html

[104] I. Daubechies, *Ten Lectures on Wavelets*. Philadelphia, USA: Society for Industrial and Applied Mathematics, 1992.

[105] H. Krim, "Wavelets: A multiscale analysis tool," in *Encyclopedia of Telecommunications*. Wiley Online, 2003.

[106] J. A. Hawkins, A. C. Warn-Varnas, and I. Christov, "Fourier, scattering, and wavelet transforms: Applications to internal gravity waves with comparisons to linear tidal data," in *Nonlinear Time Series Analysis in Geosciences*, R. V. Donner and S. M. Barbosa, Eds. Springer, 2009.

[107] C. Valens, *A really friendly guide to wavelets*, 1999. [Online]. Available: http://polyvalens.pagesperso-orange.fr/clemens/wavelets/wavelets.html

[108] S. P. Nanavati and P. K. Panigrahi, "Wavelet transform - a new mathematical microscope," *Resonance*, vol. 9, no. 3, pp. 50–64, 2004.

[109] D. Veitch, "Wavelet neural networks and their application in the study of dynamical systems," Master's thesis, University of York, 2005.

[110] R. M. Rao and A. S. Bopardikar, *Wavelet transforms - Introduction to theory and applications*. Natick, USA: Addison-Wesley, 1998.

[111] M. Misiti, Y. Misiti, G. Oppenheim, and J. M. Poggi, *Fuzzy Logic Toolbox User's guide*, 2011. [Online]. Available: http://www.mathworks.com

[112] D. W. Kammler, *A First Course in Fourier Analysis*. Cambridge, UK: Cambridge University Press, 2008.

[113] S. Haykin, *Neural networks - A comprehensive foundation*. Delhi, India: Pearson Education, 1999.

[114] G. Dreyfus, *Neural networks - Methodology and applications*. Paris, France: Springer Online, 2004.

[115] B. R. Bakshi, "Wave-nets: novel learning techniques, and the induction of physically interpretable models," *Wavelet Applications*, vol. 2242, pp. 637–648, 1994.

[116] A. A. Safavi and J. A. Romagnoli, "Application of wave-nets to modelling and optimisation of a multidimensional chemical process," in *Proc. of the IEEE International Conference on Neural Networks*, Perth, Australia, 1995.

[117] Q. Zhang and A. Benveniste, "Wavelet networks," *IEEE Transactions on Neural Networks*, vol. 3, no. 6, pp. 889–898, 1992.

[118] E. J. Hartman, J. D. Keeler, and J. M. Kowalski, "Layered neural networks with gaussian hidden units as universal approximations," *Neural Computation*, vol. 2, pp. 210–215, 1990.

[119] L. Ljung, *System Identification Toolbox 7 Userś guide*, 2010. [Online]. Available: http://www.mathworks.com

[120] D. W. Marquardt, "An algorithm for least-squares estimation of nonlinear parameters," *Journal of the Society for Industrial and Applied Mathematics*, vol. 11, no. 2, pp. 431–441, 1963.

[121] A. Rahrooh and S. Shepard, "Identification of nonlinear systems using NARMAX model," *Nonlinear Analysis: Theory, Methods & Applications*, vol. 71, no. 12, pp. e1198–e1202, 2009.

[122] "The electricity safety, quality and continuity regulations 2002," Queen's Printer of Acts of Parliament, Tech. Rep., 2002.

[123] P. McIver, "Arrays of wave-energy devices," in *Proc. of 10th Intl. Workshop on Water Waves and Floating Bodies*, Oxford, UK, 1995.

[124] B. F. M. Child and V. Venugopal, "Optimal configurations of wave energy device array," *Ocean Engineering*, vol. 37, no. 16, pp. 1402–1417, 2010.

[125] C. Fitzgerald and G. Thomas, "A preliminary study on the optimal formation of an array of wave power devices," in *Proc. of European Wave and Tidal Energy Conference 2007*, Porto, Portugal, 2007.

[126] J. Cruz, R. Sykes, P. Siddorn, and R. E. Taylor, "Estimating the loads and energy yield of arrays of wave energy converters under realistic seas," *IET Renewable Power Generation*, vol. 4, no. 6, pp. 488–497, 2010.

[127] M. Folley and T. J. T. Whittaker, "The effect of sub-optimal control and the spectral wave climate on the performance of wave energy converter arrays," *Applied Ocean Research*, vol. 31, no. 4, pp. 260–266, 2009.

[128] G. De Backer, M. Vantorre, C. Beels, J. De Rouck, and P. Frigaard, "Power absorption by closely spaced point absorbers in constrained conditions," *IET Renewable Power Generation*, vol. 4, no. 6, pp. 579–591, 2010.

[129] V. Venugopal and G. H. Smith, "Wave climate investigation for an array of wave power devices," in *Proc. of 7th European Wave and Tidal Energy Conf.*, Porto, Portugal, 2007.

[130] I. G. C. Ashton, L. Johanning, and B. Linfoot, "Measurement of the effect of power absorption in the lee of a wave energy converter," in *Proc. of ASME 2009 Intl. Conf. on Ocean, Offshore and Arctic Engineering*, Honolulu, Hawaii, 2009.

[131] A. E. Kiprakis, A. J. Nambiar, D. I. M. Forehand, and A. R. Wallace, "Modelling arrays of wave energy converters connected to weak, rural electricity networks," in *Proc. of the Intl. Conf. on Supergen*, Nanjing, 2009.

[132] P. Lagonotte, J. C. Sabonnadiere, J. Y. Leost, and J. P. Paul, "Structural analysis of the electrical system: Application to secondary voltage control in France," *IEEE Transactions on Power Systems*, vol. 4, no. 2, pp. 479–486, 1989.

[133] A. Conejo and M. Aguilar, "Secondary voltage control: Nonlinear selection of pilot buses, design of an optimal control law, and simulation results," *IEE Proc.-Gener. Transm. Distrib.*, vol. 145, no. 1, pp. 77–81, 1998.

[134] S. Repo, H. Laaksonen, and P. Jarventausta, "New methods and requirements for planning of medium voltage network due to distributed generation," in *Proc. of the Nordic Distribution and Asset Management Conf.*, Espoo, Finland, 2004.

[135] Q. Zhou and J. W. Bialek, "Generation curtailment to manage voltage constraints in distribution networks," *IET Gener. Transm. and Distrib.*, vol. 1, no. 3, pp. 492–498, 2007.

[136] T. Tran-Quoc, E. Monnot, G. Rami, A. Almeida, C. Kieny, and N. Hadjsaid, "Intelligent voltage control in distribution network with distributed generation," in *Proc. of the CIRED 19th Intl. Conf. on Electricity Distribution*, Vienna, Austria, 2007.

[137] Y. Zhang, Z. Jiang, and X. Yu, "Control strategies for battery or supercapacitor hybrid energy storage systems," in *Proc. of the IEEE Energy 2030 Conference*, Atlanta, USA, 2008.

[138] A. Babarit, H. B. Ahmed, A. H. Clement, V. Debusschere, G. Duclos, B. Multon, and G. Robin, "Simulation of electricity supply of an Atlantic island by offshore wind turbines and wave energy converters associated with a medium scale local energy storage," *Renewable Energy*, vol. 31, no. 2, pp. 153–160, 2006.

[139] J. V. Paatero and P. D. Lund, "Effect of energy storage on variations in wind power," *Wind Energy*, vol. 8, pp. 421–441, 2005.

[140] N. C. Scott, D. J. Atkinson, and J. E. Morrell, "Use of load control to regulate voltage on distribution networks with embedded generation," *IEEE Transaction on Power Systems*, vol. 17, no. 2, pp. 510–515, 2002.

[141] A. J. Collin, J. L. Acosta, I. Hernando-Gil, and S. Z. Djokic, "An 11kV steady-state residential aggregate load model. Part 2: Microgeneration and demand-side management," in *Proc. of the IEEE PowerTech*, Trondheim, Norway, 2011.

[142] *Submarine power cables*, 2008. [Online]. Available: http://www. nexans.co.uk

[143] M. J. Heathcote, *The J&P Transformer book.* Oxford, UK: Newnes, 1998.

[144] *Aluminium conductor steel reinforced*, 2011. [Online]. Available: http://www.drakauk.com

[145] J. D. Hurley, L. N. Bize, and C. R. Mummert, "The adverse effects of excitation system Var and power factor controllers," *IEEE Transactions on Energy Conversion*, vol. 14, no. 4, pp. 1636–1645, 1999.

[146] T. W. Eberly and R. C. Schaefer, "Voltage versus Var/power-factor regulation on synchronous generators," *IEEE Transactions on Industry Applications*, vol. 38, no. 6, pp. 1682–1687, 2002.

[147] J. D. Crabtree, Y. Dickson, L. Kerford, and A. Wright, "Methods to accommodate embedded generation without degrading network voltage regulation," Department of Trade and Industry, Tech. Rep., 2001.

[148] F. A. Viawan and D. Karlsson, "Combined local and remote voltage and reactive power control in the presence of induction machine distributed generation," *IEEE Transactions on Power Systems*, vol. 22, no. 4, pp. 2003–2012, 2007.

[149] J. H. Choi and J. C. Kim, "The online voltage control of ULTC transformer for distribution voltage regulation," *Electrical Power and Energy Systems*, vol. 23, no. 2, pp. 91–98, 2001.

[150] M. S. Calovic, "Modeling and analysis of under-load tap-changing transformer control systems," *IEEE Transactions on Power Apparatus and Systems*, vol. PAS-103, no. 7, pp. 1909–1915, 1984.

[151] S. K. Salman and I. M. Rida, "ANN-based AVC relay for voltage control of distribution network with and without embedded generation," in *Proc. of the Intl. Conf. on Electric Utility Deregulation and Restructuring and Power Technologies*, London, UK, 2000.

[152] S. K. Salman and Z. G. Wan, "Voltage control of distribution network with distributed/embedded generation using fuzzy logic-based AVC relay," in *Proc. of the Universities' Power Engineering Conf.*, Brighton, UK, 2007.

[153] S. K. Salman and I. M. Rida, "Investigating the impact of embedded generation on relay settings of utilities electrical feeders," *IEEE Transactions on Power Delivery*, vol. 2, no. 16, pp. 246–251, 2001.

[154] A. E. Kiprakis and R. Wallace, "Generator-OLTC transformer synergy for increased energy export and improved voltage profiles within distribution networks with large amounts of wind generation," in *Proc. of the Intl. Conf. on Deregulated Electricity Market Issues in South-Eastern Europe*, Nicose, Cyprus, 2008.

[155] M. Gillie, J. Hiscock, and A. Creighton, "On site trials of the new SuperTapp N+ AVC relay - a step towards an active network," in *Proc. of the CIRED Seminar 2008: Smart Grids for Distribution*, Frankfurt, Germany, 2008.

[156] M. Fila, J. Hiscock, G. Taylor, M. Irving, and P. Lang, "Modelling and analysis of the enhanced TAPP scheme for distribution networks," in *Proc. of the 16th Power Systems Computation Conf.*, Glasgow, UK, 2008.

[157] V. Thornley, J. Hill, P. Lang, and D. Reid, "Active network management of voltage leading to increased generation and improved network utilisation," in *Proc. of the CIRED Seminar 2008: Smart Grids for Distribution*, Frankfurt, Germany, 2008.

[158] M. Larsson, "Coordination of cascaded tap changers using a fuzzy-rule based controller," *Fuzzy Sets and Systems*, vol. 102, no. 1, pp. 113–123, 1999.

[159] Y. Nakachi, S. Kato, and H. Ukai, "Coordinated voltage control of transformer taps with provision for hierarchical structure in power systems," *Electrical Engineering in Japan*, vol. 166, no. 4, pp. 48–55, 2009.

[160] A. E. Kiprakis and A. R. Wallace, "Maximising energy capture from distributed generators in weak networks," *IEE Proc.-Gener. Transm. Distrib.*, vol. 151, no. 5, pp. 611–618, 2004.

[161] G. P. Harrison, A. E. Kiprakis, and A. R. Wallace, "Network integration of mini-hydro," *re-gen*, pp. 56–63, 2008.

[162] A. E. Kiprakis, "Increasing the capacity of distributed generation in electricity networks by intelligent generator control," Ph.D. dissertation, University of Edinburgh, 2005.

[163] P. N. Vovos, A. E. Kiprakis, A. R. Wallace, and G. P. Harrison, "Centralised and distributed voltage control: Impact on distributed generation penetration," *IEEE Transactions on Power Systems*, vol. 22, no. 1, pp. 476–483, 2007.

[164] R. Datta and V. T. Ranganathan, "Direct power control of grid-connected wound rotor induction machine without rotor position sensors," *IEEE Transactions on Power Electronics*, vol. 16, no. 3, pp. 390–399, 2001.

[165] K. Pandiaraj and B. Fox, "Novel voltage control for embedded generators in rural distribution networks," in *Proc. of the Intl. Conf. on Power System Technology*, Perth, Australia, 2000.

[166] R. C. Bansal, "Bibliography on the fuzzy set theory applications in power systems (1994 to 2001)," *IEEE Transactions on Power Systems*, vol. 18, no. 4, pp. 1291–1299, 2003.

[167] R. M. Hilloowala and A. M. Sharaf, "A rule-based fuzzy logic controller for a PWM inverter in a stand alone wind energy conversion scheme," *IEEE Transactions on Industry Applications*, vol. 32, no. 1, pp. 57–65, 1996.

[168] M. G. Simoes, B. K. Bose, and R. J. Spiegel, "Design and performance evaluation of a fuzzy-logic-based variable-speed wind generation system," *IEEE Transactions on Industry Applications*, vol. 33, no. 4, pp. 956–965, 1997.

[169] M. Lown, E. Swidenbank, and B. W. Hogg, "Adaptive fuzzy logic control of a turbine generator system," *IEEE Transactions on Energy Conversion*, vol. 12, no. 4, pp. 394–399, 1997.

[170] B. J. LaMeres and M. H. Nehrir, "Fuzzy logic based voltage controller for a synchronous generator," *IEEE Computer Applications in Power*, pp. 46–49, 1999.

[171] R. H. Liang and Y. S. Wang, "Fuzzy-based reactive power and voltage control in a distribution system," *IEEE Transactions on Power Delivery*, vol. 18, no. 2, pp. 610–618, 2003.

[172] D. H. Spatti, I. N. daSilva, W. F. Usida, and R. A. Flauzino, "Real-time voltage regulation in power distribution system using fuzzy control," *IEEE Transactions on Power Delivery*, vol. 25, no. 2, pp. 1112–1123, 2010.

[173] E. H. Mamdani and S. Assilian, "An experiment in linguistic synthesis with a fuzzy logic controller," *International Journal of Man-Machine Studies*, vol. 7, no. 1, pp. 1–13, 1975.

[174] *Fuzzy Logic Toolbox User's guide*, 2011. [Online]. Available: http://www.mathworks.com

[175] (2011) United kingdom generic distribution system. [Online]. Available: http://www.sedg.ac.uk

[176] "Long term development statement for Scottish Hydro Electric Power Distribution plc's electricity distribution system," Scottish Hydro Electric Power Distribution, Tech. Rep., 2009.

[177] *Notes of guidance for the protection of embedded generating plant upto 5 MW for operation in parallel with public electricity suppliers distribution systems*. Energy Networks Association, 1995, vol. Engineering Technical Report 113.

[178] M. A. Choudhry, K. N. Bangash, T. Mahmood, and A. Hanif, "Voltage control measures by using STATCON through PSS/E in WAPDA power system," *Advances in Computer, Information, and System Sciences, and Engineering*, pp. 53–59, 2006.

[179] Z. S. Saoud, M. L. Lisboa, J. B. Ekanayake, N. Jenkins, and G. Strbac, "Application of statcoms to wind farms," *IEE Proc.-Gener. Transm. Distrib.*, vol. 145, no. 5, pp. 511–516, 1998.

[180] T. Senjyu, N. Sueyoshi, R. Kuninaka, K. Uezato, H. Fujita, and T. Funabashi, "Terminal voltage and power factor control of induction generators for wind power generation system," *Electrical Engineering in Japan*, vol. 163, no. 3, 2008.

[181] M. Barnes, R. El-Feres, S. Kromlides, and A. Arulampalam, "Power quality improvement for wave energy converters using a D-STATCOM with real energy storage," in *Proc. of the 1st Intl. Conf. on Power Electronic Systems and Applications*, Hong Kong, 2004, pp. 72–77.

[182] E. Larsen, N. Miller, S. Nilsson, and S. Lindgren, "Benefits of GTO-based compensation systems for electric utility applications," *IEEE Transactions on Power Delivery*, vol. 7, no. 4, pp. 2056–2064, 1992.

[183] N. A. Lahacani, D. Aouzellag, and B. Mendil, "Static compensator for maintaining voltage stability of wind farm integration to a distribution network," *Renewable Energy*, vol. 35, no. 11, pp. 2476–2482, 2010.

[184] R. Tonkoski, L. A. C. Lopes, and T. H. M. El-Fouly, "Coordinated active power curtailment of grid connected PV inverters for overvoltage prevention," *IEEE Transactions on Sustainable Energy*, vol. 2, no. 2, pp. 139–147, 2011.

[185] T. Boehme, A. R. Wallace, and G. P. Harrison, "Applying time series to power flow analysis in networks with high wind penetration," *IEEE Transactions on Power Systems*, vol. 22, no. 3, pp. 951–957, 2007.

[186] (2011) North West Lewis. [Online]. Available: http://www.aquamarinepower.com

[187] "Our electricity transmission network: A vision for 2020," Electricity Networks Strategy Group, Tech. Rep., 2010.

[188] (2011) The renewables obligation (Scotland) order 2011- consultation on review of ROC bands October 2011. [Online]. Available: http://www.scotland.gov.uk/Publications

[189] (2011) Eligible renewable sources and banding levels. [Online]. Available: http://www.decc.gov.uk

[190] (2012) The renewables obligation buy-out price and mutualisation ceiling 2012-13. [Online]. Available: http://www.ofgem.gov.uk

[191] (2012) Online ROC auction service track record. [Online]. Available: http://www.e-roc.co.uk/trackrecord.htm

[192] S. Engelhardt, I. Erlich, C. Feltes, J. Kretschmann, and F. Shewarega, "Reactive power capability of wind turbines based on doubly fed induction generators," *IEEE Transactions on Energy Conversion*, vol. 26, no. 1, pp. 364–372, 2011.

[193] M. H. J. Bollen and A. Sannino, "Voltage control with inverter-based distributed generation," *IEEE Transactions on Power Delivery*, vol. 20, no. 1, pp. 519–520, 2005.

[194] C. Dai and Y. Baghzouz, "On the voltage profile of distribution feeders with distributed generation," in *Proc. of the IEEE Power Engineering Society General Meeting*, Toronto, Canada, 2003.

[195] T. E. Kim and J. E. Kim, "Voltage regulation coordination of distributed generation systems in distribution systems," in *Proc. of the IEEE Power Engineering Society Summer Meeting*, Vancouver, Canada, 2001, pp. 480–4845.

[196] M. E. Baran and M.-Y. Hsu, "Volt/Var control at distribution substations," *IEEE Transactions on Power Systems*, vol. 14, no. 1, pp. 312–318, 1999.

[197] "IEEE 34 node test feeder," Distribution System Analysis Subcommittee, Tech. Rep., 2010.

[198] S. A. Arefifar and W. Xu, "Online tracking of power system impedance parameters and field experiences," *IEEE Transactions on Power Delivery*, vol. 24, no. 4, pp. 1781–1788, 2009.

[199] G. B. Jasmon and L. H. C. C. Lee, "Distribution network reduction for voltage stability analysis and loadflow calculations," *Intl. Journal of Electrical Power & Energy Systems*, vol. 13, no. 1, pp. 9–13, 1991.

[200] J. Radosalvljevic, M. Jevtic, and D. Klimenta, "Optimal seasonal voltage control in rural distribution networks with distributed generators," *Journal of Electrical Engineering*, vol. 61, no. 6, pp. 321–331, 2010.

[201] M. H. Haque, "A general load flow method for distribution systems," *Electric Power Systems Research*, vol. 54, no. 1, pp. 47–54, 2000.

[202] ——, "Efficient load flow method for distribution systems with radial or mesh configuration," *IEE Proc-Gener. Transm. Distrib.*, vol. 143, no. 1, pp. 33–38, 1996.

[203] D. Das, D. P. Kothari, and A. Kalam, "Simple and efficient method for load flow solution of radial distribution networks," *Electrical Power & Energy Systems*, vol. 27, no. 5, pp. 335–346, 1995.

[204] M. E. Baran and A. W. Kelley, "State estimation for real-time monitoring of distribution systems," *IEEE Transactions on Power Systems*, vol. 9, no. 3, pp. 1601–1609, 1994.

[205] C. M. Hird, H. Leite, N. Jenkins, and H. Li, "Network voltage controller for distributed generation," *IEE Proc-Gener. Transm. Distrib.*, vol. 151, no. 2, pp. 150–156, 2004.

[206] I. Cobelo, A. Shafiu, N. Jenkins, and G. Strbac, "State estimation of networks with distributed generation," *European Transactions on Electrical Power*, vol. 17, no. 1, pp. 21–36, 2007.

[207] (2010) Senergy. [Online]. Available: http://www.senergyworld.com/

[208] J. Hiscock, N. Hiscock, and A. Kennedy, "Advanced voltage control for networks with distributed generation," in *Proc. of the 19th Intl. Conf. on Electricity Distribution*, Vienna, Austria, 2007.

[209] (2010) Fundamentals Ltd. [Online]. Available: http://www.fundamentalsltd.co.uk/

[210] M. Fila, D. Reid, J. Reid, P. Lang, J. Hiscock, and G. A. Taylor, "Flexible voltage control in distribution networks with distributed generation - modelling analysis and field trial comparison," in *Proc. of the CIRED 20th Intl. Conf. on Electricity Distribution*, Prague, Czech Republic, 2009.

[211] E. A. Feinberg and D. Genethliou, "Load forecasting," in *Applied Mathematics for Restructured Electric Power Systems*, J. H. Chow, F. F. Wu, and J. A. Momoh, Eds. SpringerLink, 2005, pp. 269–285.

[212] E. A. Mohamad, M. M. Mansour, S. E. Debeiky, K. G. Mohamad, N. D. Rao, and G. Ramakrishna, "Results of Egyptian unified grid hourly load forecasting using an artificial neural network with expert system interface," *Electric Power Systems Research*, vol. 39, no. 3, pp. 171–177, 1996.

[213] S. Rahman, "Formulation and analysis of a rule-based short-term load forecasting algorithm," *Proceedings of the IEEE*, vol. 78, no. 5, pp. 805–816, 1990.

[214] O. Hyde and P. F. Hodnett, "Rule-based procedures in short-term electricity load forecasting," *IMA Journal of Mathematics Applied in Business & Industry*, vol. 5, pp. 131–141, 1993/4.

[215] D. K. Ranaweera, N. F. Hubele, and G. G. Karady, "Fuzzy logic for short term load forecasting," *Electrical Power and Energy Systems*, vol. 18, no. 4, pp. 215–222, 1996.

[216] A. M. Al-Kandari, S. A. Soliman, and M. E. El-Hawary, "Fuzzy short-term electric load forecasting," *Electrical Power & Energy Systems*, vol. 26, no. 2, pp. 111–122, 2004.

[217] S. C. Pandian, K. Duraiswamy, C. C. A. Rajan, and N. Kanagaraj, "Fuzzy approach for short-term load forecasting," *Electric Power Systems Research*, vol. 76, no. 6-7, pp. 541–548, 2006.

[218] H. K. Alfares and M. Nazeeruddin, "Electric load forecasting: literature survey and classification of methods." *International Journal of Systems Science*, vol. 33, no. 1, pp. 23–34, 2002.

[219] S. Civanlar and J. J. Grainger, "Forecasting distribution feeder loads: Modeling and application to Volt/VAr control," *IEEE Transactions on Power Delivery*, vol. 3, no. 1, pp. 255–264, 1988.

[220] H. Wang and N. N. Schulz, "Using AMR data for load estimation for distribution system analysis," *Electric Power Systems Research*, vol. 76, no. 5, pp. 336–342, 2006.

[221] W. Y. Loh, "Classification and regression tree methods," in *Encyclopedia of Statistics in Quality and Reliability*, F. Ruggeri, R. Kenett, and F. Faltin, Eds. Wiley, 2008.

[222] L. Breiman, J. H. Friedman, R. A. Olshen, and C. J. Stone, *Classification and Regression Trees*. California, USA: Wadsworth Intl. Group, 1984.

[223] M. Devine and E. I. Baring-Gould, "The Alaska village electric load calculator," National Renewable Energy Laboratory, Tech. Rep., 2004.

[224] D. K. Ranaweera, G. G. Karady, and R. G. Farmer, "Economic impact analysis of load forecasting," *IEEE Transactions on Power Systems*, vol. 12, no. 3, pp. 1388–1392, 1997.

[225] K. Samarakoon, J. Wu, J. Ekanayake, and N. Jenkins, "Use of delayed smart meter measurements for distribution state estimation," in *Proc. of the IEEE Power & Energy Society General Meeting*, Michigan, USA, 2011.

[226] D. L. Brooks, R. C. Dugan, M. Waclawiak, and A. Sundaram, "Indices for assessing utility distribution system rms variation performance," *IEEE Transactions on Power Delivery*, vol. 13, no. 1, pp. 254–259, 1998.

[227] G. H. Kjolle, K. Samdal, B. Singh, and O. A. Kvitastein, "Customer costs related to interruptions and voltage problems: methodology and results," *IEEE Transaction on Power Systems*, vol. 23, no. 3, pp. 1030–1038, 2008.

[228] M. Delfanti, E. Fumagalli, P. Garrone, L. Grilli, and L. L. Schiavo, "Toward voltage-quality regulation in Italy," *IEEE Transaction on Power Delivery*, vol. 25, no. 2, pp. 1124–1132, 2010.

[229] CEER, "Guidelines of good practice on estimation of costs due to electricity interruptions and voltage disturbances," Council of European Energy Regulators (CEER), Tech. Rep., 2010.

[230] J. L. G. Iglesias and A. McEachern, "The economics of power quality - a systematic framework for the assessment," in *Proc. of the CIRED 19th Intl. Conf. on Electricity Distribution*, Vienna, Austria, 2007.

[231] *Voltage characteristics of electricity supplied by public distribution networks*. British Standards Institutions, 2007, vol. BS EN 50160:2007.

[232] P. Chiradeja and R. Ramakumar, "Voltage profile improvement with distributed generation," *IEEE Transactions on Energy Conversion*, vol. 19, no. 4, pp. 764 – 773, 2004.

[233] M. H. J. Bollen and I. Y. H. Gu, "Characterization of voltage variations in the very-short time-scale," *IEEE Transactions on Power Delivery*, vol. 20, no. 2, pp. 1198–1199, 2005.

[234] M. H. J. Bollen, M. Hager, and C. Schwaegerl, "Quantifying voltage variations on a time scale between 3 seconds and 10 minutes," in *Proc. of the 18th Intl. Conf. on Electricity Distribution*, Turin, Italy, 2005.

[235] K. Brekke, H. Seljeseth, and O. Mogstad, "Rapid voltage changes definition and minimum requirements," in *Proc. of the 20th Intl. Conf. on Electricity Distribution*, Prague, 2009.

[236] J. Schlabbach, D. Blume, and T. Stephanblome, *Voltage Quality in Electrical Power Systems*. Stevenage, UK: IEE, 2001.

[237] M. H. J. Bollen and P. Verde, "A framework for regulation of rms voltage and short-duration under and overvoltages," *IEEE Transaction on Power Delivery*, vol. 23, no. 4, pp. 2105–2112, 2008.

[238] J. C. Gomez and M. M. Morcos, "Flicker measurement and light effect," *IEEE Power Engineering Review*, pp. 11–15, 2002.

[239] *Flickermeter - Functional and design specifications*. British Standards Institutions, 1993, vol. BS EN 60868-0:1993.

[240] T. Keppler, N. Watson, and J. Arrillaga, "Computation of the short-term flicker severity index," *IEEE Transactions on Power Delivery*, vol. 15, no. 4, pp. 1110–1115, 2000.

[241] W. Freitas, J. C. M. Vieira, A. Morelato, and W. Xu, "Influence of excitation system control modes on the allowable penetration level of distributed synchronous generators," *IEEE Transactions on Energy Conversion*, vol. 20, no. 2, pp. 474–480, 2005.

[242] A. Woyte, V. V. Thong, R. Belmans, and J. Nijs, "Voltage fluctuations on distribution level introduced by photovoltaic systems," *IEEE Transactions on Energy Conversion*, vol. 21, no. 1, pp. 202–209, 2006.

[243] B. Mulgrew, P. Grant, and J. Thompson, *Digital Signal Processing Concepts and Applications*. London, UK: Macmillan Press Ltd., 1999.

[244] "Guidelines on design and operation of wave energy converters," Carbon Trust, Tech. Rep., 2005.

Appendix A
UK generic distribution network

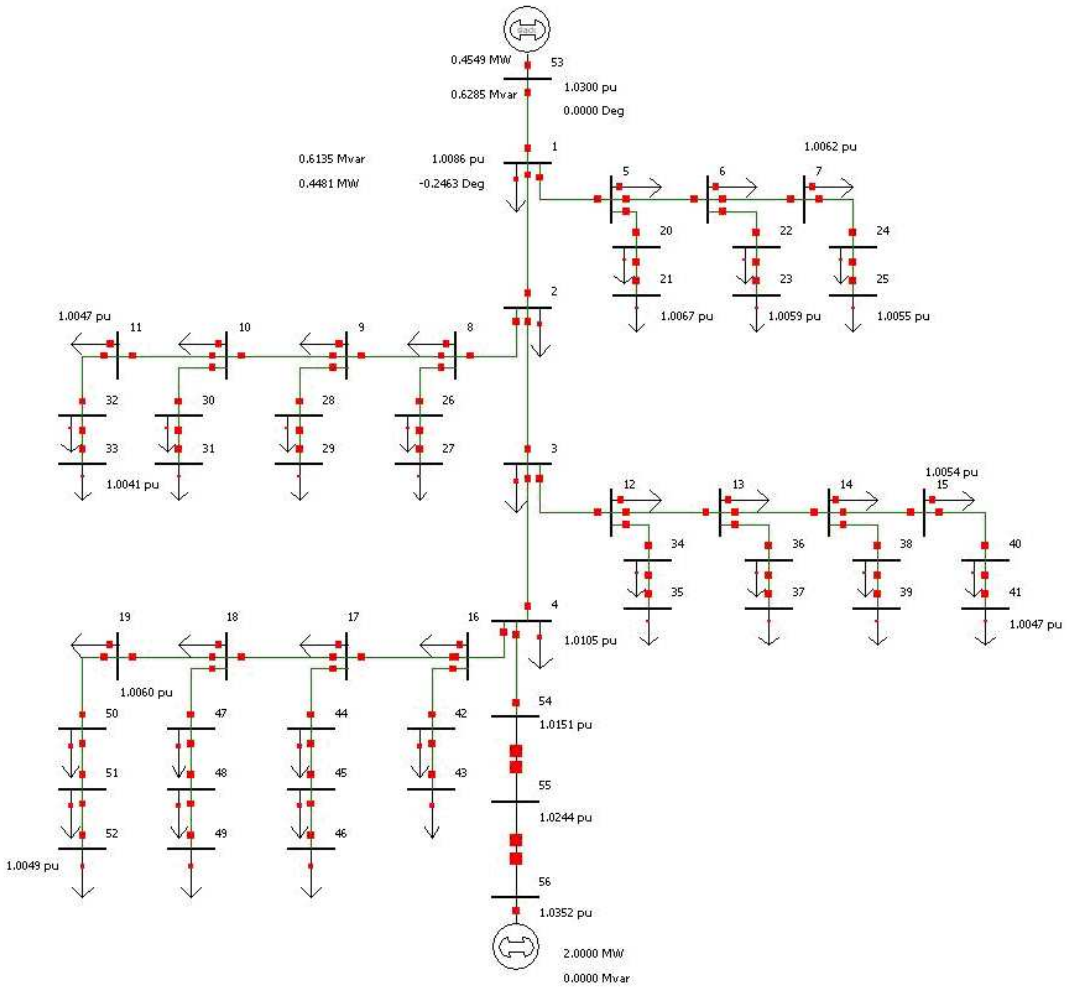

Figure A.1: *Generic 11kV UK distribution network.*

Bus 1	Bus 2	R (p.u.)	X (p.u.)	B/2 (p.u.)
53	1	1.2029	2.6435	0
1	2	0.2508	0.1698	0
2	3	0.2508	0.1698	0
3	4	0.2508	0.1698	0
1	5	0.2480	0.1780	0
5	6	0.2480	0.1780	0
6	7	0.2480	0.1780	0
2	8	0.1860	0.1335	0
8	9	0.1860	0.1335	0
9	10	0.1860	0.1335	0
10	11	0.1860	0.1335	0
3	12	0.1860	0.1335	0
12	13	0.1860	0.1335	0
13	14	0.1860	0.1335	0
14	15	0.1860	0.1335	0
4	16	0.1860	0.1335	0
16	17	0.1860	0.1335	0
17	18	0.1860	0.1335	0
18	19	0.1860	0.1335	0
5	20	0.3556	0.1331	0
20	21	0.3556	0.1331	0
6	22	0.3556	0.1331	0
22	23	0.3556	0.1331	0
7	24	0.3556	0.1331	0
24	25	0.3556	0.1331	0
8	26	0.3556	0.1331	0
26	27	0.3556	0.1331	0
9	28	0.3556	0.1331	0
28	29	0.3556	0.1331	0
10	30	0.3556	0.1331	0
30	31	0.3556	0.1331	0
11	32	0.3556	0.1331	0
32	33	0.3556	0.1331	0
12	34	0.3556	0.1331	0
34	35	0.3556	0.1331	0
13	36	0.3556	0.1331	0
36	37	0.3556	0.1331	0
14	38	0.3556	0.1331	0
38	39	0.3556	0.1331	0
15	40	0.3556	0.1331	0
40	41	0.3556	0.1331	0
16	42	0.3556	0.1331	0
42	43	0.3556	0.1331	0
17	44	0.2371	0.0887	0
44	45	0.2371	0.0887	0
45	46	0.2371	0.0887	0
18	47	0.2371	0.0887	0
47	48	0.2371	0.0887	0
48	49	0.2371	0.0887	0
19	50	0.2371	0.0887	0
50	51	0.2371	0.0887	0
51	52	0.2371	0.0887	0
56	55	0.6667	3.3330	0
55	54	0.4900	0.1288	4.94e-5
54	4	0.2480	0.1780	0

Table A.1: *UK generic distribution network line parameters*

Bus	Bus type	Load (MW)	Load (MVAr)
1	PQ	0.0065	0.00125
2	PQ	0.0065	0.00125
3	PQ	0.0085	0.00175
4	PQ	0.0085	0.00175
6	PQ	0.00425	0.00075
7	PQ	0.0065	0.00125
8	PQ	0.0065	0.00125
9	PQ	0.0065	0.00125
10	PQ	0.0065	0.00125
11	PQ	0.0065	0.00125
12	PQ	0.0065	0.00125
13	PQ	0.0065	0.00125
14	PQ	0.0065	0.00125
15	PQ	0.0065	0.00125
16	PQ	0.0065	0.00125
17	PQ	0.0065	0.00125
18	PQ	0.0065	0.00125
19	PQ	0.0065	0.00125
20	PQ	0.0150	0.00300
21	PQ	0.0150	0.00300
22	PQ	0.0150	0.00300
23	PQ	0.0150	0.00300
24	PQ	0.0150	0.00300
25	PQ	0.0150	0.00300
26	PQ	0.0065	0.00125
27	PQ	0.0065	0.00125
28	PQ	0.0150	0.00300
29	PQ	0.0150	0.00300
30	PQ	0.0150	0.00300
31	PQ	0.0150	0.00300
32	PQ	0.0150	0.00300
33	PQ	0.0150	0.00300
34	PQ	0.0065	0.00125
35	PQ	0.0065	0.00125
36	PQ	0.0150	0.00300
37	PQ	0.0150	0.00300
38	PQ	0.0150	0.00300
39	PQ	0.0150	0.00300
40	PQ	0.0150	0.00300
41	PQ	0.0150	0.00300
42	PQ	0.0150	0.00300
43	PQ	0.0150	0.00300
44	PQ	0.0150	0.00300
45	PQ	0.0150	0.00300
46	PQ	0.0150	0.00300
47	PQ	0.0170	0.00350
48	PQ	0.0170	0.00350
49	PQ	0.0170	0.00350
50	PQ	0.0170	0.00350
51	PQ	0.0170	0.00350
52	PQ	0.0170	0.00350
53	PQ	0.0	0.0
54	PQ	0.0	0.0
55	PQ	0.0	0.0
56	PQ	0.0	0.0

Table A.2: *UK generic distribution network bus parameters*

Appendix B
Publications

B.1 Journal publications

- **A J Nambiar, A E Kiprakis and A R Wallace**, 'System identification for dynamic modelling of large wave power farms for power flow studies', submitted to the IET Renewable Power Generation (August 2012) (*not included*)

B.2 Conference publications

- **A J Nambiar, A E Kiprakis, D I M Forehand and A R Wallace**, 'Effects of array configuration, network impacts and mitigation of arrays of wave energy converters connected to weak, rural electricity networks', 3rd International Conference and Exhibition on Ocean Energy (ICOE 2010), 6-8 October 2010

- **A J Nambiar, A E Kiprakis and A R Wallace**, 'Quantification of Voltage Fluctuations Caused by a Wave Farm Connected to Weak, Rural Electricity Networks', 14th International Conference on Harmonics and Power Quality (ICHQP 2010), 26-29 September 2010

- **A J Nambiar, A E Kiprakis and A R Wallace**, 'Voltage quality control of a 1MW wave farm connected to weak, rural electricity networks', 45th Universities' Power Engineering Conference (UPEC 2010), 31 August - 3 September 2010 (*not included since paper (ii) shows further work done*)

- **A E Kiprakis, A J Nambiar, D I M Forehand and A R Wallace**, 'Modelling Arrays of Wave Energy Converters Connected to Weak Rural Electricity Networks', 1st International Conference on SUPERGEN, 6-7 April 2009 (*not included since paper (i) shows further work done*)